

Trapping and cooling of single molecular ions for time resolved experiments

Dissertation der Fakultät für Physik
der
Ludwig-Maximilians-Universität München



vorgelegt von Steffen Kahra
aus Rochlitz

München, den 24. September 2010

Erstgutachter: Dr. Tobias Schätz
Zweitgutachter: Prof. Dr. Dietrich Habs
Tag der mündlichen Prüfung: 14. März 2011

Zusammenfassung

In der vorliegenden Arbeit werden isolierte, einzeln orts aufgelöste molekulare Ionen mit einer Femtosekundenspektroskopie auf der Basis von Einzelreaktionsereignissen untersucht. Für die zur simultanen Speicherung von atomaren und molekularen Ionen notwendige Radiofrequenzfalle wurde eine transportable Vakuumapparatur konzipiert und realisiert sowie die zugehörigen Lasersysteme aufgebaut und eingerichtet. Um die Ultrahochvakuumbedingungen bei $2 \cdot 10^{-10}$ mbar auch bei häufiger Molekülpräparation gewährleisten zu können, wurde ein modularer Aufbau gewählt, bei dem Präparations- und Experimentierbereich durch differentielle Pumpstrecken voneinander getrennt sind. Durch diese hindurch führt ein 48 cm langer Quadrupolionenleiter, in welchem Ionen zwischen den Kammern transferiert werden können. Entlang des Ionenleiters ermöglichen ringförmige Gleichspannungselektroden eine dreidimensionale Speicherung der Ionen.

Im Rahmen dieser Arbeit wurde mit atomaren $^{24}\text{Mg}^+$ und molekularen $^{24}\text{MgH}^+$ Ionen gearbeitet. Erstere werden durch Photoionisation von Magnesiumatomen aus einem thermischen Strahl erzeugt und ihre Bewegungsenergie durch Laserkühlung soweit reduziert, dass sie in etwa 20 μm Abstand voneinander in einer kristallinen Struktur erstarren. Magnesiumhydridionen werden nach Einleiten von Wasserstoffgas in einer photochemischen Reaktion mit $^{24}\text{Mg}^+$ generiert und – von verbleibenden atomaren Ionen sympathetisch gekühlt – auf Gitterplätze des Kristalls integriert. Bei der Laserkühlung von $^{24}\text{Mg}^+$ ausgesendete Fluoreszenzphotonen ermöglichen die optische Detektion der Ionen mit derzeit bis zu 1 μm Ortsauflösung. Die nicht fluoreszierenden molekularen Ionen werden indirekt als vermeintlich unbesetzte Stellen der Kristallstruktur sichtbar.

Neben der Demonstration des Erfolges unseres Fallenkonzepts sowie dessen Charakterisierung bildet der verlustfreie, kontrollierte Transport von atomaren und molekularen Ionen aus dem Präparations- in den Experimentierbereich, eine wichtige Errungenschaft, welche zu einem kontinuierlichen Nachladen von Ionen mit einer Rate von über 100 Hz ausgebaut werden kann.

Diese Arbeit präsentiert eine Machbarkeitsstudie zur Kombination von Präzisionsmethoden zweier Forschungsgebiete. Dazu wurde die Fallenapparatur mit einem weiteren Vakuumsystem, in dem ultraviolette Femtosekundenpulse erzeugt werden können, über ein System von differenziellen Pumpstrecken verbunden. Als Resultat werden 5 fs zeitaufgelöste Pump-Probe Experimente vorgestellt, die die Oszillation eines Vibrationswellenpaketes von individuellen $^{24}\text{MgH}^+$ Molekülionen zeigen. Dabei wird die Bewegung des Wellenpaketes auf die Dissoziationswahrscheinlichkeit in einem bestimmten Zerfallskanal abgebildet. Einzelne Reaktionsereignisse konnten eindeutig nachgewiesen und daraus das zeitabhängige Verhalten extrahiert werden. Diese Resultate untermauern das Potenzial der von uns angestrebten Kombination der exzellenten Kontrolle über externe und interne Freiheitsgrade gespeicherter Ionen mit der extremen Zeitauflösung von modernen Kurzpulslasern. Weitere Arbeiten können die Vorteile beider Gebiete nutzen um bisher unzugängliche Experimente zu realisieren. Die besonderen Eigenschaften der präsentierten Apparatur sollten es beispielsweise erlauben, einzelne isolierte molekulare Ionen mit hoher räumlicher Präzision und wohl kontrollierten Anfangsbedingungen für zukünftige Strukturuntersuchungen mittels derzeit entstehender, intensiver Kurzpuls-Röntgenquellen an freien Elektronenlasern bereitzustellen.

Abstract

In the thesis at hand, isolated, singly spatially resolved molecular ions are investigated with femtosecond spectroscopy on the basis of single reaction events. For the radio frequency trap required for simultaneous trapping of atomic and molecular ions, a movable apparatus was designed and realized as well as the corresponding laser system set up and adjusted. In order to ensure $2 \cdot 10^{-10}$ mbar ultrahigh vacuum conditions even with frequent molecular ion preparation, a modular design was opted for that separates preparation and experimental chamber by differential pumping stages. A 48 cm long quadrupole ion guide is fed through the vacuum isolation and allows to transfer ions between the chambers. Ring shaped direct voltage electrodes along the ion guide can facilitate a three-dimensional trapping potential for the ions.

In the framework of this thesis, experiments with atomic $^{24}\text{Mg}^+$ and molecular $^{24}\text{MgH}^+$ ions were performed. The former are generated by photoionization of magnesium atoms in a thermal beam. By the means of laser cooling the ions' kinetic energy is sufficiently reduced, so that their positions get frozen in a crystalline structure with typical distances of 20 μm . Magnesium hydride ions are produced in a photochemical reaction of $^{24}\text{Mg}^+$ with injected hydrogen gas. Remaining $^{24}\text{Mg}^+$ ions sympathetically cool the molecular ions and integrate them on lattice sites of the crystalline structure. Fluorescence photons emitted during laser cooling of the atomic ions allow the optical detection of $^{24}\text{Mg}^+$ with a spatial resolution of presently up to 1 μm . The non-fluorescing molecular ions become indirectly visible as seemingly unoccupied crystal lattice sites.

Besides the demonstration of the success of our trap concept as well as its characterization, the essentially lossless, controlled transport of atomic and molecular ions from the preparation chamber to the experimental chamber establishes an important achievement which can be extended to continuous reloading of ions with a repetition rate of more than 100 Hz.

This thesis is about a proof-of-method experiment that demonstrates the combination of precision methods of two research fields. To this end, the trap apparatus was connected via a system of differential pumping stages to another vacuum system inside which ultraviolet femtosecond pulses were generated. As a result, time-resolved pump-probe experiments with 5 fs resolution could be performed. They show the oscillation of a vibrational wave packet in individual $^{24}\text{MgH}^+$ molecular ions. The experimental scheme maps the wave packet's motion onto the dissociation probability in a certain decay channel. Single reaction events were clearly detectable. By counting them, the time-dependent dissociation yield could be extracted. These results substantiate the potential of our approach to combine the excellent control over external and internal degree of freedom of trapped ions with the extreme temporal resolution of modern short pulse laser systems. Further work in this direction may benefit from the advantages of both fields and might open up ways to presently inaccessible experiments. The unique properties of the presented apparatus should, for instance, allow to prepare single, isolated molecular ions with high spatial precision and well-defined initial conditions for future structure determination of organic molecules with intensive short pulse X-ray sources on currently developed free electron lasers.

Contents

Introduction	1
1. Theory	7
1.1. Radio frequency trapping	7
1.1.1. Radial confinement	7
1.1.2. Axial confinement	11
1.2. Laser cooling	12
1.3. Sympathetic cooling	17
1.4. Short optical pulses	18
2. Ion trap apparatus	22
2.1. Vacuum system	22
2.1.1. Preparation chamber	22
2.1.2. Isolation chamber	25
2.1.3. Experiment chamber	25
2.2. Radio frequency guide	27
2.3. Ring electrodes	30
2.4. Differential pumping stages	33
2.5. Atom oven	35
2.6. Imaging system	37
2.6.1. Radiation pattern of ions	38
2.6.2. Imaging objectives	39
2.6.3. Fluorescence detection	40
2.7. Ion trapping laser system	41
2.7.1. Magnesium laser system	42
2.7.2. Barium laser system	47
2.8. Experiment control	52
3. Femtosecond apparatus	55
3.1. Femtosecond laser system	55
3.2. UV pulse generation	58
3.3. Delay line	60
3.4. Beam line connection	64
4. Experimental building blocks	67
4.1. Ion trapping	67
4.1.1. Coulomb crystal structures	68

4.1.2.	Radial cooling	68
4.1.3.	Isotope cleaning by charge-to-mass filtering	71
4.1.4.	Trap frequencies	72
4.1.5.	Molecular ion preparation	75
4.2.	Ion transfer	75
4.2.1.	Transfer method 1	78
4.2.2.	Transfer method 2	79
4.2.3.	Transfer method 3	81
4.3.	Photochemical reactions induced by the cooling laser	87
4.4.	Third harmonic generation	90
5.	Results on single molecule time-resolved spectroscopy	95
5.1.	The magnesium hydride ion	95
5.1.1.	quantum chemical treatment	96
5.1.2.	pump probe excitation	101
5.2.	Experimental procedure	103
5.3.	Experimental results	108
5.3.1.	vibrational heating	108
5.3.2.	intensity dependence	111
5.3.3.	time-resolved dissociation	112
6.	Summary and Outlook	118
6.1.	Current achievements	118
6.2.	Further development and applications	120
A.	Software	124
A.1.	Laboratory software	124
A.1.1.	director	124
A.1.2.	iXon!	127
A.2.	Image analysis software	128
A.2.1.	À trous wavelet transform	128
A.2.2.	Segmentation	132
A.2.3.	Dark ion identification	135
A.3.	Simulation software	137
A.3.1.	Adaptive simulated annealing	138
A.3.2.	Particle dynamics	140
B.	Devices	142
B.1.	Electron gun	142
B.2.	Atom oven	143
B.3.	Barium handling	143
B.4.	Photo multiplier	147
B.5.	Pellicle	148

B.6.	Ring electrodes	151
B.7.	Compensation electrodes	152
C.	Concepts	154
C.1.	Maximum likelihood method	154
C.1.1.	application to simulated data	155
C.2.	Second harmonic generation	158
C.3.	Velocity filtering	159

Introduction

The microscopic perspective on structures and processes does not only reveal a fascinating view on nature but opens also a door for exploration and explanation of new phenomena. The wish to observe fundamental processes in greater detail drives the development of many experimental methods aiming for higher resolution. One of the examples where tremendous progress expresses itself in enormous precision is the single cooled atomic ion in a radio frequency trap allowing for measurements that belong to the most precise ones of today's physics. To illustrate that, the presently most accurate optical atomic clock shows a fractional frequency inaccuracy of $8.6 \cdot 10^{-18}$ and has been realized in a single aluminum ion trapped together with a magnesium ion [31]. The excellent control over motion and internal states of atomic ions in radio frequency traps offers a vast set of established methods for manipulating single particles. They can be applied for implementations of quantum information processors [180] or quantum simulations [56], for example.

This thesis aimed to develop an interface allowing to combine the well controlled, isolated particle from the field of ion trapping with the femtosecond time resolution provided by the precisely controlled generation and manipulation of short laser pulses. Our endeavor is mainly driven by the prospect to pioneer a realm that forms from the symbiosis of two fields and might lead—among other potential applications—to the development of new techniques that are envisioned to be most relevant for time-resolved structure analysis by X-ray diffraction on single molecular ions. Although still in an early stage of development, brilliant X-ray sources have become available that already now produce femtosecond pulses containing 10^{12} coherent photons of 2 keV energy. In future, single, identically initialized, isolated molecular ions are aspired to be delivered for diffraction experiments in near background-free ultrahigh vacuum conditions. Similar to a conveyor-belt but container-free localized with a precision better than 1 μm , molecular ions shall be provided with a repetition rate of at least 100 Hz. This thesis describes the development and application of an apparatus as well as suitable methods required to actualize the first steps. Important building blocks of the concept were devised and principal techniques are demonstrated.

Subsequently, a brief and not complete overview of developments in the relevant areas of short pulse physics is drafted; for a profound introduction to the topic see [22, 139, 174], for example. It follows a motivation of our proposed approach to reliably prepare identically initialized single molecular ions under precise control in a radio frequency trap and the description of a promising application. The introduction concludes with a short outline.

It took about three decades after the invention of the laser [142, 110] until the era of femtosecond laser pulses was entered and another ten years until it became possible to generate laser pulses that were sufficiently short to resolve the fastest structural changes inside molecules [119, 118], i. e. pulses on the lower 10 fs time scale. The time scale of the fastest nuclear motion inside molecules is approximately equal to the shortest possible duration of laser pulses in the near infrared and visible spectral range [29, 136]. It is encountered at a few femtoseconds when a laser pulse is formed by down to a single electromagnetic field oscillation.

Femtosecond laser pulses accompanied by the precise control of the electromagnetic field [88] provided the basis for many breakthroughs in the field of precision [184, 65] and time-resolved experiments [188]. For example, it has become possible to infer the pathway of photochemical excitations inside small diatomic molecules [35, 51, 101] up to large biomolecules [24, 75] and intramolecular chemical reactions [164, 2] from time-resolved spectroscopic results. The control over the interaction of light and molecules even allows to steer chemical reactions into dedicated product channels by exploiting quantum interference effects due to a coherently stimulated molecular excitation [25] or to concerted subsequent excitations [166].

In recent years, further progress paved the way for investigations using attosecond pulses. This is the time scale to describe the motion of electrons [100] inside atoms [152] and condensed matter [28]. Furthermore, the exploration of electronic motion in molecules reveals completely new insight [141]. Access to this time regime is granted by laser pulses of much shorter wavelength and more rapid electromagnetic field oscillations than in the visible spectral range. The extreme properties of those pulses imply elaborate laser systems with applications requiring vacuum setups.

Separately and in parallel to the improvement of the temporal resolution, imaging techniques exhibiting ever increasing spatial resolution reaching the atomic scale have been developed. Although other methods such as cryo-electron microscopy on single particles have been shown to resolve atomic scale details [190], most of today's knowledge about protein structures is based on crystallographic X-ray diffraction studies. Presently, the RCSB protein data bank [182] lists 57 544 X-ray resolved structures which amounts to 87 % of all entries. Brilliant X-ray radiation sources established at various synchrotrons [15] worldwide made it possible to resolve the structure of numerous molecules and proteins at the atomic level.

To extend the current capabilities of these instruments even further, the so called fourth generation of the large accelerator facilities focuses on the production of *coherent*, extremely brilliant pulsed X-ray radiation [112, 147] by periodically accelerated high energetic electron beams in free electron lasers [108, 52]. By the time of writing this thesis, femtosecond pulses with a fluence of 10^5 X-ray photons per \AA^2 and photon energies of up to 2 keV corresponding to a wavelength of 6 \AA have already been achieved [185]. By that, wavelengths required to resolve atomic-scale details of molecular structures are approached. In only a few years from now Europe's accelerator based free electron laser will be commissioned and provide even more energetic pulses with corresponding wavelengths down to 1 \AA . Another approach to the same goal—namely short and intense X-ray pulses—is followed in the framework of the Munich Center for Advanced Photonics (MAP). Different from the acceleration of electrons to relativistic energies in kilometer-scale common particle accelerators, the electrons shall gain a comparable amount of energy by laser wake-field acceleration [131] over a length of only a few millimeter. First encouraging results have already been reported [58]. These small-scale setups might also be more accessible and flexible to adapt to non-standard applications than accelerator-based free electron laser sources.

Since about a decade there is growing interest to combine the technological achievements of structure analysis with the progress made in short pulse generation physics. This synergy is also one of the main goals of MAP and central to the work of this thesis. Other groups worked on the visualization of movement on the atomic scale using short, pulsed electron beams before [162, 48, 187, 134]. Due to space charge effects the ultimate temporal resolution is achieved with

single electron pulses [11] only. It is thus expected to take—from the experimentalist’s point of view—unrealistically many repetitions of identically prepared diffraction experiments to build up a diffractogram containing sufficient information to compute the molecular structure of a single particle target from single electron diffraction events.

Although the elastic scattering cross section of electrons is at least 4 orders of magnitude higher than that of comparable energetic X-rays, it appears more promising to use X-rays for diffraction [30] because the lower scattering cross section is expected to be more than compensated for by the tremendous amount of 10^{12} coherent photons contained in each single pulse planned to be generated at a rate of up to several kHz at the upcoming fourth generation accelerators. While common X-ray diffraction techniques are successful for proteins that can be crystallized, only little can be learned from diffraction of randomly oriented many particle samples. This might change if it was possible to record diffraction images of single, isolated molecules [173, 161], i. e. without the need for macroscopic protein crystals. By contrast to crystallography, single particle coherent X-ray diffraction results in a continuously distributed intensity pattern of diffracted X-rays. Recording the diffraction image with sufficient spacial resolution (“oversampling”) allows to reconstruct the electronic density function of the sample even though phase information about the diffracted X-rays has been discarded by the detector [170].

The proposal described in [117] assumes a single X-ray pulse to diffract sufficiently many photons from only a single molecule to form a meaningful diffractogram. If the orientation of the molecule in the laboratory frame is not known beforehand this requires the diffraction image to contain at least the information, i. e. photon counts at non-zero scattering angles, necessary to roughly determine the orientation of the molecule by comparing different diffraction patterns. Subsequent classification and averaging of orientation-corrected diffraction images is envisioned to yield the complete three-dimensional picture. In case the recordings contain discernible signal at high scattering angles, one diffractogram of a single shot exposure might be sufficient to reconstruct the molecule’s atomic scale structure. Knowledge about the molecule’s orientation was dispensable then. The required photon flux depends on the targeted resolution but usually exceeds $1 \cdot 10^6 \text{ \AA}^{-2}$. This causes transient ionization of the molecule already during the interaction of the X-ray pulse [117, 183, 23, 80]. The onset of Coulomb explosion during the exposure limits the achievable spatial resolution. A realistic view on the undisturbed molecular structure can thus only be obtained if the X-ray pulse duration is short compared to the time it takes the molecule to change its structure significantly ($\lesssim 10 \text{ fs}$) [117, 80]. Once single molecule diffractive imaging will have been successful, it is natural to apply it in time-resolved pump-probe experiments. At this point of time, the old dream to observe nature’s microcosm by watching an molecule’s motion while it changes its structure or even during chemical reactions will have become true.

Besides the work needed to be done to realize the envisioned X-ray pulses, the capitol problem of target preparation has to be solved [173]. The above scenario assumes single molecules to be localized in the correct position at the instant when the X-ray pulse arrives. In order to reach a photon flux above $1 \cdot 10^6 \text{ \AA}^{-2}$ per pulse, a tightly focused X-ray beam is required. $1 \text{ \mu m} \times 2 \text{ \mu m}$ spot sizes have been obtained already but further reduction down to 100 nm diameter is being worked on [185]. The probability to hit a particle with these minute foci in sprayed gaseous samples by chance gets inadmissible low. It might be argued that a low hit rate could be, at least partially,

accounted for with higher particle densities—1 particle in the $0.1 \mu\text{m} \times 0.1 \mu\text{m} \times 100 \mu\text{m}$ focal beam volume corresponds to $4 \cdot 10^{-5}$ mbar at room temperature—in principle. However, charged particle densities of that size—corresponding to an average particle distance of $1 \mu\text{m}$ —in an expanding sprayed beam must be considered unrealistic at present. Neither do they solve other fundamental problems, such as partially hit particles or contributions of impurity molecular species.

Our group's approach to these problems is to prepare suitable, identically initialized, single molecular ion targets in a radio frequency trap—much like on a conveyor belt but with the distinction of being isolated from the environment by container-free preparation in ultrahigh vacuum. This will allow for samples that are expected to be reliably localized and positioned with spatial resolutions better than $1 \mu\text{m}$ right in focus of the X-ray beam. Radio frequency traps are highly developed instruments that provide excellent control over the external degrees of freedom of trapped particles [145, 1]. With the help of lasers [163, 148] and other appropriate methods [98, 130, 62], the internal degrees of freedom of molecular ions can be manipulated, too. For example, the motional and internal states of atomic ions are under such excellent control that they provide a toolbox for concepts to realize a scalable quantum computer [96]. To illustrate this point further, the position uncertainty of a single trapped ion in these experiments is determined only by the spread of its quantum mechanical ground state wave function which is on the order of 10 nm [40].

Our conveyor-belt for trapped ions can be set into operation by the external motion and hence the position of trapped ions being controlled by electrode voltages on the microsecond time scale. Replacing molecular ions at the pulse repetition rate of today's pulsed X-ray sources ($\approx 100 \text{ Hz}$) appears feasible. Especially since encouraging results have already been reported [7, 153, 1]. Additional methods required to further enhance the control over the trapped ions are foreseen to be implemented in the present apparatus. These include buffer gas cooling [50] of the molecular ions' internal degrees of freedom [62], field-free laser alignment [81, 171, 169, 103] and enhanced control over the position of individual particles with e. g. filigree segmented electrodes [151, 144].

The concept of sympathetic cooling [138] renders radio frequency traps versatile devices. In principle any (in our case positively charged) ion with suitable mass-to-charge ratio may be investigated. The requirement of molecules being charged can be fulfilled in several ways depending on the context of the experiment. Smaller molecules of which unresolved rapidly unfolding time-dependent structural changes are tantalizing to be investigated, e. g. the configuration isomerism of azobenzene [71, 167], can be charged by attaching alkaline (proton accepting) groups via electrical isolating (not conjugated double) chemical bonds. Organic molecular structures usually comprise many amino acids. Some of them (lysine, arginine, histidine, cysteine, tyrosine) are naturally protonized or can be protonized in acidic environment. By that, a macromolecule is likely to be multiply charged. This helps to account for its higher mass and obtain a suitable charge-to-mass ratio. Simulations suggest that additional do not necessarily disturb the molecular structure. A water layer around the molecule in vacuum can be utilized to stabilize it against the electrostatic influence of charges on its surface [111]. After all, many biological relevant molecules are functional in a charged state only [63]. Method of choice for charging both small and big molecules is protonation by electro-spray ionization [54, 53], a procedure that simultaneously injects the particles into the vacuum [120, 125]. By this gentle way of adding charges, the “even total number of electrons”-rule is obeyed, i. e. the molecule stays a closed shell system, which hardly alters its photochemical properties. In conclu-

sion, electro-spray ionization in combination with radio frequency traps is expected to provide a viable means for investigation of biomolecules [77] under isolated conditions [175].

Thesis outline

The present apparatus realizes three major building blocks of the envisioned deterministic precision molecular ion source. In the first place, it allows to trap and laser cool atomic ions and utilize them for sympathetic cooling of simultaneously trapped molecular ions. Within this thesis atomic $^{24}\text{Mg}^+$ were trapped together with magnesium hydride $^{24}\text{MgH}^+$ ions that were generated in a photochemically reaction of atomic $^{24}\text{Mg}^+$ with neutral hydrogen gas. Other molecular ions can be loaded by electron bombardment of gaseous neutral molecules and in near future from a realized but not yet connected electro-spray ionization source.

Furthermore, efficient and well controlled transfer of ions from the loading zone of the apparatus to the experimental chamber maintained under ultrahigh vacuum conditions ($2 \cdot 10^{-10}$ mbar)—the second building block of the main concept—was realized.

The third goal was achieved by connecting the vacuum apparatus to a beam line for short and intense ultraviolet pulses, therefore similar to future experiments at, for instance, free electron laser facilities. This connection was accomplished without affliction of the vacuum conditions on the one hand and by omission of adverse dispersive elements in the beam path on the other hand.

Finally, first femtosecond time-resolved experiments on single molecular ion targets could be demonstrated. However, suitable X-ray sources for single molecule imaging are still to be finalized. Therefore, spectroscopic studies on single molecular $^{24}\text{MgH}^+$ ions were carried out to demonstrate the proof of method. The vibration of diatomic molecular ions was investigated using the presently shortest ultraviolet laser pulses in the appropriate spectral range. The results presented in this thesis and the proficiency gained in the endeavor to merge the relevant two previously unrelated fields of research are expected to contribute to the advance of future X-ray diffraction experiments on single and isolated particles at the femtosecond time scale .

- Chapter 1 introduces the main concepts of ion trapping, laser cooling of atomic ions and sympathetic cooling of molecular ions on the one side and of short laser pulses on the other side. Instead of trying to provide a profound theoretical basis for the mathematical treatment of these disciplines, this chapter aims at a broader readership out of the two so far separated communities. Since the details of ion trapping usually do not overlap with the research focus of the photonics physicist and *vice versa*, this chapter emphasizes only the key formulas and basic concepts of both research fields combined in this thesis. Relevant literature for studies beyond that scale is specified.
- Chapter 2 is dedicated to the precise description of the ion trap apparatus that was designed and setup within this thesis. Supplemented by the appendix, all relevant information about the vacuum setup, the radio frequency trap and its technical accessories, the cw-laser setup for ion cooling as well as the experiment control is assorted.

- Chapter 3 describes the femtosecond laser system including the third harmonic generation stage that was used to generate 5 fs UV pulses and the connection of the UHV ion trap to the beam line. In particular, the adaption of that system to the requirements of the pump-probe experiments on $^{24}\text{MgH}^+$ ions and the related manipulation of the spectrum of the pulses is focused on.
- Chapter 4 concentrates on the experimental building blocks required for the realization of the femtosecond single molecule pump-probe experiments. In the beginning, basic experiments aiming at trap characterization, ion loading and molecular ion preparation are described. In the following, the ion transfer from the molecular ion preparation region to the ultrahigh vacuum chamber is discussed from a simulative and experimental point of view. Finally, the adaption of the femtosecond laser system to the requirements of the molecular ion experiments are discussed and results are presented.
- Chapter 5 describes the main result of this thesis. All previous technical achievements cumulate in the realization of the proof-of-method time-resolved dissociation experiments resolving the vibrational motion of individual and isolated magnesium hydride ions. During the preparation phase of the experiments and for the interpretation of the results, a quantum chemical *ab initio* model of $^{24}\text{MgH}^+$ was developed in close cooperation with Markus Kowalewski from the group of Prof. deVivie-Riedle. The clean, almost background-free but also isolated conditions of single molecular ions in vacuum differ significantly from studies with the targets prepared in, for instance, solution. Comparison of the simulation results with the measurements allowed to investigate how the peculiarities of isolated molecular ions can be taken into account by the model. It is the combination of $^{24}\text{MgH}^+$ being a theoretically treatable molecular system on the one side and being an almost perfectly isolated particle on the other side that gives the opportunity to observe and interpret unusual effects under well controlled conditions. One example that was actually investigated is vibrational heating induced by repeated electronic excitations of the same molecular ion.
- The summary and outlook concludes the thesis with a brief review of the presently achieved results and includes proposals for future applications. Direct extensions of the current project are discussed as well as future developments for the envisioned experiments at high-intensity X-ray sources. A not complete list of further directions of development emphasizes the broad applicability of our apparatus in various research fields.

1. Theory

1.1. Radio frequency trapping

Electromagnetic fields (\mathbf{E}, \mathbf{B}) exert a Lorentz-force $\mathbf{F} = q(\mathbf{E} + \mathbf{v} \times \mathbf{B})$ on charged particles and provide a means to influence their motion. Appropriate force fields can be tailored such that ions remain in the vicinity of some center point. The force field is then said to form a trap for the ion.

Static electric fields in a charge-free space are not able to form a trapping potential Φ for ions. This follows from the electrostatic Maxwell equations in charge-free space which require Φ to satisfy Laplace's equation $\Delta\Phi = 0$, i. e. be harmonic. Harmonic functions can be shown to take on their maximum and minimum value on the boundary of an open neighborhood (*maximum principle*). Therefore, the electric potential is maximal or minimal inside an electrode but never in free space—known as Earnshaw theorem. Its consequences for the electric potential of the particular electrode configuration of this thesis is illustrated in fig. 1.1a on the following page.

However, it is possible to trap ions using a superposition of static magnetic and electric fields (Penning trap) [37, 132], fast oscillating electrical fields of intense laser beams (dipole trap) [146] or more slowly oscillating electric fields at radio frequencies (Paul trap) [128, 132, 127]. Only the latter is considered in the following. It is not aspired to give a comprehensive presentation of the theoretical framework of ion trapping in this thesis. A good starting point for research on this topic might be [127] and the references therein.

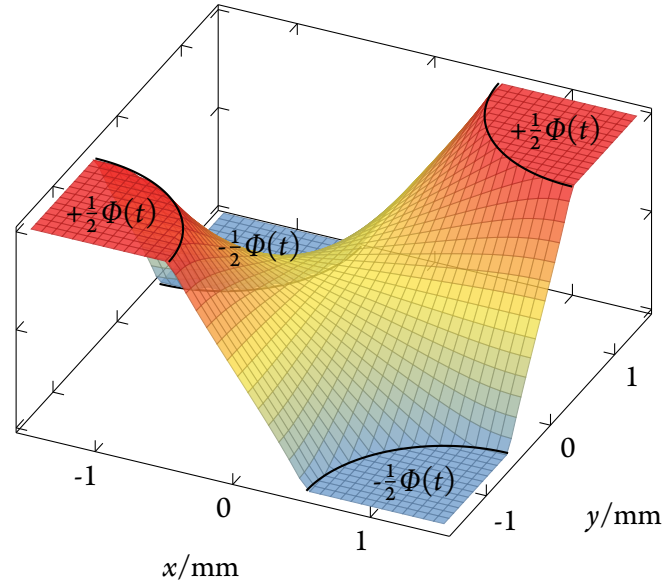
1.1.1. Radial confinement

In two dimensions, Maxwell's equations are satisfied by the quadrupole potential

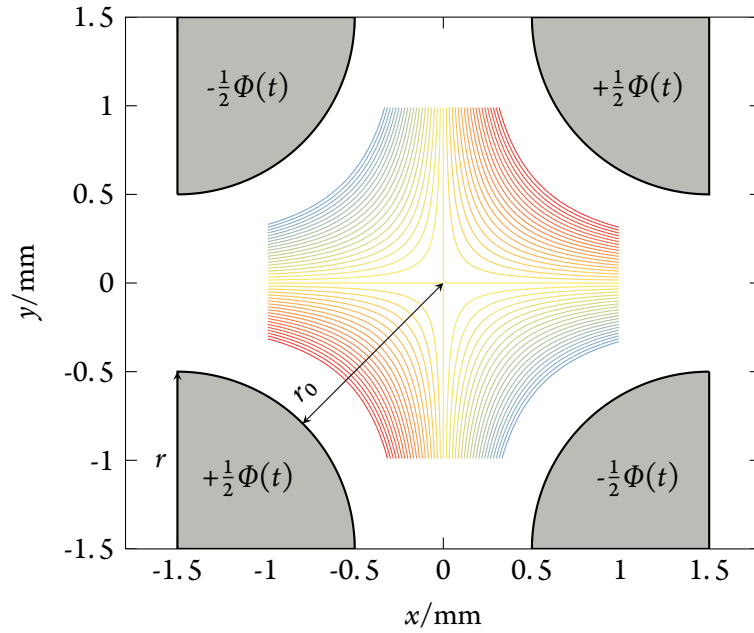
$$\Phi(x, y, t) = \Phi(t) \frac{x^2 - y^2}{2r_0^2} \quad (1.1)$$

expressed in Cartesian coordinates. Figure 1.1a on the next page illustrates the saddle-like shape of the realistic potential at the instant of maximal amplitude. It is formed by four electrodes to which diagonal-wise opposite voltages are applied. The harmonic potential $\Phi(x, y, t)$ is a good approximation close to the origin. Ions exposed to this time-varying potential experience alternating focusing and defocusing forces. Since the force field acting on them is not homogeneous but depends linearly on the distance to the trap center, ions further apart from the trap center experience a stronger restoring force. If the potential gets switched at a frequency that makes the defocusing force act on the ion when it is closer to the trap center, the defocusing effect will be weaker than the focusing on time average. If this situation does not change for an extend amount of time, trapping conditions are established.

1. Theory



(a) The electric potential takes on minimum or maximum values $\pm \frac{1}{2}\Phi$ inside the electrodes indicated by black lines and is saddle-like in the vicinity of trap center.



(b) Equipotential lines between $\pm \Phi/4$ drawn at steps of 0.025Φ .

Figure 1.1.: Simulation [105] of the time-dependent electric potential in a cross section of the quadrupole configuration used in the experiment at the moment of maximal amplitude. Four $r = 1$ mm wires are placed on a 3 mm sized square. Minimum distance between electrode surface and trap center is $r_0 = 1.121$ mm. Despite the optimum ratio $r/r_0 = 1.146$ [38] that minimizes higher order contributions in the multipole expansion of the potential formed by cylindrical shaped electrodes (hyperbolic surfaces would be needed for realizing a perfect harmonic potential) was not realized, no disturbing effects on the trapping properties were observed.

The time-varying amplitude $\Phi(t)$ is composed of a radio frequency voltage U_{RF} at frequency Ω and an additional direct current voltage component U_{DC} :

$$\Phi(t) = U_{\text{DC}} + U_{\text{RF}} \cos(\Omega t).$$

Given that, the equations of motion for an ion of charge e and mass m in the harmonic potential $\Phi(x, y, t)$ can be derived:

$$\begin{aligned} \frac{d^2 x}{dt^2} + \frac{e}{m} \frac{U_{\text{DC}} - U_{\text{RF}} \cos(\Omega t)}{r_0^2} x &= 0, \\ \frac{d^2 y}{dt^2} - \frac{e}{m} \frac{U_{\text{DC}} - U_{\text{RF}} \cos(\Omega t)}{r_0^2} y &= 0. \end{aligned} \quad (1.2)$$

Two dimensionless “stability parameters” a and q and a dimensionless time ξ

$$a_x = -a_y = a = \frac{4eU_{\text{DC}}}{m\Omega^2 r_0^2}, \quad q_x = -q_y = q = \frac{2eU_{\text{RF}}}{m\Omega^2 r_0^2}, \quad \xi \frac{1}{2} \Omega t \quad (1.3)$$

help to recover Mathieu’s differential equation from 1.2. From now on, both spatial coordinates x and y are denoted by ρ :

$$\frac{d^2 \rho}{dt^2} + (a - 2q \cos(2\xi)) \rho = 0.$$

The general solution of this ordinary linear differential equation is known [95]:

$$\rho(\xi) = A e^{\mu \xi} \sum_{n=-\infty}^{+\infty} C_n e^{2in\xi} + B e^{-\mu \xi} \sum_{n=-\infty}^{+\infty} C_n e^{-2in\xi}. \quad (1.4)$$

Initial conditions determine the parameters A and B whereas μ and C_n depend on a and q solely. Finite amplitude trajectories exist for non-integral imaginary μ only. This poses the constraints on a and q that define the zones of stable trapping. The stability diagram of a single ion in the vicinity of the a, q -origin is illustrated in fig. 1.2 on the following page. If more than one ion reside in the trap, the area of stability region shrinks [44] due to the Coulomb repulsion.

Assuming $a \ll 1$ and $q \ll 1$, the series expansion of ρ can be restricted to the terms $n = -1, 0, 1$ which allows to derive an approximate solution. This step is often referred to as the *adiabatic approximation* and is well justified because deviations from the exact solutions stay below 5 % for $q \leq 0.4$ [107]. For the particular initial conditions $\rho|_{t=0} = \rho_{\text{max}}$ and $\frac{d\rho}{dt}|_{t=0} = 0$ one can deduce $A = B = \rho_{\text{max}}/2$ and $C_{-1} = C_1 = -\frac{q}{4} C_0$ which reduces eq. (1.4) to

$$\rho(t) = \rho_{\text{max}} \left(1 + \frac{q}{2} \cos(\Omega t) \right) \cos(\omega_{\text{sec}} t).$$

This expression shows explicitly the ion’s motion to be a superposition of two oscillations: one at the radio frequency Ω (*micromotion*) and an other slower *secular motion* or *macromotion* at the frequency ω_{sec} which derives from the critical exponent $\omega_{\text{sec}} = -i\mu\Omega/2$. Within the adiabatic

1. Theory

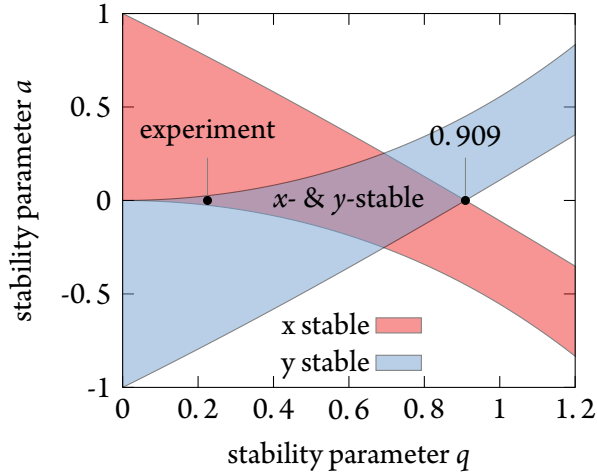


Figure 1.2.: Detail of the stability diagram of a single trapped ion in the vicinity of the a, q -origin. Trapping can be realized only when the trajectories are stable in both spatial directions. Most of the experiments were performed at $q = 0.2$ and $a = 0$.

approximation there is a closed-form expression for the exponent μ . One is therefore able to relate ω_{sec} to the stability parameters a and q :

$$\omega_{\text{sec},\rho} = \frac{\Omega}{2} \sqrt{\frac{q^2}{2} + a_\rho}. \quad (1.5)$$

Splitting of the secular frequency along $\rho = x, y$ arises from a finite stability parameter $a_\rho \propto \pm U_{\text{DC}}$. Contrastingly, $\omega_{\text{sec}} = \frac{q}{\sqrt{8}}\Omega$ is identical in both directions in absence of a DC-voltage.

Evidently, the micromotion amplitude depends on that of the macromotion ρ_{max} , or more generally speaking, on the distance from the trap center, see fig. 1.3 on the facing page. Since the motion is governed by a harmonic oscillation at ω_{sec} it is convenient to define a time-independent *pseudo potential* $\Psi(\bar{\rho})$. The pseudo potential allows to describe the *averaged* ion motion $\bar{\rho}(t) = 1/T \int_t^{t+T} \rho(t') dt'$ over a RF-period $T = 2\pi/\Omega$ correctly, at the negligence of micromotion:

$$\Psi(\bar{\rho}) = \frac{m\omega_{\text{sec}}^2}{2e} \bar{\rho}^2 = \Psi_0 \frac{\bar{\rho}^2}{r_0^2}, \quad \Psi_0 = \frac{eU_{\text{RF}}^2}{4m\Omega^2 r_0^2} = \frac{q}{8} U_{\text{RF}}. \quad (1.6)$$

Ψ_0 denotes the trap potential at the edge of the electrodes and is often also called *trap depth*. Typical experimental values for atomic ions are $\Psi_0 \leq 1$ V. Ions would need a kinetic energy that corresponds the thermal motion at 12 000 K to overcome this barrier.

Because Ψ is proportional to e/m more massive but equally charged ions experience a weaker pseudo potentials for otherwise identical parameters. This fact becomes relevant when many ions of different mass-to-charge ratio (m/q) reside in the same physical trap. Ions with smaller m/q -ratio experience a stronger confinement, i. e. will preferably gather in the trap center. Depending on the number of ions and the confinement, ions with larger m/q -ratio will be shifted to a radially displaced position where the restoring force balances the Coulomb repulsion caused by the ions in the center [138, 189].

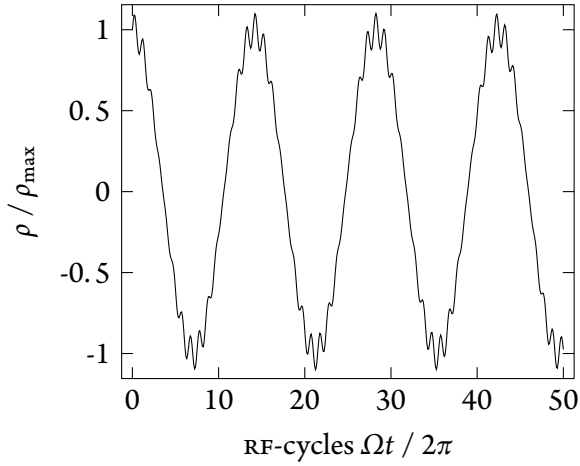


Figure 1.3.: Normalized trajectory of an ion's motion along ρ (x or y). The small amplitude, fast oscillating micromotion at the radio frequency Ω is superimposed over a harmonic oscillation in the pseudo potential at the usually much lower frequency $\omega_{\text{sec}} = \frac{1}{\sqrt{8}}q\Omega$. The curve was computed for the stability parameter q set to 0.2.

1.1.2. Axial confinement

So far, the discussion has been restricted to the two-dimensional radial confinement. The required trapping forces along the z -axis can be generated by a static electric potential. In this thesis, the axial potential was realized by pairs of ring electrodes encircling the quadrupole configuration; see fig. 2.3 on page 26. The resulting potential along the z -axis is assumed and also verified to be harmonic close to the trap center in first order approximation:

$$\Phi_z(z) = U_z \frac{z^2}{z_0^2}. \quad (1.7)$$

The amplitude of this potential is proportional to the experimentally adjustable voltage U_z applied to the ring electrodes. A characteristic length z_0 which gives the curvature of the parabolic potential is determined by geometric factors of the trap (see fig. 1.4 on the following page). The axial frequency of a singly charged ion of mass m in the potential Φ_z reads

$$\omega_z = \sqrt{\frac{2eU_z}{mz_0^2}}.$$

Consulting eq. (1.1) on page 7 and obeying the Laplace equation for Φ , an extended expression of the combined, now three-dimensional, potential for a single ion

$$\Phi(x, y, z, t) = \Phi(t) \frac{x^2 - y^2}{2r_0^2} + U_z \frac{z^2}{z_0^2} - U_z \frac{x^2 + y^2}{2z_0^2}$$

follows. Here, a symmetric quadrupole configuration as used in this thesis was assumed. The last term is readily assented to weaken the potential in the radial directions. This can be taken care of by modifying the stability parameter a defined in eq. (1.3) on page 9 for the two-dimensional case

$$a_x \rightarrow a_x - a_z, \quad a_y \rightarrow a_y - a_z, \quad a_z = \frac{4U_z e}{m\Omega^2 z_0^2}.$$

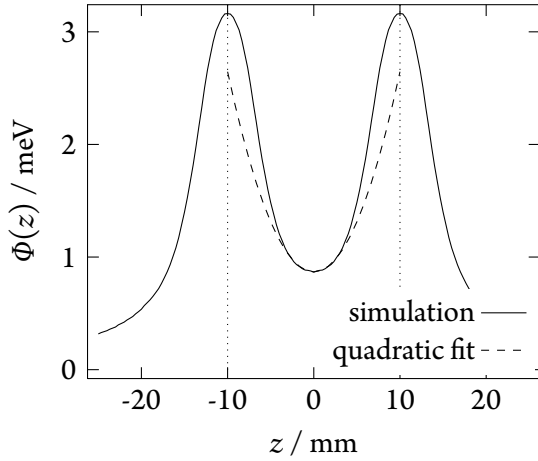


Figure 1.4.: Simulated (CPO [105]) axial potential along z formed by two 20 mm separated ring electrodes (dotted lines) at 1 V encircling the quadrupole configuration. A quadratic fit (dashed line) to the central part yields $z_0 = 7.5$ mm for $U_z = 1$ mV; see eq. (1.7) on the preceding page. The quadrupole electrodes shield the electric field of the ring electrodes (see section 2.3 on page 30) so that the scale of U_z is only $1/1000$ of the actual voltage applied to the ring electrodes. In typical experiments 200 V were applied which corresponds to $U_z = 200$ mV.

The rest of the derivation of the previous section including the expression for the secular frequencies eq. (1.5) on page 10 remains valid within the level of approximation necessary for this thesis when the altered definitions of a_x and a_y are applied. Under normal experimental conditions, the correction due to $a_z = 3 \cdot 10^{-5}$ is negligible.

1.2. Laser cooling

Laser cooling has been developed for a wide range of applications and is accompanied by an elaborate theoretical background [113]. Various methods to reduce the amplitude of the translational motion of neutral atoms and ions with the help of laser light are known since many decades. In this long history of ever beaten cooling limits by more and more sophisticated cooling methods three Nobel prizes honor the success of the struggle and its foundation for unprecedented precision measurements [32, 34, 78]. One of the most fundamental schemes is *Doppler cooling*. It allows to reduce the kinetic energy of particles at room temperature—moving at many hundred meter per second—by six orders of magnitude in less than a millisecond.

The basic mechanism relies on repeated momentum transfer from a stream of photons to a particle which is assumed to be an atomic ion in the following. If the energy related to the photon wavelength matches an electronic transition, the photon can be absorbed by the ion. The photon momentum must be taken over by the excited ion due to momentum conservation. Subsequent spontaneous emission can be assumed to be isotropic, i. e. its recoil contribution to the net momentum averages out over many excitation cycles. The key to deceleration lies in the direction from which the photons get absorbed and is readily visualized in a one-dimensional model. Counterpropagating photons can slow down the ion by consecutive momentum transfers anti-parallel to its direction of motion. Because atomic electronic transitions are usually narrow with a relative resonance width $\Delta\omega/\omega$ on the order of $1 \cdot 10^{-8}$, the resonance condition of a photon to get absorbed by the moving ion depends strongly on its velocity v owing to the Doppler effect.

Lower frequency photons (red detuned) are preferably absorbed by counterpropagating ions since they get (blue shifted) towards resonance in the ions' co-moving frame. Spontaneous emission

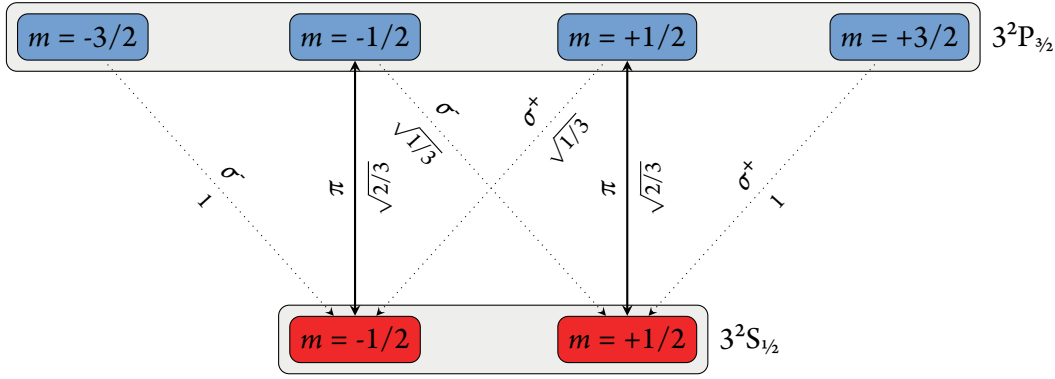


Figure 1.5.: Schematic energy diagram illustrating the relevant electronic states of $^{24}\text{Mg}^+$ and the transitions between the $3^2\text{S}_{1/2}$ and the $3^2\text{P}_{3/2}$ manifold. The numbers next to the arrows give the Clebsch-Gordan coefficients $\langle j_1 m_1 j_2 m_2 | JM \rangle$ for the spontaneous emission of π polarized light ($j_1 = 1, m_1 = 0$) and σ_{\pm} polarized light ($j_1 = 1, m_1 = \pm 1$). Solid lines represent the experimentally realized π transitions using linear polarized light. No magnetic field was applied so that all m levels of the same fine structure manifold are degenerate.

occurs at the higher frequency of the atomic transition. After averaging over many absorption-emission-cycles, kinetic energy of the ion has been transferred to the light field. Continuing one-dimensional deceleration would revert the motion at some point and accelerate the ion.

In an ion trap the acceleration of the ion is prevented by the slope of the trap potential. There is a point close to the trap center where a displaced ion experiences a Coulomb force that balances the laser cooling force and leads to a steady-state. Loosely speaking, ions are constantly pushed against the trap potential's slope due to repeated momentum transfer of absorbed photons. This position can be considered an effective trap center at which the sum of all forces vanishes on time average. The force due to the cooling laser is velocity dependent $\mathbf{F}(\mathbf{v})$ [114]

$$\mathbf{F}(\mathbf{v}) = \hbar \mathbf{k}_1 S \frac{(\Gamma/2)^3}{(\delta - \mathbf{v} \cdot \mathbf{k}_1)^2 + (\Gamma/2)^2 (1 + S)}. \quad (1.8)$$

Here, $\delta = \omega_1 - \omega_0$ denotes the detuning of the cooling laser ω_1 with respect to the atomic transition ω_0 . $|\mathbf{k}_1| = 2\pi/\lambda_1$ is the absolute value of the wave vector, λ_1 the wavelength of the cooling light, $\Gamma = 1/\tau$ the natural line width of the atomic transition defined as the reciprocal of the natural decay time τ , and S the saturation parameter defined as the quotient I/I_0 of laser intensity I and saturation intensity

$$I_0 = \frac{2\pi^2 \hbar c \Gamma}{3\lambda_1^3}. \quad (1.9)$$

For the relevant transition of this work $^2\text{S}_{1/2} \rightarrow ^2\text{P}_{3/2}$ in $^{24}\text{Mg}^+$ with $\Gamma = 2\pi \cdot 42.7$ MHz at $\lambda = 280$ nm, the saturation intensity equals 254 mW cm^{-2} . The atomic transitions used for laser cooling form a closed cycle as can be seen in fig. 1.5. The two degenerate ground states of $^2\text{S}_{1/2}$ are coupled to the excited manifold $^2\text{P}_{3/2}$ by linearly polarized light. All decay channels return the electronic excitation of the ion to the ground state and prepare it for the next cooling cycle.

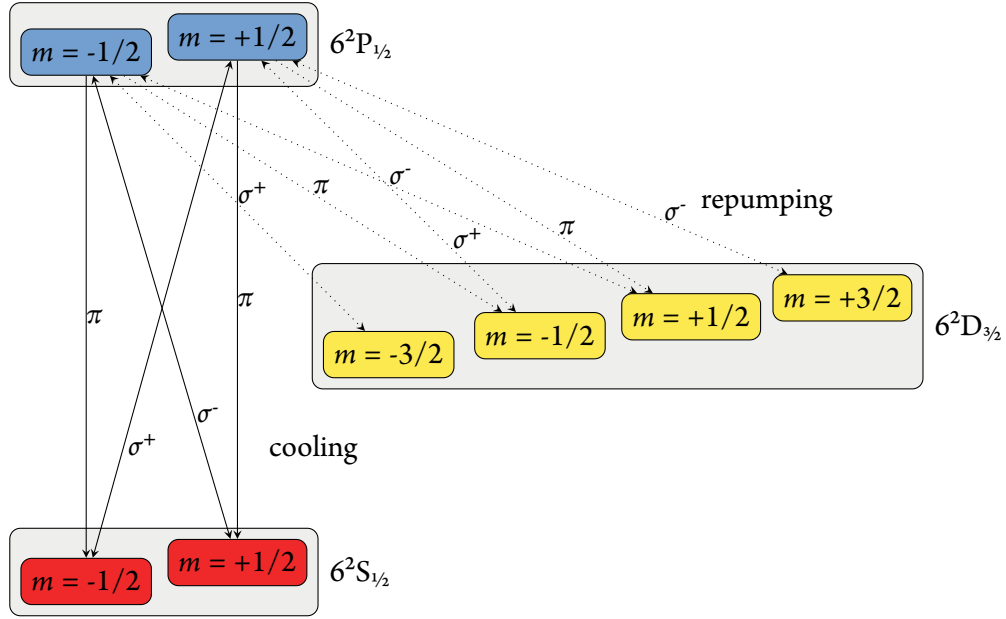


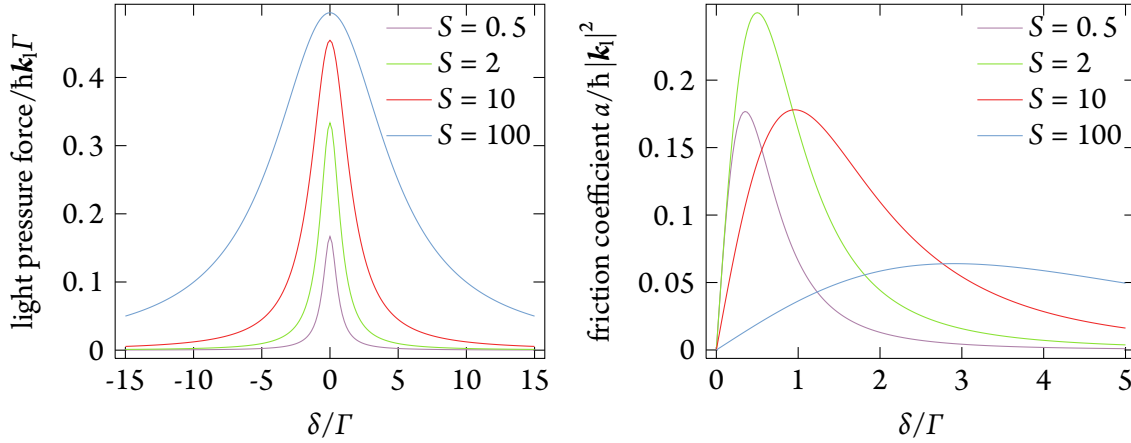
Figure 1.6.: Schematic energy diagram illustrating the relevant electronic states of $^{138}\text{Ba}^+$ with Zeeman splitting in an external magnetic field and the allowed transitions between the $6^2S_{1/2} \leftrightarrow 6^2P_{1/2}$ (cooling, solid lines) and $6^2D_{3/2} \leftrightarrow 6^2P_{1/2}$ (repumping, dotted lines) manifolds. σ^\pm polarized repumping light prevents optical pumping into the $m = \pm\frac{3}{2}$ states of $6^2D_{3/2}$. Dipolar allowed spontaneous decay can occur in all indicated ways.

Equation (1.8) on the previous page can be Taylor expanded around $\mathbf{v} = 0$ involving a constant *light pressure* force and a *friction* force term, with friction coefficient α , linear in velocity \mathbf{v} :

$$\mathbf{F}(\mathbf{v}) = \frac{\hbar \mathbf{k}_1}{2} \frac{S\Gamma}{4(\delta/\Gamma)^2 + (1+S)} + \underbrace{4\hbar |\mathbf{k}_1|^2 \frac{S(\delta/\Gamma)}{(4(\delta/\Gamma)^2 + (1+S))^2}}_{\alpha} \mathbf{v}. \quad (1.10)$$

Figure 1.7 on the facing page shows the maximum friction force at twice the saturation intensity $I = 2I_0$ and a detuning of half the natural line width $\delta = \Gamma/2$. At these values the velocity of ions with mass m is damped with a rate $\gamma = \hbar |\mathbf{k}_1|^2 / 4m$. The corresponding typical time scale at optimum settings is on the order of a few microseconds.

The light pressure force term in eq. (1.10) is maximal at zero detuning and increases with intensity but does not diverge, though. It saturates at intensities $I \gg I_0$ because the rate of momentum transfers is limited by the spontaneous decay rate which in turn depends on the occupation probability of the excited level of the cooling transition. The occupation of the excited state at zero detuning $\frac{1}{2}S/(S+1)$ cannot exceed 50% in the limit of infinite intensity. Thus, the effective line width $\Gamma_{\text{eff}} = \Gamma\sqrt{1+S}$ spreads at intensities $I \gg I_0$ what is known as *power broadening*. Consequently, the fluorescence rate saturates and, even worse, the friction force and the related cooling effect shrinks at high intensities; see fig. 1.7 on the facing page.



(a) Normalized laser force acting on an ion at rest for various saturation parameters S . For $S \gg 1$, power broadening sets in. The maximum cooling force saturates at high intensities because the population of the excited state cannot exceed 50 %.

(b) Normalized friction coefficient α for various saturation parameters S . Maximum deceleration is achieved at $S = 2$ and $\delta = \Gamma/2$.

Figure 1.7.: Doppler laser cooling force and friction coefficient of $^{24}\text{Mg}^+$ as a function of the relative detuning δ/Γ .

The random nature of spontaneous emission establishes the limitation for Doppler cooling. Each spontaneously emitted photon gives rise to a momentum transfer into some random direction. Repeated emission of spontaneous photons adds further stochastic kicks kindling a random walk, or diffusion, in momentum space which broadens the velocity distribution of an ensemble of cooled ions thus represents a heating mechanism. The one-dimensional Doppler cooling limit is often stated as a temperature

$$T_{\text{Doppler}} = \frac{\hbar\Gamma}{2k_{\text{B}}}$$

related to the kinetic energy of the ion at which the mean photon recoil of spontaneous emission prevents further deceleration of the ion. It is reached when the heating caused by momentum diffusion and cooling balance. The Doppler cooling temperature of $^{24}\text{Mg}^+$ for the $^2\text{S}_{1/2} \rightarrow ^2\text{P}_{3/2}$ transition equals $T_{\text{Doppler}} \approx 1$ mK. However, a series of practical limitations, e. g. laser frequency and intensity noise, RF-heating [17, 143], i. e. energy transfer from micromotion to random macromotion, in a not perfectly harmonic trap or by Coulomb interactions of many simultaneously trapped ions, collisions with background gas etc. have to be considered, too.

There are Doppler cooling schemes requiring more than a basic two level approximation. One example is the $^{138}\text{Ba}^+$ ion which is the other atomic laser coolable species besides of $^{24}\text{Mg}^+$ relevant for the experiments of this thesis. The energy diagram of $^{138}\text{Ba}^+$ is illustrated in fig. 1.6 on the preceding page. It can be simplified to a three-level system. The actual cooling can be realized with the $^2\text{S}_{1/2} \rightarrow ^2\text{P}_{1/2}$ transition. However, barium decays both into the ground state $^2\text{S}_{1/2}$ and to the intermediate level $^2\text{D}_{3/2}$ with branching ratio approximately 3:1 [36]. The $^2\text{D}_{3/2}$ level is metastable and decays only at a rate of 0.0125 s^{-1} [186] to the ground state. Optical pumping into $^2\text{D}_{3/2}$ interrupts

the cooling cycle. It can be closed with the help of a repumper laser coupling the states ${}^2D_{3/2}$ and ${}^2P_{1/2}$. Without external magnetic field B , each J level consists of $2J + 1$ degenerate m states and the quantization axis gets defined by the electric field vector of the cooling laser radiation. Since only π -polarized photons can excite electronic transitions from the ${}^2D_{3/2}$ manifold under these conditions, the ${}^2D_{3/2}(m = \pm\frac{3}{2})$ states become so called *dark states*, again preventing a closed transition. To overcome this hurdle, an external magnetic field must be applied which lifts the degeneracy and secondly allows also σ^\pm -polarized photons to be absorbed by the ${}^2D_{3/2}$ states. A detailed theoretical analysis of the cooling scheme of ${}^{138}\text{Ba}^+$ including the complicated interplay of cooling and repumper radiation can be found in [135, 124].

Lamb-Dicke regime

Up to now only one-dimensional cooling along the laser propagation direction with external restoring force was discussed. In free space pairs of counterpropagating cooling laser beams addressing the missing two other spatial dimensions would have to be considered, too. In ion traps this is not the case since an ion's motion in the trapping potential can couple all degrees of freedom. For this to hold, the cooling laser must not be aligned with one of the principal axes of the trapping potential. To address all degrees of freedom sufficiently with only one laser beam, some finite projection $\mathbf{k} \cdot \mathbf{r}(x, y, z) > 0$ of the wave vector \mathbf{k} on the x -, y -, and z -axis is required. In the experiments of this thesis, the cooling laser had to be close to the unpropitious configuration of being aligned with one the axes for practical reasons; see the experimental layout fig. 2.1 on page 23. However, due to the residual angle ($< 0.5^\circ$) enclosed by \mathbf{k} and the z -axis (line of pseudo potential minimum), the divergence of the laser beam close to its focus, small asymmetries in the potential caused by stray effects, the interaction of many ions trapped at the same time and species of different m/q -ratio, the mixing of the degrees of freedom sufficed to cool also the ions' radial motion; cf. also section 4.1.2 on page 68.

It should be noted that the previous description of laser cooling is strictly true only in the limit of free particles and modifications have to be made for strongly bound ions. In the Lamb-Dicke regime the energy related to a cooling photon recoil is less than the energy of one vibrational excitation in the trap's *quantized* harmonic oscillator model

$$(\hbar |\mathbf{k}_1|)^2 / 2m < \hbar\omega_{\text{sec}}.$$

The simple picture of Doppler cooling has to be extended by the explicit treatment of the quantized motional states. That was however not necessary for the experimental conditions of this thesis. In the Lamb-Dicke regime other cooling methods, e. g. *resolved side band cooling* [40], open up a way to overcome the Doppler cooling limit and allow to cool the external motion of an ion down to its quantum mechanical ground state [8]. The position of an ion in its motional ground state is determined by the width $\sqrt{\hbar/m\omega_{\text{sec}}}$ of the corresponding wave function. This defines the fundamental limit for the localization of particles in ion traps. In traps with high secular frequencies, the width is on the order of 10 nm for atomic ions.

1.3. Sympathetic cooling

Only atomic ions of simple internal electronic structure can be laser cooled. As more electronic states must be considered, the cooling scheme gets rapidly complicated because a closed transition can often only be realized with the help of additional repumper lasers needed to prevent dark states.

For ions that either do not possess any internal electronic structure, e. g. protons, or own a multitude of states, e. g. any molecular ion, laser cooling schemes like Doppler cooling will fail due to the lack of a closed optical transition. There is however another efficient and general cooling scheme that can be applied instead. *Sympathetic cooling* [138] builds on the long-range Coulomb interaction of at least two ions trapped in the same trap of which one is considered to be laser coolable. Elastic collisions transfer part of the non-laser coolable ion's kinetic energy to the cooling ion. Repeated dissipation of energy initiates rapid thermalization of the ion ensemble until the phase transition from a gas-like cloud to a crystalline structure [143] occurs.

In the crystalline state, the kinetic energy is not sufficient to overcome the Coulomb repulsion barrier between adjacent ions. Thus, the ion positions form a regular lattice similar to a solid state crystal but with much larger distances ($\approx 10 \mu\text{m}$) between the particles. In the Coulomb crystals used within this thesis, the electrostatic Coulomb energy exceeds the ions' kinetic energy by a factor on the order of 500. In the limiting case of an infinite, charged one-component plasma, the phase transition to a crystalline state occurs when this factor becomes larger than 175 [45]. In few ion crystals, this factor can be lower. For two ions, 120 was reported in [181]. In ion crystals, the collective motion (phonons) of all ions becomes the relevant coupling mechanism between coolable and not directly coolable ions which allows further reduction of the motional energy. Experimental results [116, 125] showed that translational temperatures in the millikelvin range can be reached for molecular ions in linear Paul traps.

In the field of quantum information processing based on ions confined in Paul traps, phonons can be used to mediate information between quantum bits realized by two electronic states of the ion [33]. For many protocols it is therefore important to prepare the ions close to their motional ground state. Thanks to the success of side band cooling schemes for atomic ions, it has been demonstrated that careful sympathetic motional cooling applied to homogeneous [137] and heterogeneous [8] atomic ion crystals can result in ground state population probabilities of the common normal motional modes as high as 99 %.

An important advantage of this method is the irrelevance of internal structure. Only the ion's mass m and charge q must be compatible with the stability diagram of the laser cooled ion; see fig. 1.2 on page 10. A conservative estimation [82] for the range of practical m/q -ratios of the sympathetically cooled ion yields $1/5$ to 5 times that of the laser cooled ions m/q -ratio. Ion species with larger m/q -ratios can still be sympathetically cooled. They might even form crystalline structures [125] but due to the largely different pseudo-potential they are further separated from the laser cooled ions. Therefore, the coupling strength between the different ion species will be reduced, possibly limiting the achievable temperature. Additionally, the micromotion amplitude increases with the radial distance to the trap axis. If multiple charging is an option, the m/q -ratio can be reduced to a suitable value even for organic molecular ions of mass above $1 \cdot 10^5 \text{ u}$ as has been demonstrated in [121].

1.4. Short optical pulses

Instead of a strict mathematical treatment of short laser pulses which is not necessary for the sake of this thesis, only a selection of results is presented in form of a short summary in this section. The operation and tuning of the femtosecond laser system including the optimization of the third harmonic generation requires a basic understanding of short pulse physics. A comprehensive survey of the topic can be found in textbooks such as [41], for example.

In the first part of this section, the usual notation and terms are introduced. The consequences of phase modulation are discussed using the example of linear chirped pulses. This issue was of capital importance for the experimental realization of the beam line that established the connection of the trap apparatus with the femtosecond laser. For that reason, it is briefly motivated that the action of *linear* optical elements on short laser pulses are most easily described in the spectral domain. This concept is then used to characterize the distortion effects of mirrors in the beam path; see section 4.4 on page 90. For the description of the mechanisms underlying the relevant *non-linear* processes used within this thesis, namely spectral broadening and third harmonic generation, more specialized literature is referred to [174].

Laser pulses as short as only a few cycles of the carrier frequency and 0.5 mJ energy can be produced by commercial Ti:sapphire laser systems [29]. They differ substantially from monochromatic laser radiation, hence need an adequate description. Firstly, because the considered pulses are short in the time domain, their electric field involves a broad spectrum in the frequency domain. Secondly, due to their high peak intensity, non-linear polarization effects in light-matter interaction play an important role.

In order to simplify the discussion in the following, only the time-dependent part $E(t)$ of the electric field of a laser pulse $\mathbf{E}(\mathbf{r}, t)$ that generally depends also on spatial coordinates \mathbf{r} is considered. It follows from Fourier's theorem that pulses of finite duration cannot be described by only a single frequency but must span a whole spectral range $E(\omega)$. The shorter a laser pulse, the broader its supporting spectrum:

$$E(t) = \frac{1}{\sqrt{2\pi}} \int_{-\infty}^{+\infty} E(\omega) e^{i\omega t} d\omega = \text{Re}(\mathcal{E}(t) e^{i\Gamma(t)}).$$

A convenient mathematical choice is to define a *pulse envelope* function $\mathcal{E}(t)$ and a *time-dependent phase* $\Gamma(t)$ together with the *instantaneous frequency* $\omega(t)$:

$$\omega(t) = \frac{d\Gamma(t)}{dt}.$$

The related inverse Fourier transform is given by

$$E(\omega) = \frac{1}{\sqrt{2\pi}} \int_{-\infty}^{+\infty} E(t) e^{-i\omega t} dt = |E(\omega)| e^{i\Phi(\omega)}. \quad (1.11)$$

The electric field is a measurable observable and thus has to be real. This mathematical constraint connects negative and positive frequency components by complex conjugation

$$E(\omega) = E(-\omega)^*.$$

Since the complex-valued representation of the pulse in the spectral domain is fully equivalent to the knowledge of its temporal structure, it is sufficient to measure the pulse spectrum in intensity $|E(\omega)|$ and phase $\Phi(\omega)$. Although the spectrum can be broad—spanning an interval of some 10 % of the *carrier frequency* $\bar{\omega}$ —it is often meaningful to Taylor expand $\Phi(\omega)$ around $\bar{\omega}$:

$$\begin{aligned} \Phi(\omega) &= \sum_n \frac{\Phi_n}{n!} (\omega - \bar{\omega})^n = \varphi_0 + \varphi_1 (\omega - \bar{\omega}) + \frac{\varphi_2}{2} (\omega - \bar{\omega})^2 + \dots \\ \bar{\omega} &= \frac{\int \omega |E(\omega)|^2 d\omega}{\int |E(\omega)|^2 d\omega}. \end{aligned} \quad (1.12)$$

There is a direct physical interpretation to the first three expansion coefficients. φ_0 is known as *carrier envelope phase* and refers to a global shift of the fast oscillating light field with respect to the temporal envelope. Throughout this thesis, φ_0 is irrelevant. The coefficient φ_1 of the linear term acts as a global time delay. This is easily verified by inserting a linear phase function in eq. (1.11) on the facing page. The quadratic term with coefficient φ_2 has an important influence on the temporal shape of the pulse. Its consequences can be demonstrated in an example.

A Gaussian shaped spectrum with the aforementioned quadratic phase function can be written

$$E(\omega)|_{\omega>0} = E_0 e^{-\frac{(\omega-\bar{\omega})^2}{2\delta^2}} e^{i\frac{\varphi_2}{2}(\omega-\bar{\omega})^2}. \quad (1.13)$$

Here, δ denotes the $1/e^2$ -width of the electric field. This corresponds to a spectral intensity FWHM $\Delta\omega = \delta\sqrt{4\ln(2)}$. The temporal electric field can be calculated as follows:

$$\begin{aligned} E(t) &= \frac{E_0}{2} \left(\frac{1}{\sqrt{2\pi}} \int_{-\infty}^{+\infty} e^{-\frac{(\omega-\bar{\omega})^2}{2\delta^2}} e^{i\frac{\varphi_2}{2}(\omega-\bar{\omega})^2} e^{i\omega t} d\omega + c. c. \right) \\ &= \frac{E_0}{2} \left(\frac{\delta}{1+i\varphi_2\delta^2} \exp\left(i\frac{i2\varphi_2\delta^2\bar{\omega} + i\delta^2 t + 2\bar{\omega} t}{1+i\varphi_2\delta^2} \frac{t}{2}\right) + c. c. \right) \\ &= \frac{E_0}{2} \left(\underbrace{\frac{\delta}{1+i\varphi_2\delta^2} \exp\left(-\frac{\delta^2}{1+\varphi_2^2\delta^4} \frac{t^2}{2}\right)}_A \underbrace{\exp\left(i\frac{\varphi_2\delta^4/2}{1+\varphi_2^2\delta^4} \frac{t^2}{2}\right)}_B \underbrace{\exp(i\bar{\omega}t)}_C + c. c. \right) \end{aligned} \quad (1.14)$$

and can be further simplified to

$$E(t) = E_0 \frac{\delta}{\sqrt{1+\varphi_2^2\delta^4}} \exp\left(-\frac{\delta^2}{1+\varphi_2^2\delta^4} \frac{t^2}{2}\right) \sin\left[\left(\bar{\omega} + \frac{1}{4} \frac{\varphi_2\delta^4}{1+\varphi_2^2\delta^4} t\right) t + \arctan\left(\frac{1}{\varphi_2\delta^2}\right)\right]. \quad (1.15)$$

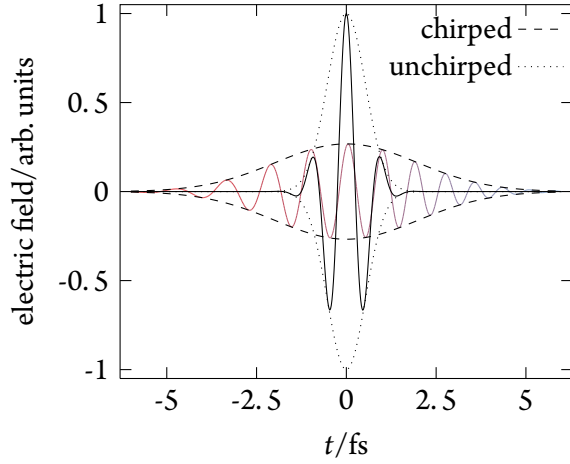


Figure 1.8.: A transform limited single-cycle 0.8 fs pulse (unrealistically short for visibility reasons) at 280 nm is compared with a pulse of identical spectrum but additional phase function with chirp parameter $\varphi_2 = +40 \text{ fs}^2$. One recognizes the varying instantaneous frequency with the lower frequencies at the leading edge (red) of the chirped pulse, the longer pulse duration and the reduced peak intensity. The dashed and dotted lines indicate the respective temporal envelope functions $\mathcal{E}(t)$.

A visualization of the electric field is presented in fig. 1.8. It can be decomposed into three factors. Term (A) describes a Gaussian temporal envelope. This is an expected result since the Fourier transform of a Gaussian is again a Gaussian. The associated temporal width or *pulse duration* Δt usually defined by the FWHM of the temporal intensity profile proportional to $|E(t)|^2$ can be derived from eq. (1.14) on the preceding page:

$$\Delta t = \frac{1}{\delta} \sqrt{4 \ln(2)} \sqrt{1 + \varphi_2^2 \delta^4}.$$

Term (C) is a rapidly oscillating phase term at the carrier frequency. Term (B) can be interpreted as a phase modulation. Its consequence displays in the instantaneous frequency

$$\omega(t) = \bar{\omega} + \frac{1}{2} \frac{\varphi_2 \delta^4}{1 + \varphi_2^2 \delta^4} t$$

or can be read off from eq. (1.15) on the previous page. The frequency of the pulse changes over time thus shows a *chirp*. Due to the linear frequency sweep, one says the pulse is linearly chirped. The sign of φ_2 defines the order of frequencies. A positively chirped pulse is headed by low frequency components and has higher ones at its trailing edge. In negative chirped pulses the ordering is opposite.

If all expansion terms φ_n , $n > 1$ vanish, the pulse is said to be *Fourier* or *transform limited* because the pulse duration is minimal for a given spectral intensity. Expressed differently, the transform limited pulse minimizes the *time-bandwidth product*. For a linearly chirped pulse with Gaussian spectrum, this quantity can be deduced from the above expressions:

$$\Delta t \Delta \omega = 4 \ln(2) \sqrt{1 + \varphi_2^2 \delta^4}.$$

The prefactor $4 \ln(2)$ depends on the temporal shape of the pulse, here a Gaussian pulse was assumed. If one factors out 2π in order to convert from radial to regular frequencies $f = \omega/2\pi$, one obtains the often quoted time bandwidth factor 0.441 for Gaussian pulses.

Another important result that follows from the analysis of short pulse propagation through media with *linear* polarization dependence is

$$E(z, \omega) = E(0, \omega)e^{i\Phi(\omega)} = E(0, \omega)e^{ik(\omega)z}.$$

The great simplification of this formula lies in the easy description of the interaction in the frequency domain where the interaction with the medium is nothing else than an additional phase that is picked up after a propagation over a distance z . Reflections are treated in essentially the same way. The additional phase in this case describes retardation effects on the surfaces of reflection. Similar to what has been done in eq. (1.12) on page 19 for the phase $\Phi(\omega)$, the wave vector $k(\omega)$ can also be Taylor expanded:

$$k(\omega) = \sum_n \frac{k_n}{n!} (\omega - \bar{\omega})^n = k_0 + k_1(\omega - \bar{\omega}) + \frac{k_2}{2}(\omega - \bar{\omega})^2 + \dots$$

The coefficient k_0 denotes the the trivial phase shift $\varphi_0 = k_0z$ of a propagating wave. Using the *index of refraction* $n(\bar{\omega})$ of the material evaluated at the carrier frequency $\bar{\omega}$, k_0 can be written

$$k_0 = n(\bar{\omega}) \frac{\bar{\omega}}{c} = \frac{\bar{\omega}}{v_{\text{ph}}}$$

and related to the *phase velocity* v_{ph} . The second coefficient k_1 is related to the time T it takes the pulse to travel a distance z and can be expressed by the *group velocity* v_g :

$$k_1 = \frac{T}{z} = \frac{1}{v_g}. \quad (1.16)$$

The third coefficient k_2 determines by how much v_g varies with the frequency ω and is therefore also called *group velocity dispersion* (GVD). Multiplication with the propagation distance z results in the dispersion of the propagation time which is called *group delay dispersion* (GDD):

$$k_2 = \frac{d}{d\omega} \frac{1}{v_g} = \text{GVD} = \frac{\text{GDD}}{z}. \quad (1.17)$$

The temporal envelope of the pulse is influenced by k_2 and higher expansion coefficients. In particular, k_2 (GVD) is readily recognized to cause a linear chirp whose consequences have been discussed above. The GVD is a function of the second derivative of the index of refraction n with respect to frequency. UV pulses are extremely sensitive to dispersive effects because n is strongly frequency-dependent in the ultraviolet for most materials. For example, the 280 nm pulses used in this thesis would have been stretched from 5 fs to more than 20 fs by the propagation through a hypothetical 0.5 mm MgF₂ window already. Therefore, reflective optics which can have substantially smaller GDD values is usually preferential.

2. Ion trap apparatus

A detailed description of the ion trap setup developed in preparation for this thesis is presented in the following chapter. The setup is called τ IA μ O—abbreviating *trapped ions and molecules*. That name has also been given to the experimental approach as a whole.

2.1. Vacuum system

Figure 2.1 on the next page shows the core of the apparatus which is embedded in three vacuum vessels that are connected via differential pumping stages. A continuous radio frequency (RF) quadrupole guide runs through the differential pumping stages and allows to transfer ions between the chambers. Each chamber has specific features that entail the usage of particular components and materials. However, all work shares a common design principle: The setup was conceived with the aims to achieve lowest possible vacuum pressure, to be as modular as possible and to be easily assembled.

Only ultrahigh vacuum (UHV) with pressures below $1 \cdot 10^{-9}$ mbar can be considered sufficient for the experiments of this thesis and for the anticipated experiments beyond this framework; see chapter 6 on page 118. First of all, collision between trapped ions and residual gas particles can transfer momentum to the trapped ions which might lead to melting of a crystalline structure, charge transfer reactions leading to trapping of unwanted ion species and even loss of trapped ions. If collisions are too frequent, they can prevent the occurrence of a crystalline structure at all. The mean time between two collisions of a trapped ion with a residual gas particle, e. g. hydrogen molecule, under typical experimental conditions ($2 \cdot 10^{-10}$ mbar, room temperature) is on the order of 10 min. Although collisions of neutral molecules and ions pose an interesting research field on their own [12] that could be pursued in the present apparatus, those events were tried to be effaced since they were not topic of this thesis. For the experiments performed so far, hydrogen collisions are considered the most critical ones. This is because, on the one hand, the H_2 partial pressure contributes most to the residual gas background due to the pumping speed of vacuum pumps depending on the gas species. On the other hand, the central experiments of this thesis (see chapter 5 on page 95) aim at the same chemical reaction involving trapped ions and hydrogen that causes reaction events regarded as adverse background. In order to prevent spurious reaction events induced by collisions with the residual gas as much as possible (see section 4.3 on page 87 for measurements) various ways to reduce the hydrogen content of the residual gas were already followed in the design phase.

2.1.1. Preparation chamber

The main purpose of chamber 1 is loading and preparation of atomic and molecular ions. To this end, a cryogenic injection system for gaseous neutral molecules is installed and aligned with the entrance

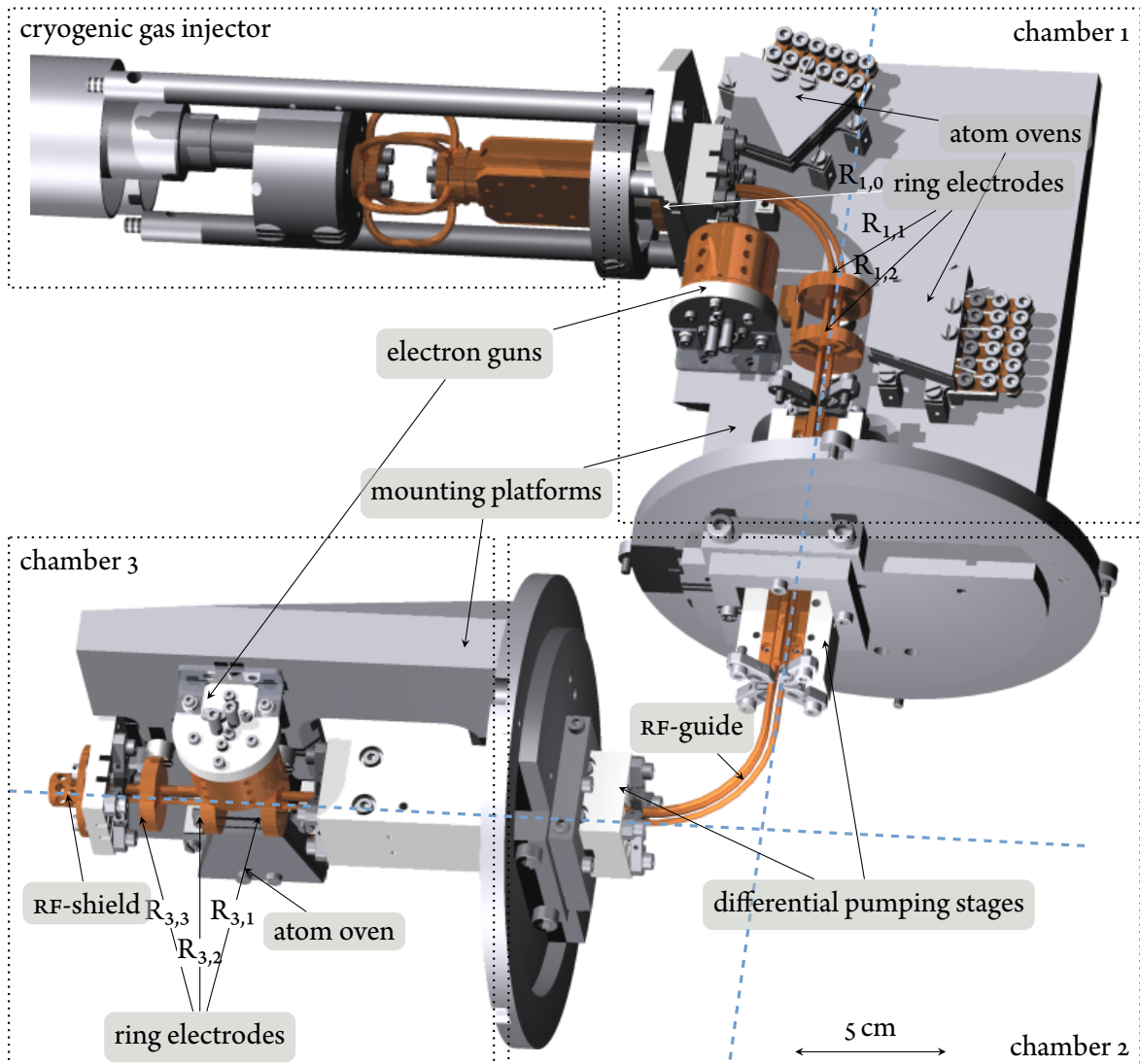


Figure 2.1.: Computer drawing of TIAMO's basic mechanical layout. For the sake of clarity and visibility, various mechanical elements have been suppressed. Instead, dotted lines indicate the belonging to the three vacuum vessels and the injector system. The chambers 1 and 3 are made of 150 mm tubes that are mounted to a cube (chamber 2) of equal size. Dashed lines show the two optical axes on which laser beams can propagate through the apparatus.

2. Ion trap apparatus

of the quadrupole guide. The layout of this injection system follows closely the description in [91] but was modified for ultrahigh vacuum demands. The modifications are: deaeration slits, materials with better vacuum compatibility, e. g. oxygen free copper, and a high speed electro-pneumatic operated valve¹ for pulsed gas injection.

In order to arrange for optimum injection conditions, a manually operated leak valve² allows to fine-tune the gas pressure in front of the electro-pneumatic valve. For the experiments of this thesis, hydrogen gas was injected and best results were achieved at a backing pressure³ of 0.3 mbar in front of the cryogenic gas injector.

To summarize briefly, gas can be injected in short pulses (few millisecond duration), runs through a meandering capillary made of copper that is in massive thermal contact to a liquid nitrogen reservoir. The cooler itself can also be heated giving the possibility to control the gas temperature at the exit. When the gas jet effuses from the exit capillary it has a pronounced forward angular distribution [91] that optimizes the coupling into the RF-guide which is separated by a small gap of about 1 mm from the exit of the capillary. Hence, the injection system is modular in the sense that it connects self-contained to chamber 1. For the sake of modification, it can be taken off from chamber 1 and easily be replaced by another injection system. It is assumed that the extension of the present apparatus by an electrospray-ionization source as injector will greatly improve its applicability for experiments on generic molecular ions. An appropriate source has been prepared in parallel to this thesis. It will be described in the thesis of Günther Leschhorn.

Chamber 1 itself is enclosed inside a 150 mm four-way-cross of which two arms where shortened. An additional 100 mm tube welded on top of the cross is used for a re-entrant window. The four arms connect to: the gas injection system, a vacuum pump, an interface flange, and the central cube. In order to contend with the expected high gas loads during injections, a 500 l s^{-1} turbomolecular pump⁴ is installed. Another smaller 70 l s^{-1} turbomolecular pump system⁵ acts as backing pump for both chambers 1 and 2. In case of stalling turbomolecular pumps due to electrical power failure, two emergency electro-pneumatic operated valves⁶ cut off the backing line from chambers 1 and 2 automatically. All connections of the 32-pin electrical feed-troughs⁷ are equipped with noise suppressing low-pass filters blocking frequencies above 300 kHz [42] and consisting of a $25 \text{ }\mu\text{H}$ inductor⁸ as well as 2 nF ceramics feed-through capacitor⁹. The electrical feed-throughs, a cold cathode pressure gauge¹⁰ and a laser window are combined on the interface flange. A small stainless steel mounting platform is enclosed in the last arm that connects to the central cube. A big advantage of this approach is the ability to maintain maximal accessibility during the assembly of the filigree

¹ series 99,099-0080-900, Parker

² UDV046, Pfeiffer

³ CMR263, Pfeiffer

⁴ TMP 551, Varian

⁵ TurboCube TSU-071, Pfeiffer

⁶ AVC016PX and AVC025PX, Pfeiffer

⁷ 16884-01-CF, Ceramtec

⁸ 74D5266, Bürklin

⁹ 62D576, Bürklin

¹⁰ IKR261, Pfeiffer

structures on the mounting platform. The actual vessel comes into existence in the last step, when the four-way-cross is put over the platform assembly and bolted to the central cube.

Two atomic oven ensembles (section 2.5 on page 35), one electron gun (see appendix B.1 on page 142), the RF-guide, three ring electrodes for axial confinement and compensation electrodes are mounted on the platform. These electrodes are imperative to counteract adverse electric fields that can be caused by patch potentials on electrode surfaces [27], charged isolators close to the ions, or imperfections in the RF-electrode shape or position; see also appendix B.7 on page 152. They have been realized in form of 0.5 mm diameter copper wires that run next to the RF-guide except of in one place where a small copper shielding plate is used instead. Vapor from the atom oven is deposited on this shield preventing the electron gun from staining. It is possible to substitute dedicated compensation electrodes by suitable DC-voltages on the RF-electrodes directly in principle. From a practical point of view this is not advisable. First of all, DC-voltages on the RF-electrodes affect the RF-guide as a whole which might be undesirable in regard to the locality of the distortions to be compensated. Secondly, the present electrical layout does not allow for separate DC-voltages on the RF-electrodes since all of them are connected to a common DC-potential; see section 2.2 on page 27. More flexibility of the electrical configurations would be accessible if capacitive filter elements were included in the setup but this contradicts the preassigned design goal of a high trap resonance frequency.

2.1.2. Isolation chamber

The central vacuum cube is referred to as chamber 2. By the time of writing this thesis, the purpose of this chamber is mainly to isolate the vacuum conditions of chamber 1 from 3. To this end, a turbomolecular pump¹¹ with 300 l s^{-1} pumping speed is mounted to the cube and two differential pumping stages are installed into the walls connecting to chambers 1 and 3. Also, the electrical contacting of the RF-guide (see fig. 2.7 on page 31) is realized in chamber 2. This point is further discussed in section 2.2 on page 27.

The two optical axes on which laser beams can propagate through the TIAMO setup cross in chamber 2. Two windows¹² (see fig. 2.2 on the next page) allow the beams to enter and exit. For the majority of experiments contained in this thesis, one of the windows had been taken off and a link to another vacuum system was established instead. By that, TIAMO was connected to the femtosecond laser system described in section 3.1 on page 55.

2.1.3. Experiment chamber

In many respects chamber 3 and 1 are similar. The concept of a mounting platform containing electron gun, atom ovens, compensation & ring electrodes and RF-guide clamps (see section 2.2 on page 27) is the same. Figure 2.3 on the following page shows a photograph of the platform. The vessel for chamber 3 was realized by an about 0.5 m long tube with a diameter of 150 mm. Great care has been taken both in design of the installed components and in choice of materials so as to guarantee

¹¹ TMP 301, Varian

¹² custom design, allectra

2. Ion trap apparatus

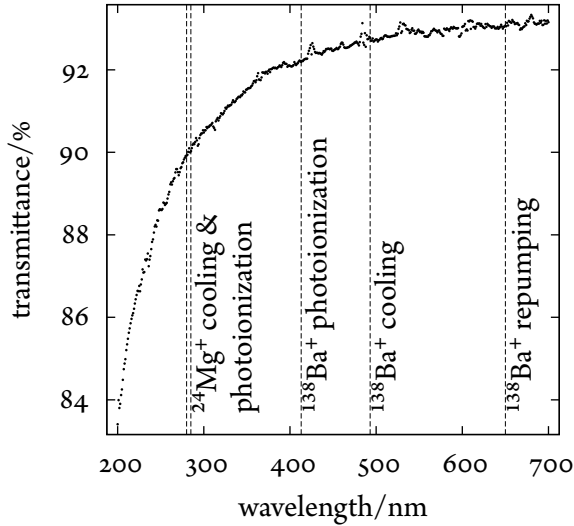


Figure 2.2.: Normal incidence transmittance through the used fused silica windows measured with a transmission spectrometer (Bruins instruments). All windows of the setup are alike. Due to the variety of laser wavelengths for photoionizing and laser cooling of $^{24}\text{Mg}^+$ and $^{138}\text{Ba}^+$, no all-encompassing anti-reflection coating was realized.

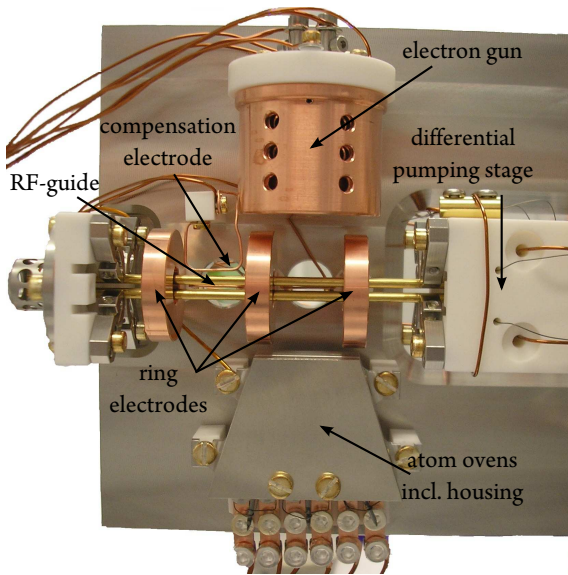


Figure 2.3.: Top view on the components assembled on the mounting platform in chamber 3. The three ring electrodes around the RF-guide define the actual two three-dimensional trapping regions along the RF-guide. One bent wire compensation electrode is easily recognizable, two similar, orthogonal ones are installed beneath the RF-guide but hardly visible. The housing of the atom ovens is used as a fourth compensation electrode.

best possible vacuum conditions and minimize potential disturbances like parasitic magnetization. Different from chamber 1, all stainless steel parts including internal and external screws, nuts and washers are made from type 316L which is a less magnetic material. All copper parts are made from oxygen free material¹³. All screws used inside chamber 3 have complanated threads, screws with blind bore holes are additionally vented through their shaft in order to avoid virtual leaks. A thin silver layer on the screws (ZTE, Max-Planck-Institut für Plasmaphysik) provides the lubricant. The outgassing rate at room temperature was reduced by baking the completely assembled apparatus at the maximum allowed temperature range 170° to 190° limited by the viewports for seven days.

A custom designed reentrant window¹⁴ allows to image ions from short distances, see section 2.6 on page 37 for further details about the imaging system. An ion getter pump in combination with a

¹³ Cu 99.99% OFHC C110, Advent

¹⁴ Vacom

titanium sublimation pump¹⁵ maintains a vacuum at $2 \cdot 10^{-10}$ mbar. It was observed that the final pressure in chamber 3 is about $1.3 \cdot 10^{-9}$ mbar when pumped by the ion getter pump alone. After engaging the titanium sublimation pump it dropped to about $2.6 \cdot 10^{-10}$ mbar over two days. From this follows a four times higher pumping speed of the titanium sublimation pump compared with that of the ion getter pump which is about 175 l s^{-1} for nitrogen gas according to its specifications. A combination of these two complementary pump types assures sufficient pumping of getterable gases such as hydrogen and nitrogen by chemisorption [72] on the large renewable titanium coated surface generated by the sublimation pump and non-getterable gases like argon and methane by implantation in the surface layer of the ion getter pump. The pressure is measured with a Bayard-Alpert type ion gauge¹⁶ which is located on an interface flange that also accommodates a laser window and an all metal corner valve. The latter had been used during bake-out only.

In the name of broad experimental flexibility, a residual gas analyzer¹⁷ is installed directly at the exit of the RF-guide. A radio frequency shield minimizes cross-talking effects between both RF-operated devices. On a line that is orthogonal to the RF-axis and the observation direction, two CF63 blind flanges on both sides of chamber 3 allow to extend the apparatus with further equipment. Since this mounting position gives good optical access to the trapped ions, it is possible to apply laser or X-ray pulses from there in future experiments.

2.2. Radio frequency guide

Capitol element of an ion trapping setup is the electrode structure to which the radio frequency is applied. In the case of TIAMO, it is elongated and has a length of 48.5 mm; see fig. 2.4 on the following page. It forms a guide along which ions can move freely in one dimension. Three-dimensional traps along the guide are constituted by the ring electrodes for axial confinement; see also section 2.3 on page 30.

In order to attain the desired double bend wires (see appendix C.3 on page 159 for an explanation) an aluminum plate with milled notches of the desired shape was devised. The wires could be pressed into it and fixed by a weight. It was found that *soft annealing* the electrodes inside this tool at around $160 \text{ }^\circ\text{C}$ for several hours helped much to overcome the wire's resilience and to maintain an ample rigidity of the metal at the same time. Too soft copper can be plastically deformed rather easily which gives a high risk for accidental deflections of the electrodes that would not suffice the precision requirements of the presented experiments.

As is discussed in section 1.1 on page 7, the frequency Ω of the RF-voltage that is applied to the quadrupole electrodes is one of the central parameters of an ion trap. In order to provide stable trapping conditions, the stability parameter $q \propto U_{\text{RF}}/\Omega^2$ (see eq. (1.3) on page 9) should not exceed 0.5. Since the trap depth is proportional to q and the RF-amplitude (see eq. (1.6) on page 10), stiff and deep confinement is reached for high RF-voltages. Via the constraint $q < 0.5$ this implies a high trap frequency.

¹⁵ StarCell Plus 300, Varian

¹⁶ 274023, Vacom

¹⁷ PT M2S91 QMA 200M, Pfeiffer

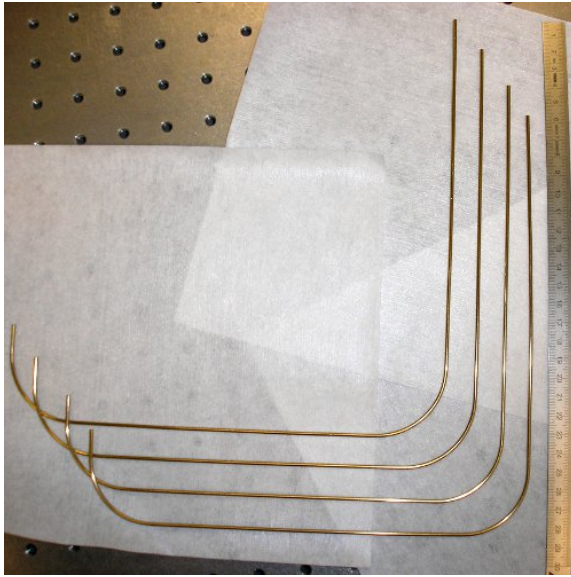


Figure 2.4.: The four wire electrodes used to form the quadrupole guide. The electrodes are made of 2 mm diameter copper wires and were gold-plated ($\approx 2 \mu\text{m}$) to prevent oxidation of the copper. They are fixed at 1 mm distance to each other with the help of special clamps visible in fig. 2.7 on page 31. The U-shape of the guide implied two pairs of electrodes with slightly different lengths (489.2 mm, 479.8 mm) owing to the two radii of curvature (37 mm and 34 mm). Two bents by 90° with 35.5 mm on-axis radius of curvature were realized; see appendix C.3 on page 159 for a motivation of the bents.

The resonance condition

$$f_{\text{res}} = \frac{1}{2\pi} \frac{1}{\sqrt{L(C + C_p)}}$$

of an electrical resonator is defined by its capacitance C and inductance L . Both quantities are determined by the components making up the helical enhancement resonator: the RF-guide itself, a big resonating coil, and the involved electrical connections; see fig. 2.5 on the facing page. Aiming at high resonance frequency, any parasitic capacitive effects C_p had to be minimized.

The avoidance of unnecessary capacitance is addressed in several aspects of the electrical design, e. g. by using specific low loss radio frequency feed-throughs¹⁸ and by eliminating any dielectric material close to radio frequency conduction parts. The latter led to the development of the resonating inductor being a free-standing air coil with big winding pitch that equals three times the used copper conduit diameter (10 mm). In order to reduce the capacitance induced by the shielding of the coil, it had to be made big, too. The result is called *Thor's hammer* and has a 40 cm diameter at a height of 50 cm. A previous but similar development version has already been described in more detail by Günther Leschhorn [104].

The input voltage U_{in} to the helical enhancement resonator is supplied by a radio frequency generator¹⁹ that can be tuned to match the resonance frequency. The signal gets first pre-amplified²⁰ by 39.6 dB, taking already all losses of downstream RF-equipment into account, before it is inductively coupled into the helical enhancement resonator. Impedance matching is optimized by adjusting the incoupling loop's position inside the big resonating coil. Successful impedance matching was signaled by minimizing the reflected input voltage which was singled out with the help of a bi-directional coaxial coupler²¹ and detected with a spectrum analyzer²².

¹⁸ 16991-01-CF, CeramTec

¹⁹ HP8640A, Hewlett Packard

²⁰ AR 10W1000, amplifier research

²¹ 3020A, Bell electronics narda

²² HMS1000, Hameg

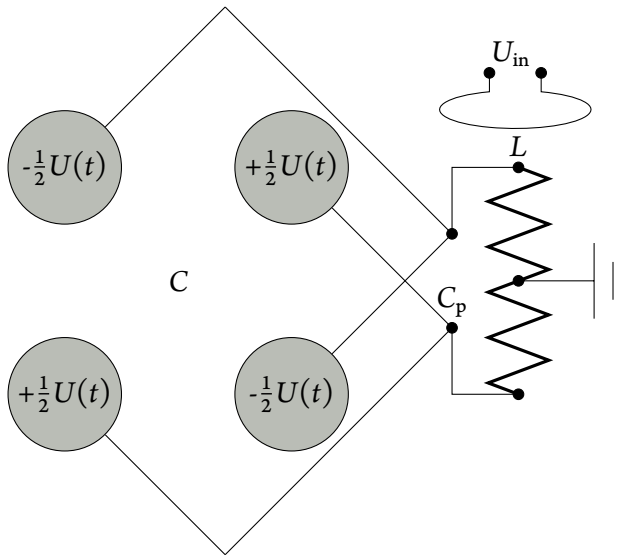


Figure 2.5.: Electrical layout of the helical resonator used for the RF-voltage enhancement. The resonator is driven by U_{in} applied to an adjustable looped wire which is loosely inductively coupled to the resonator coil (inductance $L = 5.95$ H, self-capacitance 7.4 pF). The position of the incoupling loop is chosen to fulfill the impedance matching condition. The total capacity of the system at resonance ($\Omega = 2\pi \cdot 6.81$ MHz) including all parasitic capacitance C_p equals $C = 91.7$ pF. Symmetric voltage build-up at the two opposing ends of the coils was achieved by careful adjustment of the grounding.

A large Q -factor was another important design goal of the enhancement resonator. Q is proportional to the fraction of stored energy that is lost per oscillation cycle from the system $Q = 2\pi \times \text{energy stored}/\text{energy lost per cycle}$. The less losses, the higher the Q -factor and the higher the voltage enhancement

$$\frac{U_{\text{RF}}}{U_{\text{RF,in}}} = \sqrt{\frac{2\pi f_{\text{res}} L Q}{50 \Omega}} \quad (2.1)$$

of the helical resonator. From the measurement (see fig. 2.6 on the next page) of the Lorentzian shaped resonance

$$\frac{U_{\text{RF}}}{U_{\text{RF,in}}} \propto \frac{1}{\sqrt{(f_{\text{res}}^2 - f^2)^2 + f_{\text{res}}^2 f^2 / Q^2}}$$

it was possible to deduce $Q = 734$. By an alternative definition, the Q -factor can be directly read off as the quotient of resonance frequency divided by the $1/\sqrt{2}$ -width of the curve. The experimentally determined Q -factor yields a voltage enhancement $U_{\text{RF}}/U_{\text{RF,in}} = 61$ where eq. (2.1) and $L = 5.95 \mu\text{H}$ (see fig. 2.5) has been used. Measurements of the voltage enhancement using trapped ions as detector are discussed in section 4.1.4 on page 72.

The most powerful RF-amplifier²⁰ used was able to drive a RF-voltage $U_{\text{in}} = 45$ V (Vp) corresponding to 20 W at 50Ω . This voltage is enhanced by 61 to almost 2700 V in the helical resonator which corresponds to ± 1350 V at the two opposing electrode pairs of the RF-guide. For switching the electrodes' polarity at the resonance frequency $f = 6.8$ MHz RF-currents as high as 10.5 A (I_p) are needed. Under these extreme conditions, the oscillating stored energy gives rise to a power of $Q \times 20$ W = 14.7 kW and heats the electrodes up to 200 °C [104]. Highest voltages are expected to become relevant in experiments on guiding of neutral molecules (see appendix C.3 on page 159), for example. In order to trap $^{138}\text{Ba}^+$ ions with the stability parameter $q = 0.22$, that was used in most of the experiments of this thesis, a RF-voltage $U_{\text{rf}} = 375$ volt will be required. For $^{24}\text{Mg}^+$ ion trapping, a lower RF-voltage ≈ 65 V is appropriate; see section 4.1.4 on page 72.

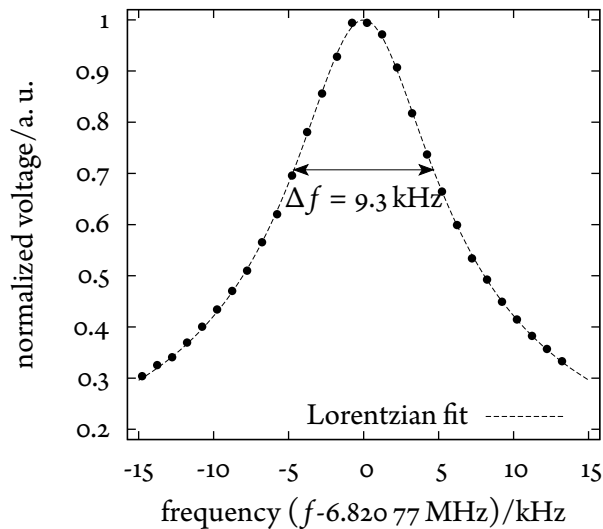


Figure 2.6.: Normalized voltage in the resonance circuit as a function of frequency. The signal was picked up by a small ring shaped electrode inside the RF-shielding of the helical resonator and was detected by a spectrum analyzer. Voltage measurements directly at the electrodes would be severely biased because touching the resonating system adds not negligible capacitive load. From the Lorentzian fit follows $Q = 734$. This matches the alternative definition of $Q = f_{\text{res}} / \Delta f$.

Ohmic resistance is one major loss contribution lowering Q . Several actions were taken to minimize ohmic losses. Owing to the *skin effect*, RF-currents flow only in a thin surface layer. For TIAMO the characteristic depth δ in copper is $25 \mu\text{m}$. Consequently, conductors with large surface area are required to compensate the reduced effective volume. Additionally, a $2 \mu\text{m}$ to $3 \mu\text{m}$ thick gold layer was electroplated (ZTE, Max-Planck-Institut für Plasmaphysik) on top of the RF-electrodes because pure copper develops a poor conducting copper oxide layer when exposed to air which affects the conductive “skin”. Contrastingly, gold does not corrode thus protects the thin conducting layer. Contacting of the RF-electrodes was realized with massive and firm gold plated clamps (see fig. 2.7 on the next page) that established electrical contact over a large surface. The clamps were positioned half way of the RF-guide inside chamber 2 for reasons of symmetric electric potentials and in order to optimize heat transfer from the electrodes to the supply lines. For the rest of the electrical circuit, big surface structures like copper tapes (cf. fig. 2.7 on the facing page) and wide tubes were used instead of thin, poor RF-conducting wires.

Mounting of the RF-guide was realized with the help of clamps similar to that used for rf-contacting. However, they are made of stainless steel in order to attain maximum solidity. A set of four clamps holds the RF-guide in place at altogether six positions along the guide: two clamp sets at both ends of the guide and four sets on the ends of the two differential pumping stages. The positions of the six sets are visible in the schematic fig. 2.1 on page 23. One of each clamp sets is also contained in the image in fig. 2.7 on the facing page.

2.3. Ring electrodes

In section 1.1.2 on page 11 it is pointed out that the electric potential formed by a pair of copper ring electrodes encircling the quadrupole guide establishes the axial confinement for trapped ions. Hence, these rings, besides the RF-rods, form a second set of electrodes that had to be carefully designed. Starting from the derivation in appendix B.6 on page 151, two ring shaped electrodes are easily understood to make up a doubly humped potential that can confine ions in the axial direction.

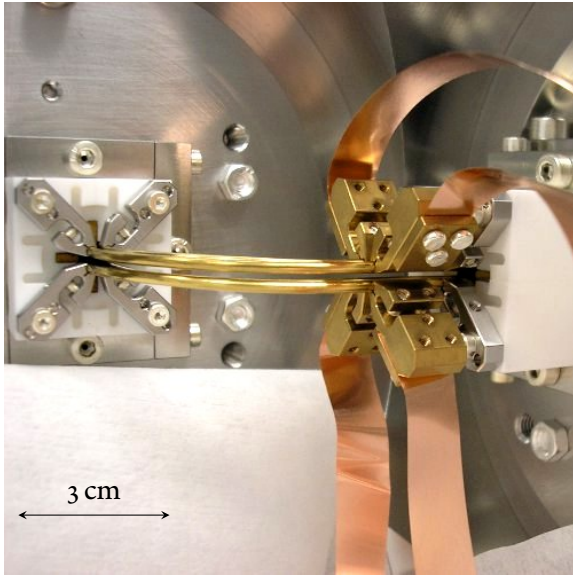


Figure 2.7.: View into chamber 2 during the assembly. The two outer electrodes of the radio frequency guide are visible as golden bent structure in the middle. A set of four gold plated clamps establish firm contact to both the RF-electrodes and the copper tape supply lines. In the background, the guide disappears into the differential pumping stage connecting to chamber 3. On its front surface, one can see a set of four stainless steel clamps that hold the RF-electrodes in place.

In order to find the optimum geometry of the rings, the influence of the parameters indicated in fig. 2.8 on the potential form was studied with the help of the commercial software CPO [105]. A summary thereof is compiled in fig. 2.9 on the following page.

It is evident from the absolute values of the electric potential along the symmetry axis of the RF-guide (see fig. 2.10b on page 33) that the RF-electrodes cause a substantial shielding effect. The maximal amplitude of the electric potential $\Phi(z)$ between the ring electrodes is less than 1 mV even though the ring electrode voltage was set to 1 V in the simulation. The shielding is due to many field lines ending on the RF-electrodes. Only few of them penetrate into the inner region between the RF-electrodes. That effect is visualized in fig. 2.10a on page 33. Electrical charges outside the RF-guide, such as undeliberately charged insulators, are effectively shielded as well. Since the shielding strength is not constant along the RF-axis but increases with the distance to the ring electrodes, the slope of the axial potential gets much steeper. This implies higher axial trap frequencies than one would calculate for a homogeneously shielded trap; cf. fig. 2.10b on page 33. The actually used ring electrode configuration: $r_i = 4$ mm, $r_o = 12$ mm, $w = 5$ mm, $d = 20$ mm is shown in fig. 1.4 on page 12. Around its center, the axial potential is approximately harmonic $\Phi(z) \approx U_{\text{ring}} / 1000 \cdot (z/z_0)^2$, $z_0 = 7.5$ mm. Typical experimental values for the ring electrode

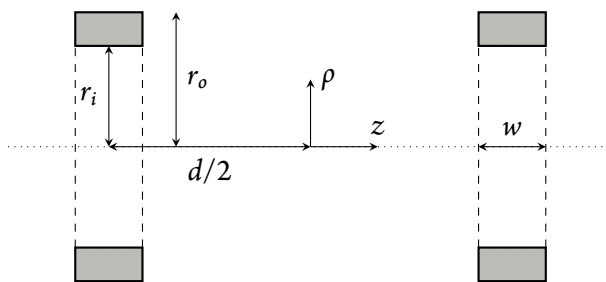


Figure 2.8.: Axial cross section showing coordinate system and geometric parameters of a ring electrode pair used to provide a confining electric potential in the axial direction z . In the radial directions ρ , ions are confined by the quadrupole guide (not shown). The geometry is defined by the outer radius r_o , inner radius r_i , width w and separation d of the two rings.

2. Ion trap apparatus

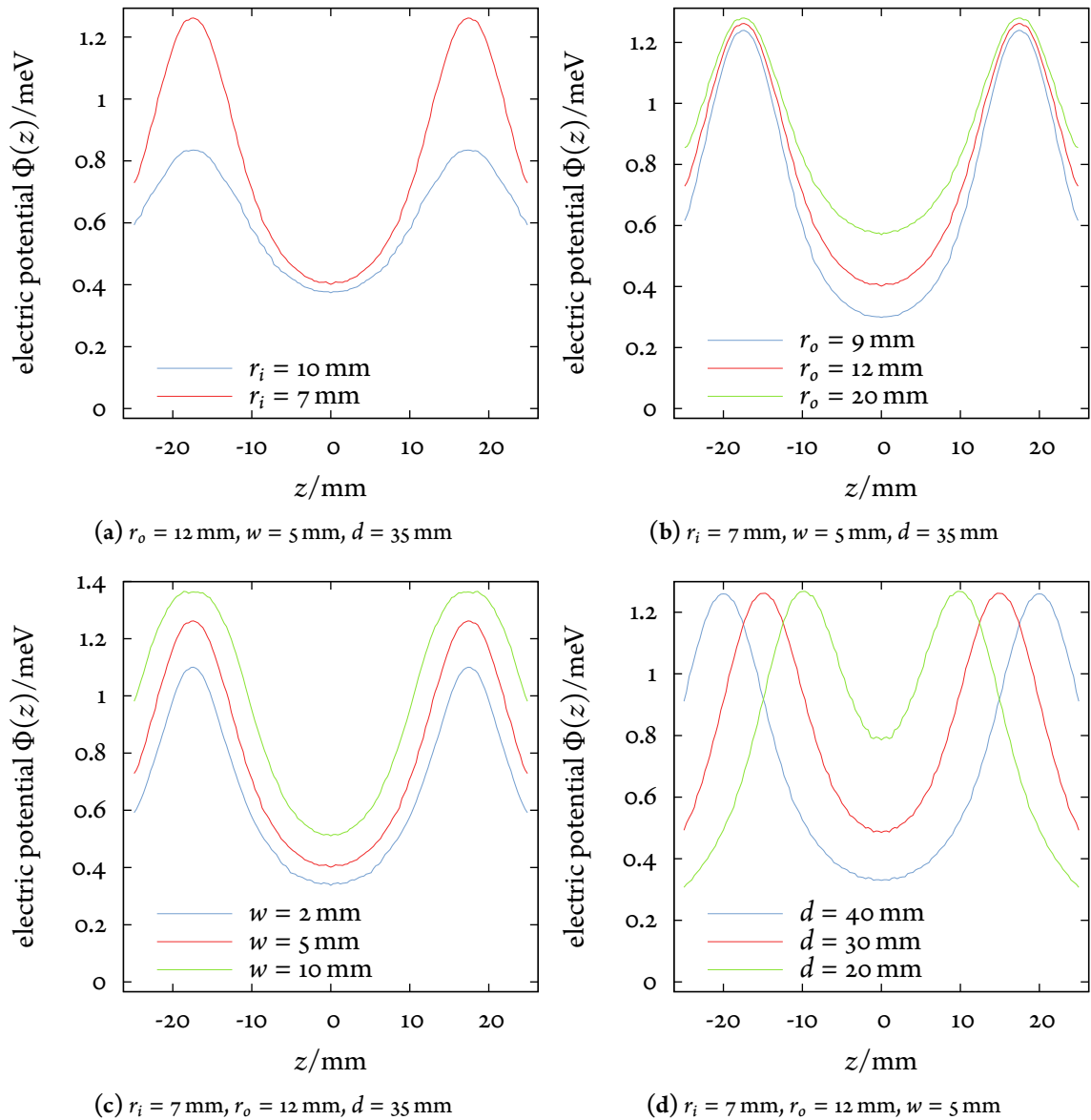
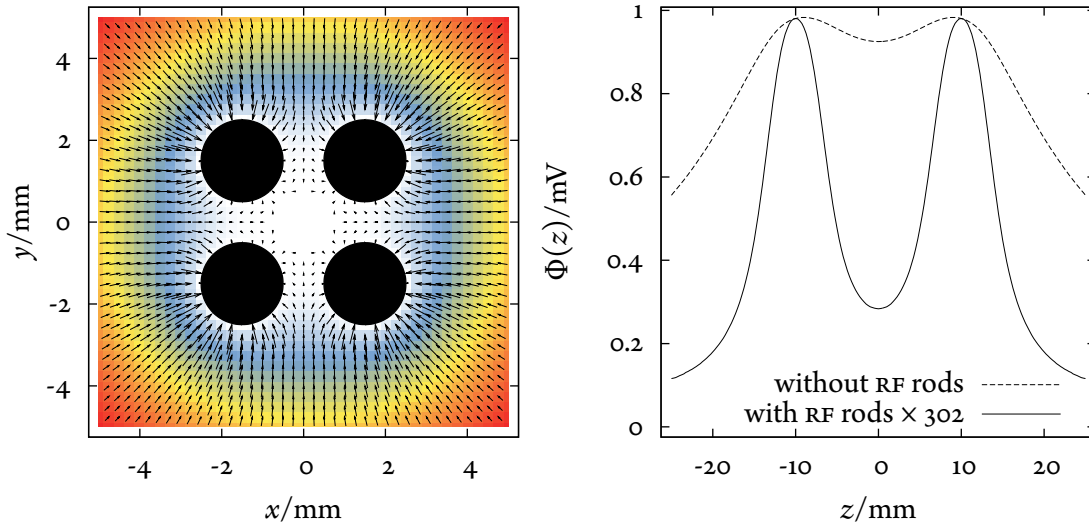


Figure 2.9.: Simulated [105] electric potentials $\Phi(z)$ illustrating the dependence of the axial potential formed by a pair of ring electrodes along the symmetry axis of the RF-guide on the geometric parameters r_i , r_o , w , and d defined in fig. 2.8 on the previous page. A voltage of 1 V is assumed to be applied to the ring electrodes in all cases. The electric potential formed by the finally realized configuration ($r_i = 4$ mm, $r_o = 12$ mm, $w = 5$ mm, $d = 20$ mm) shown in fig. 2.10b on the facing page combines a stiff axial potential with other requirements such as good optical access to the trapped ions and mechanical stability of the electrodes. Its small inner radius $r_i = 4$ mm increases the axial trap depth but does hardly affects the potential curvature at the center; see (a).



(a) Electric field lines (arrows) in a plane normal to the RF-axis and symmetric with respect to a pair of ring electrodes. The arrow length is proportional to the electric field amplitude, the color shade to the potential. Only few field lines reach the region between the RF-electrodes (black circles, electrical ground), causing a shielding effect on the order of $1/1000$. (b) Axial electric potential along the RF-axis. The shielding effect is stronger at larger axial distance from the ring electrodes. At the trap center $z = 0$, the electric potential is reduced by a factor of 985. The potential in the shielded case (solid line) is scaled by 302 for visibility reasons.

Figure 2.10.: Simulation (CPO [105]) of the electric field and potential formed by a pair of ring electrodes ($r_i = 4$ mm, $r_o = 12$ mm, $w = 5$ mm, $d = 20$ mm; see fig. 2.8 on page 31) illustrating the shielding effect caused by the RF-electrodes.

voltages U_{ring} ranged from 150 V to 250 V leading to axial trapping frequencies ω_z of $2\pi \cdot 30$ kHz to $2\pi \cdot 50$ kHz for $^{24}\text{Mg}^+$ ions at 10 μm to 20 μm mutual distance; see also section 4.1.4 on page 72.

2.4. Differential pumping stages

Purpose of the differential pumping stages (DPS) is the reduction of the gas conductance between two neighboring vacuum vessels with the aim to maintain a high pressure gradient. At the same time it shall be possible to guide ions from one chamber to the other. In order to satisfy both needs, the DPS design described by Junglen [91] for neutral molecules was adapted for the requirements of an ion trapping experiment. Most remarkable addition are the four gold plated copper inlay electrodes inside the Macor ceramics body of the DPS; see fig. 2.11 on the following page. These electrodes prevent possible charging effects of the ceramics insulator along the pathway where a direct line of sight to the ions exists. On the Macor surface, it is suspected that photo-effect assisted charges might form due to the high photon energy of the UV cooling laser and the additional high intensities of the femtosecond pulses. Once charges are deposited or generated there, they can diffuse over the surface for long times (minutes) until they reach a conductor or get neutralized by, for instance, collisions with the background gas. By all means, charges on the DPS body, close to

2. Ion trap apparatus

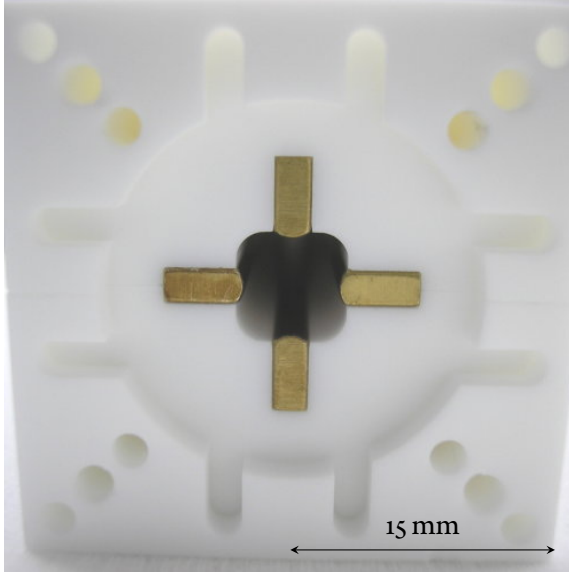


Figure 2.11.: View on the front side of a 10 cm long differential pumping stage body without RF-electrodes. Voltages can be applied separately to the four gold plated electrodes. They can be used as compensation electrodes or make up a drift tube for (de)acceleration or bunching of guided ions. If not used actively, they prevent charges from building up on the Macor ceramics. The clover leaf-shaped profile maintains a minimum distance of 0.5 mm to the surface of the RF-electrodes.

RF-guide, may compromise its trapping and guiding properties for ions but are prevented by the inlay electrodes. Since separate voltages can be applied to all four of them, they can also be used as compensation electrodes for this section of the guide or act as drift tubes. In the latter case, a common and quickly switched voltage would have to be applied to all inlay electrodes. This can be used to accelerate or decelerate ions and in this way provide bunches with increased particle density.

The gas isolating property of the DPS depends on length and aperture. According to [89], in the molecular flow regime a circular long tube of diameter d and length l has a conductance $L = \pi d^3 \bar{c} / 12l$ with $\bar{c} = \sqrt{8k_B T / \pi m}$ denoting the mean velocity of particles of mass m at temperature T . In order to estimate the order of magnitude of L , one can define an effective diameter of the DPS by $A_{\text{DPS}} = \pi d_{\text{eff}}^2 / 4$. A circle width diameter $d_{\text{eff}} = 5$ mm has the same area as the aperture of the DPS $A_{\text{dps}} = 19.4 \text{ mm}^2$ where the cross section surface of the RF-rods has already been subtracted. If one further assumes H_2 to dominate the residual gas pressure at $1 \cdot 10^{-10}$ mbar, with $\bar{c} = 1760 \text{ m s}^{-1}$ and $l = 10$ cm, an estimation of $L \approx 0.6 \text{ l s}^{-1}$ follows. The vacuum conductance L of both DPS together was measured as 0.25 l s^{-1} . Because they are used in series, the conductance of a single DPS is $L = 0.5 \text{ l s}^{-1}$, in good agreement with the estimation above. In a more practical sense, it is interesting to ask for the maximal pressure difference Δp sustained by the DPS between the UHV experiment chamber and the preparation chamber. From the definition of the conductance $L = q_{pV} / \Delta p$ with q_{pV} denoting the throughput, one can calculate Δp . In a steady-state at pressure p_{exp} , the throughput must be equal to the amount of gas removed from the experiment chamber $q_{pV} = S p_{\text{exp}}$ [89] at pumping speed $S \approx 1000 \text{ l s}^{-1}$; see section 2.1.3 on page 25. Using the numbers from above, one finds that a pressure difference to chamber 1 $\Delta p = 4000 p_{\text{exp}}$ should be sustainable. This could be verified inversely in a situation when the pressure in chamber 3 had risen to $1 \cdot 10^{-6}$ mbar while the pressure in chamber 1 stayed well below the lower limit of the reliable vacuum gauge's measurement range $2 \cdot 10^{-9}$ mbar. Thus, a pressure gradient of at least three orders of magnitude can be maintained. By that, an increased gas load raising the pressure to $\approx 1 \cdot 10^{-7}$ mbar, as it will be likely to occur when

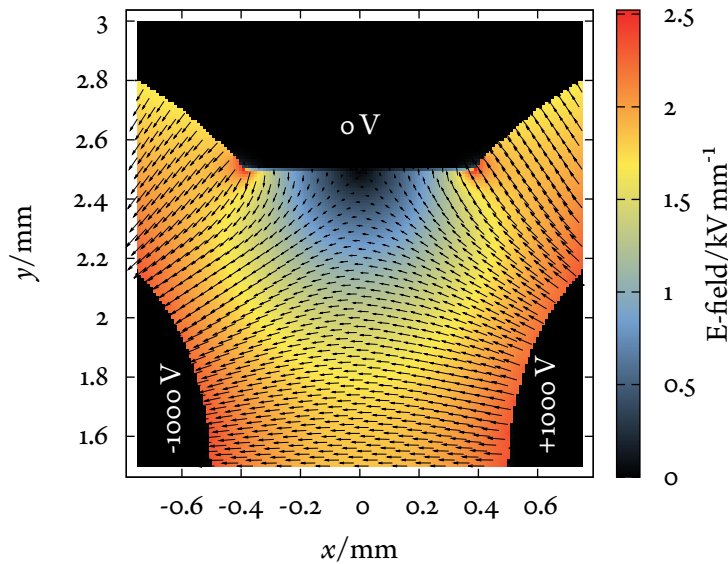


Figure 2.12.: Detail of the simulation [105] of the electric field in a cross section perpendicular to the RF-axis in the middle of the differential pumping stage. Voltages of ± 1000 V on the RF-electrodes were assumed. Maximum field strengths occur at sharp corners. Possible problems related to this were circumvented by using inlay electrodes with rounded and polished surface as can be seen in fig. 2.11 on the facing page. In this figure, a flat surface has been assumed instead.

an electro-spray source is used to inject molecular ions into the experiment chamber (see chapter 6 on page 118), will be tolerable.

A trade-off between maximum disruptive strength and good vacuum isolation is realized in the clover leaf-shaped aperture with 0.5 mm clearance between the electrodes and the DPS walls. A simulation of the resulting electric field is shown in fig. 2.12. The experimental results presented in section 4.1.4 on page 72 showed that at rms RF-voltages as high as 1000 V arc-overs do not occur. The length of the DPS (10 cm) was chosen so as to find a good compromise between large vacuum isolation and sufficiently short RF-guide.

2.5. Atom oven

Atomic ions are generated from atoms in a thermal beam by photoionization. The small resistively heatable tantalum tubes from which the atom vapor evaporates are referred to as atom ovens within this thesis. One of them can be seen in fig. 2.13 on the next page with its dimension given in the caption.

A current through the tantalum wires heats the attached tube and the metal inside up to the temperature at which the vapor pressure of the respective metal rises sufficiently above the residual gas pressure. The temperature is chosen for the flux of atoms in the thermal beam emitted from the tube to meet the experimental requirements on the photoionization rate. For the current experiments, an ion loading rate of approximately 1 s^{-1} was sufficient. The photoionization scheme of magnesium and the relevant atomic transitions are described in [97]. The optimum temperature

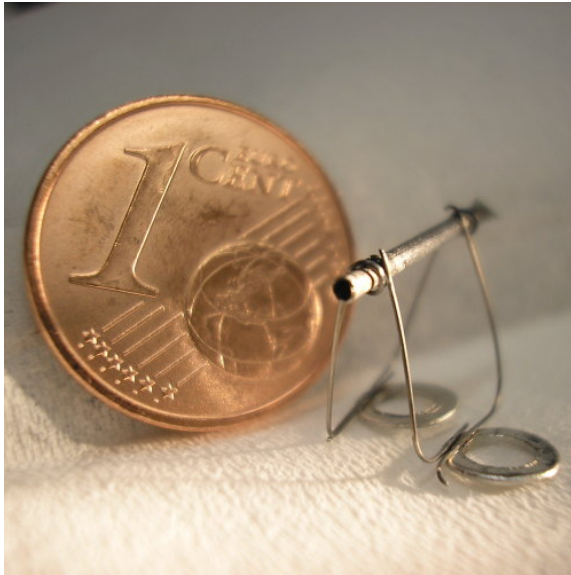


Figure 2.13.: Atom oven tantalum tube (1 mm outer diameter, 15 mm long) ready to be loaded with magnesium or barium. The back-side of the tube is closed by tight crimping. The front side is sealed with indium after barium chips were inserted under dry nitrogen to prevent oxidation; see appendices B.2 and B.3 on page 143. During bake-out the sealing melts and allows evaporated barium atoms to exit. The tantalum heating wires looping around the tube are spot-welded and act also as support. Washers allow to mount the oven securely. In total nine of these tubes—a set of three tubes in each oven ensemble—are installed in TIAMO.

depends on the metal's vapor pressure and additional experimental and geometric parameters. The higher the photoionization laser power, the lower is the atom flux needed to sustain a certain ionization rate. On the one hand, the rate depends on the overlap volume of thermal atomic beam and the laser beam. On the other hand, owing to the broadening of the transition frequency induced by the Doppler effect, the ionization rate is also function of the velocity distribution of the thermal beam depending on the angle between the beams and its temperature. It is hard to measure the oven temperature because its dimensions are tiny but the temperature distribution over the tube inhomogeneous though; cf. fig. B.6a on page 147. However, the oven does not glow in the visible spectral range but can be seen with night vision gear at regular operation conditions. The oven tubes were chosen to be tiny because in this way also the heat capacity is small and the oven stops emitting atoms shortly (a few seconds) after the heating current is interrupted. Appendix B.2 on page 143 provides more detailed information about the heating characteristics, appendix A.1.1.a on page 124 focuses on the integration of an automated loading procedure in the experimental control scheme.

When the atomic beam exits from the oven tube, its angular distribution is wide. The estimated opening angle of the emission cone surpasses 90° , cf. fig. B.6b on page 147. In order to prevent staining of the RF-electrodes with metal deposits, a restrictive aperture was placed in front of the oven. It is realized in a $200\ \mu\text{m}$ wide slit-shaped opening at a distance of 21 mm as part of a protective housing (see fig. 2.14 on the next page) around the atom oven. The slit clips the atomic beam in one direction such that it is 1 mm wide and just fits through the 37.5 mm distant RF-guide. In the other (axial) direction, no aperture is used in order to maximize the photoionization volume.

For trapping experiments with two different atomic ion species, ovens for magnesium and barium were prepared and grouped into three ensembles which are composed of three single tubes each; see fig. 2.3 on page 26 and fig. 2.14 on the next page. One of these tubes contains a magnesium wire, the other two contain barium chips. Both fillings reflect the natural abundances of the respective metal's isotopes. The magnesium oven is aligned perpendicular to the laser axis

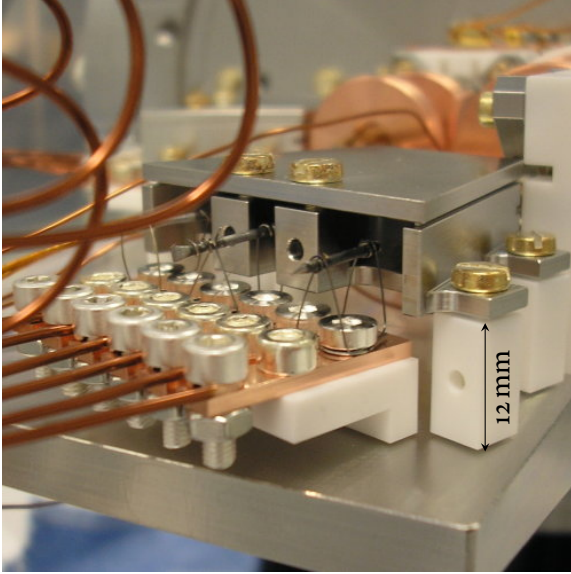


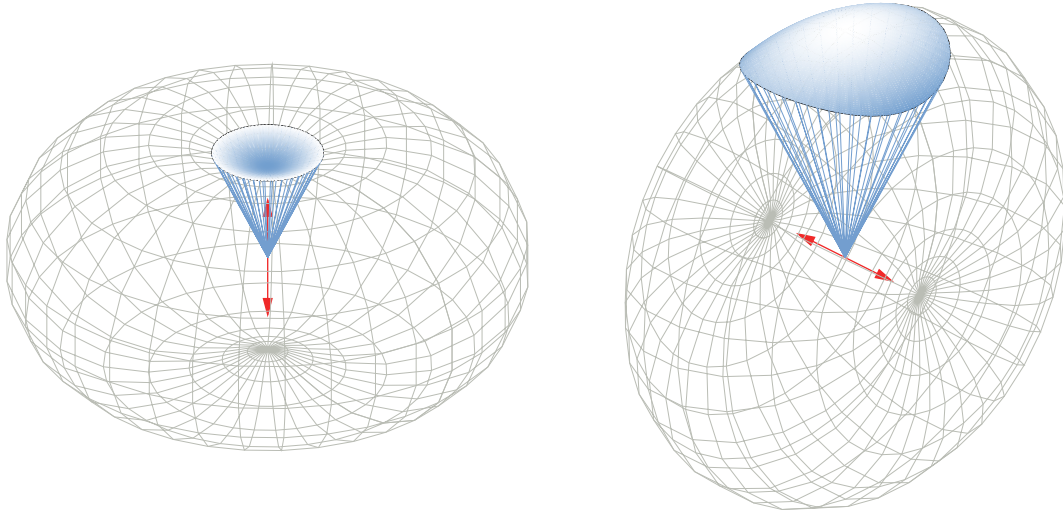
Figure 2.14.: View on one atom oven ensemble during assembly of chamber 1. Three atom oven tubes for magnesium (middle) and barium (left and right) are mounted such that they point to a common spot inside the RF-guide 37.5 mm away from the opening of the tubes. The tubes extend into a protective housing that has a 200 μm wide horizontal slit in its front surface (not visible) collimating the atomic beam. The ceramics bank in the front carries copper strips that connect the atom oven heating wires to the supply lines (thick brown wires at the left).

to avoid Doppler broadening of the photoionization transition. In this way, the spectral width of the different magnesium isotopes' transitions is kept smaller than their respective frequency shifts (see fig. 2.19b on page 46) and allows to ionize the isotopes selectively. The barium ovens enclose angles of $(90 \pm 18)^\circ$ with the laser beam axis. For further information about the preparation of the tubes see appendices B.2 and B.3 on page 143.

Typically, $^{24}\text{Mg}^+$ ions were loaded by heating the atom oven in chamber 1 with a current of 3.4 A and focusing 3.5 mW photo-ionization laser power, and 1.5 mW cooling-laser power to a waist of 80 μm into the trapping region. The trap was operated with RF-voltage $U_{\text{RF,rms}} \approx 45 \text{ V}$ and 250 V DC-voltage applied to the ring electrodes $R_{1,1}$ and $R_{1,2}$; see fig. 2.1 on page 23. Loading of 50 ions was completed after about 100 s, additionally depending on the idle period of the oven, i. e. the time elapsed after the previous loading; cf. fig. B.4 on page 146. The loading rate at the end of the heating period is estimated to be at least one ion per second which was sufficient and adequate for the experiments within this thesis. In order to satisfy the need for possibly higher loading rates in future experiments, the emitted flux of atoms related to the heating current can easily be increased.

2.6. Imaging system

A fraction of the spontaneous fluorescence photons emitted during the laser cooling cycle described in section 1.2 on page 12 is set out to be collected and imaged onto suitable detectors. By that, fluorescing atomic ions can be detected and crystalline structures observed. Furthermore, non-fluorescing sympathetically cooled molecular ions embedded in the Coulomb crystal become visible indirectly; see appendix A.2.3 on page 135. An imaging system capable to resolve individual ions in modestly sized ion crystals (usually 50 to 60 in total) was designed and is described in this section. It was of uttermost importance to guarantee single particle resolution for the experiments presented in chapter 5 on page 95. Because it turned out that the requirements for sufficiently low statistical uncertainties are best fulfilled by observing several (about 20) molecular ions embedded



(a) collection efficiency $C = 2.6\%$ along the polarization axis (b) collection efficiency $C = 5.6\%$ perpendicular to the polarization axis, realized in the experiment

Figure 2.15.: Angular distribution of photons emitted by spontaneous decay of electronically excited $^{24}\text{Mg}^+$ ions that are laser cooled close to the $3^2\text{S}_{1/2} \rightarrow 3^2\text{P}_{3/2}$ transition by linear polarized light (red arrow); see fig. 1.5 on page 13. The wire-mesh surface represents the fraction of the total emission into the corresponding direction defined by the distance from the origin to the point on the surface. Two different configurations (detection always from above) are considered. In (a), the optical axis of the objective is parallel to the polarization of the cooling laser, in the experimentally realized configuration (b) it is orthogonal. The cones mark the solid angle that is covered by a $f/1$ objective at magnification $M = 12$ (half opening angle 24.7°). The area of the shaded patch on top of the cone gives the collection efficiency since the integral over the whole surface evaluates to unity.

in the same crystal simultaneously, a lower magnification of the imaging system using a less optimized objective was opted for. In consequence, the fluorescing atomic ions appear “bigger” on the CCD images than their expected motional amplitude, i. e. the related spatial uncertainty ($\approx 1 \mu\text{m}$), would allow for in principle. An imaging system with higher optical resolution power has been tested for further applications but turned out to be less suitable for the experiments of this thesis.

2.6.1. Radiation pattern of ions

The angular distribution of fluorescence photons emitted by $^{24}\text{Mg}^+$ ions in the laser cooling scheme presented in section 1.2 on page 12 does not have to be exactly dipole-like following [149, 176]. For instance, if the cooling laser radiation is linear polarized there are spontaneous electronic transitions that give rise to σ^\pm polarized photons which contribute $1/3$ to the total spontaneous fluorescence rate. The photons emitted upon these transitions are characterized by a different angular distribution than the dipole-like of π polarized photons.

Table 2.1.: Collection efficiency C (in %) of fluorescence photons depending on their angular distribution, the observation direction θ and the imaging objectives f-number.

f-number	realistic π, σ^\pm radiation		hypothetic isotropic radiation
	$\theta = 0^\circ$	$\theta = 90^\circ$	
1	2.6	5.6	4.6
1.7	0.9	2.1	1.7

The combined emission pattern $f(\varphi, \theta)$:

$$f(\varphi, \theta) = \frac{1}{16\pi}(2 + 3 \sin^2 \theta), \quad C(\varphi, \theta) = \int_{A(\varphi, \theta)} f(\varphi', \theta') d\Omega'$$

of π and σ^\pm polarized photons contains a dipole-like and an isotropic component. Figure 2.15 on the facing page visualizes how the amount of light $C(\theta, \varphi)$ collected by a given objective depends on the observation direction relative to the emission pattern. The polarization axis of photons in the incident cooling beam defines the direction along which the collection efficiency is minimal (see 2.15a). Orthogonal to that direction (see 2.15b), the collection efficiency is optimal. As shown in fig. 2.1 on page 23, the polarization directions were arranged for optimal collection efficiency at both observation ports of trap apparatus. A summary comparing the collection efficiencies of the imaging objectives used within this thesis depending on the observation direction and the radiation pattern is given in table 2.1.

2.6.2. Imaging objectives

Three different condenser objectives were tested for imaging. One is a four lens $f/1$ condenser from Halle ($f = 19.3$ mm) borrowed from a different experiment. It is anti-reflection coated and optimized for imaging of 280 nm light with a magnification $M = 50$ at which the resolution is near-diffraction limited. However, deviations from these conditions result in severe degradation of its specifications. The other two condenser objectives from Melles Griot²³ and Sill²⁴ are not that specialized. They are designed for smaller magnifications and can also be used at other wavelengths with tolerable aberration. This makes them suited for experiments using more than one laser cooled atomic ion species. The Melles Griot condenser is broad band anti-reflection coated for visible wavelengths which enhances the transmission of, e. g., the $^{138}\text{Ba}^+$ fluorescence light at 493 nm. The anti-reflection coating spectral width of the Sill objective for light at 266 nm covers also the $^{24}\text{Mg}^+$ cooling radiation wavelength 280 nm. However, due to its f-number = 1.708, it collects three times less photons than the other two objectives with f-number = 1; see table 2.1. The typical working distance between ions and objective (housing) ranges from 24.1 mm for the Halle objective at magnification factor $M = 50$ to 48 mm for the objective from Sill at $M = 10$. The big magnification

²³ 01CMP119, doublet, $f/1$, focal length 50 mm

²⁴ SAASS2060, triplet, $f/1.708$, focal length 58.09 mm

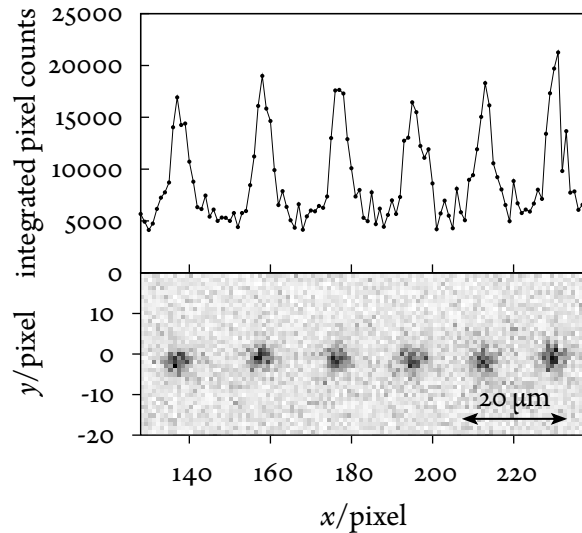


Figure 2.16.: Part of the fluorescence image shown completely in fig. 4.3a on page 73. The image (total exposure time 500 ms) was recorded with the Sill objective at a magnification $M = 9.8$ and the CCD camera settings of table A.1 on page 128 and demonstrates that typical ion distances in the Coulomb crystals of this thesis ($\approx 10 \mu\text{m}$ to $20 \mu\text{m}$) are easily resolved. In the upper panel, the vertically integrated pixel count is plotted as function of the pixel number. Individual atomic ions are imaged as bright Gaussian intensity discs with $\text{FWHM} = 5 \text{ pix}$ equivalent to $4.7 \mu\text{m}$ in the object plane.

factor of the Halle objective implies a long imaging distance of about 1.8 m between ions and detector. In comparison, using the Sill objective, the total imaging path length between the ions in chamber 3 to the sensor inside the CCD equaled only 692 mm. The Melles Griot's total imaging length 679 mm for ions in chamber 1 corresponds to a magnification factor $M = 12.3$.

Despite the Halle condenser's superior quality, its high magnification factor turned out to be impractical for the present experimental requirements. The complete $160 \mu\text{m} \times 160 \mu\text{m}$ field of view of the CCD detector imaged by the Halle objective was too little for imaging crystals with the aspired approximately 1 mm length. Thus, most of the time, the Melles Griot objective was used to image the fluorescence photons in chamber 1 and the Sill objective for the same task in chamber 3. An optimum trade-off between field of view, the objective point spread function, single particle detection ability and the CCD's pixel structure was found in the Sill objective at magnification $M = 9.8$ rendering a $800 \mu\text{m} \times 800 \mu\text{m}$ field of view on the sensor. Under these conditions, individual ions in typical sized Coulomb crystals were readily resolved. Figure 2.16 shows a small part of a fluorescence image. Each ion is imaged as a disc of approximately Gaussian shaped intensity distribution corresponding to $4 \mu\text{m}$ to $5 \mu\text{m}$ FWHM in the object plane. The spread of this disc reduces drastically to below $1 \mu\text{m}$ [129] if the optimized Halle objective is used.

2.6.3. Fluorescence detection

Vacuum requirements and the need for flexibility prohibited to install the objectives directly into the vacuum. Reentrant windows for chamber 1 and 3 were foreseen to be used instead. They permit to hold the objectives in the appropriate distance to the ions. However, space limitations inside chamber 1 precluded a reentrant window that would have allowed to use the Halle objective. Thus, only the other two condensers could be used there. This poses however no limitation of experimental flexibility in chamber 3. The atmosphere face of the reentrant window in chamber 1 is 30.3 mm away from the ions. In chamber 3, this distance measures only 22 mm and is perfectly tailored to match the conditions for which the Halle objective is optimized.

The window part of the reentrant port is made of sapphire. Other UV transparent materials would not resist the strong force exerted by the atmospheric pressure against the 55 mm diameter and 2.4 mm thick surface. Only one of the asked manufacturers (Vacom) could comply with our demands including also bake-ability and stringent leak-rate specifications. For chamber 1, a reentrant port from a disused experiment was shortened and refurbished. Because no specification about the window material was found, it is assumed that it is made of sapphire for the above reasons.

The objectives connect to a light tight tubing system which is coupled to a detector on the other end. In order to doubly protect the detector against stray light in the visible spectral range, a UV transparent and anti-reflection coated UG-5 glass filter with 88 % transmittance at 280 nm was included in the imaging beam path. With these provisions, working at normal laboratory illumination did not affect the signal to noise ratio. The light from chamber 1 travels on direct way to a CCD camera but can be deflected with a flip mirror to a photo multiplier tube, too. The beam path from chamber 3 to the detector had to be folded owing to space limitations. To this end, a 25 mm diameter dielectric high reflective (280 nm) mirror inside the light tight tubing deflects the light to the detector.

An UV sensitive (27 % quantum efficiency at 280 nm) electron multiplying CCD camera²⁵ was used. It facilitates an up to 1000 fold on-chip signal amplification if it is cooled to -80 °C. By that, the camera is sensitive almost on the single photon level. The 8 mm × 8 mm big CCD consists of 1002 × 1004 pixels. The camera can be connected to the imaging system of chamber 1 or chamber 3. Moving the camera from chamber 1 to 3 took about 15 min. Although a mature software comes with the camera, it turned out that a specialized program had to be developed and written to meet the needs of the experiments of this thesis. This software and typical camera setting are described in appendix A.1.2 on page 127.

The photomultiplier tube's²⁶ quantum efficiency reaches 14 % at 280 nm while being almost insensitive in the visible. Influence of UV stray light was minimized by a variable slit right in front of the PMT's entrance window. Measurements revealed that the transmittance of the cooling laser beam through chamber 1 and 2 after optimized focusing through the RF-guide is 79 %. Fresnel losses (85 %) on the uncoated laser windows (cf. fig. 2.2 on page 26) do not explain the measured value completely. The missing part of the beam is clipped at the RF-electrodes inside chamber 1. Reflections of this light or from the laser windows are expected to cause UV stray light. However, there were laser beam alignments found at which the ions in chamber 1 are not perfectly in focus of the cooling beam but the stray light problems are reduced. More details about the PMT can be found in appendix B.4 on page 147.

2.7. Ion trapping laser system

Trapping of $^{24}\text{Mg}^+$ and $^{138}\text{Ba}^+$ ions requires two different sets of laser systems. Because the experiments of this thesis were performed with $^{24}\text{Mg}^+$ and the related molecular $^{24}\text{MgH}^+$ ions, the corresponding laser system is described in more detail. The other one required for future $^{138}\text{Ba}^+$

²⁵ iXon DV885LC-VP with *virtual phase* sensor, Andor

²⁶ H8259, Hamamatsu

trapping experiments has also been set up but will be described by Günther Leschhorn. A schematic of the beam path and how it is arranged on the optical table is depicted in fig. 2.17 on the facing page. It shall be emphasized that TIAMO's vacuum apparatus is movable thanks to optical fiber links to the cooling (560 nm) and photoionization 570 nm radiation source before frequency doubling. This allowed to move the vacuum apparatus at the femtosecond beam line; see section 3.1 on page 55. The spatial separation of experiment and laser system can thus be considered contributing one tessera to the mosaic of techniques required to actualize our approach of preparing single molecular ions under precise control for single particle experiments.

2.7.1. Magnesium laser system

The laser system for photoionization of magnesium ^{24}Mg atoms [109, 97] ($3^1\text{S}_0 \rightarrow 3^1\text{P}_1 \rightarrow \text{continuum}$, $\lambda_{\text{vac}} = 285.2965 \text{ nm}$) and for cooling $^{24}\text{Mg}^+$ ions ($3^2\text{S}_{1/2} \rightarrow 3^2\text{P}_{3/2}$, $\lambda_{\text{vac}} = 279.6352 \text{ nm}$) [9, 76] consists of two dye cw ring lasers from Coherent whose output is transferred to the femtosecond beam line via optical fibers. There, it is frequency doubled in home-built second harmonic generation enhancement resonators based on BBO.

Rhodamin 19²⁷ diluted in ethylene glycol is used as lasing dye. A small volume ($\approx 5 \text{ ml}$) KOH solution (0.45 g dissolved in 50 ml methanol) is added to the dye solution of the cooling laser to shift the emission spectrum of the dye towards shorter wavelengths and thereby enhance the laser output power. Both lasers are pumped with 3.5 W of a frequency doubled Nd:YAG laser²⁸ yielding about 500 mW at 570 nm and 300 mW output power at 560 nm. Under these conditions, the dye solution had to be exchanged after two to three months of regular use.

In future, the dye lasers are planned to be replaced by a solid state laser system operating in the infrared: one erbium doped fiber laser²⁹ at 1120 nm and a diode laser³⁰ at 1140 nm. For the fiber lasers, efficient frequency conversion to the ultraviolet has already been demonstrated in our group [56]. The diode laser system is currently about to be finalized [47].

a. frequency stabilization

The laser frequency of the dye-lasers (line width $\approx 0.5 \text{ MHz}$) is stabilized to a heated reference cavity in order to correct for high-frequency noise. Long-term absolute frequency drifts were taken care of by stabilizing the laser frequency to molecular transitions in iodine. To this end, Doppler-free saturated absorption spectroscopy [158] was set up for the cooling laser, Doppler-free polarization spectroscopy [178] for the photoionization laser. Further details about the experimental realizations are given in fig. 2.18 on page 45. Low noise data are presented in fig. 2.19 on page 46.

The polarization spectroscopy gets along with less electronic equipment compared with absorption spectroscopy. Neither acusto-optic modulators nor any lock-in technique is involved. However, one has to trade-off simplicity with a 500 times weaker signal since there is no amplification stage in the polarization setup. Nonetheless, this turned out to be no limitation since the mainly thermal

²⁷ LC5750, Lambda Physik

²⁸ Millennia XP, SpectraPhysics

²⁹ orange one, Menlo Systems

³⁰ DL pro with laser diode LD-1150-0100-AR-1, Toptica

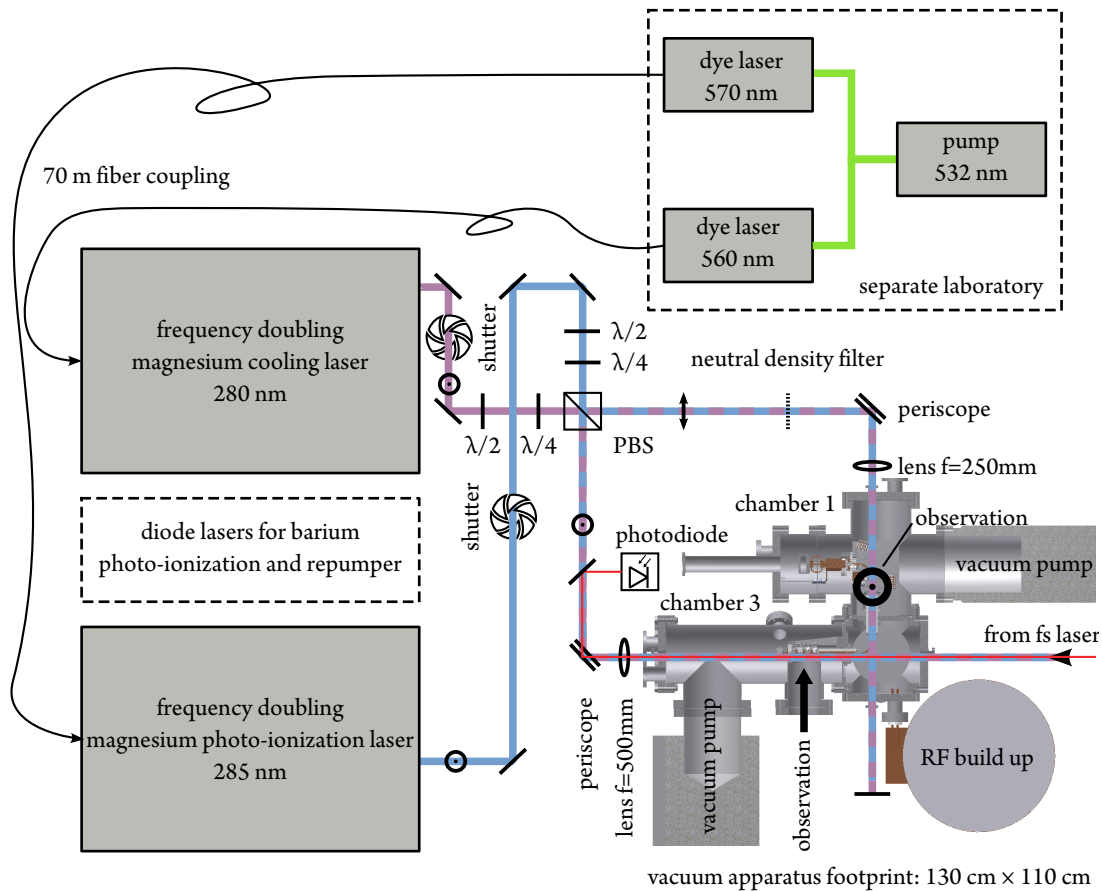


Figure 2.17.: Beam path schematic for $^{24}\text{Mg}^+$ photoionization and cooling contained on a $1.8\text{ m} \times 1.2\text{ m}$ optical table. The laser light for the two frequency doubling stages is supplied by through 70 m long optical fibers that are coupled to two dye lasers in a distant laboratory in the same building. Both UV output beams are overlapped on a polarizing beam splitter from where the light can be directed to chamber 1 and 3 with adjustable power. A flipper mounted neutral density filter in the beam path to chamber 1 is used to repeatedly reduce the intensity in this arm during the automatic loading scheme; see appendix A.1.1.a on page 124. Mechanical shutters in the respective beam paths allow to block the light. The ions in chamber 1 are irradiated with linearly and parallel to the optical table polarized light focused by a 250 mm lens. Their fluorescence is detected “from above” the apparatus perpendicular to the optical table. In chamber 3 the cooling laser light is polarized linearly and perpendicular to optical table. It is focused by a 500 mm lens and detection is “from the side” parallel to the optical table. Periscopes lift the beam from 100 mm outside to 254 mm in order to match the height of the RF-guide inside the vacuum. TIAMO was connected to the femtosecond laser system FP2 (see section 3.1 on page 55) at chamber 2 for the majority of the experiments of this thesis. The pulsed beam path is shown in red. A photodiode in front of chamber 3 is used to monitor the pulse energy. The laser system for photoionization and cooling of $^{138}\text{Ba}^+$ is not shown explicitly for visibility reasons. It will be described in the thesis of Günther Leschhorn.

drifts occur on a minute time scale. A slow integrator circuit adapted to that time scale averages over noise contributions and allows to keep the photoionization laser frequency drift sufficiently small.

b. optical fiber link

The TIAMO approach of connecting an ion trap to a femtosecond laser setup and one day to a X-ray beam line requires a movable, preferentially small apparatus. By contrast, the stability requirements on the cooling and photoionization laser system imply a laboratory with sufficient space, air condition and otherwise clean and stable environment. Thus, it was opted for to separate the UHV apparatus from the laser system and transfer the laser light via optical fibers to the actual experiment. It is expected that a similar procedure will be followed in future applications of TIAMO at big accelerator facilities.

For most of the time, the UHV apparatus has been connected to the femtosecond beam line situated one floor beneath and about 30 m away from the laser laboratory which necessitated to install two 70 m long single mode optical fiber links³¹ equipped with precisely adjustable fiber couplers³². In parallel with the two main optical links also one backup optical fiber, three coaxial cables and one 2×10 data cable were installed in order to be prepared for further communication needs between the two laboratories.

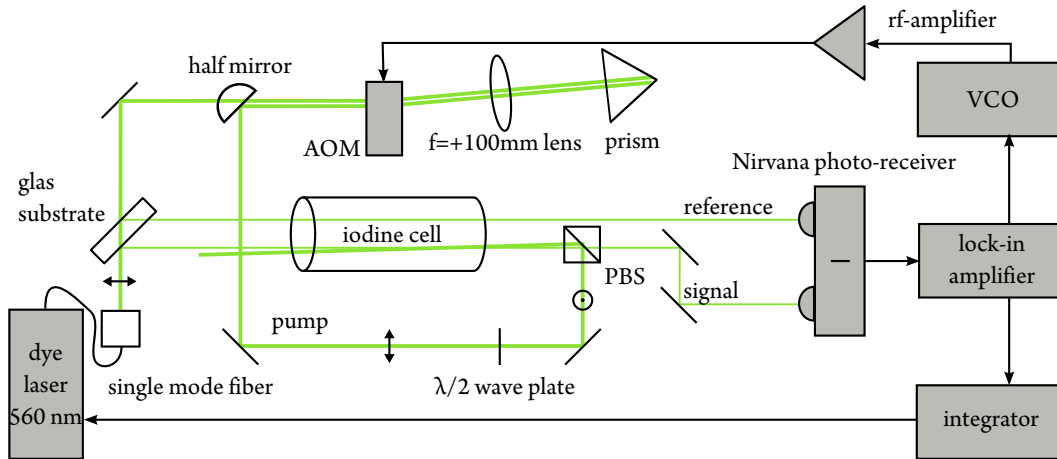
The manufacturer discourages using the optical fibers at lengths exceeding a few meters and powers above some tens of milliwatts [55]. However, after more than one year, no degradation was observed even at input powers as high as 500 mW. Nonetheless, whereas the transmittance of the optical link at low input power (< 200 mW) is about 55 % including in- and out-coupling losses, it drops significantly at input powers above 300 mW. It is supposed that stimulated Brillouin backscattering [159] causes the reduced transmittance. For this reason, the maximum transmissible power is limited to 135 mW. Figure 2.20 on page 47 illustrates the attenuation effect and demonstrates that no hint for degradation of the optical fibers has been observed by the end of this thesis.

c. frequency doubling

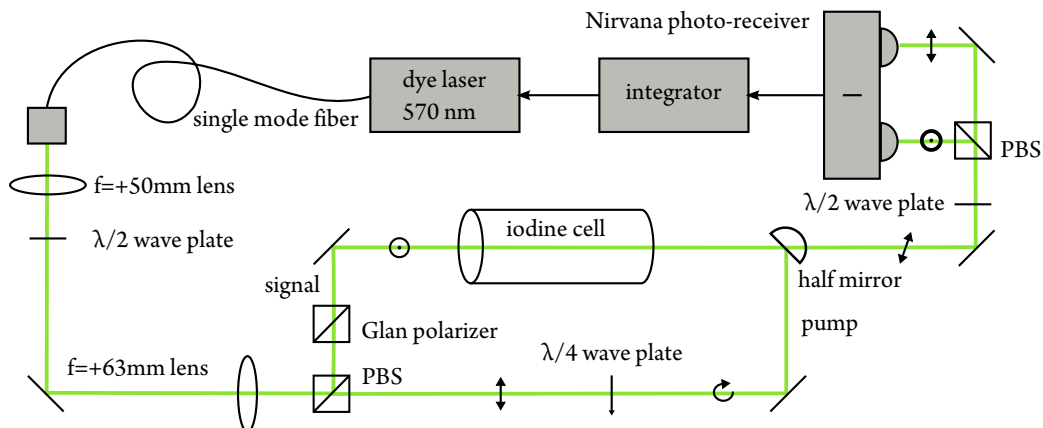
The second harmonic of the visible laser radiation transferred via the optical fiber link must be generated on the table that also carries the vacuum apparatus since highly UV transparent single mode optical fibers are not available. The frequency is converted using the birefringent non-linear optical crystal β -barium borate (BBO) in an enhancement resonator. The basic idea is to exploit a high-finesse resonator's ability to store an enhanced amount of circulating energy. The related power is focused to a tiny beam waist inside the non-linear crystal and can result in second harmonic generation efficiencies of a few ten percent. A detailed description of the highly optimized frequency doubling resonators that we developed in close collaboration with TIAMO's partner group QSIM and the laser spectroscopy division at the MPQ is reported by Friedenauer et al. [56] and briefly repeated in fig. 2.21a on page 48. Although these resonators were developed for erbium doped fiber lasers operating in the infrared, the second frequency conversion stage of the mentioned reference

³¹ purchased as F-SA-C from Newport, cut-off wavelength 488 nm, Fibercore

³² 60FC-4-A4.5S-01, Schäfter-Kirchhoff



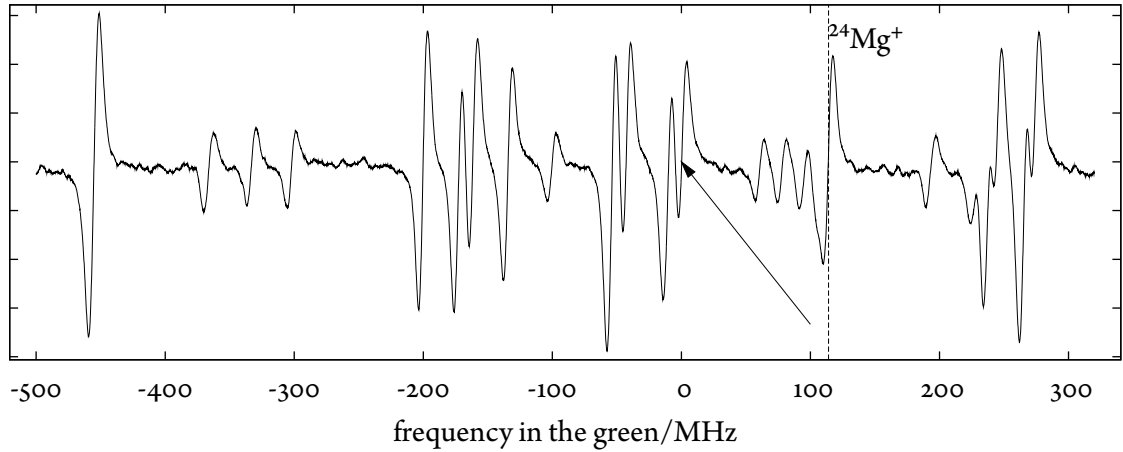
(a) Absorption spectroscopy. Signal and reference beams (thin lines) are picked by a glass substrate (5% each) from the input beam (5 mW), pass through an 10 cm long iodine cell (Sacher Lasertechnik) and hit a differential photodetector. The pump beam (thick line) passes through an AOM-setup (ATM-801A1, IntraAction) where it undergoes a double-pass 2×93 MHz frequency red shift. Its frequency is adjusted with the voltage controlled oscillator (VCO) and additionally frequency modulated with a 20 kHz reference generated by the lock-in amplifier (Model 116, Princeton Applied Research). After overlapping the pump with the signal beam on a PBS, the pump beam saturates the iodine transitions for the counterpropagating signal beam. The detector output being the difference between signal and reference power is demodulated using the lock-in amplifier and converted into a feed-back signal to the laser by an integrator circuit. A typical differential error signal is depicted in fig. 2.19a on the next page.



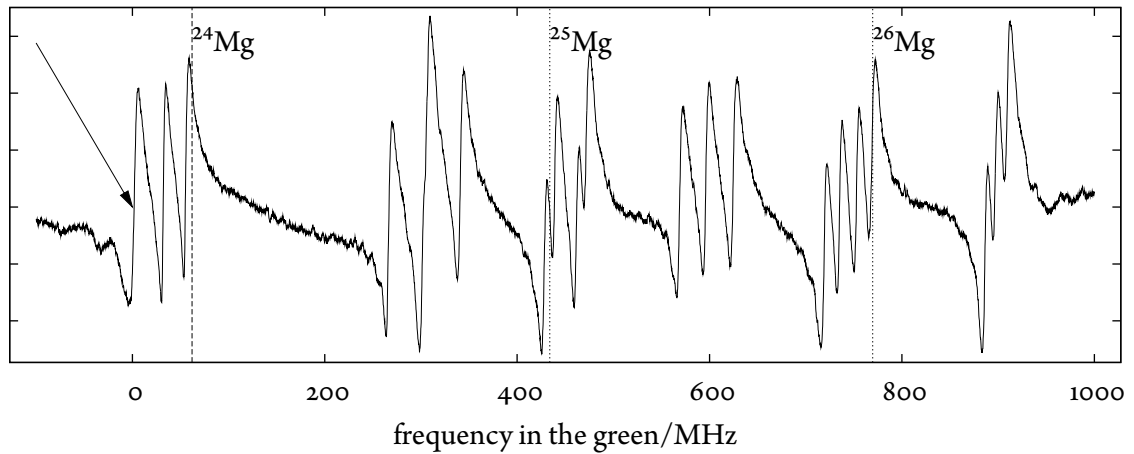
(b) Polarization spectroscopy. After a collimation telescope (50 mm and 63 mm lens), the input beam (< 5 mW) is split into pump and signal beam with adjustable power ratio by a polarizing beam splitter (PBS) and a half wave plate. The signal beam is further polarization cleaned by a Glan polarizer and finally passes through an 7.5 cm long iodine cell (Sacher Lasertechnik). The pump beam becomes circular polarized after passing through a quarter wave plate and is sent to the iodine cell counter-propagating to the signal beam. The signal is rotated by another half wave plate such that it splits into orthogonal polarization components at a PBS whose power difference is detected using a differential photo receiver (Nirvana, New Focus). An integrator circuit generates a feedback signal to the laser. A typical error signal is depicted in fig. 2.19b on the next page.

Figure 2.18.: Doppler-free spectroscopy setups. (a) shows the setup used to stabilize the cooling dye-laser, (b) shows the setup used to stabilize the photoionization dye-laser.

2. Ion trap apparatus



(a) Absorption spectroscopy iodine lines used in the cooling laser stabilization, the dashed line marks the atomic transitions reported in [9]. The frequency difference (2×114 MHz in the UV) between the lock point ($5.360\,413\,53 \cdot 10^{14}$ Hz) marked by an arrow and the reference is composed of a frequency shift induced by the AOM (2×93 MHz) in the spectroscopy setup (see fig. 2.18a on the previous page) and a frequency red shift (42 MHz) of about one natural line width required for laser cooling. The isotopic frequency shifts of $^{25}\text{Mg}^+$ (1621 MHz) and $^{26}\text{Mg}^+$ (3087.6 MHz) [9] make the respective atomic transition frequencies lie far outside to the blue of the shown iodine absorption lines.



(b) Polarization spectroscopy iodine lines $R_{115}(20-1)$ used in the photo-ionization laser stabilization, the dashed line marks the atomic resonance of neutral ^{24}Mg . The lock point ($5.254\,052\,88 \cdot 10^{14}$ Hz) marked by an arrow is red-shifted relative to the reference in order to reduce residual photoionization of ^{25}Mg and ^{26}Mg (isotopic frequency shifts 2×371.9 MHz and 2×707.7 MHz in the UV, dotted lines). All frequency values are taken from [14].

Figure 2.19.: Doppler-free iodine transition lines used for frequency locking as seen on an oscilloscope. The actual lock point is indicated by an arrow, the position of the transition by a dashed line. The frequency calibration of the x -axis is based on data from Iodine Spec from Toptica Photonics with the largest uncertainty given by the dye laser scan being not strictly linear.

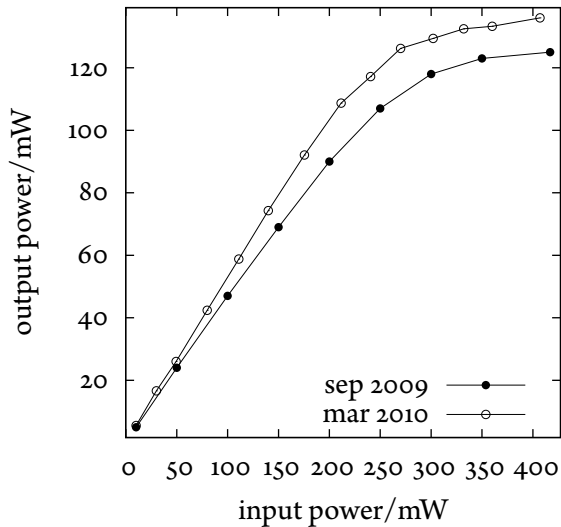


Figure 2.20.: Output power of the optical fiber link connecting the TIAMO setup with the photoionization laser as function of the input power measured twice with a temporal delay of six months. No degradation of the transmission characteristic was observed. The higher transmittance in the later measurement indicates an improved fiber coupling. Increasing the input power above 350 mW does not yield more laser power at the experiment. Brillouin backscattering losses inside the optical fiber are assumed to saturate the transmission [159].

could be adopted without major modifications. TIAMO's dye laser system operating in the visible superseded the otherwise first IR→VIS frequency doubling stage. There has been another infrared fiber laser available for TIAMO as well but due to in the meantime resolved stability problems and temporal reasons, the dye laser solution has been opted for.

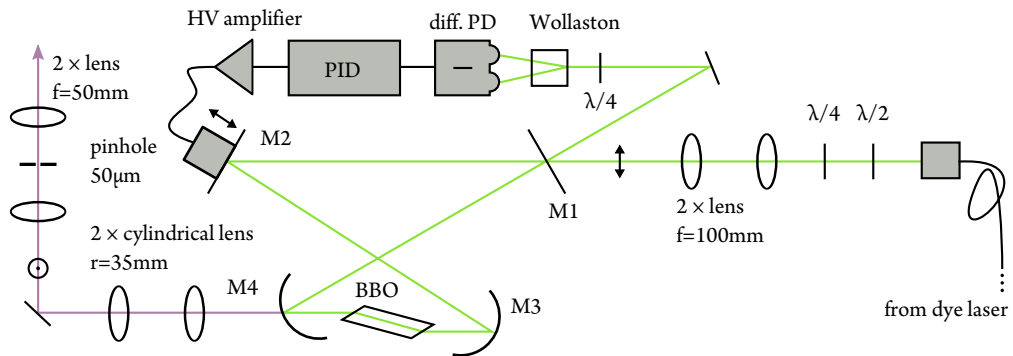
Typical UV output powers from the second harmonic stages measured about 1.5 mW at 280 nm and 4 mW at 285 nm. Although higher values should be obtainable in principle, the experimental needs allowed to save the tedious daily optimization routines required for maximum output since less than 100 μ W were actually used for laser cooling.

The UV cooling and photoionization beams were overlapped on a polarizing beam splitter. Rotating the polarization of the light with the half wave plates depicted in fig. 2.17 on page 43, allowed to adjust the power going into the beam paths leading to chamber 1 and 3. Focusing lenses right in front of the vacuum chamber generated a beam waist of approximately 80 μ m in the respective trapping regions. The polarization direction of the cooling laser light is chosen to maximize the amount of collectible fluorescence photons along the observation direction; see section 2.6 on page 37 for a detailed discussion.

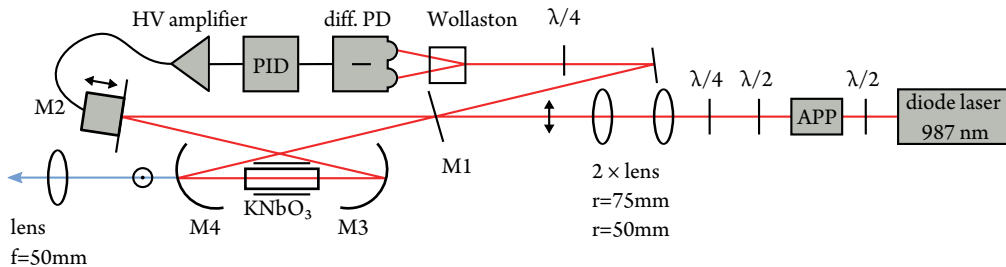
2.7.2. Barium laser system

The laser system for photoionizing barium and trapping $^{138}\text{Ba}^+$ is based on three diode lasers. By that, it is a lot easier to move along with the vacuum apparatus. At the time of finishing this thesis, all diode lasers had been set up and characterized. Trapped barium ions have not been observed yet. This section limits itself to the delineation of the frequency doubling stage which has been designed during the course of this thesis. Despite its similarity to the BBO frequency doubling stages used in the $^{24}\text{Mg}^+$ laser setup, a detailed description of the KNbO_3 based SHG enhancement resonator (see fig. 2.21b on the following page) is presented since the design has not been published elsewhere.

2. Ion trap apparatus



- (a) A 560 nm respectively 570 nm light beam from a single mode optical fiber link gets p-polarized by a half and a quarter wave plate. With the help of two $f = 100$ mm lenses the input beam is precisely mode matched to the secondary focus ($131 \mu\text{m}$, $1/e^2$ -intensity radius) of the resonator in the middle of in-coupling mirror M1 (98.4 % reflectivity) and the small, displaceable (4 mm diameter) piezo-mounted mirror M2. M2 is used to stabilize the resonator length in a Hänsch-Couillaud-stabilization scheme [79]. Light reflected on M1 is split into two orthogonal polarized components in a Wollaston prism and falls on a differential photodiode (S5821-01, Hamamatsu) circuit from which the error signal is obtained. That signal is fed to a PID servo which generates a voltage that is suitable to stabilize the resonator length by amplifying the voltage and applying it to the piezo of M2. The focusing mirrors M3 and M4 (ROC = 50 mm) define the $16 \mu\text{m}$ primary focus inside the 10 mm long BBO crystal. The BBO is cut at brewster's angle to compensate the astigmatism induced by the tilted (27.4° full angle) focusing mirrors. The second harmonic walk-off leads to an astigmatic output beam that is collimated with a cylindrical lens telescope and projected into a Gaussian mode through a $50 \mu\text{m}$ spatial filtering pinhole. In order to protect the setup from acoustic noise and thermal fluctuations it is encased in a sound absorbing wooden box.



- (b) The basic layout for the 987 nm frequency doubling stage coincides with (a) except of the following aspects: the input beam is not fiber coupled since the diode laser head is mounted on the same bread board; an anamorphic prism pair is inserted after the laser head to compensate astigmatism in the IR beam; 94 % reflectivity of in-coupling mirror M1; 38 mm ROC of mirrors M3 and M4; 14° full resonator folding angle; crystal front sides orthogonal to resonator mode; heater around KNbO₃ crystal used for non-critical phase matching at 41.4°C ; mode cleaning telescope not needed since harmonic beam is walk-off free.

Figure 2.21.: Second harmonic generation enhancement resonators in bow-tie configuration. (a) shows one of the two identical frequency doubling stage belonging to the $^{24}\text{Mg}^+$ laser system, (b) shows the frequency doubling stage of $^{138}\text{Ba}^+$ cooling laser.

a. KNbO₃

The biaxial birefringent crystal KNbO₃ has been chosen because it exhibits an exceptionally high effective nonlinearity $d_{\text{eff}} = 9.21 \text{ pm V}^{-1}$ [126] at the relevant wavelength $\lambda = 987 \text{ nm}$. In an inquiry to Forschungsinstitut für mineralische und metallische Werkstoffe, Idar-Oberstein an even higher value 12 pm V^{-1} is mentioned. However, the crystal is expensive and delicate to handle. In particular, no mechanical stress must be exerted to it. Elsewise, the material develops ferroelectric domain walls [87] that will render the crystal useless for SHG. The domains can be remediated with strong electric fields only in some cases.

The $3 \text{ mm} \times 3 \text{ mm} \times 10 \text{ mm}$ big KNbO₃ crystal³³ used in the enhancement resonator is cut at $\theta = 0^\circ$, $\varphi = 0^\circ$ (b-cut) and anti-reflection coated for the fundamental wavelength (reflectivity $< 0.5\%$). Irregularities around the crystal border which resembled small needles extending from the lateral surface towards the bulk were visible but the crystal seemed to be faultless along the central axis.

There is a discussion about losses in KNbO₃ in the literature, e. g. [106], of which a short summary follows. Three loss mechanisms for the infrared light are proposed: linear absorption α , two-photon absorption β , and so called *blue light induced infrared absorption* (BLIIRA). In good crystal samples, α can be as low as $3 \cdot 10^{-3} \text{ \% cm}^{-1}$ although it is often only specified less than 0.1 \% cm^{-1} . Even the higher specification can be considered a small number since the cumulated loss in a 1 cm long crystal does not surpass the sum of other passive losses in a typical enhancement resonator such as imperfect reflectivity of the mirrors, for example. Estimated two-photon absorption losses are irrelevant (1%) at the maximum focal power levels (250 kW cm^{-2}) achievable with the present diode laser system. In [154] it is argued that BLIIRA losses are smaller than the intrinsic passive losses of a typical SHG resonator if the SHG intensity remains below 10 kW cm^{-2} assuming a high purity crystal. This value has to be compared with the second harmonic intensity 7.5 kW cm^{-2} that might be generated in the presented enhancement cavity under optimum conditions. In conclusion, no significant optical losses in KNbO₃ are expected.

b. resonator design

The resonator design is determined by the parameters of efficient second harmonic generation. Non-critical phase matching is achieved by adjusting the temperature (optimum at $T_{\text{opt}} = 41.45^\circ$) such that the propagation direction of fundamental and harmonic radiation inside the crystal are simultaneously collinear with the principal z -axis of the crystal; consult appendix C.2 on page 158 for details. This avoids walk-off effects inside the crystal, allows for efficient second harmonic generation and results in a Gaussian mode profile of the second harmonic beam.

There are values describing optimum focusing into the crystal derived in the in-depth treatment by Boyd and Kleinman [21]. The relevant expressions valid for the above situation, namely collinear SHG without walk-off are:

$$\xi = \frac{l}{b} = \frac{\lambda}{2\pi} \frac{l}{w_0^2} = 2.838, \quad \Delta k = \frac{4\pi}{\lambda} (n(987 \text{ nm}) - n(493 \text{ nm})) = \frac{3.2}{l}. \quad (2.2)$$

³³ GB group (USA)

They relate crystal length $l = 10$ mm, focal parameter b , focal beam waist w_0 , phase mismatch Δk and index of refraction n . In general there is an optimum value for l depending on the absorption losses in the crystal but this does not need to be considered owing to the expected low losses in KNbO_3 ; see previous section. With l given by the available crystal, the optimal focal beam waist $w_0 = 15.77 \mu\text{m}$ follows directly from the above formula. According to [21] the focus should be placed in the middle of the crystal.

Different from the usual phase matching condition $\Delta k = 0$ (see also appendix C.2 on page 158), optimum conversion efficiency is achieved at finite phase mismatch $\Delta k \geq 0$. A physical understanding of that can be gained by realizing that the focused fundamental laser beam cannot be correctly described by a single wave vector \mathbf{k} only but is better modeled by a bunch of such vectors pointing around a central axis. At $\Delta k = 0$, phase matching is fulfilled for the central wave vector only. There is however an optimum value Δk which allows also the surrounding wave vector components to make resonant contributions to the second harmonic generation. With the help of the program SNLO [157] one can evaluate the expression for Δk given in eq. (2.2) on the previous page for the given crystal length and finds that optimal phase matching is achieved if the indexes of refraction of fundamental and second harmonic beam differ by $\Delta n = 1.2 \cdot 10^{-5}$. This difference corresponds to a temperature variation of only 0.18 K which is close to irrelevant in practice since it must be compared with the temperature tuning range of the crystal. This range is defined by the temperature span over which the index of refraction changes by so much that the correspondent phase mismatch $\Delta k \cdot l$ varies from $-\pi$ to π . SNLO states a value of 0.73 K for this range which is about four times greater than the temperature deviation resulting from the discussed phase matching considerations.

A stable optical cavity that generates the optimal focus inside the crystal, minimizes astigmatism and respects the commercially available spherical mirror substrates was realized within this thesis; see fig. 2.21b on page 48 for a definition of the notation used in the following description. The two curved mirrors M_3 and M_4 with 38 mm radius of curvature are separated by 45 mm and centered about the crystal. The second arm, closing the bow-tie resonator, is 490 mm long with the second focus ($275 \mu\text{m}$) of the resonator centered between M_1 and M_2 .

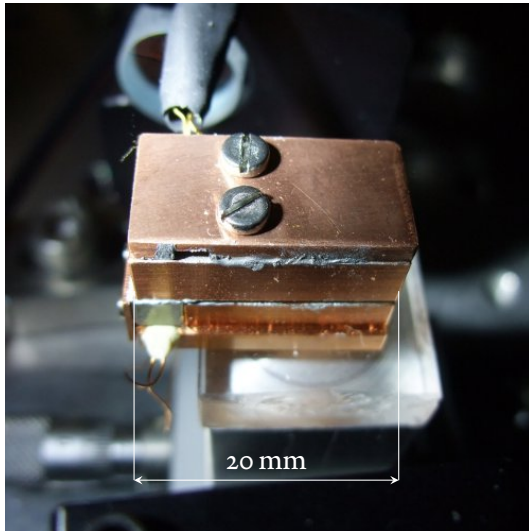
Due to the high nonlinearity of KNbO_3 , the conversion losses inside the cavity are high even at modest input power compared with the BBO based enhancement resonators, for example. This has to be accounted for by the reflectivity of the in-coupling mirror M_1 which is used to satisfy the impedance matching condition. Simulations with SNLO predicted the optimal reflectivity to be between 94 % and 95 %. A dielectric coated surface of M_1 facing the cavity realizes this reflectivity. On the backside, M_1 is anti-reflection coated. All other mirrors are highly reflecting³⁴ (≥ 99.5 %) on the cavity side, the out-coupling mirror M_4 is additionally broad-band anti-reflection coated³⁵ on the backside.

M_2 is glued to a piezo³⁶ used to stabilize the cavity length. It has $4.6 \mu\text{m}$ maximum displacement and an unloaded resonance frequency 261 kHz. The small size of M_2 (4 mm diameter and length) is comparable to that of the piezo. This reduces the inertia of the coupled piezo-mirror system and allows for a loop bandwidth > 20 kHz covering the important acoustic frequency range.

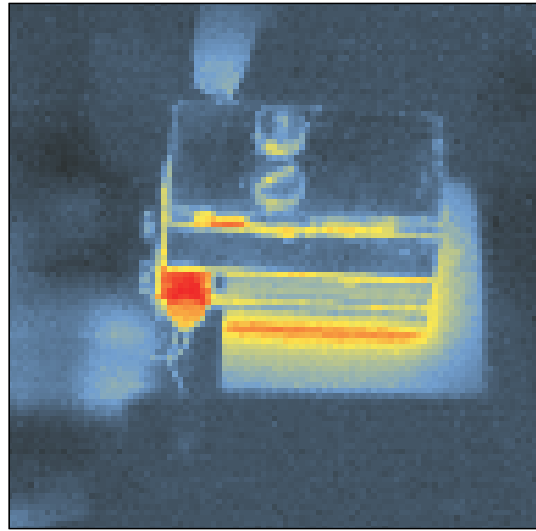
³⁴ HT 493 nm & HR 987 nm/7° to 10°, Laseroptik

³⁵ BBAR 400 nm to 700 nm, Laseroptik

³⁶ AE0203D04F, Thorlabs



(a) Photographic image. The copper bulk provides a heat reservoir for the crystal. It is heated by a small platinum PT100 element beneath the crystal (not visible, wires in the front) and is thermally isolated by an acrylic glass disk. For good thermal contact the crystal is wrapped in indium foil and heat-conductive paste used between junctions. The wires in the back connect to a temperature sensor in the upper part of the copper bulk.



(b) Heat image (from black 23° to red 35.6°) recorded with the infrared camera T120 from Fluke. Absolute temperatures cannot be read off directly because of the different emission coefficient ϵ of the materials present in the image (for instance copper with $\epsilon \approx 0.1$ appears unrealistically cold). However, within the resolution of the image, the temperature on the crystal front face is homogeneous when the temperature stabilization is in a steady state.

Figure 2.22.: Heater of the KNbO_3 crystal.

The resonator's relatively small 14° full folding angle, defined by the tilt of the spherical mirrors, keeps astigmatism a small effect. Reducing the folding angle further is limited by spatial restrictions such as beam clipping on the crystal or its heater.

The crystal heater (see fig. 2.22 for details) is used to stabilize the crystal temperature with deviations below 10 mK. It has been designed with two goals: to establish a sufficient heat reservoir and to take as little space as possible. Both requirements can be met using a tiny heating element. A good solution was found in a platinum heater³⁷ measuring only 9.5 mm × 1.9 mm × 0.3 mm, i. e. being of about the same size as the crystal's footprint. It was sunk in a mold directly beneath the crystal. A temperature transducer³⁸ above acts as sensor element. In order to have a temperature stabilization loop, a specialized PID controller developed by Helmut Brückner (MPQ) is employed.

³⁷ 32208172, Heraeus

³⁸ AD590

c. characterization

The input beam to the SHG resonator is supplied by an infrared diode laser³⁹ that provides up to 135 mW power⁴⁰ at 987 nm including losses at a 30 dB optical isolator. Since frequency tuning has an influence on the output power, it will usually be a few percent less at the desired wavelength. In any case, about 120 mW should be available in front of the resonator.

Confer to fig. 2.21b on page 48 for a schematic of the components described in the following. The infrared laser beam exits the laser head with strong ellipticity. Directly behind the head's front plate, the beam waists are 374 μm in the vertical direction and 1431 μm in the horizontal direction. An anamorphic prism pair (APP) is inserted to correct for the ellipticity. The reflection losses inside the APP can be kept small (2.8 %) by rotating the polarization with a half wave plate behind the laser head. Due to the spatial modulated beam profile, the beam deviates not negligibly from a circular shape. Nonetheless, the central part contributes about 92 % to the total intensity and can be approximated with a Gaussian. Withing this approximation, the beam after the APP can be described by a beam waist $w_0 = 295 \mu\text{m}$ and a focus position $z_0 = -160 \text{ mm}$ relative to the exit face of the laser head. Mode matching this beam to the SHG resonator mode was achieved using one $f = 162 \text{ mm}$ lens 49.5 cm and one $f = 108 \text{ mm}$ lens 15.6 cm in front of the surface of M1. The waist of the mode-matched beam at the position of the secondary focus in the horizontal direction measures $(284 \pm 3) \mu\text{m}$ and $(273 \pm 3) \mu\text{m}$ in the vertical direction which is close to the optimum value 275 μm according to the simulation of the resonator.

Under the assumption of 120 mW input power, optimum mode matching, optimum impedance matching, and 0.5 % linear absorption losses inside the KNbO₃ crystal, the SNLO simulation predicts 60 mW second harmonic output power. After having set up the resonator and first optimizations of the most relevant elements, 20 mW of the 493 nm radiation were measured. Improvement in this point is expected from further fine-tuning. However, this power level readily complies with ¹³⁸Ba⁺ laser cooling demands requiring much less than a milliwatt of the second harmonic cooling light.

2.8. Experiment control

The proof-of-method character of the experiments presented in this thesis entailed a considerable amount of flexibility in the laboratory work. Nevertheless, for some applications, e. g. the shuttle experiments of molecular ions along the RF-guide (see section 4.2 on page 75), precise computer control was vital. It can be assumed that considerable progress on the way towards realization of the envisioned single particle preparation with high repetition rate will be made by further automation. Figure 2.23 on the facing page depicts the present status of the experimental control scheme.

Two personal computers "tiamo" and "tibmo" are used to control the experiment. The latter presents the control center whereas the former is mainly used to communicate with the CCD camera. The key role in synchronizing all computerized tasks plays the real-time (300 MHz CPU clock) measurement system⁴¹. It is essentially a computer on its own optimized for fast input and

³⁹ DL100, Toptica

⁴⁰ powermeter S130A, Thorlabs

⁴¹ ADwin-Pro-II-light, Jäger

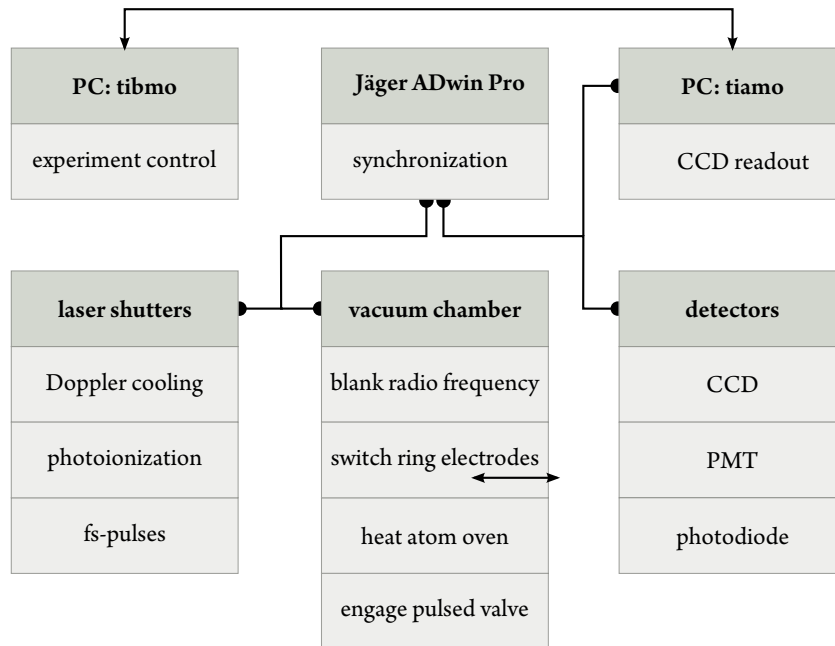


Figure 2.23.: Schematic of the experiment control software. Central element is the real-time measurement system ADwin used to generate precisely timed analog and digital voltages and controlled by the PC “tibmo”. The voltages connect directly or via additional components to elements in the laser beam paths and inside the vacuum chamber. ADwin reads also data from the photomultiplier and a photodiode. The second PC “tiamo” controls input and output of the CCD camera. Both computers and the ADwin system are linked via LAN.

output. Its integration into the rest of the experiment control scheme is presented in appendix A.1 on page 124. Pre-compiled programs are loaded into ADwin’s memory. They are executed upon software or hardware trigger events. The system’s speed on the one hand could be fully tapped in the ion transfer experiments; see section 4.2 on page 75. There, the maximal temporal resolution is currently limited by the digital-to-analog converter’s settling time of $2.5 \mu\text{s}$. The hardware triggering possibilities on the other hand became important in the pump-probe experiments using short laser pulses. Besides speed, the ADwin system provides a versatile interface offering eight analog outputs and eight analog inputs, a digital counter, and 32 digital configurable input/outputs.

The digital TTL outputs were used to operate

- three mechanical shutters—two 846HP from Newport (see fig. 2.17 on page 43) and one homebuilt based on D24BOR-F-DS9429 from Kuhnke in the femtosecond beam path,
- flip⁴² a neutral density filter in and out the cw-laser beam path (see fig. 2.17 on page 43,
- engage the pulsed valve on chamber 1 for hydrogen gas injection (see section 4.1.5 on page 75),
- blank the radio frequency in order to empty the trap,
- activate the PMT (see section 2.6 on page 37),
- gate an arbitrary waveform generator (see section 4.1.3 on page 71), and

⁴² flipper mount 9891, New Focus

2. Ion trap apparatus

- control the atom oven heating (see section 2.5 on page 35)

in a concerted manner (see appendix A.1.1.a on page 124).

The analog outputs were connected to high-voltage MOSFET transistor⁴³ circuits [42] which allowed to switch the voltages on the ring electrodes (see section 2.3 on page 30) and the inlay electrodes of the differential pumping stages (see section 2.4 on page 33) inside the vacuum chamber. Voltage ramps from up to 400 V to ground or vice versa within less than 1 μ s were achieved. The digital counting module of the ADwin system was used to determine the PMT count rate and to count the laser pulses during the pump-probe experiments. With the help of the analog inputs it was possible to record the pulse energy of each single laser pulse; see appendix A.1.1.c on page 126. To this end, a UV-sensitive photodiode⁴⁴ was placed in front of chamber 3; cf. fig. 2.17 on page 43. The photodiode voltage is proportional to the power of the pulsed beam. This signal was fed to a peak detection circuit with sample-hold functionality. The output of this device is proportional to the peak value of the photodiode signal until it has been read and reset by the ADwin system.

⁴³ SPW20N60S5, Infineon

⁴⁴ S5821-01, Hamamatsu

3. Femtosecond apparatus

Ultraviolet laser pulses with the presently shortest realized pulse duration [70] in the required spectral range were applied in the main experiment of this thesis. It is one of the key achievements of this thesis to connect the apparatus described in the previous chapter to a short pulse laser system. This step mimics the envisioned connection of TIAMO to the beam line of a free electron laser X-ray facility. The following chapter describes the technical challenges that had to be solved in order to accomplish the link between trapped ions and the world of short pulses.

3.1. Femtosecond laser system

This section gives a brief survey of the femtosecond laser system—in the following short FP2. In many aspects the description is by far not comprehensive owing to the complexity of the system. A good starting point for a more in-depth introduction might be found in the thesis of Goulielmakis [68]. We had to operate the laser independently because several relevant parameters of the system needed to be adjusted for the experiments. This is why a basic understanding of the laser system was indispensable. Some of the foundations of short pulse physics have already been described in my Diploma thesis [94].

To summarize, the striking property of the applied Ti:sapphire femtosecond laser system [29] is the shortness of the generated infrared laser pulses (sub-4 fs) paired with their big energy content (500 μ J). While the bandwidth of Ti:sapphire is large, spanning a broad spectral range 650 nm to 1100 nm, it is difficult to completely exploit it in high power lasers. Usually, the usable spectrum shrinks by gain narrowing limiting the achievable pulse duration. One concept that is also followed in FP2 is to live with slightly longer and powerful pulses. Their spectrum is expanded by the means of spectral broadening which allows to recompress them to extremely short pulses afterwards. Subsequently, the infrared laser pulses are frequency converted into similar or even shorter ultraviolet laser pulses by third harmonic generation in a noble gas target. A schematic outline of the complete setup is depicted in fig. 3.1 on the following page.

Source of the laser pulses is a commercial Ti:Sapphire oscillator¹. It generates 6 fs, 2 nJ pulses at a repetition rate of about 71 MHz in *mode-locked* operation and is pumped by a cw laser² with 4.35 W at 532 nm. The amplification of these pulses follows the lines of *chirped pulse amplification* [165]. A portion of the oscillator output corresponding to 75 mW first passes through a piece of glass where the pulse duration is stretched to about 10 ps before these pulses become *seed* pulses when they are injected into the amplifier, again a commercial device³. The Ti:sapphire amplifier crystal is pumped by a pulsed laser source⁴ with 20 W average power close to its damage threshold

¹ femtosource rainbow, Femtolasers

² Verdi, Coherent

³ femtopower compact pro, Femtolasers

⁴ Photonics Industries

3. Femtosecond apparatus

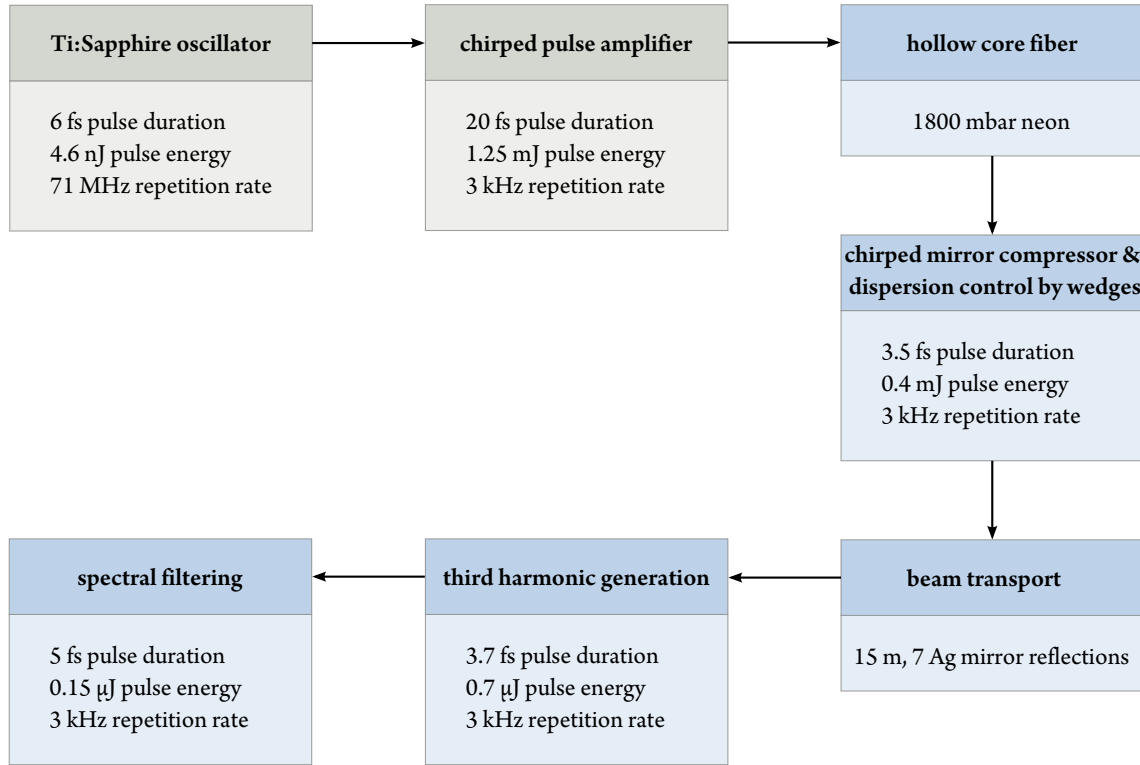


Figure 3.1.: Schematic of the femtosecond laser system FP2. Stages that we adjusted for the experiments of this thesis are shown in blue.

which requires to keep it in rough vacuum and cool it to -80°C . Altogether nine passes through the crystal boost the energy of every picked pulse (Pockels cell operated at 3 kHz) by a factor of more than $1 \cdot 10^6$ to typically 1.25 mJ.

In the next step, these strong pulses are set out to be compressed in the time domain again. The commercial system's prism compressor setup has been modified in this aspect. It is stated by Cavalieri et al. [29] that non-linear light-matter interaction (more precisely *self-phase modulation*) inside the last prism of the standard configuration had been identified as limiting factor of the achievable pulse duration. A work-around has been found in a modification of the prism compressor setup and the addition of a *chirped mirror compressor*. These special mirrors imply a precisely optimized group delay dispersion (see section 1.4 on page 18) that after a number of reflections eventually cancels the residual dispersion (chirp) of the pulse. Final pulse compression is thus achieved in reflection and not transmission (through the apex of a prism) resulting in shorter pulses (20 fs) with at this stage approximately 1 mJ of energy. A tenth of the energy of each pulse is split off and deflected to another experiment leaving 2.75 W average power for TIAMO.

The crucial step to reach quasi single-cycle pulses is called spectral broadening. To this end, the compressed pulses are focused into a 1 m long hollow core glass fiber (HCF) with 250 μm inner diameter. The glass tube is mounted inside a closed pipe in which a neon atmosphere with 1800 mbar pressure is arranged. The light-matter interaction inside the noble gas filled HCF is highly non-linear and has been thoroughly investigated [119, 46, 49]. Approximately 50 % of the input power can

be transmitted through the HCF depending on the alignment. It was observed that the alignment through the HCF influenced not only the transmission and the broadening characteristics but also the divergence of the output beam. The output spectrum extended to a significant fraction into the visible, letting the beam appear almost white. Although the changes were often not very well visually perceptible, the alignment of the HCF and the related modification of the spacial mode of the output beam was used as important fine-tuning parameter for the third harmonic generation. Since the spectral broadening depends also strongly on the duration of the input pulses, the alignment of the prism compressor after the amplifier was used as tuning parameter. It did not only influence the yield of the third harmonic generation but also the spectrum of the UV pulses.

Dispersion management after the HCF is mainly based on another chirped mirror compressor. Six reflections of these mirrors spanning a wavelength interval between 450 nm and 1000 nm compress the pulse to the extreme short duration stated above. Two thin glass wedges in between the HCF and the chirped mirror compressor were used to fine-control the dispersion compensation and thereby optimize the third harmonic generation.

After the beam exits the chirped mirror compressor it enters a vacuum system that spreads to various locations one floor beneath the laser hall. It connects the source of short pulses to the actual experimental stations. Tiamo was able to access one of these beam lines—AS4B, short for attosecond beam line with a certain order number appended—for the duration of the time-resolved experiments. In order to deflect the pulsed beam towards the various experiments a number of so called *switch-boxes* are installed along the vacuum system. They are also kept under vacuum ($\approx 1 \cdot 10^{-6}$ mbar) and encase irides that define the optimum beam path and piezo-motor driven displaceable mirrors. These mirrors do not only allow to switch between experiments but they are also used to precisely align the beam with a defined path. Most reproducible results were achieved by centering the attenuated (neutral density OD₃ filter) beam on an adjustable iris aperture in the switch-box and another iris aperture inside the harmonic generation chamber approximately 6 m downstream.

The complete beam path between the exit of the HCF to the harmonic generation gas target measures about 15 m. In view of this length, the alignment through the two irides worked astonishingly well for a rough alignment. The precision requirements of the actual experiments were a lot higher, though. They required the beam pointing to be stable to a fraction of its focal waist (50 μm) at the molecular ion target. Delicate repeated fine-tuning of other mirrors downstream was required to satisfy these high demands over the duration of one measurement day. The big amount of involved elements in the beam path precludes to pin-point a single source of beam pointing instability. In fact a combination of many effects is assumed to accumulate over time and cause the missing of the molecular ion target by the focused beam after 2 h to 5 h on average. A beam stabilization in front of the HCF works highly reliable but cannot account for drifts further downstream. It is envisioned that another beam stabilization in front of the experiment will reduce beam pointing instabilities significantly.

3. Femtosecond apparatus

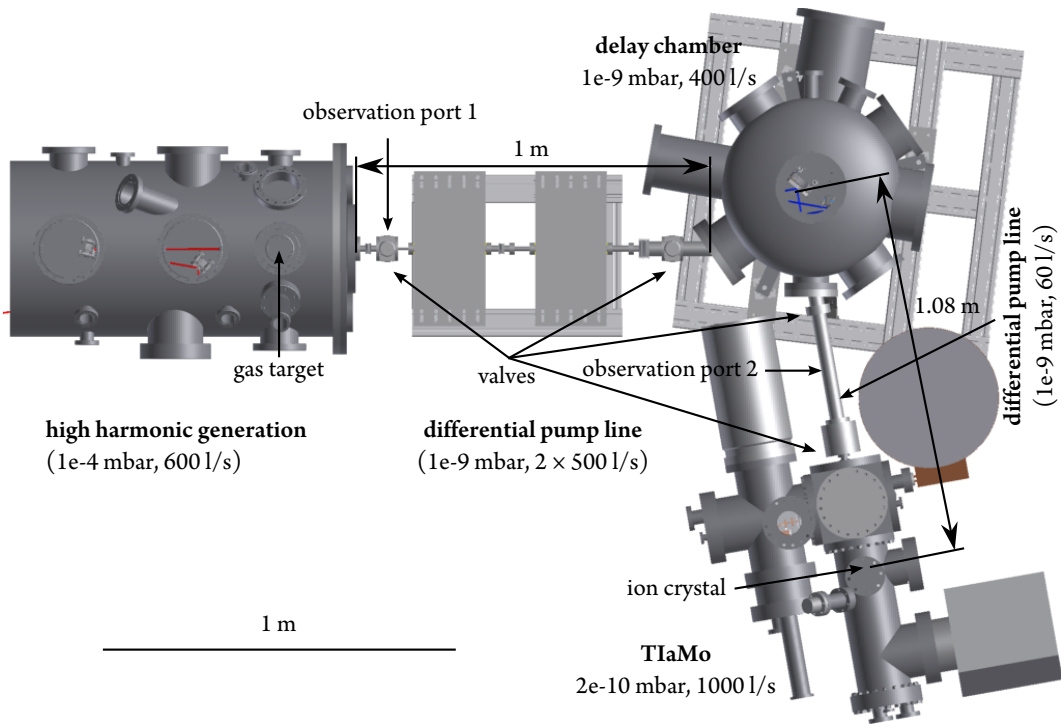


Figure 3.2.: Computer drawing of a top view on the AS4B beam line including the high harmonic generation chamber, the differential pumping line to the delay chamber and the second differential pumping line to the TIaMo apparatus.

3.2. UV pulse generation

Due to the broad spectrum of the near single-cycle infrared driver pulses, phase matching in non-linear optical crystals is not easily fulfilled [10], especially not in the case of sub-4 fs pulses. Thus, the conventional method for frequency conversion cannot be efficiently applied in the case of extremely short pulses. Permanently searching for new ways to generate ever shorter pulse durations, several new experimental schemes have been studied. Frequency mixing processes in gas filled capillaries [46, 59] were successful but the recent approaches [70, 136] in the group of Prof. Krausz at the MPQ could demonstrate unprecedented short UV pulses. These schemes are based on frequency up-conversion in noble gas targets—usually employed for *high harmonic generation* entering the extreme ultraviolet (XUV). The efficiency of this method depends strongly on the duration of the driver pulses. If these are sufficiently short (few cycle limit), it is possible to efficiently generate third harmonic UV pulses that are as long as or even shorter than the driver pulse [70]. Because this method allows to generate not only short but also powerful ($\approx 1 \mu\text{J}$) UV pulses, the possibilities of many experimental techniques, including spectroscopy of molecular and condensed matter objects are extended. The enhanced capabilities emerging from shorter pulses for the field of molecular spectroscopy are demonstrated within this thesis by applying them for time-resolved experiments on single $^{24}\text{MgH}^+$ ions; see chapter 5 on page 95.

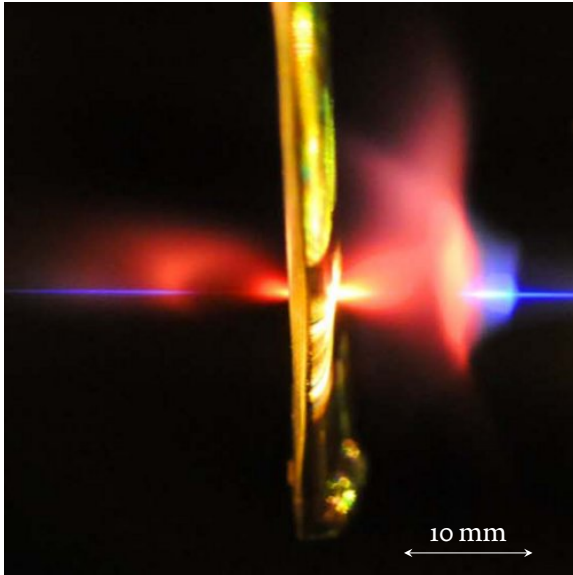


Figure 3.3.: Photographic image of the third harmonic generation process in a noble gas target. The target nickel tube is squeezed to 1 mm inner width. The strong $7 \cdot 10^{14} \text{ W cm}^{-2}$ infrared laser beam (left to right) is used to “drill” (laser ablation) two holes ($\approx 100 \mu\text{m}$ diameter) allowing the pulses to interact with the gas in the region of its highest density. In this thesis neon at 5000 mbar and argon at 800 mbar were used. The reddish lobes to the left and right are caused by emission from plasma clouds and are a sign of profuse ionization of the gas in consequence of excessive focal intensity.

The short pulses in the ultraviolet are generated inside a dedicated vacuum chamber located at the end of the AS4B beam line. Elisabeth Bothschafter reported about the technical details of the *harmonic generation chamber* in [18, 19] recently. Her approach offers the additional advantage to generate UV and XUV pulses simultaneously in a collinear fashion. However, in the time-resolved experiments within this thesis only pulses in the ultraviolet were applied. Another modification to previous experimental realizations [69, 136] is the encapsulation of the noble gas target in a nested vacuum vessel inside the main chamber. The small vessel is evacuated by a strong $200 \text{ m}^3 \text{ h}^{-1}$ backing pump⁵ that copes with the gas load of the target (up to 6000 mbar). Replaceable apertures (0.25 mm to 1 mm diameter) allow only a small fraction of the gas to leak into the surrounding main chamber in which a pressure less than $1 \cdot 10^{-3}$ mbar is sustained with the help of a 600 l s^{-1} turbomolecular pump⁶. Omission of that nested chamber approach reduce the acceptable gas flow through the target [70].

After seven reflections on silver mirrors (reflectivity $> 97\%$) placed along the beam transport line, the infrared driver pulses arrive at the gas target with an energy of $330 \mu\text{J}$. They are focused onto the target to a spot size of $50 \mu\text{m}$ waist by a spherical mirror with 1200 mm radius of curvature resulting in maximum peak intensities on the order of $7 \cdot 10^{14} \text{ W cm}^{-2}$ [18]. A motorized iris at the entrance to the harmonic generation chamber is used to adjust the focal intensity.

The gas target is displaceable with a resolution of $10 \mu\text{m}$. This allows to position it precisely in the focus, perpendicular to the laser beam axis. It is made of a 3.2 mm nickel tube that is closed by soldering on one end; see fig. 3.3. On the other side it is connected to the noble gas supply. Two small holes in the target tube are exactly aligned with the beam axis and allow the pulses to propagate through the region of highest gas density (500 mbar to 5000 mbar). In order to make the holes perfectly match the beam waist, laser ablation, accessible with the strong infrared pulses, is used to “drill” holes into the tube. Gas in front and behind the target interacts with the short

⁵ ScrewLine SP250, Leybold

⁶ TMP600C, Oerlikon

pulses as well; see fig. 3.3 on the preceding page. If the gas density inside the target is chosen too high, the gas cloud in front of the actual gas target can cause significant self focusing of the beam that leads to a shift of the focus along the propagation axis. The gas cloud can also give rise to phase matching bandwidth narrowing that is detrimental to the third harmonic generation yield and the UV spectral width [18]. If the laser intensity is too high, ionization of the gas takes off and plasma absorption limits the third harmonic yield. Furthermore, in this regime it was observed that the spatial mode profile of the pulsed UV beam undergoes a transition from a smooth circular shape to a more divergent, radially modulated, ring-like structure. For that reason, the onset of this transition was used as indicator marking the optimal focal intensity.

In summary, we performed an iterative process of adjusting gas target position, gas density and laser intensity a couple of times until the optimum setting was found. In parallel, we optimized the above mentioned parameters of the laser system in order to generate the desired spectrum. Pulses with 300 μJ energy right after the target and with suitable spectrum (cf. chapter 5 on page 95) were available at days of good laser performance; see also section 4.4 on page 90.

3.3. Delay line

After the third harmonic generation chamber, the UV pulses propagate collinear with the IR pulses through a 1 m long *differential pumping line* made up by CF16 and CF40 tubing elements inside which a vacuum pressure in the low $1 \cdot 10^{-9}$ mbar regime was sustained by two 500 l s^{-1} turbo molecular pumps⁷. The differential pumping line isolates the varying vacuum conditions of the harmonic generation chamber from that of the delay chamber.

The optical setup inside the *delay chamber* (see fig. 3.4 on the next page for details) was foremost conceived for the applications of this thesis. A description of an early version has already been presented [42] by a Diploma student of our group. Although not strictly required, owing to the good vacuum isolation properties of the connection to TIAMO (see next section), all optical and mechanical parts of the setup were selected with ultrahigh vacuum compatibility in mind and allow the chamber also to be used separately in other experiments with high vacuum demands. Among the special components are aluminum-based mirror mounts⁸, vacuum compatible piezo-operated actuators⁹, and vacuum versions of several motion control stages.

The first three dichroic mirrors M1–M3 of the setup separate the UV pulses from the collinear fundamental pulses which are stronger by three orders of magnitude. In order to distort the spectral phase of the UV pulses as little as possible, custom designed nearly dispersion-free dielectric mirrors¹⁰ were used; see fig. 3.5 on page 62. The design of the optical coating is optimized for high transmission ($> 95\%$) in the infrared and high reflection ($\approx 99\%$) in the wavelength range from 265 nm to 310 nm; see fig. 3.6 on page 63. The modulated reflectivity on the short wavelength side outside the high reflectivity interval depends on the angle of incidence which allowed to damp the modulation amplitude and thereby enhance the suppression of shorter wavelengths by using

⁷ TMU 521 YP, Pfeiffer

⁸ Mayer

⁹ picomotor, New Focus

¹⁰ H0809005/08, Layertec

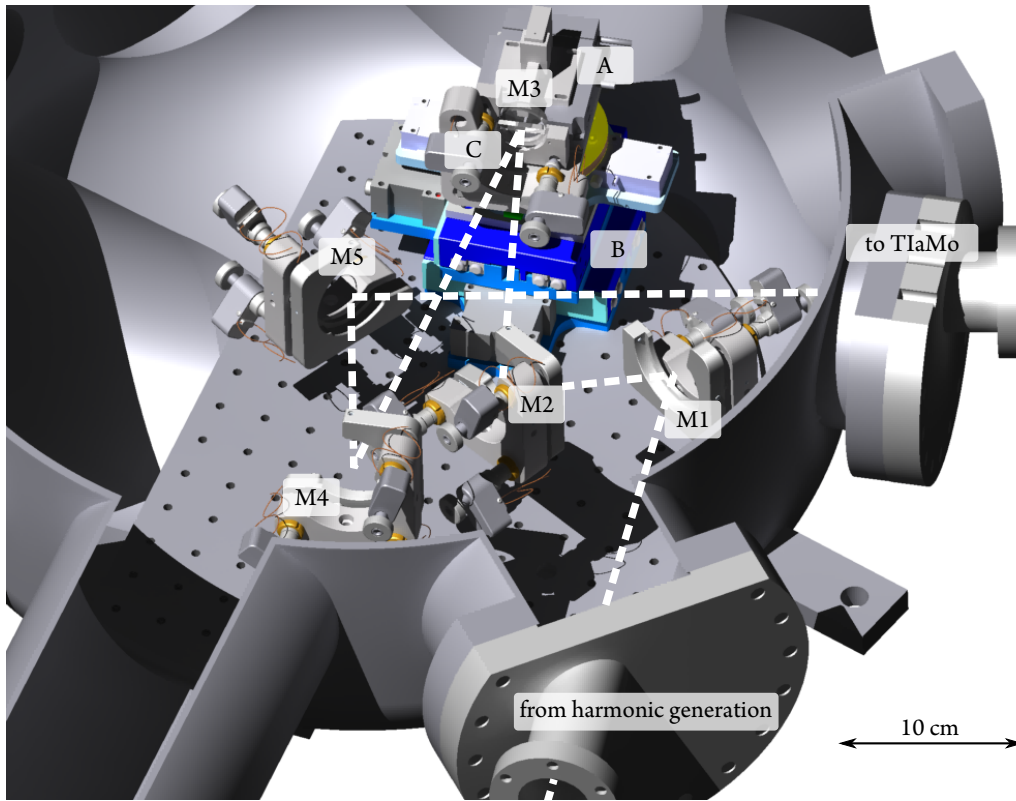
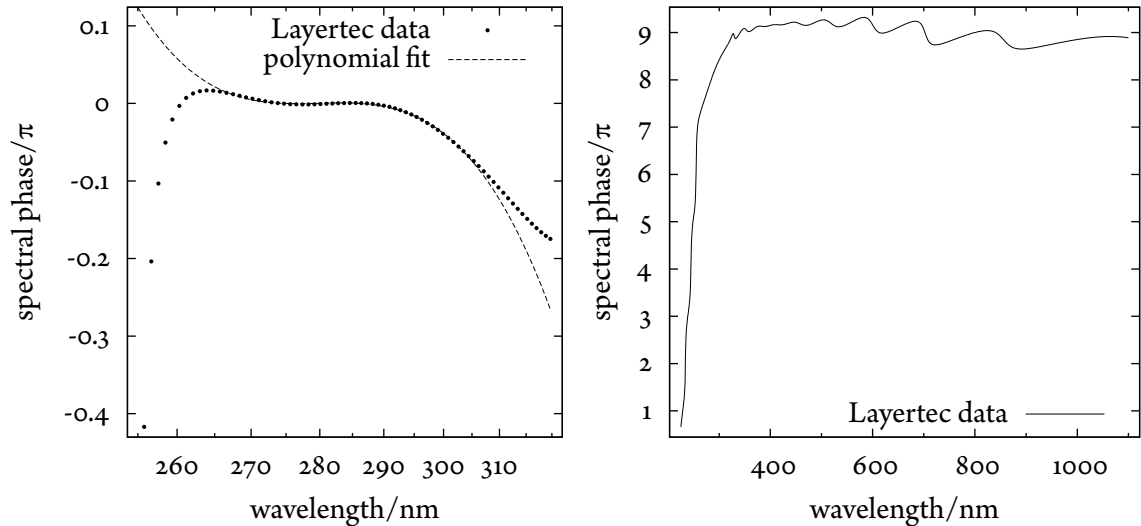


Figure 3.4.: Computer drawing of the delay chamber. The chamber has an oblate shape (major axis diameter 50 cm) accommodating a small optical setup together with a high resolution motion control systems. A $1 \cdot 10^{-9}$ mbar vacuum was sustained by a 400 l s^{-1} turbomolecular pump (not shown). The pulsed beam enters the chamber 1 m downstream of the high harmonic generation. UV and the about 1000 times more intensive IR pulses propagate collinear. The mirrors M1, M2 and M3 are used for dichroic filtering and reduce the IR intensity by a factor of at least 20 by each reflection; see fig. 3.6 on page 63. M1 and M2 are also used to align the beam with mirror M3. On M3 the UV beam waist is about 10 mm. The beam is split into two separate parts by the divided surface of a half mirror setup. The pulse energy in the two beam components is controlled by the incident beam's centroid position relative to the slit of M3. One half mirror can be displaced relative to the other by the piezo translation stage (A). By that, the delay between corresponding pulses in the two beam parts is defined. The other mirror half is tip and tilt adjustable. To this end, the mirror mount is equipped with piezo driven actuators (B) as are all other adjustable mirror mounts axes, too. In order to address the remaining degrees of freedom, the double mirror setup is mounted on two piezo operated orthogonal linear translation stages (C) supplemented by a similar rotation stage. The spherical focusing aluminum mirror M4 images the two beam components onto the 1.08 m distant trapped ions inside the Tlamo apparatus. Minute corrections to the beam pointing were applied with mirror M5 (aluminum). The distances between the mirrors measured M1-M2: 100 mm, M2-M3: 225 mm, M3-M4: 181 mm, M4-M5: 57 mm; the full reflection angle at M1 was 36° , at M2 30° , at M3 16° , at M4 13° .

3. Femtosecond apparatus



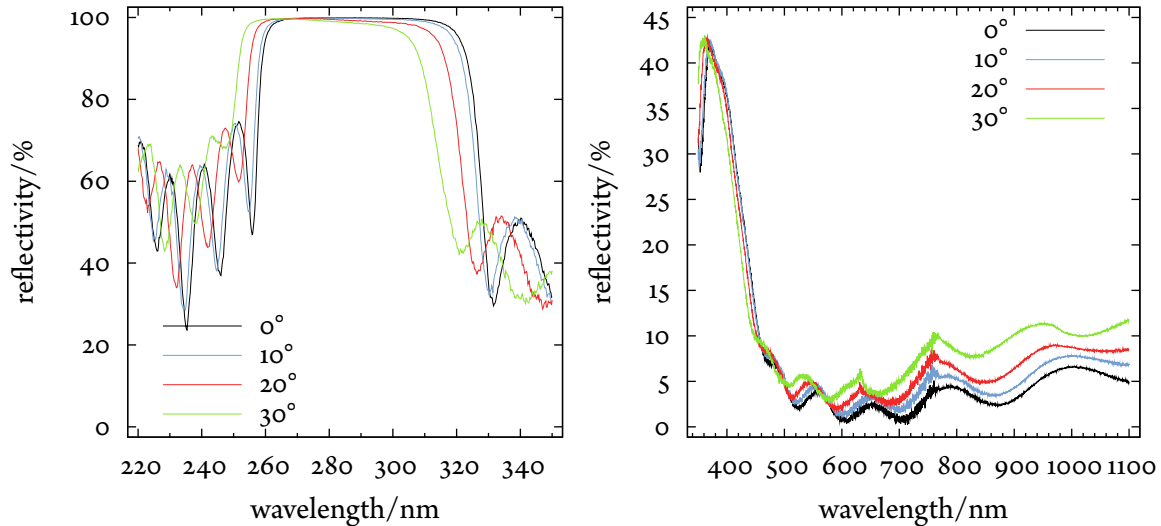
- (a) Phase modulation in the high reflectivity interval. Approximate Taylor expansion coefficients (see eq. (1.12) on page 19) can be extracted from a third order polynomial fit: $\varphi_1 = -4.2$ fs, $\varphi_2 = 0$ fs², $\varphi_3 = 8.7$ fs³. The steep linear term φ_1 —only delaying the pulse by 4.2 fs—has been subtracted for reasons of better visibility. The vanishing coefficient φ_2 signals a (linear) chirp-free pulse after reflection.
- (b) The spectral phase is mainly dominated by a linear dependence on the frequency in the high reflectivity ultraviolet region. To preserve comparability, the data is shown as function of the wavelength instead. Outside the high reflectivity interval strong but irrelevant modulations are visible.

Figure 3.5.: Spectral phase modulation (see section 1.4 on page 18) by the dichroic dielectric mirrors used in the delay chamber for spectral filtering. The data presented has been provided by the manufacturer and results from a simulation of the layer design.

slightly differing angles of incidence at M_1 , M_2 , and M_3 . This suppression is needed to account for molecular properties of $^{24}\text{MgH}^+$ that are discussed in section 5.1.2 on page 101.

By the last dielectric reflection off the complex mirror setup M_3 , the UV beam is split into two components that provide time-delayed pulse replica required for the time-resolved pump-probe experiments. This is achieved by two mirror halves which are mounted such that they complement each other to a flat 25 mm round mirror with only a thin (≈ 200 μm) slit in between. One half mirror is freely adjustable in tip and tilt relative to the fixed half. Tip and tilt were used to adjust the relative angle between the two beam components. The fixed half mirror is vacuum-compatibly glued to a piezo translation stage¹¹ with 320 μm maximum displacement and 1 nm resolution. It moves parallel to the normal of the mirror surface and thereby implements an adjustable delay line for one of the two pulse replica. The whole double mirror setup is mounted on top of a stack of two orthogonal piezo-operated linear translation stages (60 mm maximum displacement, 100 nm resolution) and a similar rotation stage (24 μrad resolution) from nanomotion. In this way, access is given to the remaining degrees of freedom of the mirror setup.

¹¹ nanoSX 400 CAP, piezosystem jena



(a) 50 nm wide interval of high reflectivity in the ultraviolet with a steep edge at 260 nm beyond which short wavelength components of the spectrum are partially suppressed. (b) The low reflectivity in the visible and near infrared allows for separation of the fundamental from the third harmonic pulses.

Figure 3.6.: Reflectivity of the dichroic dielectric mirrors (Layertec) used in the delay chamber for spectral filtering as a function of wavelength and angle of incidence measured using a transmission spectrometer (Bruins Instruments). The high reflectivity interval is shifted towards shorter wavelengths under tilted incidence. This allows to damp the oscillations outside this interval by combining consecutive reflections at different angles of incidence.

The following reflection off the spherical ($ROC = 1400$ mm) aluminum mirror M_4 focuses the pulses on the trapped ions in chamber 3 of the TIAMO apparatus. By that, the mirror effectively images the focus of the UV beam in the third harmonic gas target (object distance 2045 mm) onto the trapped ions (image distance 106.5 cm). It turned out that the corresponding spot size inside the TIAMO apparatus initially was much bigger (diameter 250 μm) than expected (25 μm). Aberrations, in particular astigmatism and coma induced by the tilted reflection off the spherical focusing mirror were identified to limit the focusing properties. By rearranging the setup targeting on a smaller angle of incidence (6.5°) at the spherical mirror, aberration effects could be drastically reduced; see fig. 3.8 on page 66. It was even preferential to trade a smaller focal spot against minor beam clipping on some of the optical elements inside the delay chamber. Calculations assuming a Gaussian intensity profile of the UV beam show that a focal beam waist of 60 μm is realistic for the given angle of incidence. In the limit of normal incidence, the beam waist would amount to 15 μm . Thus, the spot size was still dominantly limited by the tilted spherical mirror. Aspherical focusing optics, e. g. an off-axis parabola, would allow to further reduce the aberration. The flat aluminum mirror M_5 was used to control the overlap the pulses with the ions.

Although the peak intensity is inversely proportional to the square of the focal spot diameter it must be doubted that the presented experiments would have been able to benefit from a still smaller waist. Beam pointing instabilities and high frequent vibrations created by the turbomolec-

ular pumps on the beam line are suspected to limit the actual precision. For the proof-of-method experiments, currently still uncorrected beam pointing causes large systematic errors since the target reaches already the aspired pointlike dimensions. This will be especially relevant for single trapped molecular and atomic ions which can be described by wave functions with a width on the order of 10 nm and the envisioned X-ray laser beam to be focused to a 100 nm diameter spot. Under these conditions, great care will have to be spent on a rigid connection of the ion trap apparatus to the pulsed beam source which in turn is expected to provide a stable output beam whose actively controlled beam pointing will have to deviate much less than its focal spot size. It shall be emphasized that these stringent requirements are specific to single particle targets. Currently used spatially extended gaseous, liquid or solid state targets are much more tolerant in this respect.

3.4. Beam line connection

As pointed out in appendix B.2 on page 143, a degradation of the vacuum conditions in TIAMO would not only compromise the average life time of trapped ions but also the viability of the barium atom ovens. It has thus been of utmost concern not to spoil the ultrahigh vacuum by connecting the femtosecond beam line to the ion trap setup. Therefore, the link between TIAMO and the delay chamber incorporates an additional 40 cm long differential pumping line; see fig. 3.2 on page 58. From its length and the used CF₄₀ and CF₁₆ tubing, a vacuum conductance $L < 20 \ell \text{ s}^{-1}$ is estimated. Due to the low vacuum pressures in the delay chamber it was sufficient to evacuate the differential pumping line with a small $60 \ell \text{ s}^{-1}$ turbomolecular pumping system¹².

An all-metal gate valve¹³ that is mounted directly to TIAMO's chamber 2 (see fig. 2.1 on page 23) can be closed to permanently separate the UHV apparatus from the beam line. In order to be protected also in emergency situations, e. g. a leak in the beam line, an automatically operated electro-pneumatic valve¹⁴ was mounted to the delay chamber. It was programmed to disrupt the connection of delay chamber and differential pumping line if a tolerable pressure threshold is exceeded. In between the two mentioned valves, there is a third manual operated window valve¹⁵ that holds a 1 μm thin pellicle; see appendix B.5 on page 148. If that valve is closed, a transparent, practically dispersion-free ($\text{gdd} = 0.05 \text{ fs}^2$; see appendix B.5 on page 148) optical connection to TIAMO remains while the vacuum systems are kept hermetically separated. The option to slide in the pellicle might be relevant if the vacuum pressure or, e. g. dust in the beam line, precludes a direct connection. Within this thesis, that option was abandoned since the vacuum pressure in chamber 3 was not affected to a detectable level when the gate valve between TIAMO and AS4B was opened. This is due to the low pressure in the delay chamber as well as in the differential pumping line but also to the good isolating properties of the differential pumping section connecting chamber 2 and chamber 3; see section 2.4 on page 33.

In order to monitor the pointing of the pulsed UV beam, a second pellicle under 45° was inserted into the beam path. It reflects a small part of the UV beam (see fig. B.10 on page 149) through a

¹² TPS compact, Varian

¹³ 48124-CE01, VAT

¹⁴ 01032-CE31, VAT

¹⁵ 01032-CE01, VAT

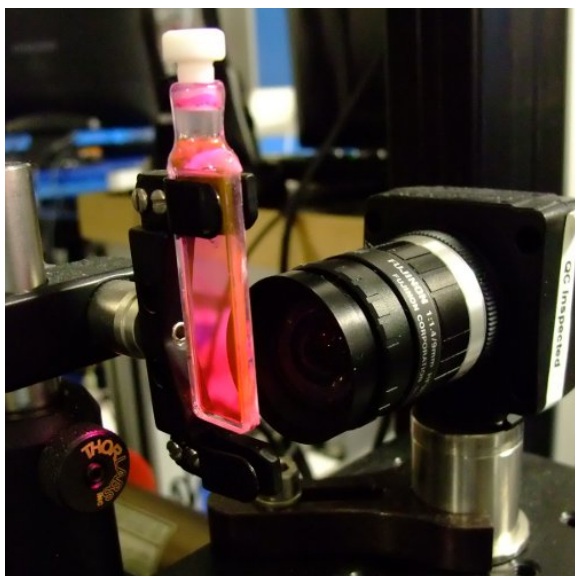


Figure 3.7.: Photograph of the setup used to monitor the beam pointing of the UV femtosecond beam. The laser dye sulforhodamin B absorbs UV photons and fluoresces at 600 nm. A video camera aligned with the beam axis is used to image the fluorescence spot. The spatial resolution of the setup is limited by the pixel size of the camera and amounts to 10 μm in the object plane.

fused silica window (“observation port 2” in fig. 3.2 on page 58) towards a small imaging system outside the vacuum. Since the pointing and time-independent intensity profile of the beam are measured, the dispersion properties of the view port are irrelevant. The UV beam passes through a 1 mm dye-filled (sulforhodamin B in methanol) quartz cuvette¹⁶ where it gets partially absorbed. Some dye molecules are (single-photon) excited by the UV irradiation and emit a fluorescence photon in the orange at about 600 nm. In this way, the UV intensity distribution of the beam, which is identical to that of the fluorescence, can be easily imaged with the help of an ordinary CCTV camera¹⁷. The camera was centered and aligned with the UV beam. Even at average UV powers of a few microwatts and below, the fluorescence signal and the associated image quality sufficed to detect changes on the single pixel level corresponding to a deviation of 10 μm in the object plane. A photograph of the setup is shown in fig. 3.7.

The fluorescence setup turned out to be an indispensable tool for the alignment procedure. The cuvette was positioned at the same distance to the pick-up pellicle as the trapped ions. Hence, the image of the fluorescence spot inside the cuvette is similar to the intensity distribution of the beam inside the vacuum at the position of the trapped ions. However, although the cuvette was aligned with greatest care, it is not sure if reliable images of the the focal spot were obtained at all times. Figure 3.8 on the next page shows the currently smallest focus that was achieved in targeted effort. When the mirror configuration in the delay chamber that provided both a small focus size and a focus position coincident with the position of the trapped ions simultaneously had been found, this configuration served as a rule for the rest of the measurement campaign. Nonetheless, slight beam pointing adjustments, differing optimum gas target positions, and varying divergence of the generated UV beam (see section 4.4 on page 90) influenced the spot size in the imaging plane that was fixed by the predetermined and stable position of the ion target in TIAMO. Over a period of several weeks, the apparent diameter of the focal spot size in the cuvette increased by

¹⁶ Hellma

¹⁷ Chameleon, PointGrey

3. Femtosecond apparatus

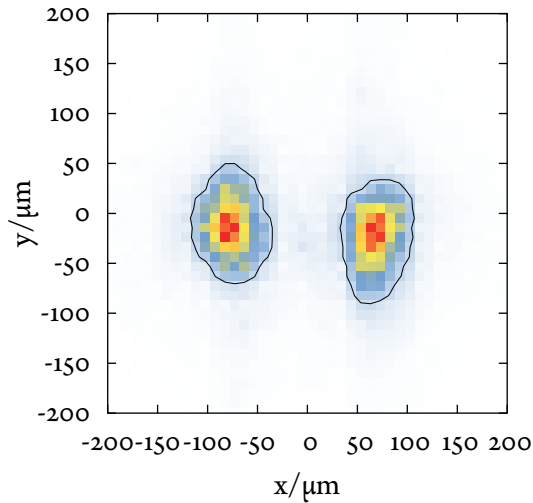


Figure 3.8.: False color representation of the smallest attained profiles of pump and probe beam approximately equal to the respective expected intensity distribution at the position of the trapped ions. The image shows the fluorescence generated inside a Sulforhodamin B filled cuvette (see fig. 3.7 on the preceding page) placed in the approximate focal plane of both beams. The black lines indicate the e^{-2} -contour suggesting a $40 \mu\text{m} \times 60 \mu\text{m}$ (radius) beam spot for both beams.

almost a factor of three. This is why it must be assumed that the true focal spot size, and by this the associated peak intensity on the ions, was not ascertained precisely. In future applications with envisioned 100 nm focal spot sizes, the difficulty to measure the exact intensity at the point-like target particle independently, will be increased. It can be expected, that the molecular ions will rather serve as detector themselves. Similarly, in this thesis, the experimental results of the time-resolved experiments could be used to determine the intensity later. This value matched the estimations based on the described fluorescence setup; see section 5.3.3 on page 112.

4. Experimental building blocks

This chapter describes the realization and perspectives of first important building blocks on the way towards reliably initialized and reproducible positioned single molecular ion targets. In the beginning, a selection of measurements that characterize the apparatus described before are presented. In the following, experimental procedures are discussed that allow to reliably load, cool and prepare the desired ion crystals containing individually resolvable molecular $^{24}\text{MgH}^+$ ions and to connect the ion trap vacuum apparatus to the femtosecond beam line. That laid the foundations for the central experiment of this thesis: the proof-of-method time-resolved dissociation of $^{24}\text{MgH}^+$ demonstrating the feasibility to observe single photochemical reaction events with femtosecond time resolution using spatially resolved single molecular ions in an isolating environment; see chapter chapter 5 on page 95.

4.1. Ion trapping

The ability to control trapped atomic and molecular ions in a reliable manner is the capitol prerequisite of this thesis. It is the topic of this section to present the basic parameters of the ion trap and typical experimental procedures that allowed to reach the aspired goal but that also show potential for further improvement.

As discussed in section 2.5 on page 35, atomic ions were generated by photoionization of atoms in a thermal beam inside the RF-guide. Typical loading parameters can be found in this section, too. Ions were loaded almost exclusively in chamber 1 even though atom ovens are installed in chamber 3 as well. This was opted for mainly because the photochemical reaction $^{24}\text{Mg}^+ + \text{H}_2 \rightarrow ^{24}\text{MgH}^+ + \text{H}$ was accomplished in chamber 1 where the pulsed valve for hydrogen injection is available; cf. section 2.1.1 on page 22. In this way, the ultrahigh vacuum conditions in chamber 3 are preserved and the RF-electrodes in this chamber are defended from adverse staining by magnesium vapor deposits during the loading process.

Loading of a suitable amount of atomic ions (see section 4.1.1 on the following page) was followed by an cleaning procedure to separate different atomic isotopes (see section 4.1.3 on page 71) and the molecular ion generation step (see section 4.1.5 on page 75). The complex process of preparing a crystal containing an optimum number of molecular ions has been assigned to the automatic loading software described in the next chapter; see in particular appendix A.1.1.a on page 124. With the help of this software, loading of ions in chamber 1 simultaneous to performing the actual experiments in chamber 3 was possible. Although the presented experimental loading scheme turned out to be sufficiently fast for the experiments of this thesis, a higher repetition rate (> 100 Hz) is desirable in future experiments. Based on the results with the current setup this is expected to be feasible. See chapter 6 on page 118 for a further discussion.

4.1.1. Coulomb crystal structures

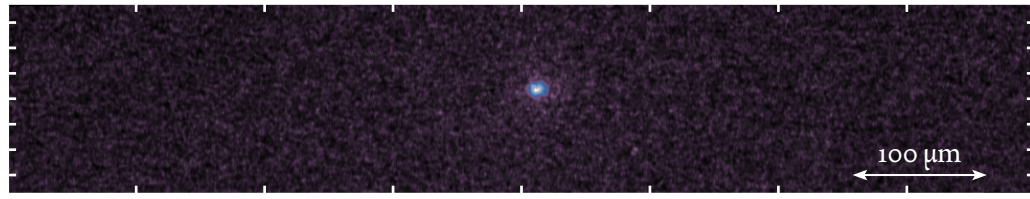
In a linear radio frequency trap like the one realized in TIAMO, several crystalline ion structures with cylindrical symmetry can be formed depending on the linear density λ of ions in the trap. A detailed molecular dynamical analysis of the topic is explicated in [74]. The sequence of structures related to an increasing value of λ emerging from an increasing number of ions in a trap with otherwise fixed parameters is illustrated by showcase examples in fig. 4.1 on the next page. In short, the sequence starts with a single ion and continues with an increasing number of ions lining up on a string that points into the direction of weakest confinement (axial confinement in TIAMO) until the density of ions in the trap makes it energetically more favorable to form a zigzag shaped two-dimensional structure extending also in the direction of next weakest confinement (in the weaker of two radial directions in TIAMO). If the radial pseudo-potential was of perfect cylindrical symmetry, the radial confinement was equal and the crystalline structure free to rotate about the axial direction. In reality, unavoidable minute asymmetries fix a plane, though. After having increased the ion density in the trap beyond approximately unity, the crystal extends into the remaining third dimension, too. First, tetrahedra chains alternate with helices, at higher densities the helices interweave with each other, forming shell like layers of ions that in the end get onion-like interleaved.

A zigzag Coulomb crystal consisting of in total about 50 to 60 ions, including 20 to 30 molecular ions turned out to be ideal for the time-resolved dissociation experiments without compromising the vital single particle resolution; cf. the examples in fig. 5.8 on page 107. At the same time it provided the means to efficiently collect enough data to obtain sufficiently small statistical uncertainties. The fluorescence images of two-dimensional crystals containing even more ions would either trespass the detector width or—if stronger axial confinement was applied to restrict the crystal length to the detector width—would increase the linear density such that three-dimensional crystalline structures would form. Two-dimensional projections of those do currently not guarantee unambiguous single ion resolution.

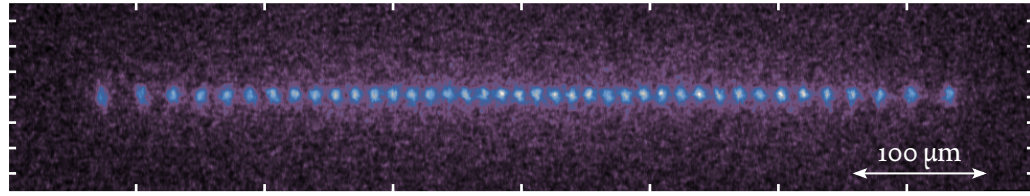
4.1.2. Radial cooling

The geometry of the RF-guide in TIAMO is particularly suited for trapping extended, long prolate crystals. Due to the continuity of the RF-electrodes only minor drags in the axial potential are observed. By that, near-ideal harmonically trapped ion crystals of up to 1 mm length with single particle resolution could be worked with. In order to observe all fluorescing ions at the same time, the cooling laser beam must overlap with the complete crystal. This has been achieved by aligning the laser with the RF-axis, i. e. the symmetry axis of the crystal. The comparably big beam waist $w \approx 80 \mu\text{m}$ and the corresponding long Rayleigh length $z_R = 72 \text{ mm}$ of the cooling laser beam allowed to irradiate and cool all atomic ions equally.

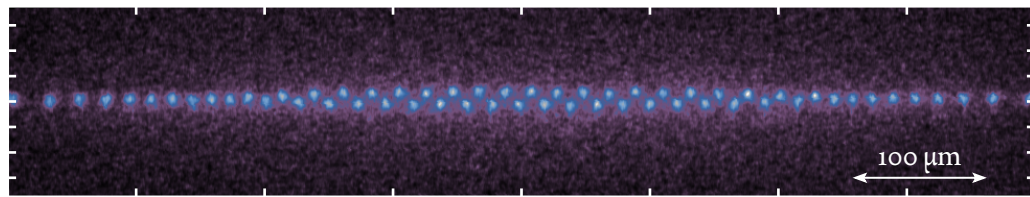
The drawback of this approach is that the cooling laser barely addresses the radial degree of freedom; see section 1.2 on page 12. For ion crystals with high linear density, corresponding to a zigzag structure and onwards, this poses no severe problem since the crystal's vibrational normal modes sufficiently couple radial and axial degrees of freedom. Radial motion can thus be cooled even by a laser aligned with the axial direction; see also the discussion in section 1.2 on page 12.



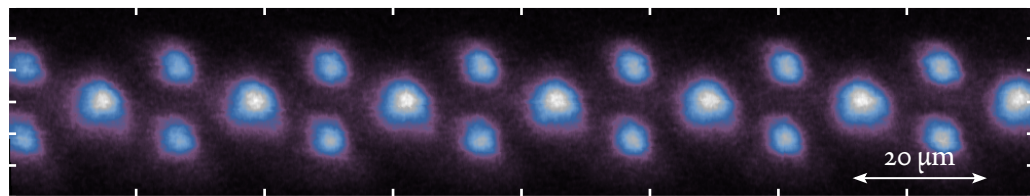
(a) single ion



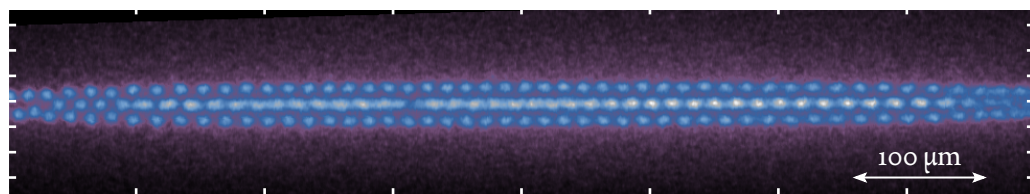
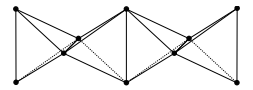
(b) linear string, $0 < \lambda < 0.709$



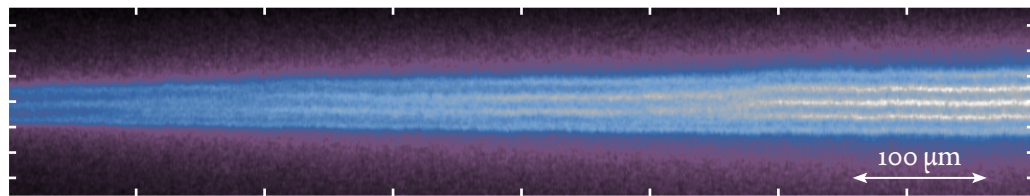
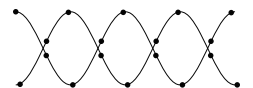
(c) zigzag, $0.709 < \lambda < 0.964$; lower linear density at the ends causes transition to one-dimensional string



(d) tetrahedral, $1.25 < \lambda < 1.39$ and $1.70 < \lambda < 2.19$



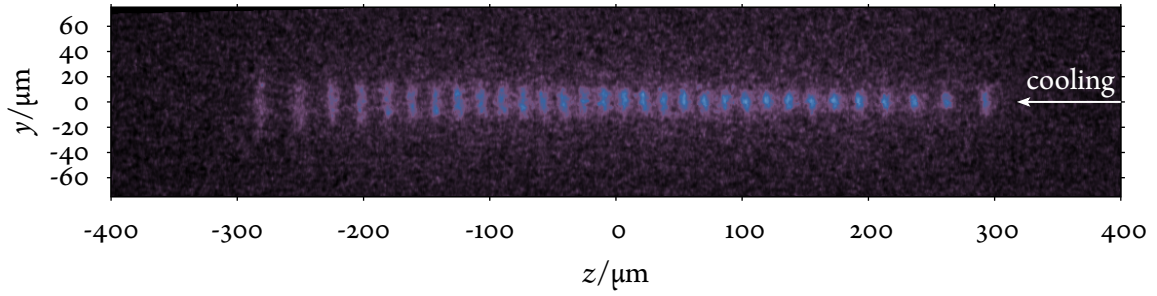
(e) helix, $0.964 < \lambda < 3.1$ if not tetrahedral



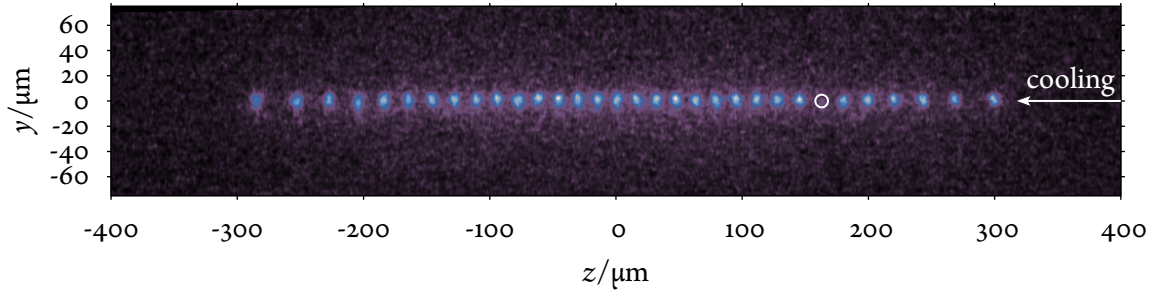
(f) shells, $\lambda > 3.1$

Figure 4.1: Two-dimensional false color fluorescence images of crystalline structures at comparable trap confinement but increasing density of ions λ recorded on a CCD.

4. Experimental building blocks



(a) Radially smeared fluorescence light by secular motion in a linear pure $^{24}\text{Mg}^+$ crystal.



(b) Coupling of radial and axial degrees of freedom mediated by an dark ion (circle) of different charge-to-mass ratio reduces the radial motional amplitude.

Figure 4.2.: False color fluorescence image of a linear ion crystal containing 31 $^{24}\text{Mg}^+$ ions. The ion chain is stabilized in the radial direction by the presence of one additional sympathetically cooled molecular $^{24}\text{MgH}^+$ ion (circle).

The situation is different for linear ion chains. Here, the coupling between radial and axial motion is greatly reduced. As a consequence, linear chains of ions were observed to show big motional amplitude in the radial direction; see fig. 4.2, for example. The ions move however not uncorrelated, i. e. they oscillate collectively in phase. If that was not the case, the crystalline order in the axial direction would not be sustained for the observed radial amplitude of oscillation.

Exactly this reasoning allows a single sympathetically cooled ion to stabilize the whole chain. In [149] it is argued that because the mass-to-charge dependent pseudo-potential for a molecular ion having not that of $^{24}\text{Mg}^+$ will lead to the motional amplitude being different, too. The molecular ion's neighboring co-oscillating $^{24}\text{Mg}^+$ ions experience thus a repulsion that depends on the molecular ions distance from the trap axis. The two contiguous $^{24}\text{Mg}^+$ of the molecular ion can come closer if the motional amplitude of the molecular ion is big and *vice versa*. This mechanism establishes a coupling of the molecular ion's radial motion to the axial motion of the contiguous ions and inversely, allows to cool the radial motion with an axial aligned laser. In this way, the presence of molecular $^{24}\text{MgH}^+$ ions in a chain of otherwise $^{24}\text{Mg}^+$ ions stabilizes it and helps the single particle resolution in unpropitious situations. By stabilizing the chain, the radial motional amplitude of the molecular ion itself is also reduced because it is coupled to the laser cooled axial degree of freedom of the atomic ions in the chain.

4.1.3. Isotope cleaning by charge-to-mass filtering

Despite the potential isotope selectivity of the photoionization scheme [97] in general, a small but not negligible contribution of other magnesium isotopes $^{25}\text{Mg}^+$ and $^{26}\text{Mg}^+$ was loaded as well. Because the evaluation of the fluorescence images recorded for the time-resolved experiments rely on $^{24}\text{MgH}^+$ being the only non-fluorescing (“dark”) ions, any other ion species also appearing dark in the fluorescence images distorts the measurements. The atomic transition line shifts [9] of the naturally occurring isotopes $^{25}\text{Mg}^+$ (1.62 GHz) and $^{26}\text{Mg}^+$ (3.09 GHz) to the blue of the transition frequency of $^{24}\text{Mg}^+$ causes the laser adjusted for $^{24}\text{Mg}^+$ cooling to be far detuned from the resonances (line width $2\pi \cdot 42.7$ MHz) of the other naturally occurring isotopes. These ion species appear thus also dark and must be omitted in the experiments. Ionized residual gas particles that might be formed by charge transfer collisions appear also dark. Since these formations cannot be precluded by means of particle separation at the beginning of the experiment, their occurrence must be reduced by performing the experiment in ultrahigh vacuum; see section 4.3 on page 87.

Driving the respective radial secular motion, which depends on the charge-to-mass ratio (section 1.1.1 on page 7), resonantly, offers a possibility to increase the chosen ion species’ kinetic energy above the trap depth and thus get rid of the respective ions selectively. The resonance frequency of $^{24}\text{Mg}^+$ was resolved with 1 kHz precision using the method explained in the next section. Since the radial secular frequency is inversely proportional to the mass (only singly charged ions are considered), the relative mass differences between the magnesium isotopes implies separate well-resolved radial secular frequencies of $^{24}\text{Mg}^+$ (500 kHz), $^{25}\text{Mg}^+$ (480 kHz), and $^{26}\text{Mg}^+$ ions (462 kHz).

In order to speed up the process of isotope cleaning, the radial motion of $^{25}\text{Mg}^+$ and $^{26}\text{Mg}^+$ were driven simultaneously. The sum of the two slightly different oscillating voltages yields an amplitude modulated beat signal which was produced by an arbitrary wave form generator and applied to the wire-shaped compensation electrode beneath the trap of chamber 1; similar to the correspondent electrodes in chamber 3 visible in fig. B.12a on page 153. If the amplitude of the driving voltage was high enough ($V_{\text{rms}} \approx 250$ mV) a 1 s to 3 s long pulsed excitation was sufficient under the regular trapping conditions—specified in the next section—to get rid of the perturbing isotopes.

Excitation in the radial direction worked best for cleaning purposes. Owing to the particularity of the TIAMO setup, the cooling laser addresses the axial degree of motion almost exclusively. This means, mainly sympathetically cooled parasitic atomic isotopes and molecular ions are generally lost in the radial direction, because the counteracting cooling effect is much weaker in this direction and gets further weakened by an increased radial motional amplitude. The ions behave like a weakly damped resonantly driven oscillator. Blocking the cooling laser completely during the resonant excitation resulted in a clean crystal, though a fluctuating fraction (about $\frac{1}{3}$) of the $^{24}\text{Mg}^+$ ions was lost. In contrast, cleaning the crystal by driving the radial motion with at simultaneously, moderate laser cooling turned out to be efficient. Almost all dark ions were expelled from the trap after three cleaning pulses while more than 95 % of the $^{24}\text{Mg}^+$ ions could be retained. By using more cleaning pulses, the probability to obtain a pure crystal can be further increased but was not needed for the experiments of this thesis. It is estimated that more than 98 % of all observed “dark” ions in the time-resolved experiments have indeed been $^{24}\text{MgH}^+$.

4.1.4. Trap frequencies

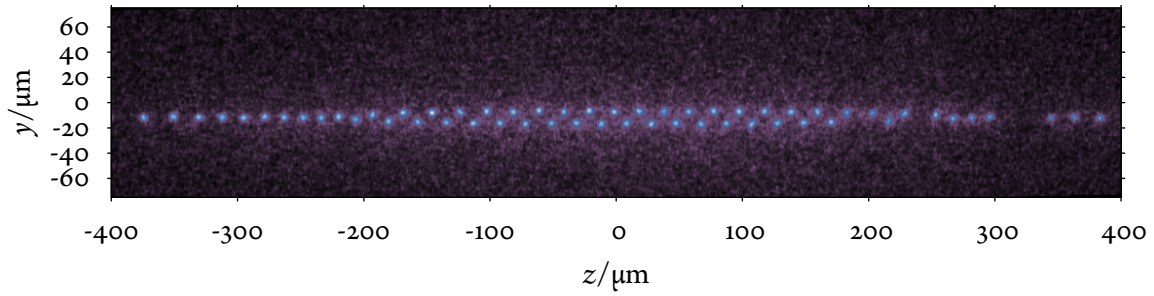
Weak excitation of the secular motion was used to determine the secular trap frequencies. The motional amplitude of all ions with equal mass-to-charge ratio increases significantly if the frequency of the resonant driving voltage matches the respective trap frequency. In this situation, the fluorescence photons are spread over more detector pixels (see section 2.6 on page 37). Additionally, the cooling laser frequency appears frequency modulated in the rest frame of the ion if its motion has a component along the laser beam direction and can lead to decreased fluorescence. The principal trap frequencies were detected by scanning the excitation voltage frequency and looking for an blurred fluorescence spot with the CCD imaging system or a drop in the photomultiplier count rate. Figure 4.3 on the facing page shows fluorescence images that demonstrate the effect of resonant excitation of radial and axial motion in comparison with the undisturbed situation.

By adjusting the amplitude of the RF-voltage U_{RF} , the radial frequency ω_{sec} characterizing the harmonic pseudo potential can be chosen within the limits defined by the related stability parameter q (see section 1.1 on page 7). The pseudo potential is expected to be constant along the RF-guide to first approximation. The radial frequency of the traps in chamber 1 and 3 should therefore be about the same. However, small deviations for instance implied by variations of the RF-electrode geometry are possible. Indeed, two radial frequencies were observed in the traps of chamber 1 and 3. The splitting might be explained by a slight geometric deformation of the RF-electrode configuration in both trapping regions. If the center points of the electrodes do not form a square, the pseudo potential becomes elliptic and the secular radial frequencies split. Even though the electrodes are manually bent (see section 2.2 on page 27) a frequency splitting of the observed size (30 %) was not expected. Whether geometric deformations are the only reason for the frequency splitting needs further investigation since the splitting was also observed to be dependent on the RF-voltage amplitude and of comparable size in the traps in chamber 1 and 3 with independent geometry. However, split radial frequencies do not harm the applicability of the trap. Table 4.1 on page 74 summarizes the measured radial frequencies in the two chambers as a function of the RF-voltage applied to the guide electrodes; see section 2.2 on page 27 for details.

The enhancement factor of the helical resonator can be calculated by relating the supplied RF-power to the actual root mean square voltage $U_{\text{RF,rms}} = 1/\sqrt{2}U_{\text{RF}}$ of the RF-electrodes. The latter is expressed using eq. (1.5) on page 10 and the definition of the stability parameter q eq. (1.3) on page 9 as

$$U_{\text{RF,rms}} = \frac{1}{e} m r_0^2 \omega_{\text{sec}} \Omega.$$

With $\omega_{\text{sec},1} = 2\pi \times 542$ kHz, $\Omega = 2\pi \times 6.8$ MHz and $r_0 = 1.12$ mm, the stability parameter $q = 0.225$ and $U_{\text{RF,rms}} = 45.5$ V follow. The voltage after the power amplifier corresponding to -32 dBm + 39.6 dB = 7.6 dB amounts to 536 mV. Thus, the loaded enhancement factor of the helical resonator should equal $45.5 \text{ V} / 536 \text{ mV} = 85$. Inserting the second measured radial frequency of chamber 3, $\omega_{\text{sec},2} = 2\pi \times 410$ kHz, yields an enhancement of only 63. It is assumed, that in reality the value of r_0 , measuring the minimal distance between ion and RF-electrode, is different (relative deviation ≈ 30 %) in the respective directions of the four RF-electrodes; see above. The actual enhancement factor is assumed to lie in between the two values derived above. The enhancement factor 61 derived



(a) Undisturbed, near ideal trapping conditions

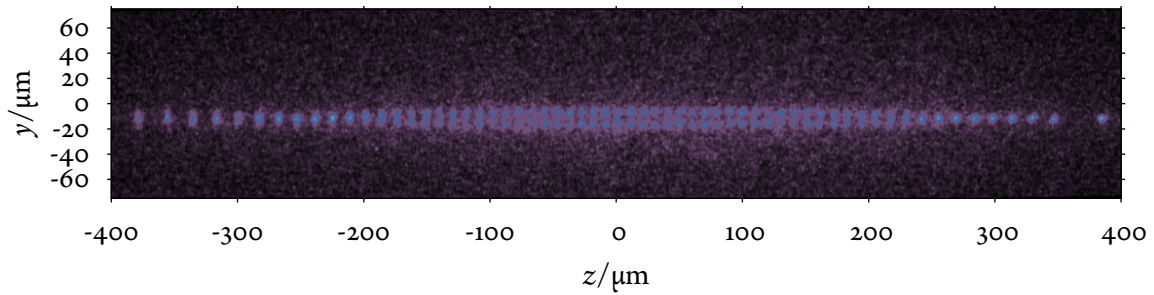
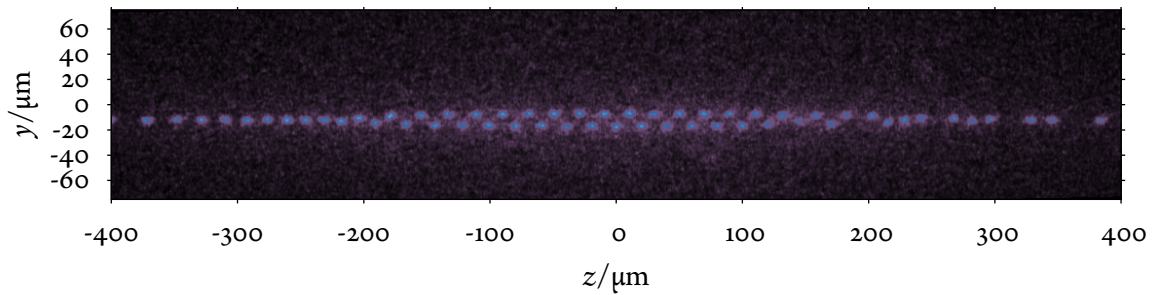
(b) Resonant excitation of the radial secular motion, $\omega_{\text{sec},1} = 2\pi \times 496$ kHz(c) Resonant excitation of the axial motion, $\omega_z = 2\pi \times 30$ kHz

Figure 4.3.: False color fluorescence images of an ion crystal containing mostly $^{24}\text{Mg}^+$ atomic ions and a few non-fluorescing “dark” ion species in the first trap of chamber 3 formed by the RF-guide and the ring electrodes $R_{3,1}$ and $R_{3,2}$; see fig. 2.1 on page 23. The crystal is shown undisturbed and when a resonant voltages are applied on the ring electrode $R_{3,2}$. The same color scale was used in all three images in order to make the drop of brightness in the images recognizable. In (b) the ions are clearly seen to remain in a crystalline state but being flipped between two zigzag-configurations by the radial excitation. In the axial direction (c), the much stronger laser cooling largely prevents ion hopping.

4. Experimental building blocks

Table 4.1.: Radial secular frequencies in the traps of chamber 1 ($R_{1,1}$ - $R_{1,2}$) and chamber 3 ($R_{3,1}$ - $R_{3,2}$) as function of the RF-voltage amplitude; see fig. 2.1 on page 23 for the notation. The given U_{RF} values are based on the helical resonator's estimated enhancement factor of 61 (see section 2.2 on page 27) and can be expressed by the stability parameter q (see section 1.1 on page 7) for $^{24}\text{Mg}^+$ ions. The remaining columns compare the expected radial frequency ω_{sec} with the actual measured frequencies in chamber 1 and 3. The splitting of the measured radial frequencies is attributed to the four RF-electrode-ion distances r_0 (see fig. 1.1a on page 8) being probably slightly different. By the same reasoning and the additional uncertainty of the enhancement factor, deviations of the expected radial frequency from the measured value(s) can be explained.

U_{RF} (V)	q	radial frequencies/ 2π (kHz)				
		expected	chamber 1		chamber 3, trap 1	
		$\omega_{\text{sec}} = \frac{q}{\sqrt{8}}\Omega$	$\omega_{\text{sec},1}$	$\omega_{\text{sec},2}$	$\omega_{\text{sec},1}$	$\omega_{\text{sec},2}$
46	0.16	389			542	410
52	0.18	437	578	421		
65	0.23	550	696	570		
82	0.29	692	867	771		

in section 2.2 on page 27 from independently measured properties of the helical resonator compares well with the measurements using the trapped ions being the most sensitive detector.

The axial frequency is chosen by varying the voltage applied to the ring electrodes. The voltage range is limited to 400 V by the transistors used in the fast voltage switching circuit; see section 2.8 on page 52. Omission of those allows for up to 1000 V limited then by the dielectric strength of the electrical feed-through; see section 2.1.1 on page 22. At higher voltages (> 400 V) the ions were radially displaced so far that it became increasingly difficult to counteract with compensation voltages appropriately. Firstly, because the action of the compensation electrodes is not perfectly homogeneous over the length of the Coulomb crystal and secondly because some compensation electrodes are not realized by close-by wires, thus are more shielded by the RF-electrodes and possess only small reach-through; cf. fig. 2.3 on page 26. It is assumed that the radial force is caused by slight deviations of the ring electrodes from perfect symmetry about the RF-axis. Another possible explanation might be the shielding effect of the RF-electrodes (see section 2.3 on page 30) to be dependent on the azimuthal angle about the RF-axis due to non-perfect RF-electrode geometry, thus giving rise to a potential gradient in the associated direction.

Nevertheless, good working conditions were found at axial trap frequencies of about $2\pi \times 30$ kHz related to 210 V and 100 V applied to the ring electrodes $R_{3,1}$ and $R_{3,2}$ in chamber 3. To the ring electrodes $R_{1,1}$ and $R_{1,2}$ in chamber 1, 250 V were applied which led to an axial frequency of approximately $2\pi \times 50$ kHz. The radial frequency measured typically $2\pi \times 500$ kHz and could be determined with an accuracy of 1 kHz.

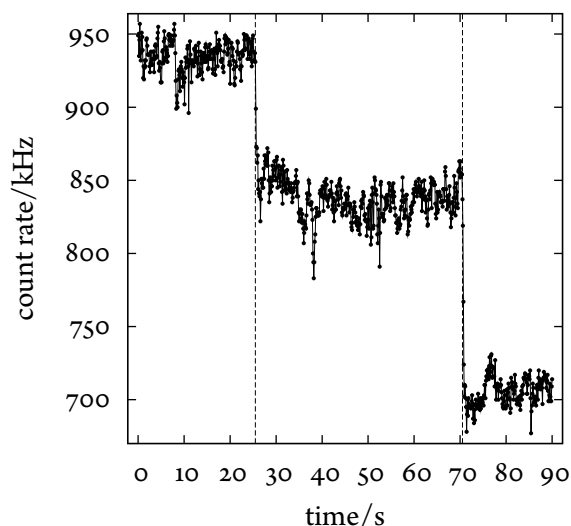


Figure 4.4.: Photomultiplier count rate (see section 2.6 on page 37) proportional to the flux of fluorescence photons emitted from $^{24}\text{Mg}^+$ ions in the trap of chamber 1. Hydrogen was injected for 5 ms at the indicated instants (dashed lines) when 16 % and 24 % of the atomic ions were converted into $^{24}\text{MgH}^+$. The stray light induced background count rate (no ions in the trap) was 320 kHz, each data point represents an accumulation time of 100 ms.

4.1.5. Molecular ion preparation

Preparing molecular ions for the $^{24}\text{MgH}^+$ time-resolved dissociation experiments has been straightforward. The photochemical reaction $^{24}\text{Mg}^+ + \text{H}_2 \rightarrow ^{24}\text{MgH}^+ + \text{H}$ occurs upon collisions of excited $^{24}\text{Mg}^+$ ions with molecular hydrogen. It has been studied intensively before; see [116], for example. It was sufficient to inject small amounts of hydrogen gas into chamber 1 while the atomic $^{24}\text{Mg}^+$ ions were excited as often as possible by irradiating them intensively (1.5 mW focused to a beam waist of $80\ \mu\text{m}$, $I \gg I_{\text{sat}} = 254\ \text{mW cm}^{-2}$) with near resonant (about half line width red detuned) cooling radiation. By that, the magnesium ions are close to half of the time in the excited state, cf. section 1.2 on page 12. The collision rate can be controlled by the amount of hydrogen gas injected into chamber 1. The pulsed valve (see section 2.1.1 on page 22) needed to be opened for 5 ms to 15 ms only. This kept the degradation of the vacuum conditions low and limited the pressure rise to a few 10^{-9} mbar for a period lasting less than 2 s. The hydrogen pressure in front of the pulsed valve was arranged to measure 0.3 mbar.

Figure 4.4 shows the PMT count rate during hydrogen injection and reveals that the fluorescence rate decreased suddenly after the pulsed valve had been opened. The fluorescence rate drops because a certain fraction of the $^{24}\text{Mg}^+$ ions is converted into non-fluorescing molecular ions. After about 250 ms the reaction stopped as abruptly as it started indicating fast pumping of the injected hydrogen gas.

4.2. Ion transfer

TIAMO's ability to transfer ions along a RF-guide from one ion trap to another—both in separated vacuum chambers—is pivotal. Since this feature might be of particular interest for the envisioned well controlled, repeated preparation of molecular ion targets for X-ray diffraction experiments, the currently realized ion transfer technique and the related limits were studied in experiment and theory. A summary of the results is presented in this section.

4. Experimental building blocks

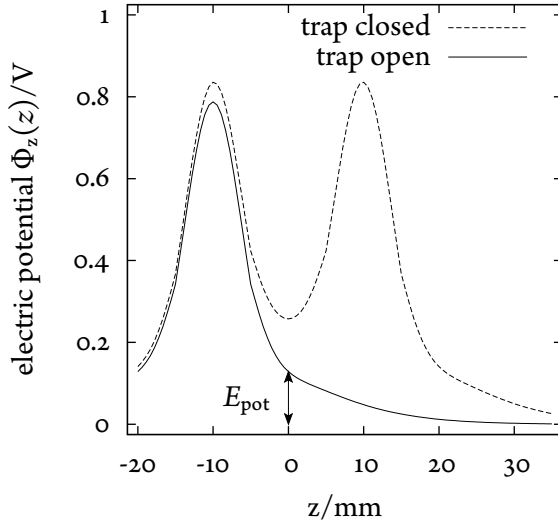


Figure 4.5.: Axial electric potential formed by a pair of ring electrodes in closed and open configuration of the ion trap. When a voltage of $U = 250$ V is applied to both ring electrodes, the trap is closed and ions are trapped. Setting one of the ring electrodes to electrical ground opens the trap, i. e. the electric potential gradient gives rise to an accelerating force on the ions that makes them leave the former trapping region. The ions' initial potential energy E_{pot} relevant for accelerating their center of mass equals the electric potential at the trap center at the instant when the ions begin to move.

Transferring ions in TIAMO is particularly convenient and efficient because the ion guide itself is also part of the ion traps, i. e. the ions stay in the same continuous electrode structure during the transfer. Trapped ions are currently accelerated by electric grounding (or sufficient lowering) the voltage applied to one of the ring electrodes that form the axial trapping potential; see section 2.3 on page 30. When the voltage has dropped by so much that the axial potential barrier cannot longer confine the ions, they are accelerated by the remaining potential slope. Switching the electrode voltages takes currently less than $1 \mu\text{s}$ [42]; see also section 2.8 on page 52. Figure 4.5 illustrates the axial potentials in trapping configuration (trap “closed”), and compares it to when one electrode has been switched off (trap “open”). The ions begin to leave the previous trapping region and escape along the the RF-guide. Their velocities during the acceleration phase are given in fig. 4.6 on the next page. See appendix A.3.2 on page 140 for a description of the software that was used for the simulations of this section.

The axial electric potential in the opened configuration defines the excess potential energy above electrical ground that is converted into kinetic energy. From the simulated axial potential (see section 2.3 on page 30) and the experimentally applied voltage to the ring electrodes in chamber 1 (250 V) one would deduce 129 meV excess energy. However, time of flight measurements revealed an average $^{24}\text{Mg}^+$ ion velocity of 1850 m s^{-1} corresponding to an energy of 425 meV. The discrepancy reveals that other contributions to the axial potential like that of the compensation electrodes cannot be neglected. Furthermore, it is assumed that the actual shielding effect of the RF-electrodes is different from the simulation; see fig. 2.10 on page 33. Deviations can be implied by deformations of the RF-electrodes in the trapping region. In order to correctly simulate the measured time of flight, the originally expected accelerating potential resulting from the ring electrode simulation had to be scaled by a factor of approximately three.

Three different scenarios to stop the ions' motion and trap them between the ring electrodes in chamber 3 after they had been accelerated and traveled 35 cm through the RF-guide are discussed in the following. Figure 4.7 on the facing page summarizes the differences between the methods by comparing the voltages applied to the involved ring electrodes.

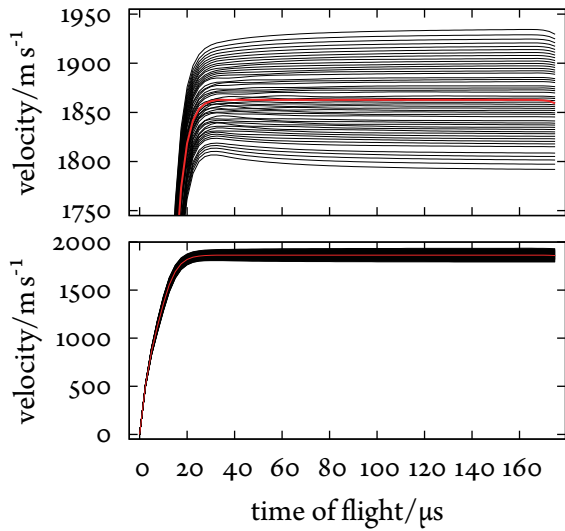


Figure 4.6.: Velocities of 55 ions, initially in a crystalline state, during the acceleration phase $0 \mu\text{s}$ to $20 \mu\text{s}$ after opening the trap in chamber 1 and the subsequent passage through the RF-guide to the traps in chamber 3. The center of mass velocity (single ion trajectory) is shown in red. The simulation (appendix A.3.2 on page 140) is adapted to the measured time of flight through 35 cm from chamber 1 to 3 along the RF-guide after acceleration by 250 V ring electrode voltages.

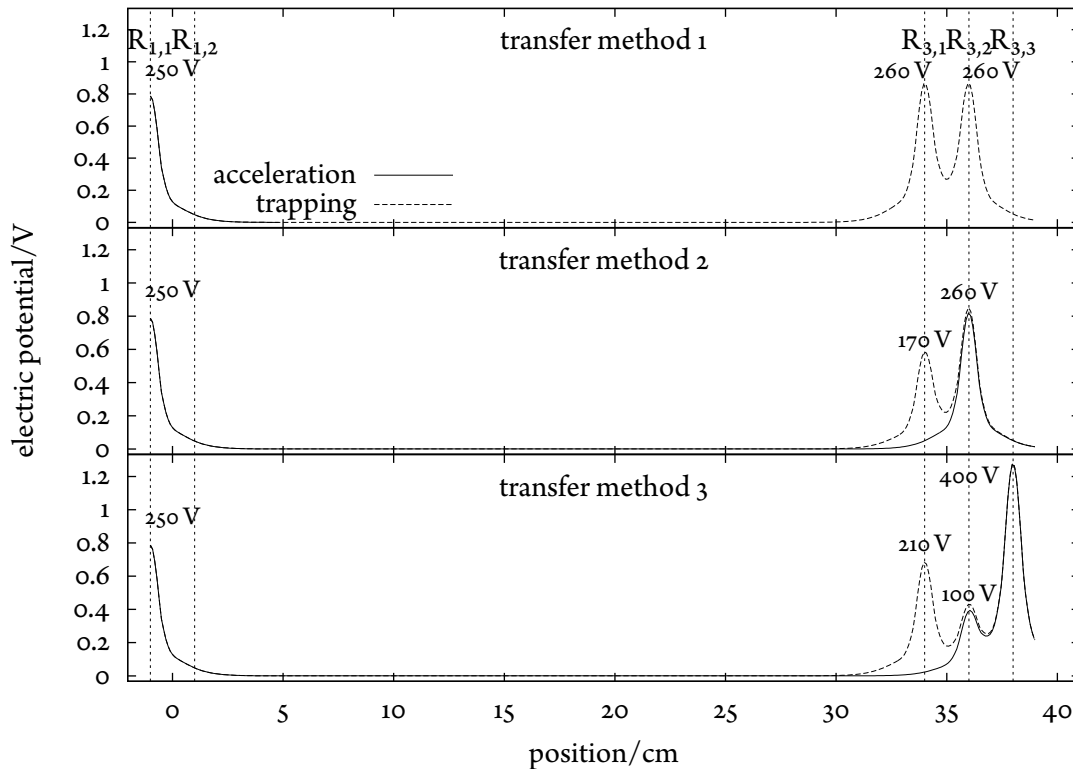


Figure 4.7.: Comparison of three different methods to stop and trap the accelerated ions at the end of the transfer process. The methods differ in when and which voltages applied to the ring electrodes $R_{3,1}$, $R_{3,2}$ and $R_{3,3}$ in chamber 3 (see fig. 2.1 on page 23) are switched. The accelerating potential of ring electrode $R_{1,1}$ in chamber 1 is the same for all three scenarios. Solid lines show the potentials used in the simulation (see appendix A.3.2 on page 140) during the acceleration phase, dashed lines during the trapping phase, dotted lines illustrate the position of the ring electrodes. In all cases, the axial electric potentials at the center of the RF-guide are shown, the shielding effect of the RF-electrodes has been taken into account; see section 2.3 on page 30.

4.2.1. Transfer method 1

The first method is characterized by switching the voltage applied to the first two initially grounded ring electrodes of chamber 3 ($R_{3,1}$ and $R_{3,2}$) simultaneously to 260 V right in the moment when the ions arrive. The last ring electrode in chamber 3 is grounded all the time.

Figure 4.8 on the next page illustrates the most important result of simulation and experiment: the efficiency of the shuttling process depends critically on the number of ions in the crystal. On the way through the RF-guide, the crystal is free in the axial direction, thus expands due to the Coulomb repulsion. The finite trap length in chamber 3 (ring electrode distance 20 mm) prevents to decelerate and trap all ions if the crystals contains more than some critical initial number of ions. The size of this number depends on the trap length, the time of flight and the initial crystal confinement; see below. If the ion structure is too long when it arrives at the trap in chamber 3, ions “standing out” of the trapping region will spill over either in forward or backward direction when the voltage to the ring electrodes is applied. One can think of the ring electrodes as knives, cutting a portion of the crystal that fits into the trapping region.

In this context it is important to investigate how the length of the ion ensemble in front of the trap in chamber 3 depends on the axial confinement in chamber 1. Figure 4.9 on page 80 presents simulation results aiming at this question. On the one hand, higher voltages applied to the ring electrodes of the trap in chamber 1 lead to initially stronger confinement in axial direction but also to more potential excess energy. Hence, the time of flight through the RF-guide should be shorter and the ions should have less time to separate. On the other hand, the Coulomb repulsion increases with stronger axial confinement and therefore should lead to a faster separation during the flight through the RF-guide. The simulation results show that within our parameters the former effect dominates. However, the increased Coulomb expansion indeed has a noticeable influence on the order of a few percent. This can be seen in the dependence of the length of the ion ensemble when it arrives at chamber 3 on the confinement in chamber 1. This dependence is different from the dependence of the time of flight on the confinement. A comparison of both quantities is presented in fig. 4.9 on page 80. The length of the ion structure has a polynomial dependence on the axial frequency with exponent -0.614, whereas the time of flight is inversely proportional to the square root of the axial frequency (exponent -0.5). Hence, the length cannot be explained with the time of flight solely. The initially higher Coulomb repulsion also needs to be taken into account. This shows additionally that there is in principal potential for improvement of the many ion shuttle efficiency of method 1 by further increasing the axial confinement in the trap of chamber 1.

There is another property connected to the previous result. The ions separate during their flight through the RF-guide because all of them travel at different and constantly changing velocities. Ions in the front are fastest because they are constantly pushed by the following ones. At the rear end the situation is inverse. The last ions are constantly decelerated by the ions heading them. How these velocities depend on the distance to the center of mass at the moment when the ions arrive at the trap in chamber 3 and how this depends on different initial axial confinements in the trap of chamber 1 is given in fig. 4.10 on page 80. One can describe the velocity distribution with a linear function. This linear relationship is universal in the sense that the velocity spread divided by the center of mass velocity does not depend on the axial trap frequency in chamber 1. Independent of

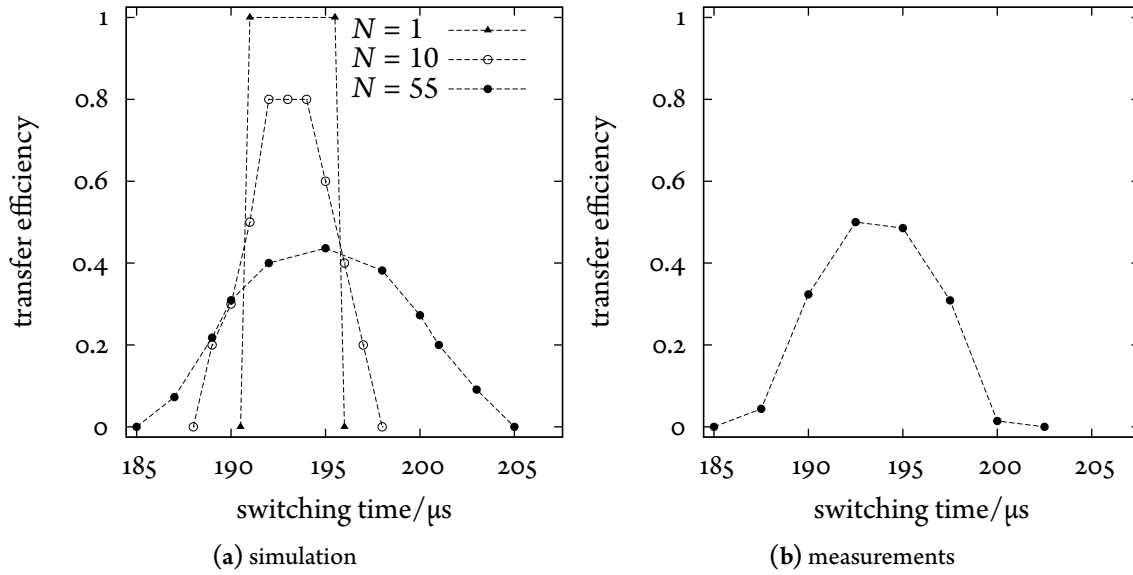


Figure 4.8.: Transfer efficiency of “method 1” (electrode voltages given in fig. 4.7 on page 77) as a function of the switching time of the voltage applied to electrodes $R_{3,1}$ and $R_{3,2}$ and the initial number of ions. The simulation (a) predicts a single ion to be transferred reliably within a $5 \mu\text{s}$ time window. For larger initial ion crystals ($N = 10$, $N = 55$), the transfer efficiency decreases because the Coulomb repulsion during the passage through the RF-guide leads to an extension of the ensemble in the axial direction. Figure (b) shows measurements under conditions that were comparable with those assumed in the simulation. The temporal width and shape of the data are in good agreement with the simulation of larger ($10 < N < 55$) initial number of ions. However, the absolute scale of the transfer efficiency includes big systematic errors ($\pm 15\%$). At the time of the measurement, the photomultiplier on chamber 1 did not allow to derive the exact number of initial ions but was used to load ion crystals of similar size based on the averaged fluorescence rate; see appendix B.4 on page 147.

the initial conditions, the velocity v after the flight through the RF-guide can be expressed with the help of the ion distance to the center of mass of the ion ensemble:

$$v(x) = 3.8 \cdot 10^{-3} \text{ mm}^{-1} (x - x_{\text{cm}}) v_{\text{cm}}.$$

Here, x_{cm} and v_{cm} denote the the center of mass position and velocity.

4.2.2. Transfer method 2

An alternative way to stop and trap the ions in chamber 3 is to sustain the voltage of ring electrode $R_{3,2}$ and ramp up only the voltage applied to the first ring electrode $R_{3,1}$ when the ions arrive. The related electric potentials are illustrated in fig. 4.7 on page 77. The main idea is to reflect the ions at the electric potential hill generated by $R_{3,2}$ before the trap is closed by switching the voltage applied to $R_{3,1}$. During the time it takes the ions to decelerate and accelerate again in the opposite

4. Experimental building blocks

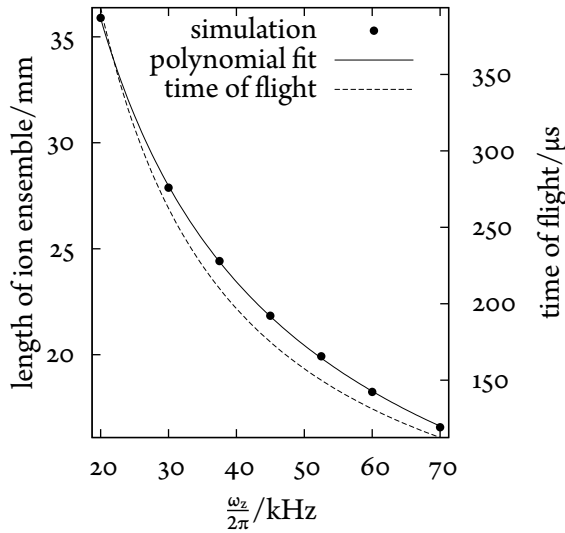


Figure 4.9.: Simulated dependence of the distance between first and last ion (solid line) and time of flight to the trap in chamber 3 (dashed line) on the axial trap frequency ω_z in chamber 1 for 55 initial ions. Higher voltages applied to $R_{1,1}$ and $R_{1,2}$ increase the electrostatic Coulomb repulsion between ions and their potential energy with respect to electric ground resulting in higher velocities and faster extension of the ensemble during the shuttle process. The time of flight is proportional to $\omega_z^{-0.5}$, the length of the ensemble to $\omega_z^{-0.614}$.

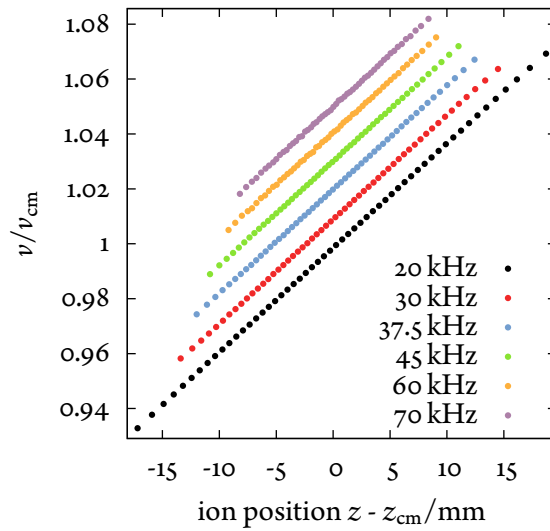


Figure 4.10.: Simulation of velocities of individual ions in front of the electric reach of electrode $R_{3,1}$ after having been transferred 26.7 cm along the RF-guide. The velocities are shown in units of the center of mass velocity v_{cm} of the ion ensemble. The velocity ratio depends linearly on the ion distance to the center of mass z_{cm} . This linear relationship does not depend on the initial axial confinement in chamber 1. In order to enhance the visibility, the graphs of the velocity distributions related to $\omega_z/2\pi = 30$ kHz to 70 kHz are shifted in steps of 0.01.

direction, they bunch in the trapping region. The increased ion density increases also the number of trappable ions. Because the ions pass the trapping region almost twice, the temporal *collection interval* is prolonged. Therefore, almost twice as many ions can be caught in the trapping region which increases the ion transfer efficiency.

The trap in chamber 3 is closed, i. e. a sufficiently high voltage is applied to $R_{3,1}$, ideally at the instant when the last ions of the ensemble are just about to enter the trapping region while the first transferred ions have been reflected and are about to leave the trap again. A diagram illustrating the influence of the switching time on the transfer efficiency can be found in fig. 4.11 on the facing page. It distinguishes between ions that are trapped and those that are lost. Depending on the moment of ramping up the voltage applied to $R_{3,1}$ not-trapped ions are reflected in forward or backward direction. Ions that are close to electrode $R_{3,1}$ but outside the trapping region when the voltage is ramped up are rapidly accelerated in the backward direction. The Coulomb force in the vicinity of

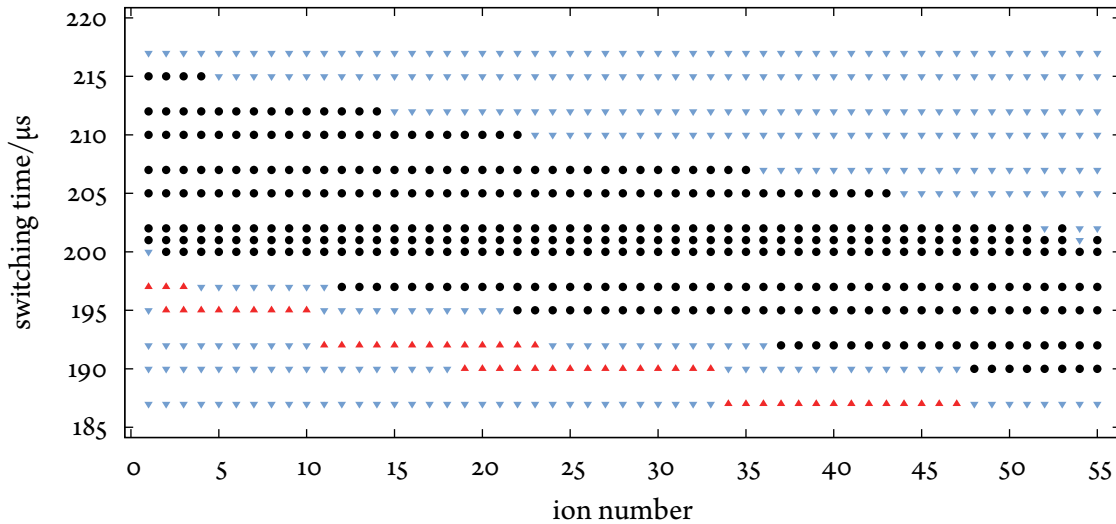


Figure 4.11.: Ion transfer losses of “method 2” depending on the switching time of the voltage applied to electrode $R_{3,1}$. The ions are depicted as symbols along a line according to their ordering at the moment of arrival at the trapping region. Ions at the right arrive first. Circles (black) denote trapped ions, upside down triangles (blue) denote ions that are reflected back into the RF-guide, upright triangles (red) denote ions that are pushed over the ring electrode $R_{3,2}$ and thus leave the trapping region in forward direction; see the text for details. At the optimum switching time $200 \mu\text{s}$ all but the last ion are successfully trapped after the transfer.

$R_{3,1}$ is strong enough that ions inside the trapping region can be pushed over the potential hill of the adjacent ring electrode $R_{3,2}$ and thereby leave the trap in forward direction.

The major improvement of “method 2” compared with “method 1” is the higher efficiency of successfully transferring and subsequently trapping ensemble of many ions. The time window of lossless transfer of single ions is expected to be extended by a factor of two. Simulation results corresponding to realistic experimental conditions are presented in fig. 4.12 on the next page. They predict that only one out of $N = 55$ ions is lost after the transfer process. This must be compared with “method 1” that allowed only 40 % of the same initial number of ions to be re-collected. Although the uncertainty of the photon count rate of the photomultiplier used in chamber 1 (see appendix B.4 on page 147) did not allow a precise measurement of the absolute transfer efficiency, the trend seen in the simulation is confirmed by the experiment. Using “method 2”, ion crystals of approximately the same size were transferred with 80 % efficiency while using “method 1” allowed only for 50 %. It shall be emphasized that the losses are expected to be caused by the large number of ions simultaneously transferred only. Single ions can be assumed to be reliably transferred.

4.2.3. Transfer method 3

In order to provide the required number of atomic and molecular ions repeatedly and with high efficiency for the femtosecond pump-probe experiments (see chapter 5 on page 95) a third method was developed. It further increases the efficiency of “method 2” by making use of the additional

4. Experimental building blocks

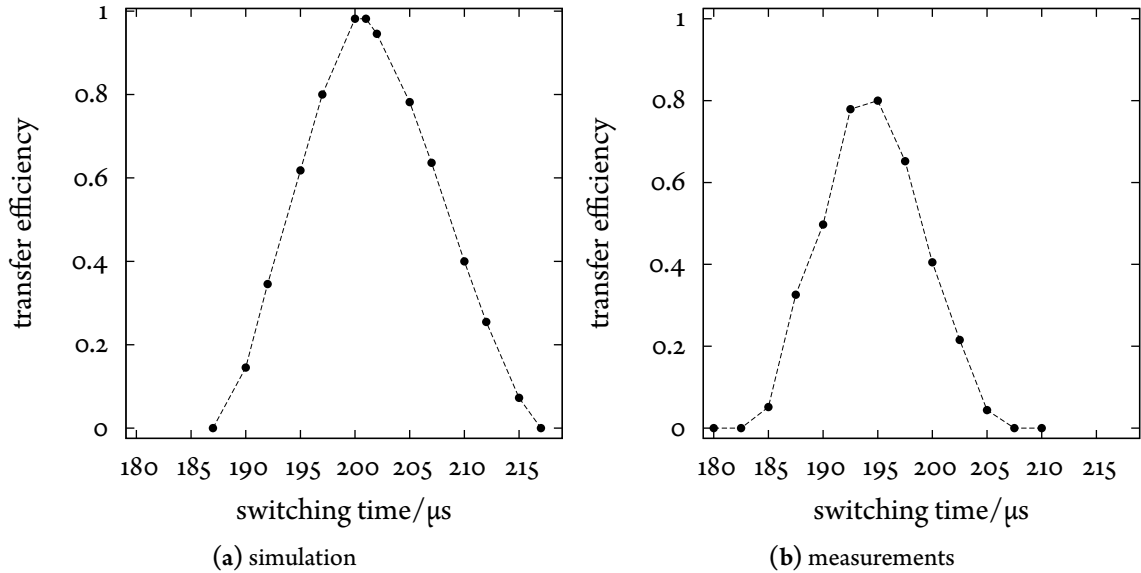


Figure 4.12.: Transfer efficiency of “method 2” (electrode voltages given in fig. 4.7 on page 77) as a function of the switching time (time of flight of the ion ensemble) of the voltage applied to electrode $R_{3,1}$. The simulation (a) shows the transfer efficiency for an ion crystal containing 55 ions. All but one ion are successfully trapped after the transfer through the RF-guide. In comparison with “method 1” (fig. 4.8a on page 79), the interval during which ions are successfully decelerated and trapped is extended, the transfer efficiency is higher, and the ideal switching time occurs 6 μs later. In the experiment (b) comparably sized ion crystals as in the simulation were used. The trends of the simulation were confirmed qualitatively: the total transfer efficiency and width of the trapping time window are increased in comparison with the transfer experiments using “method 1”; see fig. 4.8b on page 79. Discrepancies between (a) and (b) at the quantitative level are attributed to uncertainties about the exact shape of the axial electric potential and errors in preparing ion crystals of equal size based on the average fluorescence rate detected by a photomultiplier on chamber 1; see appendix B.4 on page 147. The experimental *single ion* transfer efficiency can be assumed to be close to 100 %.

ring electrode $R_{3,3}$; see fig. 2.1 on page 23. The voltages applied to $R_{3,3}$ (400 V) and the electrode $R_{3,2}$ (100 V) are kept constant at all times during the transfer process. The voltage applied to the first electrode $R_{3,1}$ is switched from electrical ground to 210 V in the ideal moment when the ions have arrived in the trapping region. The high electric potential hill generated by $R_{3,3}$ reflects the ions and prevents them from leaving the trap in forward direction. The voltage applied to $R_{3,1}$ is sufficiently high to hinder ions being pushed out of the trap in backward direction. Refer to fig. 4.7 on page 77 for a summary of the electric potentials.

In order to illustrate the deceleration of the ions before closing the trap, and the subsequent impetuous motion inside the trapping potential in more detail, relevant quantities extracted from the simulation are assorted in fig. 4.13 on page 85. Shortly after closing the trap, the length of the transferred ion ensemble is shorter than the axial trap length. Thus, the center of mass of all ions in the ensemble moves like a single particle would do. However, at least two effects lead to dephasing of the individual ions' motion. One of which is dephasing of particles with differing energies in the anharmonic (double-well) potential. The other is dephasing caused by elastic Coulomb collisions. These collisions occur latest when the first ions have been reflected at the potential barrier generated by electrode $R_{3,3}$ and subsequently propagate opposite to the rest of the ensemble. When the Coulomb repulsion between the ions will have increased the ensemble length to the length of the trapping potential, collisions at both turning points will occur. The collision rate will further grow until an equilibrium state is reached. Figure 4.7 on page 77 illustrates how the initial oscillatory motion of the center of mass of all ions is damped after a few oscillations in the combined double-well trapping potential. From a thermodynamic point of view, according to the second law of thermodynamics $\Delta S \geq 0$, a closed system is in the equilibrium state if its entropy S is maximal. Since the axially ordered ensemble of ions oscillating in phase directly after closing the trap is a highly unlikely configuration of particles with high energy, the anharmonicity of the trap and elastic Coulomb collisions will rapidly increase the phase space volume, i. e. the associated entropy, of the system and steer it into the state of maximal entropy. After only a few 100 μs the individual axial velocities of the ions are homogeneously and symmetrical dispersed about zero. The center of mass comes to standstill. The individual ions oscillate still fast but completely dephased until laser cooling is applied and decreases the entropy again; see section 1.2 on page 12.

According to the simulation results presented in fig. 4.14 on page 86, "method 3" is superior by its transfer efficiency. This is firstly due to the twice as long effective trap length formed by the three ring electrode configuration and secondly to the avoided loss of ions in forward direction by closing the trap via electrode $R_{3,1}$ as discussed for "method 2". The electric potential of the middle ring electrode can be overcome by fast ions. By that, ions are constantly exchanged between the two potential wells formed in chamber 3 (see fig. 4.7 on page 77)—a behavior that is observed concordantly in the simulation and in the experiment. Of course, the exchange is only possible as long as the kinetic energy of the ions stays sufficiently high. Simultaneous laser cooling reduces the ions' motional energy until the number of ions trapped in the two axial potential wells stays constant. Cooling all transferred ions to the crystalline state took normally a few seconds. When the cooling laser power was reduced below the minimum ($< 50 \mu\text{W}$) value used during the femtosecond pump-probe experiment, the time until all ions were re-crystallized again amounts to 10 s to 20 s. This comparably long cooling time is due to the near-resonant (about one natural line width Γ

4. Experimental building blocks

red detuned) cooling laser that appears far off-resonant in the co-moving frame of a fast ion; see section 1.2 on page 12. Detuning the cooling laser frequency further to the red of the resonance or even scanning it constantly over several hundred MHz has the potential to reduce the cooling time significantly. Due to time constraints during the measurement, it was opted for a few seconds longer cooling time instead of readjusting the laser frequency in the distant laser laboratory repeatedly; see section 2.7.1 on page 42.

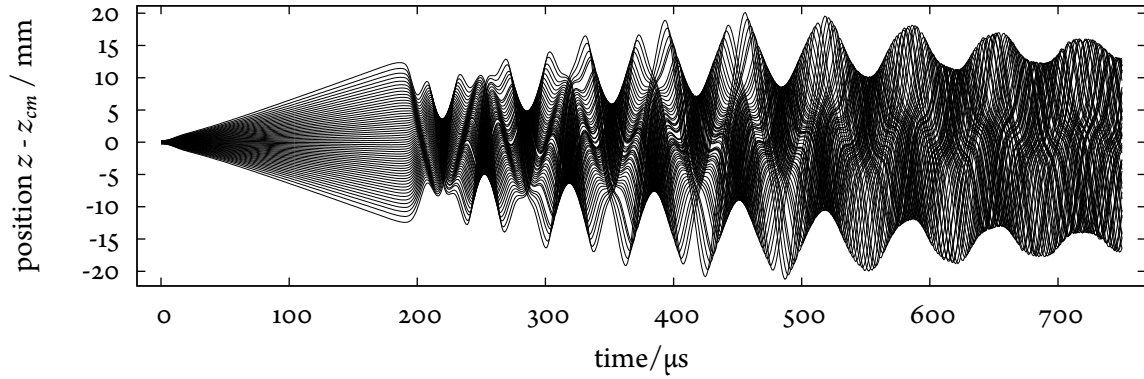
Without laser cooling, the simulation predicts equal population of the two traps formed by the electrodes $R_{3,1}$ - $R_{3,2}$ and $R_{3,2}$ - $R_{3,3}$. In which trap the ions gather preferentially after they were cooled down to the crystalline state is strongly dependent on the intensity and alignment of the cooling laser beam but also on the exact electric potential landscape influenced by RF-electrodes, ring electrodes, compensation electrodes, and stray fields induced by, for instance, charged surfaces close to the ions. Because the cooling laser beam is aligned almost perfectly with the symmetry axis of the RF-guide, the beam overlap with a hot ion cloud (the situation directly after closing the trap, see above) does not differ substantially between the two traps of chamber 3. However, a small deviation of the beam axis from the RF-axis of the guide becomes noticeable in the crystalline state of the ions, when the transversal spatial width of the ion crystal shrinks to a few micrometers. The overlap of the cooling laser with the trap center and the crystallized ions at this position will be better for one of the two traps. Fast ions overcome the separating electric potential at $R_{3,2}$ until they gather preferentially in the trap with “better” laser cooling conditions. Besides the geometric overlap, the efficiency of the cooling conditions depends also on the laser detuning from the atomic transition, the power broadening given by the intensity of the cooling light and the Doppler shift caused by the motion of the ions; see section 1.2 on page 12.

a. ion swapping

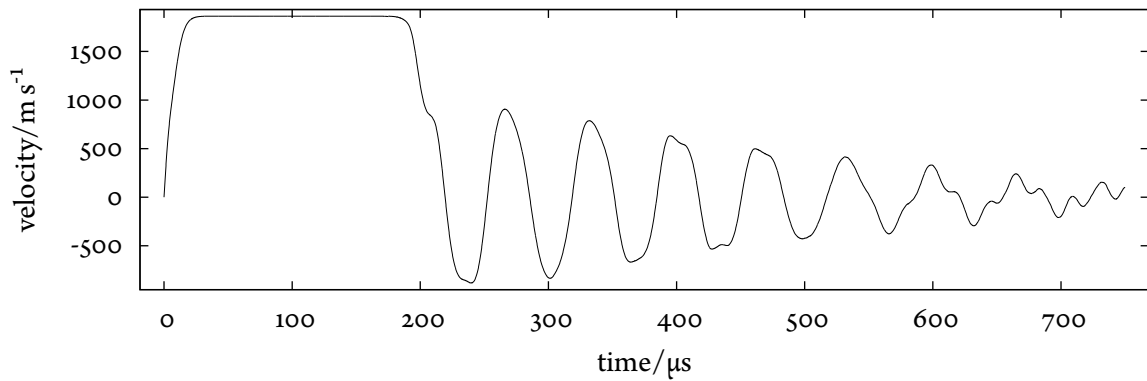
The term *swapping* refers to the exchange of crystalline ion structures along the RF-guide between the two traps formed by the ring electrodes $R_{3,1}$ - $R_{3,2}$ and $R_{3,2}$ - $R_{3,3}$ in chamber 3; see fig. 2.1 on page 23. Since both traps share the ring electrode $R_{3,2}$, ions can be exchanged by lowering the voltage of $R_{3,2}$ sufficiently (for example setting it to electrical ground) for approximately 25 μ s and restore the voltage afterwards.

An ion crystal trapped in one of the two traps has considerably less time to expand in that short amount of time compared with the transfer from chamber 1 and 3; cf. fig. 4.13a on the next page. Hence, cooling the ions to the crystalline state after the transfer has been accomplished was much quicker compared to cooling ions that were transferred from chamber 1; cf. section 4.2.3 on page 81. In some cases, the ions were cooled so efficiently that no change in the fluorescence video signal of the crystal was visible, indicating that the crystalline state was either preserved or reestablished in less than the CCD's 100 ms exposure time; see appendix A.1.2 on page 127.

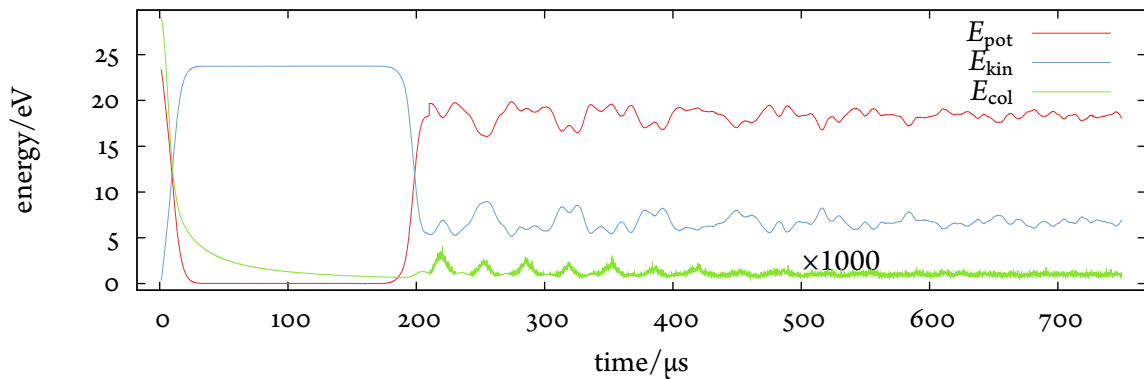
It is possible to swap the identical ion crystal forty times without loss of any ion. Furthermore, it was observed that two separate ion crystals trapped in the two adjacent traps simultaneously can be interchanged, i. e. having the two crystals traveling in opposite directions. At the middle ring electrode $R_{3,2}$ both crystals meet but they seem to interact weakly enough so as not to noticeably influence each others motion or even cause mixing of ions.



(a) Ion positions relative to the center of mass of the ensemble. The ensemble first expands during the flight through the RF-guide. After closing the trap, the ions oscillate at first with given phase relations, later chaotically.



(b) The center of mass motion gets damped after a few oscillations in the double-well axial potential. The two major sources of dephasing of the individual ions' oscillation are anharmonicity of the potential and elastic collisions.



(c) Total kinetic, potential, and Coulomb interaction energy of all ions as function of time. The initial electrostatic potential energy accelerates the center of mass of all ions. The Coulomb interaction energy leads to increasing inter-ion distances. After trapping the ions, the energy forms are interchanged until an equilibrium state is reached when $E_{\text{pot}} \approx 2.7E_{\text{kin}}$. The graph showing the Coulomb energy is scaled by 1000 for better visibility.

Figure 4.13.: Simulation results of the ion transfer of 55 ions by “method 3” during the acceleration phase (0 μs to 20 μs), the propagation phase through the RF-guide (until 190 μs), and after closing the trap by applying a voltage of 210 V to the ring electrode $R_{3,1}$; see fig. 4.7 on page 77.

4. Experimental building blocks

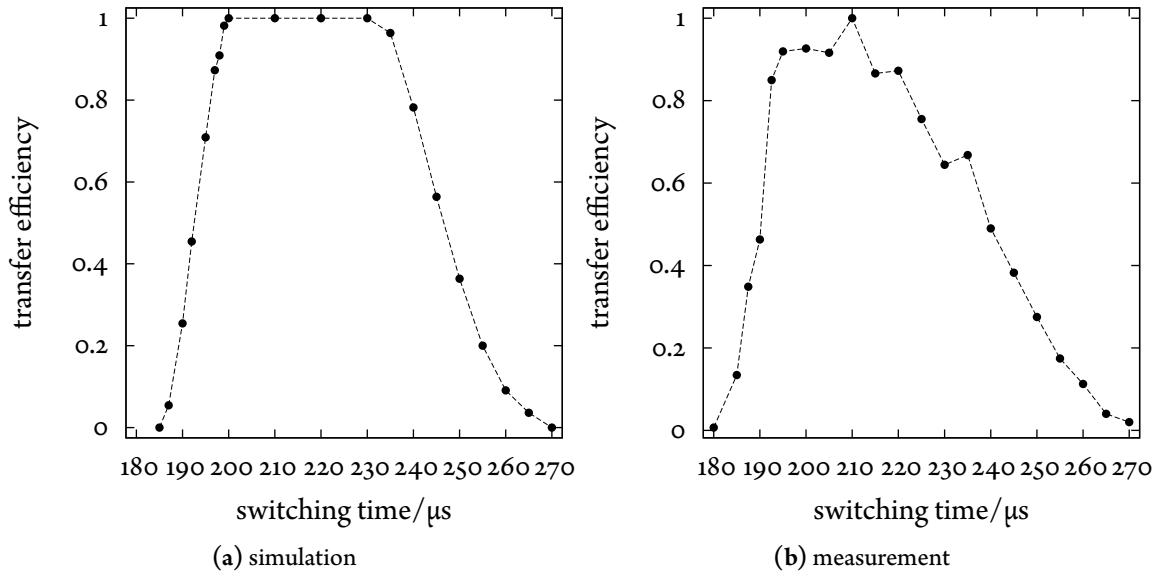


Figure 4.14.: Transfer efficiency of “method 3” (electrode voltages given in fig. 4.7 on page 77) as a function of the switching time (time of flight of the ion ensemble) of the voltage applied to electrode $R_{3,1}$. The simulation (a) predicts the transfer efficiency for an ion crystal containing 55 ions. For a 30 μs long time window it reaches 100 %. The leading edge of this time window is steeper than the trailing edge. The measurements (b) were performed with Coulomb crystals containing approximately the number of ions assumed in the simulation. The measurements confirm the duration of the time window of high transfer efficiency and the asymmetric shape qualitatively. Differences between simulation and experiment at the quantitative level are attributed to uncertainties about the exact electric potential landscape which depends also on sources not considered in the simulation, for example the compensation electrodes and parasitic charges on nearby insulating surfaces. Additionally, the absolute scale of the measured data includes systematic uncertainties ($\pm 15\%$) related to the loading of ion crystals of similar size by evaluating the fluorescence rate using a photomultiplier at chamber 1 at the time of the experiment. Calibration of the fluorescence rate on independently recorded fluorescence images with single particle resolution indicates close to 100 % transfer efficiency in the interval between 195 μs and 220 μs .

A procedure similar to “swapping” allowed to redistribute the ions over the two traps in chamber 3. To this end, the voltage applied to the ring electrode $R_{3,2}$ was reduced for an amount of time different from the value that is optimal ($25 \mu\text{s}$) for interchanging ions. For example, switching the voltage of $R_{3,2}$ just when the ions “swing” through it leads to strong forces on the ions. The crystal structure is torn apart, the ions are accelerated and begin to oscillate through the combined trapping potential similar to the situation described in section 4.2.3 on page 81. The ions therefore distribute randomly and can be cooled again to the crystalline state containing a possibly different number of ions depending on, e. g., the cooling laser power. If switching the voltage applied to $R_{3,2}$ is delayed with respect to the optimum value $25 \mu\text{s}$, the crystalline structure is less distorted. It was observed that the distribution of ions over the two traps could indeed be controlled to some degree by varying the switching time. It was even possible to make most of the ions ($\approx 90\%$) in chamber 3 gather in only one of the traps. Subsequently, the ions could be transferred into the trap of choice by applying the optimal $25 \mu\text{s}$ voltage ramp.

Based on these observations it is expected that continuous loading of ions is feasible with the present or a similar electrode setup. It is envisioned that ions will be transferred to the first trap in chamber 3 by “methode 2”. The ions in the second trap of chamber 3 remain influenced. They can be manipulated separately and simultaneously. If these ions need to be replaced for some reason, they might be first dismissed and subsequently spare ions from the first trap of chamber 3 will be handed over. In parallel to the last step, a new ion might be transferred from chamber 1 to chamber 3.

Molecular ions must be sympathetically cooled. In order to detect the molecular ion as a dark spot in an otherwise fluorescing Coulomb crystal, it must be allowed to interact sufficiently long with the laser cooled atomic ions (already present in the trap) and thereby reduce its motional energy. It is expected that optimized, time-dependent voltage ramps used to open and close the traps for the transfer will reduce the excess kinetic energy of transferred ions and therefore also the required sympathetic cooling time. It is the goal of our group to realize a replacement of molecular ions at a repetition rate on the order of 100 Hz.

4.3. Photochemical reactions induced by the cooling laser

During the preparation of the femtosecond pump-probe dissociation experiment, it has been observed that trapped molecular ions disappeared with a small rate. They were seemingly lost despite stable trapping conditions and uninterrupted laser cooling of the atomic $^{24}\text{Mg}^+$ ions in the Coulomb crystal. It is unlikely that those ions escaped due to collisions with the background gas. First of all because these collisions are rare at a vacuum pressure of $2 \cdot 10^{-10}$ mbar, occurring on the minute time scale, and secondly, because the trap depth of about 1 eV (see section 1.1 on page 7) is too deep to be overcome by ions moving at velocities corresponding to a room-temperature thermal energy distribution (≈ 25 meV).

An explanation might be events of the photochemical reaction $^{24}\text{Mg}^+ + \text{H}_2 \rightleftharpoons ^{24}\text{MgH}^+ + \text{H}$ [116] triggered by the cooling laser. This assumption is supported by the additional observation that the number of atomic $^{24}\text{Mg}^+$ ions increased over time. To the present understanding, it is most

4. Experimental building blocks

likely that events in the two cooling laser induced dissociation reactions $^{24}\text{MgH}^+ \rightarrow ^{24}\text{Mg}^+ + \text{H}$ and $^{24}\text{MgH}^+ \rightarrow ^{24}\text{Mg} + \text{H}^+$ were observed.

The former reaction dissociates the molecular ion into $^{24}\text{Mg}^+$ and a hydrogen atom resulting in one additional fluorescing ion in the trap at the expense of one (dark) molecular ion. The latter reaction leads to a loss of one ion from the trap since neither of the two product particles is trapped; see also fig. 5.1 on page 97. The magnesium atom is not trapped because it carries no electric charge, the proton H^+ is not trapped because of its low mass and the related stability parameter q (see section 1.2 on page 12) lying outside the stable trapping region of the stability diagram; see section 1.1 on page 7. Thus, there are assumed to be in total three competing photochemical reactions driven by the cooling laser. Despite the small reaction rate, these rare events were of uttermost importance since the time-resolved experiments (see chapter 5 on page 95) spotted on the very same dissociation reactions. Any parasitic contribution to the femtosecond pump-probe dissociation by cooling laser induced events implies systematic errors.

To investigate this phenomenon more quantitatively, ion crystals containing different fractions of molecular ions were observed in five experiments over periods between one and three hours. These experiments were performed at low pressure ($2 \cdot 10^{-10}$ mbar) and reduced cooling laser power. The power was set to just provide the cooling required to sustain the crystalline structure and therefore being similar to the settings used in the time-resolved experiments. The fluorescence of the crystals was continuously monitored to guarantee uninterrupted laser cooling and also otherwise constant conditions. During the course of the experiments, the numbers of atomic and molecular ions were recorded. The result of these measurements are presented in fig. 4.15 on the facing page together with a simulation based on rate equations.

The model was set out to reproduce the measured course of all five experiments with the same set of rates. In principal, the reasoning about stochastic fluctuations of appendix C.1.1 on page 155 applies also here, since the observation is based on a few statistical events of a few-particle ensemble. An accurate determination of the reaction rates would either require many more measurements of the above kind or a much larger amount of molecular ions in one dedicated experiment. Because the experiments within this thesis are based on single particle targets, a rough estimation of the reaction rates was appropriate and sufficient.

The rate equations modeling the time-dependent expectation value of the fractions of atomic (n_{atom}) and molecular (n_{mol}) ions in a Coulomb crystal under the influence of the three mentioned cooling laser induced photochemical reactions read

$$\begin{aligned}\frac{dn_{\text{atom}}}{dt} &= -k_1 n_{\text{atom}} + k_2 n_{\text{mol}}, \\ \frac{dn_{\text{mol}}}{dt} &= k_1 n_{\text{atom}} - k_2 n_{\text{mol}} - k_3 n_{\text{mol}}.\end{aligned}$$

Here, rate k_1 describes the reaction constant at which an atomic $^{24}\text{Mg}^+$ ion is converted into a molecular $^{24}\text{MgH}^+$. k_2 gives the rate of the reaction running backwards, and k_3 describes the loss of molecular ions due to the dissociation into a neutral magnesium atom and a proton. The limited number of experiments cause big uncertainties ($\pm 20\%$) of the rates: $k_1 = 0.13 \text{ h}^{-1}$, $k_2 = 0.79 \text{ h}^{-1}$,

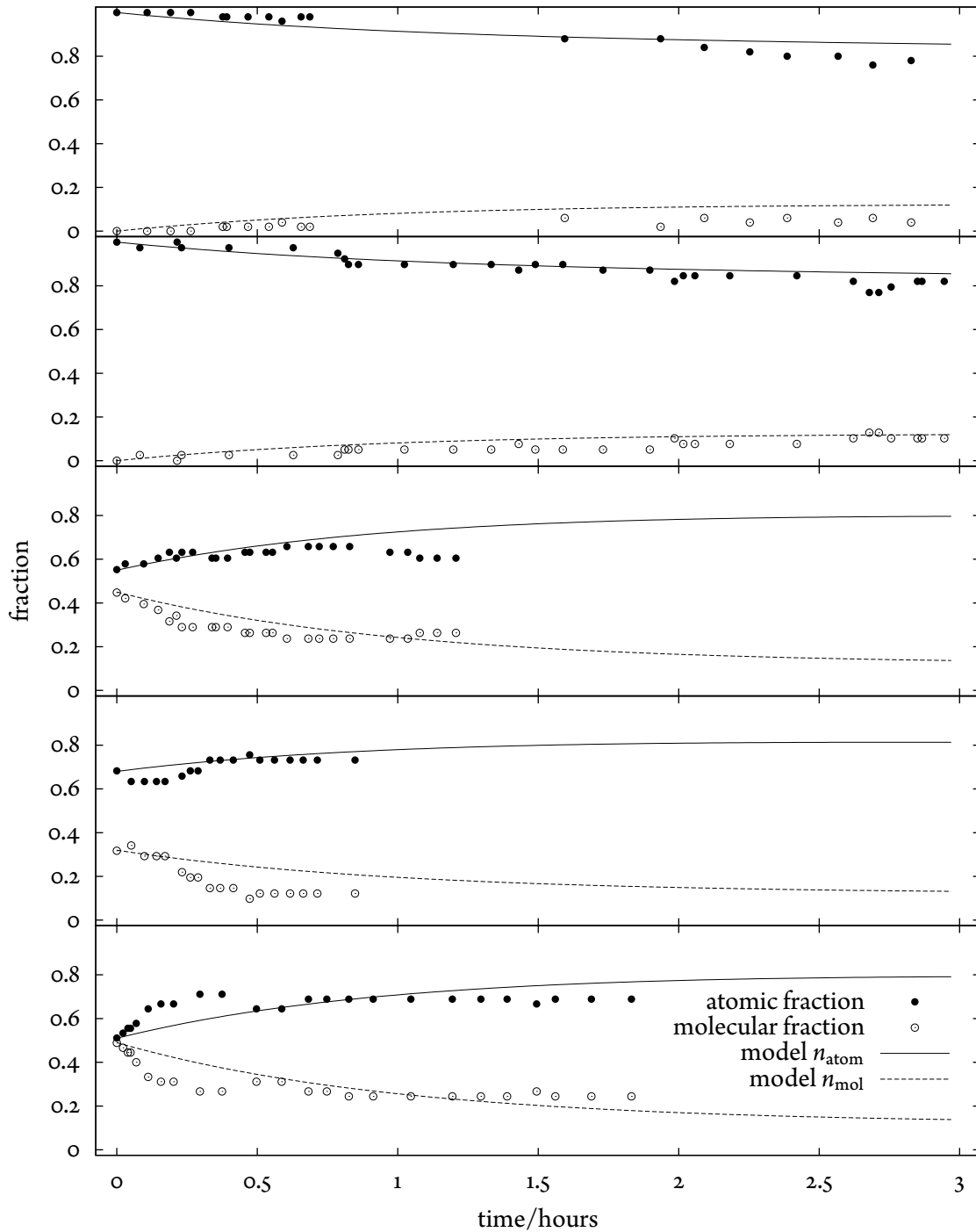


Figure 4.15.: Bright (atomic $^{24}\text{Mg}^+$) and dark (molecular $^{24}\text{MgH}^+$) ion composition of five Coulomb crystals under minimal laser cooling irradiation and good vacuum conditions of about $2 \cdot 10^{-10}$ mbar observed over an extended period of time. The composition of bright and dark ions was extracted from fluorescence images (see appendix A.2.3 on page 135) and plotted as function of time. The respective fractions according to a rate equation model are shown as solid and dashed lines. Deviations from the model are attributed to the stochastic nature of the process; cf. appendix C.1.1 on page 155.

and $k_3 = 0.10 \text{ h}^{-1}$. These values are valid for the aforementioned experimental conditions at low pressure and cooling laser intensity.

It may be summarized, that all relevant reactions occur on a many minute time scale. This is reconcilable with the duration (1 min to 4 min) of a typical time-resolved dissociation experiment. During that time, the number of cooling laser induced reaction events is still negligible. Nevertheless, a minute parasitic contribution on the few-percent level cannot be excluded. Our observations are consistent with the experiments reported in [163]. There, photochemical reactions in the absence of other excitations except of laser cooling have been observed, but with an irrelevant small rate on the time-scale of the experiment duration (several minutes) [43]. The cooling laser driven dissociation probability of molecular ions in an excited rovibronic state, after, e. g., excitation by a femtosecond UV laser pulse, was not studied. However, these dissociation events are expected to be even more seldom due to the short electronic state life time (few nanoseconds for $^{24}\text{MgH}^+$).

4.4. Third harmonic generation

This section reviews the experimental adaption of the performance and parameters of the femtosecond laser system (see section 3.1 on page 55) and the third harmonic generation setup (see section 3.2 on page 58) to the requirements of the molecular $^{24}\text{MgH}^+$ ions that were investigated in the proof-of-method pump-probe experiments; see chapter 5 on page 95.

There are two major constraints on the UV pulses: the targeted temporal resolution requires them to be short ($\leq 5 \text{ fs}$) and the spectrum should not extend substantially below 255 nm. The latter constraint derives from the requirement to control the excitation of single electronic states selectively in $^{24}\text{MgH}^+$ and is further discussed in section 5.1.2 on page 101. Whereas the aspired shortness of the UV pulses had been verified before [70], the corresponding spectrum of the pulses used for those measurements did not meet our requirements. The spectrum of the third harmonic UV pulses regularly generated at the AS4B beam line is normally centered at 245 nm [18, 19], i. e. much too energetic for the aspired experiments.

Fortunately, the complexity of the femtosecond laser system offers a variety of adjustable parameters that we used to shift the spectrum of the pulses to longer wavelength; see section 3.1 on page 55. For example, the spectral broadening in the hollow core fiber (HCF) can be controlled by the neon gas pressure and the input pulse duration. Figure 4.16 on the next page compares the UV spectrum and energy content of the pulses behind the neon gas target for third harmonic generation as a function of the neon pressure in the HCF. The most preferential pressure regime is between 1.8 bar and 2.1 bar where the UV spectrum shifts by 15 nm to 20 nm towards longer wavelengths at the expense of an acceptable drop in pulse energy. Further tuning of the spectrum was achieved by translating one of the prisms of the prism compressor after the amplifier stage perpendicular to the pulsed beam. This changes the path length through the dispersive medium of the prism apex and can be used to control the spectral phase and thereby the pulse duration in front of the HCF. Translating the HCF relative to the input beam influenced the transmittance as well as the beam profile and divergence of the output beam which in turn had an influence on the spectrum and pulse energy of the third harmonic pulses. The dispersion management wedges behind the HCF were used as

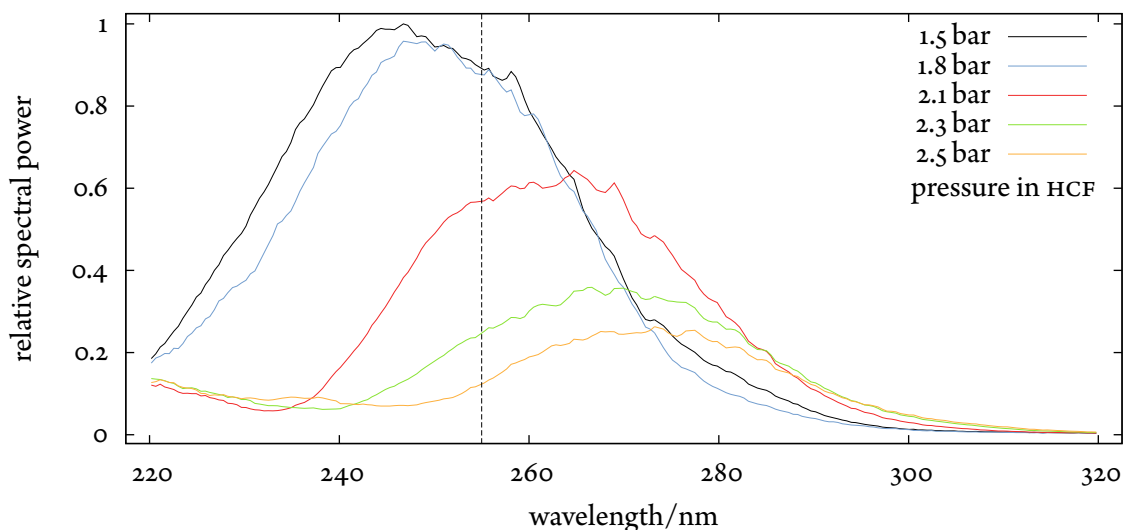


Figure 4.16.: Shifting the third harmonic spectrum to the red: measurements after the gas target (neon 4 bar) and two reflections on silicon substrates (omitted in the final experiments, see text) recorded with a fiber coupled spectrometer (MayaPro, Ocean Optics) as a function of the neon pressure inside the hollow core fiber (HCF); see section 3.1 on page 55 are shown. At higher pressures, the spectrum is shifted to longer wavelengths at the expense of pulse energy. The latter can only be partially compensated by adjusting the driver laser pulse intensity in the gas target and the pulse duration by optimizing the dispersion management of the beam line. The dashed line at 255 nm indicates the short wavelength limit for the time-resolved $^{24}\text{MgH}^+$ dissociation experiments; see section 5.1 on page 95.

still another accessible element for spectral adjustments. The two thin wedges are mounted such that they complement each other similar to a plane parallel plate. By translating one of the wedges relative to the other, the thickness of the “plate” and therefore the dispersion experienced by the pulses can be controlled. To fully adapt the femtosecond laser system to the requirements of the experiments on $^{24}\text{MgH}^+$, the system’s 3 kHz repetition rate was reduced by blocking a predetermined number of pulses by a mechanical shutter as explicated in detail in section 5.2 on page 103.

The maximal spectral shift that could be achieved with the mentioned tuning elements was not sufficient to suppress wavelength shorter than 260 nm. This is why customized dielectric mirrors (cf. section 3.3 on page 60) had to replace broad band reflecting aluminum mirrors in the beam path. They are designed to filter the blue fraction of the UV spectrum. They also offer higher reflectivity in the desired UV spectral range compared with the metallic mirrors. In addition, the dielectric mirrors allow to separate the UV pulses from the infrared background of the fundamental beam due to their dichroic reflectivity; cf. also fig. 3.6 on page 63. The spectral filtering success of these mirrors in a real femtosecond application is demonstrated in fig. 4.17 on the next page that compares the influence of two and three such reflections.

In order to measure the pulse energy right after third harmonic generation but before spectral filtering, an aluminum mirror could be translated into the beam path and reflect the pulses through

4. Experimental building blocks

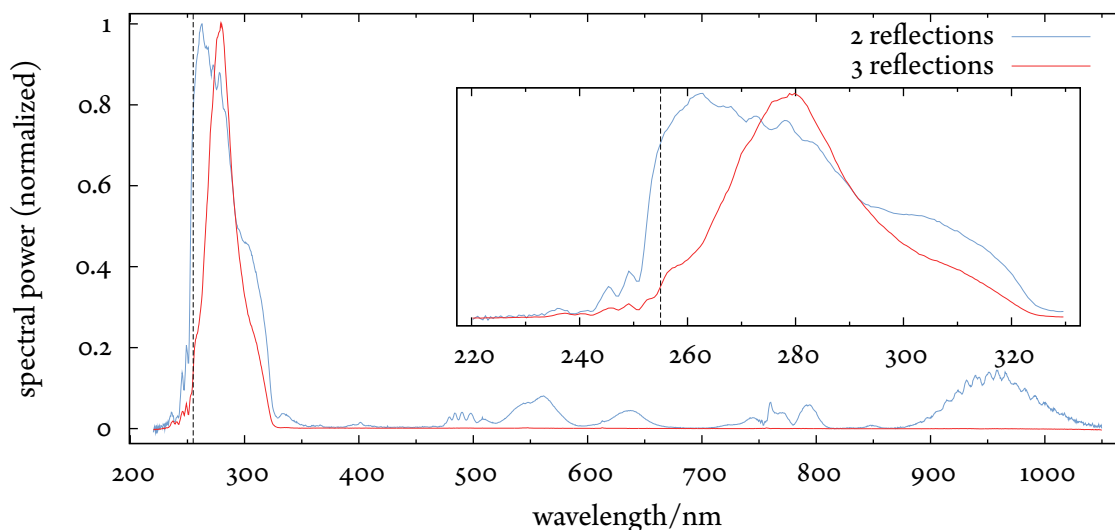


Figure 4.17.: Normalized spectra of UV pulses and IR fundamental background after cleaning the spectrum by filtering the UV and IR part by two (blue line) and three (red line) reflections off dielectric mirrors (see fig. 3.6 on page 63) recorded with a fiber coupled spectrometer (MayaPro, Ocean Optics). After three reflection, the IR contribution of the fundamental pulse is below 1%. The inset shows a close-up view of the UV part in which wavelengths shorter than 255 nm are seen to be suppressed as desired. The spectra corresponding to two and three reflections were recorded at two days with different but still representative laser settings. The angles of incidence of the final setup are given in fig. 3.4 on page 61.

a fused silica window onto a photodiode based sensor¹. This position is marked “observation port 1” in fig. 3.2 on page 58. A band pass filter² with 38 % peak transmission centered at 260 nm (40 nm FWHM) in front of the energy detector was used to suppress the about thousand times stronger fundamental pulses to about $\frac{1}{3}$ of the UV pulse energy. Since the generated UV spectrum was not fully contained in the filter’s transmission band it is not possible to report precise absolute values of the true UV pulse energy. Nevertheless, the filter turned out to be a valuable tool during the alignment procedure since relative energy measurements were still meaningful. More accurate pulse energy measurements are reported in [18], for example.

Highest UV pulse energies were achieved using neon at a pressure of 5 bar in the noble gas target. Under conditions compatible with the requirements of the pump-probe experiments, the highest measured pulse energy without spectral filtering amounts to 500 nJ. Comparably strong pulses could also be attained with argon which is much less expensive and available at all times from the gas supply lines at MPQ. UV pulses with 450 nJ energy were generated repeatedly with argon at a pressure of approximately 800 mbar in the noble gas target.

For several reasons, the absolute UV intensity focused onto the trapped ions is difficult to state. Firstly, due to the uncertainty of the UV pulse energy after the noble gas target as discussed above. Secondly, the fractional suppression of spectral components in the dielectric filtering process

¹ PD10, Ophir

² 25260FBB, eSource Optics

depends strongly on the overlap of pulse spectrum and reflectivity window of the mirrors but is hard to determine since the spectrum right after third harmonic generation is not easily measured owing to the overwhelming infrared background. Thirdly, the waist of the focused beam at the position of the molecular ions in chamber 3 is not accessible to direct measurements; see section 3.4 on page 64. Last but not least, the UV pulse duration after reflection off the dielectric mirrors could not be measured within this thesis.

In order to still try an attempt of estimating the focal intensity on the molecular ions, the value of 10 % from [42] giving the total transmission efficiency between third harmonic generation and chamber 3 of TIAMO is considered. In contrast to the setup described in that reference, two reflections off silicon surfaces (reflectivity $\approx 40\%$, [69]) could be omitted and replaced by aluminum mirrors. By that, the overall transmittance was enhanced by a factor of five. Thus, a conservative estimation of the pulse energy at the position of the ions is 150 nJ. This assumes 250 nJ to 300 nJ pulse energy before spectral filtering and takes additional minor losses, e. g. beam clipping inside the delay chamber (see section 3.3 on page 60) and reflection on the monitoring pellicle (see appendix B.5 on page 148), into account. The pulse peak intensity I_p

$$I_p = \sqrt{\frac{16 \ln(2)}{\pi}} \frac{E}{t_0 \pi w_0^2}$$

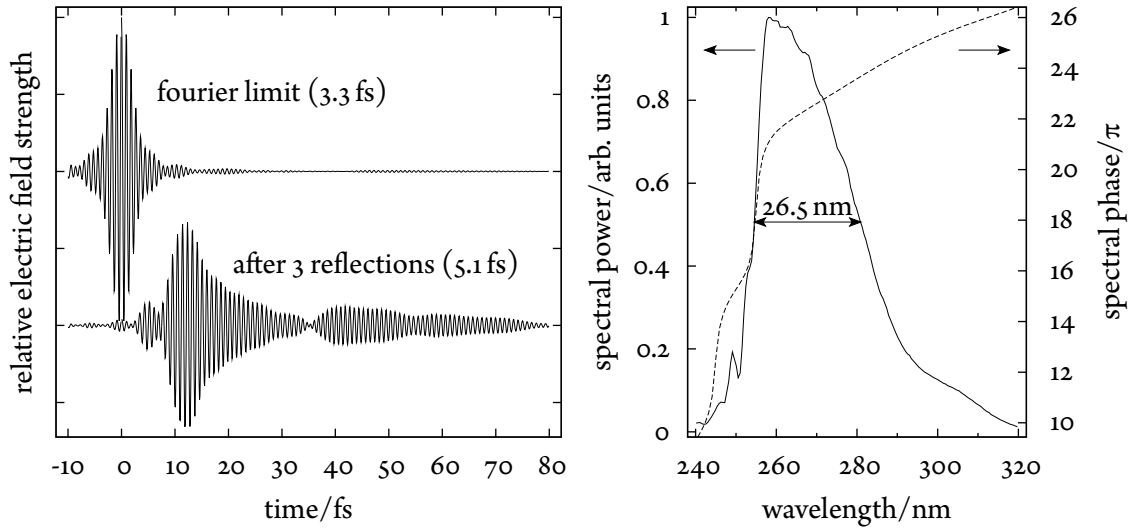
in pump and probe beam assuming Gaussian temporal and spatial profiles, $t_0 = 5$ fs pulse duration and $w_0 = 75 \mu\text{m}$ focal beam waist amounts to about 320 GW cm^{-2} . A bigger beam waist than that given in fig. 3.8 on page 66 is assumed here because the spot size in the beam monitoring cuvette was larger during the actual measurement campaign; see the discussion in section 3.4 on page 64.

According to the experience of the author's co-workers at the attosecond beam lines, pulse duration measurements using self-diffraction FROG [168], which is a χ^3 -process, are challenging due to the extremely low autocorrelation signal of the weak UV pulses. It was expected that the further reduced third harmonic pulse energies that were resulting from the spectral shift of the infrared driver pulses and the dielectric spectral filtering would have led to extraordinary weak signals that would have presented a demanding measurement task of its own. Considering the limited available measurement time and the effort of additional customized vacuum components, this far from routine technique could not be pursued within this thesis.

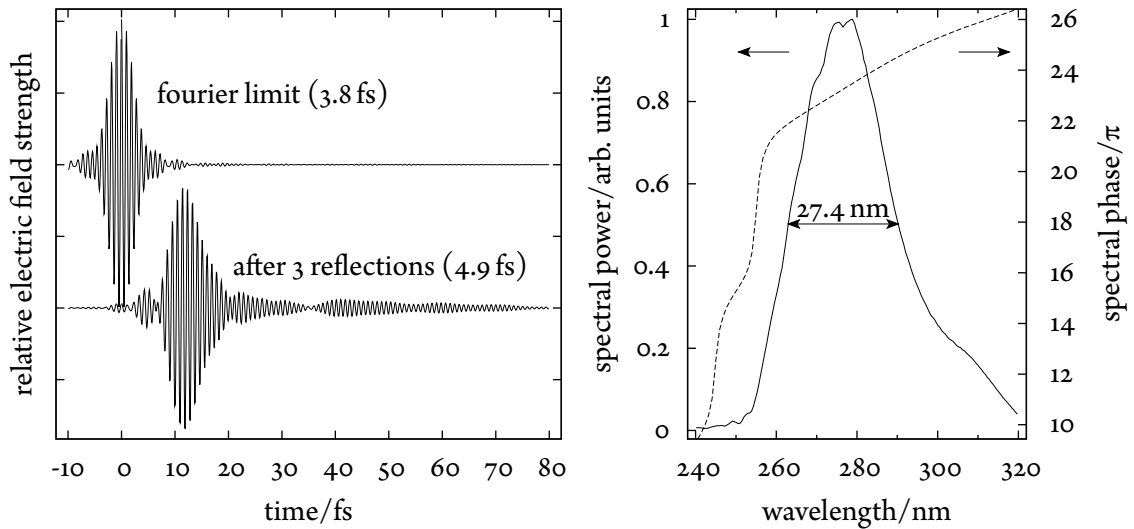
In order to solve the problem of low autocorrelation signal, an approach extending previous work [115] was proposed. Solutions based on photomultiplier tube equipped with a diamond photocathode for time-resolved two-photon photoemission were discussed with Hamamatsu. Even a simplified version using a small diamond fragment and a multi-channel plate as detector might have worked but were not realized due to time constraints.

Instead, a Fourier transform of the measured spectra in assumption of the GDD data provided by the manufacturer of the dielectric mirrors is used to estimate the pulse duration. The results of that calculation are summarized in fig. 4.18 on the following page. If the third harmonic UV pulses were generated transform limited with 4 fs duration, like reported in [70], and if the GDD data of the mirrors was correct, the reflected pulses are expected to be 5 fs long. After all, the results of the $^{24}\text{MgH}^+$ experiments confirm the assumed duration of the spectrally filtered pulses.

4. Experimental building blocks



(a) electric fields related to spectrum (b), fourier limited (b) spectral power of partially reflected pulse centered at time-bandwidth-product $\Delta\omega \cdot \Delta t = 0.39$ 260 nm



(c) electric fields related to spectrum (d), fourier limited (d) spectral power of fully reflected pulse centered at time-bandwidth-product $\Delta\omega \cdot \Delta t = 0.40$ 280 nm

Figure 4.18.: Calculated influence of the dielectric mirrors (see section 3.3 on page 60) on the temporal profile of the third harmonic UV pulses based on GDD data (dashed lines in (b) and (d)) provided by the manufacturer. Figures (a) and (c) show the electric field resulting from a Fourier transform of the measured spectra in (b) and (d). The two graphs in each of the diagrams refer to a hypothetic transform limited pulse and to the expected distortion after three reflections. The delay of the reflected pulses is implied by the linear spectral phase function coefficient $\varphi_1 = -4.2$ fs applied three times; cf. fig. 3.5a on page 62. The situation in (b) differs from that in (d) in regard to the reflectivity edge of the window cropping the short wavelength wing of the spectrum. In this part of the spectrum, the modulated spectral phase function implies stronger distortion effects.

5. Results on single molecule time-resolved spectroscopy

The femtosecond time-resolved dissociation study of $^{24}\text{MgH}^+$ on the single particle level is the central experiment of this thesis. It is at the very heart of this endeavor to combine the research field of short laser pulses with the excellent control over the translational degrees of freedom of individual particles in a radio frequency trap. In that respect, the results presented in this chapter can be considered a proof of methodology since they demonstrate the principal feasibility of investigating individual, isolated molecular ions in ultrahigh vacuum on the basis of single (within this thesis photochemical) reaction events. Despite its envisioned exceptional relevance for—not yet realizable—single-shot femtosecond time-resolved X-ray diffraction studies [117] with focal beam waists below $1\ \mu\text{m}$, some of the key concepts of our method were demonstrated. This was done in an experiment on single color pump-probe vibration spectroscopy of isolated, single molecular $^{24}\text{MgH}^+$ ions. Our experimental idea has been inspired by previous work on $^{24}\text{MgH}^+$ ions in the group of Prof. M. Drewsen [13, 90].

The necessary technical prerequisites are discussed in the previous two chapters. This chapter concentrates on the molecular properties of $^{24}\text{MgH}^+$ and how they relate to the experimental results. To begin with, the magnesium hydride molecular ion is introduced and its quantum chemical treatment is briefly sketched. In the following sections, the experimental findings are presented and discussed.

5.1. The magnesium hydride ion

$^{24}\text{MgH}^+$ is a positively charged heteronuclear diatomic molecular ion consisting of one magnesium and one hydrogen atom. For this thesis, it was generated in less than a second from collisions of excited trapped magnesium ions with molecular hydrogen gas in vacuum; see section 4.1.5 on page 75. This reaction has been intensively investigated before [116]. The reverse photochemical reaction is used as a tool to investigate vibrational wave packets using a pump-probe technique.

An intuitive understanding of the experiment might be attained from a look on the potential energy diagram in fig. 5.1 on page 97. It shows the energy of the eight lowest electronic states as functions of the internuclear distance r . The states are labeled by their molecular term symbols $^{2S+1}\Lambda^\pm$. The total spin quantum number S vanishes for all involved states. Λ represents the projection of the total orbital momentum of all electrons along the internuclear axis. $\Lambda = 0$ is expressed by the symbol Σ , $\Lambda = 1$ by Π , and $\Lambda = 2$ by Δ . The \pm superscript on the Σ^\pm symbols indicates the symmetry property of the wave function with respect to reflection on any plane containing the internuclear axis. Because only the $+$ symbol occurs, all wave functions are symmetric with respect to that operation. Instead of referring to the states by their term symbols, an unambiguous

capital letter shorthand notation is used in the following. X denotes the ground state, A refers to the second electronic state, the next more energetic electronic state is associated with B and so on.

The three lowest electronic states X, A, and B are bound states, i. e. they correspond to molecular electronic wave functions that—in simple words—attract the two atomic constituents so that a chemical bond forms. At short distances the Coulomb repulsion of equally electrically charged particles overcomes the binding effect. This gives rise to a potential well and a related equilibrium position at which the opposing effects balance. Looking more closely, one recognizes a shallow binding potential well even in state C which is however of no practical relevance. The confinement of the nuclei (and the inner-shell electrons) in the electronic potentials (formed by the valence electrons) gives rise to a discrete set of vibrational states of which four in two lowest electronic states are also shown in the same diagram fig. 5.1 on the next page. Rotational states have not been taken into account within this thesis since the associated transition frequencies are in the THz regime, well separated from optical frequencies and thus not resolved in the experiment.

In contrast to the first three, the electronic state C is repulsive. An electronically excited molecule in this state is not stable but will dissociate, i. e. split into two components, in this particular case into Mg and H⁺. There are no vibrational states associated with the instable configuration of a repulsive potential.

The still higher lying electronic states are bound again but possess a more modulated potential landscape. This is due to interaction terms between increasingly dense lying highly excited electronic states [3] that lead to a repelling effect on the associated potential energy surfaces—usually called *avoided crossings*. In dynamic (diabatic) situations where the molecular configuration rapidly passes through regions where two such electronic states come close, e. g. by varying the bond length in a fast expansion, the molecular quantum state may deviate from the adiabatic evolution and traverse the energy gap between two potential surfaces, thus change the electronic quantum state without emitting radiation. Future experiments on ²⁴MgH⁺ might allow to explore the properties of these couplings in more detail.

Many properties of bound ²⁴MgH⁺ have been derived from spectroscopic investigations [6, 83] since almost 40 years ago. Table 5.1 on page 98 lists the most important properties gathered from the literature. Usual for diatomic molecules, the vibrational level spacing is much bigger than the mean energy of the radiation field at room temperature. In consequence, the vibrational ground state is populated to more than 99.9 % in thermal equilibrium at room temperature. Likewise, the sum of the population of rotational states in the electronic potentials of X and A (cf. fig. 5.2 on page 98) up to $J = 16$ is above 99.8 % since the rotational energy of state $|J = 16\rangle$ equals approximately one vibrational quantum in the respective potential.

5.1.1. quantum chemical treatment

Contrary to the existent precise spectroscopic studies, a flexible *dynamic* quantum chemical treatment of ²⁴MgH⁺ has not been available. A dedicated model needed to be developed in order to estimate the strength, contrast and time-dependence of the experimental signal. The computational framework was also needed to assess possible difficulties that could arise from experimental conditions, e. g. vibrational heating, beforehand but also to assist the interpretation of the measurements

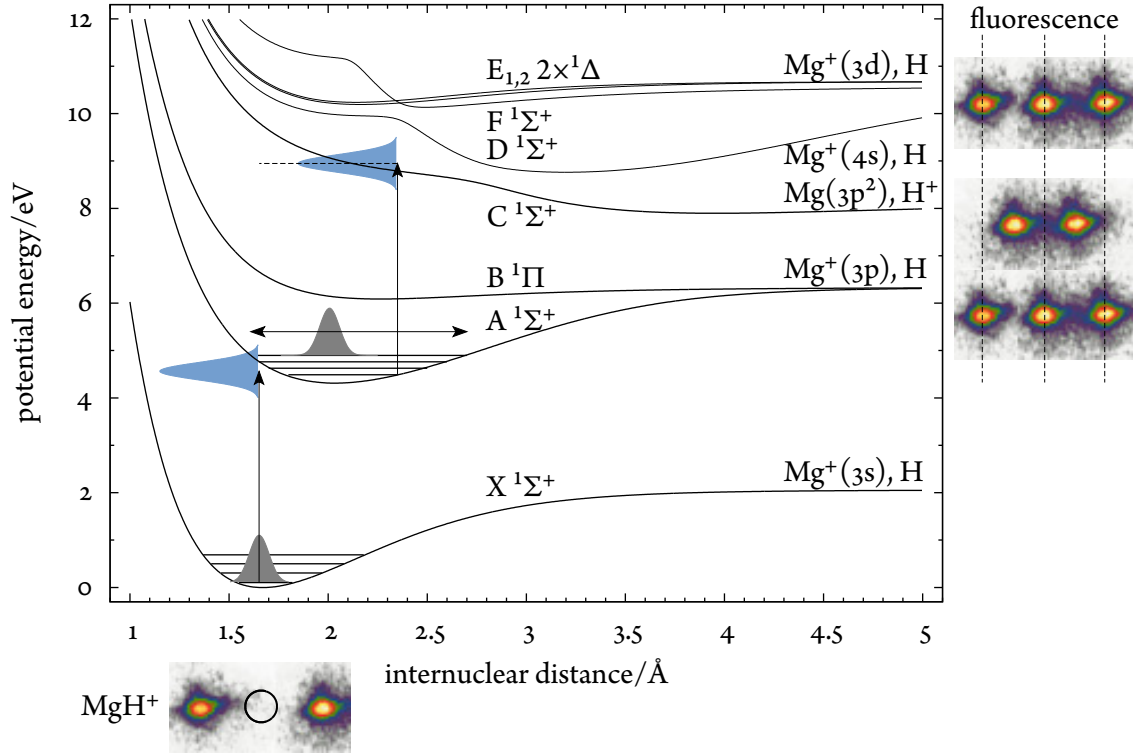
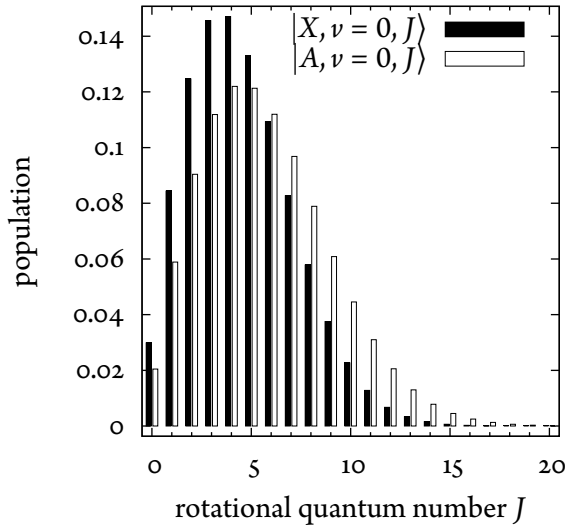


Figure 5.1.: Potential energy diagram of the first eight electronic states calculated in the framework of this thesis' quantum chemical model of $^{24}\text{MgH}^+$. The four lowest vibrational states in the ground (X) and first excited electronic state (A) are shown according to the energies reported in [6]. The Gaussian vibrational ground state in X and a coherent superposition of vibrational states in A (oscillation period 30 fs) are symbolized by wave packets (grey). In the dissociation limit, the atomic configuration and charge state of magnesium as well as of hydrogen are given. The arrows indicate a particular choice of the central wavelength (278 nm) of pump and probe pulse. Their respective spectral widths (27 nm, see section 4.4 on page 90) are plotted as vertical Gaussian profiles (blue). The false color fluorescence image insets at the right and bottom depict symbolically how the dissociation event of a $^{24}\text{MgH}^+$ ion (represented by the black circle) in the respective channel can be detected by the loss of one dark ion ("neutral channel", electronic state C) or the conversion of one dark into an additional bright ion ("charged channel", all other electronic states).

Table 5.1.: Spectroscopic constants (R_e equilibrium distance, D_e potential well depth, ω_e harmonic constant, B_e rotational constant) of $^{24}\text{MgH}^+$ in the first four electronic states according to experimental [6, 83] and theoretical [3] studies.

electronic state	R_e (Å)	D_e (cm^{-1})	ω_e (cm^{-1})	B_e (cm^{-1})
X	1.652	16 553	1699	6.296
A	2.007	16 656	1135	4.296
B	2.265	1943	588	3.38
C	3.958	1860	319	

**Figure 5.2.:** Rotational population distribution in the vibrational ground state of the electronic bound states X and A assuming thermal equilibrium at $T = 300$ K; see table 5.1 for the relevant spectroscopic constants. All $J + 1$ degenerate rotational m_J states are summarized under the quantum number J .

in hindsight. To this end, a cooperation with the group of Prof. deVivie-Riedle from the chemistry department of the LUDWIG-MAXIMILIANS-UNIVERSITÄT MÜNCHEN was initiated. Markus Kowalewski set up a computational framework that can account for various technical determining factors that were encountered in the laboratory work. His simulation was therefore developed closely following the experimental progress. It extends the previous static [3] and picosecond dynamic [90] theoretical treatments by the electronic states D to E, is adopted to the broad spectra of short femtosecond pulses and allows the simulation of vibrational heating through the course of repeated excitation followed by spontaneous emission by employing an extensive set of 20 eigen states in the bound electronic potential.

Details about the applied “standard” quantum chemical formalism can be looked up in [66], for example. In the framework of this thesis, the topic can only be sketched briefly. The molecular Hamiltonian \hat{H}_{mol}

$$\hat{H}_{\text{mol}} = \hat{T}_{\text{nuc}} + \hat{T}_{\text{el}} + \hat{V}_{\text{nuc-nuc}} + \hat{V}_{\text{nuc-el}} + \hat{V}_{\text{el-el}} = \hat{T}_{\text{nuc}} + \hat{H}_{\text{el}} \quad (5.1)$$

splits up into a nuclear kinetic energy part \hat{T}_{nuc} and an electronic part \hat{H}_{el} the latter of which includes all interaction energies. The solutions to eq. (5.1) are formulated as products of electronic Ψ_{el} and nuclear Ψ_{nuc} wave functions which allows to compute them separately given the decoupled

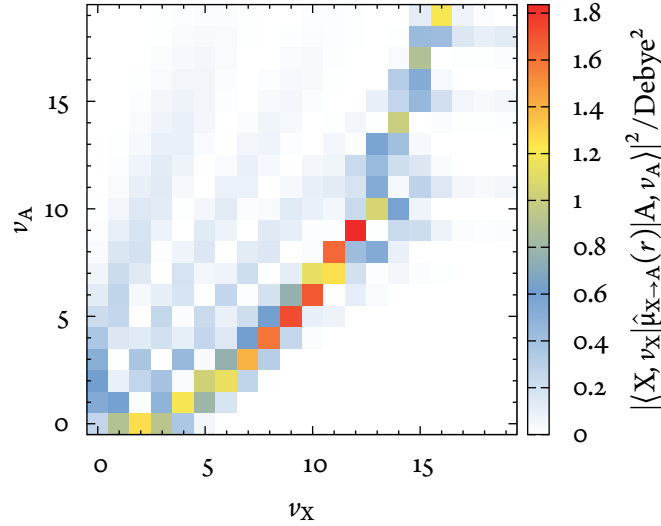


Figure 5.3.: Absolute square of the position-dependent dipole operator $\hat{\mu}(r)$ matrix elements coupling the first 20 vibrational states ν_X and ν_A of the electronic ground state X and the first excited state A of $^{24}\text{MgH}^+$ computed using the quantum chemical framework of this thesis. The appreciable shift of the equilibrium position in the respective electronic states (see fig. 5.1 on page 97 and table 5.1 on the facing page) implies strong coupling (Franck-Condon factors) between vibrational states of differing quantum number ν . This coupling becomes relevant in the electronic excitation $X \rightarrow A$ and the spontaneous decay $A \rightarrow X$. 1 Debye $\approx 3.336 \cdot 10^{-30}$ C m

structure of the Hamiltonian. In the *Born-Oppenheimer approximation*, the electronic wave functions $\Psi_{\text{el}}(\mathbf{r}_{\text{el}}; \mathbf{r}_{\text{nuc}})$ are assumed to depend only parametrically on the nuclear coordinates, i. e. the molecular geometry. In a first step, the electronic wave functions and the associated energies are computed for a set of meaningful nuclei configurations, mostly on an evenly spaced grid, resulting in the (electronic) *potential energy surfaces*. For this step, *configuration interaction* methods, namely CASSCF/MRCI/CC-pVQZ and CAS/MRCI/ROOS were employed by Markus Kowalewski.

The wave functions of the slowly moving nuclei are computed in a second step. They result from the previously calculated potential energy surfaces. Loosely speaking, the second step is approximately correct in situations where the energy difference between two electronic states is much bigger than the kinetic energy of the nuclei at this position, more precisely $|E_n - E_m| \gg \langle \Psi_{\text{el}}^n(\mathbf{r}_{\text{el}}; \mathbf{r}_{\text{nuc}}) | \hat{T}_{\text{nuc}} | \Psi_{\text{el}}^m(\mathbf{r}_{\text{el}}; \mathbf{r}_{\text{nuc}}) \rangle$ [155]. In $^{24}\text{MgH}^+$, this condition is satisfied almost everywhere, except of the aforementioned avoided crossings of the highly excited electronic states (cf. fig. 5.1 on page 97) where a more elaborate treatment had to be pursued.

The first $n = 8$ eigen energies $E_{\text{el}}^n(\mathbf{r}_{\text{nuc}})$ of the stationary electronic Schrödinger equation

$$\hat{H}_{\text{el}} \Psi_{\text{el}}^n(\mathbf{r}_{\text{el}}; \mathbf{r}_{\text{nuc}}) = E_{\text{el}}^n(\mathbf{r}_{\text{nuc}}) \cdot \Psi_{\text{el}}^n(\mathbf{r}_{\text{el}}; \mathbf{r}_{\text{nuc}})$$

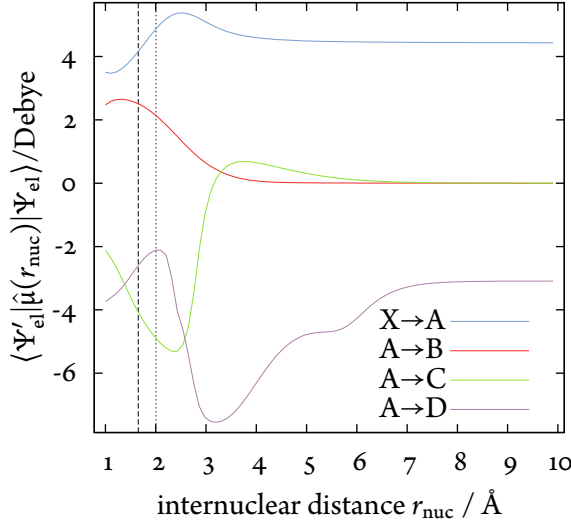


Figure 5.4.: $^{24}\text{MgH}^+$ transitions dipole moments of the relevant electronic transitions occurring in the pump-probe dissociation experiments as functions of the internuclear distance r_{nuc} . The equilibrium positions R_e of X and A are indicated as dashed and dotted lines respectively. The presented graphs were computed using the quantum chemical model of this thesis. 1 Debye $\approx 3.336 \cdot 10^{-30}$ C m

as a function of the molecular geometry \mathbf{r}_{nuc} are shown in fig. 5.1 on page 97. The vibrational (and rotational) energy levels follow from the solutions of the nuclear stationary Schrödinger equation

$$(\hat{T}_{\text{nuc}} + E_{\text{el}}^n(\mathbf{r}_{\text{nuc}}))\Psi_{\text{nuc}}^{\nu,J} = E_{\text{nuc}}^{\nu,J}\Psi_{\text{nuc}}^{\nu,J}.$$

The interaction with the femtosecond laser can be taken into account by regarding it a perturbation to the molecular Hamiltonian in the time-dependent Schrödinger equation

$$i\hbar \frac{\partial}{\partial t} \Psi(t) = [\hat{T}_{\text{nuc}} + \hat{H}_{\text{el}} + \hat{H}_{\text{int}}(t)] \Psi(t).$$

The interaction $\hat{H}_{\text{int}}(t) = -\hat{\mu}(r_{\text{nuc}}) \cdot \mathcal{E}(t) = e \hat{\mathbf{r}}_{\text{el}} \cdot \mathcal{E}(t)$ involves a geometry dependent dipole matrix $\hat{\mu}(r_{\text{nuc}})$. It couples the electronic states in a time-dependent way via the electric field $\mathcal{E}(t)$ of the laser pulse. $\mathcal{E}(t)$ contains all radiation characteristics such as e. g. pulse duration, intensity, spectrum, and chirp; cf. section 1.4 on page 18. The absolute square of transition dipole matrix element values coupling the electronic ground (X) and first excited state (A) of $^{24}\text{MgH}^+$ for a series of nuclear wave functions are presented in fig. 5.3 on the previous page. More general information about the dependence of the dipole operator $\hat{\mu}(r_{\text{nuc}})$ on r_{nuc} can be extracted from fig. 5.4. To emphasize the electronic transition strengths, the nuclear wave function overlap integrals are omitted in this diagram.

The evolution of the coupled light-molecule system is symbolically noted by the time-dependent wave function at time t being the result of applying the *propagator* $\hat{U} = e^{-\frac{i}{\hbar}\hat{H}_{\text{nuc}}(t-t_0)}$ to a known solution at t_0

$$\Psi(t) = e^{-\frac{i}{\hbar}\hat{H}_{\text{mol}}(t-t_0)}\Psi(t_0).$$

Non-vanishing commutator relations $[\hat{T}_{\text{nuc}}, \hat{V}_{\text{nuc}}]$ complicate the numerical evaluation of the propagator because the Baker-Hausdorff relation describes the fact that the exponentiated sum of operators is different from a product of exponentiated operators. This difficulty can be worked around

using the well-established *split operator method* with sufficiently small time steps

$$e^{-\frac{i}{\hbar}(\hat{T}_{\text{nuc}}+\hat{V}_{\text{nuc}})(t-t_0)} \approx e^{-\frac{i}{2\hbar}(\hat{T}_{\text{nuc}})(t-t_0)} e^{-\frac{i}{\hbar}(\hat{V}_{\text{nuc}})(t-t_0)} e^{-\frac{i}{2\hbar}(\hat{T}_{\text{nuc}})(t-t_0)} + O[(t-t_0)^3].$$

Another computational trick—known as *dynamic Fourier method*—allows to compute the kinetic energy terms in the above expression without actually calculating time-consuming derivatives in position space $\hat{T} = -\frac{\hbar^2}{2m} \frac{d^2}{dx^2}$. Instead, a fourier transform \mathcal{F} to momentum space, where the action of the kinetic energy operator is a computational efficient multiplication, is performed and followed by the inverse transformation \mathcal{F}^{-1} . Together with another suitable unitary rotation \hat{X} into a diagonal basis of the transition dipole matrix, the complete propagation operator for one time step Δt reads

$$e^{-\frac{i}{\hbar}(\hat{T}_{\text{nuc}}+\hat{V}_{\text{nuc}}+\hat{H}_{\text{int}})\Delta t} = \mathcal{F}^{-1} e^{-\frac{i}{2\hbar}\hat{T}_{\text{nuc}}\Delta t} \mathcal{F} e^{-\frac{i}{\hbar}\hat{V}_{\text{nuc}}\Delta t} \hat{X}^{-1} e^{\frac{i}{\hbar}\hat{\mu}\mathcal{E}\Delta t} \hat{X} \mathcal{F}^{-1} e^{-\frac{i}{2\hbar}\hat{T}_{\text{nuc}}\Delta t} \mathcal{F}.$$

5.1.2. pump probe excitation

Provided with the previous definitions and information about the molecular ion $^{24}\text{MgH}^+$, one can formulate the mechanism of the time-resolved pump probe experiment.

Starting from the electronic and vibrational ground state $|X, v_X = 0\rangle$, the pump pulse can couple to the first excited electronic state A. Due to the 0.35 Å offset of the equilibrium position in the excited state (see fig. 5.1 on page 97) and the related Franck-Condon progression (see fig. 5.3 on page 99), the broad spectrum of the laser pulse can coherently excite several vibrational modes. They form a vibrational wave packet that oscillates in the electronic potential of state A. The period of that oscillation $T_{\text{osc}} \approx 30$ fs is directly related to the harmonic constant ω_e ; see table 5.1 on page 98.

$$T_{\text{osc}} = \frac{1}{c \omega_e} \approx 30 \text{ fs} \quad (5.2)$$

The characteristic spontaneous decay time on the order of 10 ns from A into the electronic ground state X is given by the wavelength $\lambda \approx 280$ nm and the transition dipole moment $\mu_{A \rightarrow X} \approx 1$ Debye; cf. fig. 5.3 on page 99:

$$\frac{1}{\tau} = \Gamma_{\text{rad}} = \frac{8\pi^2}{3\epsilon_0 \hbar \lambda^3} |\mu_{A \rightarrow X}|^2. \quad (5.3)$$

Hence, spontaneous decay is unlikely to happen during the presented femtosecond pump-probe experiment since the maximal delay between pump and probe pulse was below 100 fs, i. e. six orders of magnitude shorter than the spontaneous decay time.

After the excitation from the ground into the excited state A via the pump pulse, the probe pulse of similar intensity and spectral properties can couple the vibronic excitation onwards to the dissociative state C. The probability of this transition depends on the position of the vibrational wave packet since the energy difference $E_{\text{el}}^A - E_{\text{el}}^C$ is a function of the internuclear distance. As can be seen in fig. 5.1 on page 97, this energy difference matches the photon energy of the probe pulse at about the outer turning point ($r_{\text{nuc}} \approx 2.5$ Å) of the oscillation for the wavelength given in the diagram. At the inner turning point ($r_{\text{nuc}} \approx 1.6$ Å), the photon energy is not sufficient to populate state C. In this way, the vibration of the molecular ion in state A modulates the transition moment

Table 5.2.: Spontaneous radiative decay time of the vibrational transition $\nu'_X \rightarrow \nu_X$ in milliseconds.

ν_X	1	2	3	4
0	$9.10 \cdot 10^1$	$3.17 \cdot 10^2$	$1.65 \cdot 10^3$	$1.76 \cdot 10^4$
1		$3.71 \cdot 10^1$	$1.35 \cdot 10^2$	$4.19 \cdot 10^2$
2			$2.10 \cdot 10^1$	$9.30 \cdot 10^1$
3				$1.39 \cdot 10^1$

$\mu_{A \rightarrow C}$ and thus leads to a time-dependent dissociation yield oscillating with 30 fs. At time zero, i. e. vanishing pump-probe delay, the dissociation probability is minimal. It attains its maximum half an oscillation period later when the molecular ion is stretched before it gets minimal again by the return to the inner turning point and the completion of one oscillation cycle.

With this qualitative picture in mind, the need for spectral filtering discussed in section 3.3 on page 60 can be explained. A probe pulse that contains too high frequency components can populate the repulsive state C almost independently of the position of the vibrational wave packet position and would reduce the contrast of the time-dependent component of the signal. In order to work around that problem, the laser spectrum had to be red shifted as much as possible and additionally spectrally filtered on the blue side. How this was accomplished is detailed in section 4.4 on page 90.

For the parameters given in section 5.2 on the facing page only about 3 % of all laser pulses led to the excitation $X \rightarrow A$ and dependent on the position of the vibrational wave packet and the excited vibrational states about the same fraction of pulses can cause a transition to the dissociation channel $A \rightarrow C$. Whenever a molecular ion has been excited by a pump pulse, it will most probably decay into the ground state and not absorb a second, dissociating photon from the probe pulse. Furthermore, the molecular ion is essentially guaranteed to decay into the electronic ground state before a new pump-probe pair arrives at the position of the molecular ion because the pulse repetition rate of 3 kHz is much lower than the spontaneous decay rate on the order of 100 MHz.

By spontaneous decay, the vibrational state distribution in X tends to get broadened. This behavior is caused by the pronounced Franck-Condon mixing of vibrational states; see fig. 5.3 on page 99. The broader the distribution of populated vibrational states in the electronic excited state A is, the more vibrational states in the electronic ground state X are accessible. Inversely, the more vibrational states in X are populated, the higher vibrational states in A are accessible in the next vibronic pump transition. Repeated excitation cycles heat up the vibrational manifold quite rapidly because the vibrational spontaneous radiative decay time is much longer than that of the electronic transitions. Table 5.2 summarizes these times for the allowed transitions between the lowest vibrational states in X.

A vibrational basis set of 20 states in A and X is used in the computational framework developed for this thesis to account for the heating effect. Furthermore, the simulation can also be run in a mode mimicking the experimental situation in which the average heating rate is reduced by exposing the molecular ion to a train of an adjustable number of laser pulses. Between two adjacent exposure intervals, a certain number of femtosecond laser pulse are mechanically blocked (see appendix A.1.1.a on page 124) giving the molecular ions time to decay to the vibrational ground state.

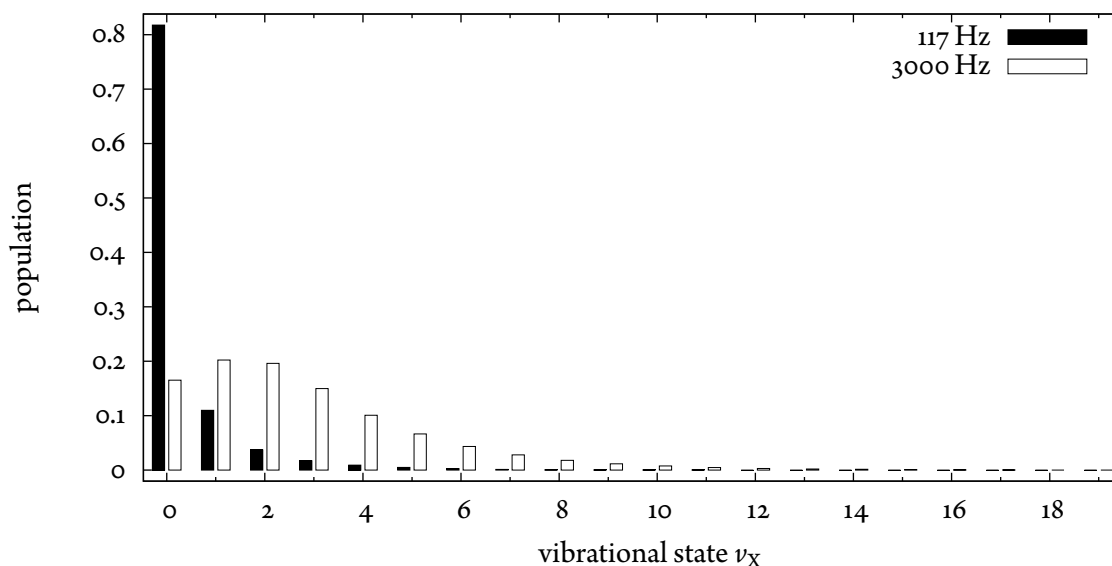


Figure 5.5.: Simulated distribution of the vibrational state population in the electronic ground state X in the steady-state of repeated pump-probe cycles at the full 3 kHz pulse repetition rate of the femtosecond laser system (see section 3.1 on page 55) and the experimentally realized reduced effective rate 117 Hz corresponding to the usage of only 5 out of 128 laser pulses. Considerable vibrational heating is observed at 3 kHz repetition rate, indicated by the many (non-thermally distributed) occupied vibrational states. The approximately thermal distribution related to 117 Hz is much narrower and similar to the distribution in equilibrium with a radiation field corresponding to a temperature of about 1500 °C.

As long as the probability to excite the same molecular ion more than once during one exposure period is low, the situation is equivalent to using less laser pulses at a constant but correspondingly lower pulse repetition rate. This effective repetition rate is determined by the exposure duty cycle $T_{\text{exposure}}/(T_{\text{block}} + T_{\text{exposure}})$ multiplied by the unaltered pulse repetition rate. Figure 5.5 compares the vibrational heating for two different effective pulse repetition rates.

The pump-probe scheme described above builds on the dissociation of $^{24}\text{MgH}^+$ via the electronic state C. However, dissociation events can also occur in other channels. Although not comprehensively investigated but observed, it is likely that a broad vibrational distribution in X combined with the shortest wavelength components of the pulse spectrum allows to excite vibrational wave packets in the weakly bound states D and E comprising sufficiently highly excited vibrational states which surpass the dissociation limit. Due to this reasoning, the time-resolved experiments were performed using a reduced pulse repetition rate which prevented excessive vibrational heating and thereby dissociation in unintended ways.

5.2. Experimental procedure

Generating sufficiently energetic, short UV pulses in the desired spectral range required substantial optimization effort in the beginning of each measurement day; see section 4.4 on page 90. Even

though the femtosecond laser beam alignment was not touched once satisfying UV pulses were generated, the overlap of pulsed UV beam (focal waist $\approx 75 \mu\text{m}$) and molecular ion target was lost occasionally, usually after 2 to 5 hours. In view of the in total about 17 m long beam line of AS4B extending over many separate tables and supports on the one hand and the diminutive sized molecular ion target ($\approx 1 \mu\text{m}$) on the other hand, small drifts were likely to accumulate over time and made the femtosecond focus miss the molecular ions at some point. The preferred method to verify that the femtosecond pulses still hit the molecular ions sufficiently well was to steer one of the pulsed beams (see section 3.3 on page 60) over the expected position of the molecular ions both in the vertical and horizontal direction by using mirrors M₄ and M₅ of the delay chamber. The beam's movement could be followed by watching the corresponding fluorescence spot in the monitoring cuvette (see section 3.4 on page 64). When one of the beams hit the molecular ions, the dissociation reaction set in, i. e. "dark" ions began to disappear from the heterogeneous Coulomb crystal. Due to the stochastic occurrence of dissociation events, the determination of the reaction rate ($\approx 1 \text{ s}^{-1}$ on average) and thereby the optimum beam position was limited by statistical fluctuations. The related uncertainty in both spatial directions amounts to about 50 % of the fluorescence spot waist. At larger beam displacements the dissociation rate dropped rapidly. The spatial sensitivity rendered it an utmost challenging task to pinpoint the molecular ion target since a "gradual" approach was not possible under the given conditions. After the overlap of one of the UV beams with the molecular ions had been found, the position was marked and the beam shifted aside. The same alignment procedure was repeated for the second beam. Finally, both beams were put into their respective optimum overlap position again. To verify the optimized beam alignment, the dissociation rate was checked to be about four times (quadratic dependence on intensity) faster.

The temporal overlap of both beams was adjusted by looking closely on the fluorescence signal in the monitoring cuvette. When both beams overlapped geometrically and temporally inside the cuvette, the fluorescence signal developed dark interference fringes (see fig. 5.6 on the facing page) which moved randomly at the time scale of below one second over the fluorescence spot due to the beams being not interferometrically stable. The number of visible fringes depended on the focus size inside the cuvette, the spacing ($\approx 30 \mu\text{m}$) between two adjacent fringes on the angle (0.6°) enclosed by pump and probe beam. Using this method, time zero of the pump-probe delay was determined with an uncertainty of $\pm 5 \text{ fs}$. For larger delays no such interference fringes were observed. The alignment that corresponded to spatial overlap of both beams with the trapped ions turned out to be different from the one determined by overlapping them spatially inside the cuvette. When the trapped ions were hit, the separation between the beams in the cuvette amounted to about one beam diameter explainable with a displacement of the cuvette by approximately 1 cm along the beam axis. However, no cuvette position was found, where beam overlapping with the trapped ions and in the cuvette coincided. In order to observe the interference fringes, beam overlap in the cuvette was required. After determining time zero as described above, the beams were repositioned to overlap with the ions. Considering this small discrepancy and the stated uncertainty, a 7 fs to 8 fs deviation of time zero to the value that follows from a detailed evaluation of the the time-resolved dissociation measurements appears reasonable.

In the beginning of each experimental iteration, magnesium ions were loaded and cooled in chamber 1, the Coulomb crystal cleaned from isotopes other than $^{24}\text{Mg}^+$, $^{24}\text{MgH}^+$ ions generated

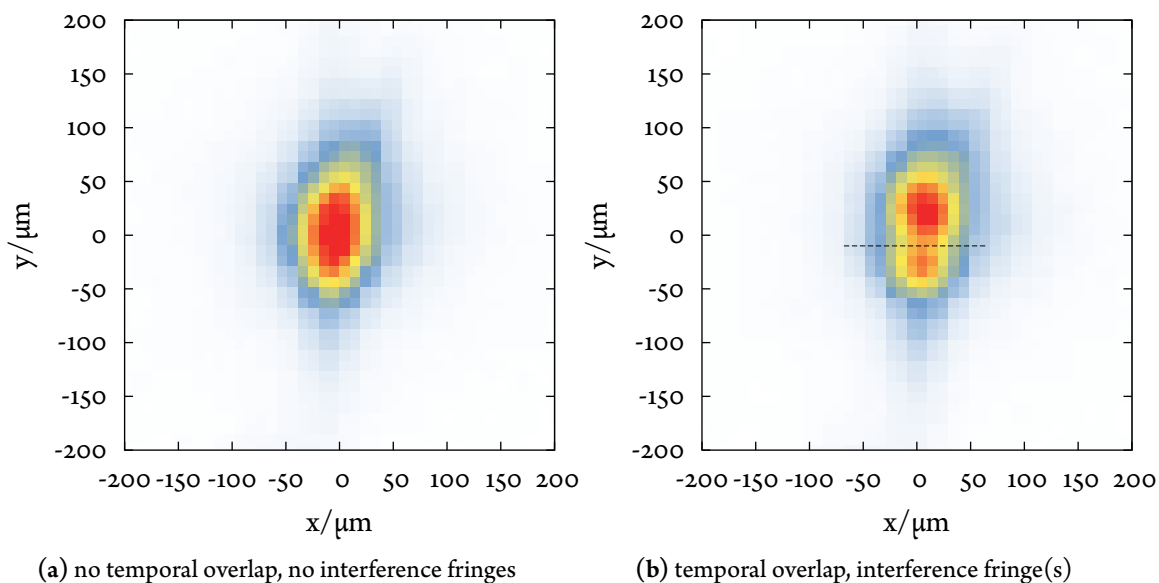


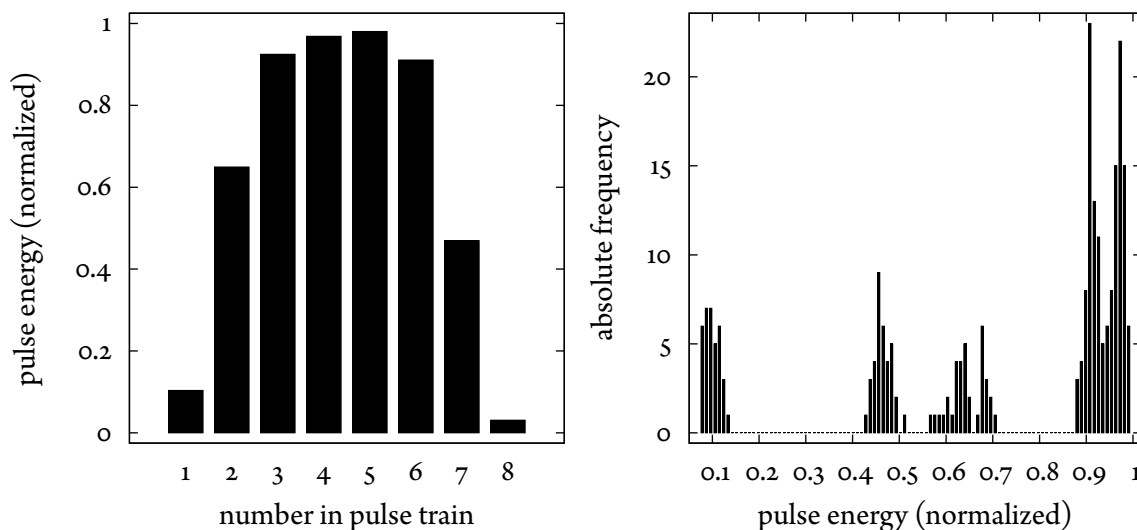
Figure 5.6.: False color representation of the UV beam fluorescence spot intensity distribution in the monitoring cuvette; see section 3.4 on page 64. Pump and probe beam overlap spatially. If they are also coincident in time, interference fringes such as in (b) occur.

photochemically and the resulting mixed ion crystal transferred to chamber 3 following the lines of section 4.1 on page 67. Depending on the experimental needs, either both or only one of the traps in chamber 3 was filled with up to 60 ions, a known amount (typically 20) of them being $^{24}\text{MgH}^+$ ions. After a subsequent laser cooling period of about 10 s during which the transferred hot ion cloud (section 4.2 on page 75) crystallized, including the sympathetically cooled molecular ions, the cooling laser power was reduced ($P \lesssim 50 \mu\text{W}$) such that the crystalline structure could be sustained and the signal to noise of the fluorescence images (see appendix A.1.2 on page 127) was sufficient for the image analysis algorithm (see appendix A.2 on page 128) to reliably identify dark and bright ions. In this way, any adverse contributions to the dissociation probability stemming from the cooling laser radiation interacting with $^{24}\text{MgH}^+$ (see section 4.3 on page 87) were minimized.

During the aforementioned mainly automated (see appendix A.1.1 on page 124) preparation procedure, the femtosecond laser pulses were blocked by a mechanical shutter preventing the molecular ions from being irradiated. A mechanical chopper¹, also in the beam path of the femtosecond laser, divided the stream of pulses into trains of transmitted and blocked pulses. In all presented experiments, the total of all transmitted pulses in one contiguous train and the subsequent train of blocked pulses added up to 128. The fraction of blocked and transmitted pulses contained in one such “chopper cycle” was controlled by the relative orientation of two partially overlapping chopper wheels. Because chopper wheels with two slits of 90° opening angle were used, one revolution comprised two chopper cycles. Omission of the chopper wheel allowed to use the complete pulse stream. Figure 5.7a on the next page shows the pulse statistics of one 1.5 s long exposure with 6 to 8 transmitted and 120 to 122 blocked pulses per chopper cycle.

¹ model 3501, New Focus

5. Results on single molecule time-resolved spectroscopy

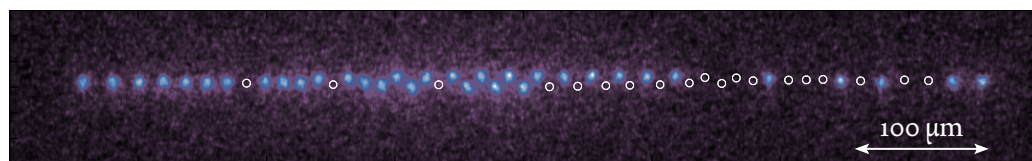


(a) Over 35 chopper cycles averaged distribution of pulse energies along the sequences of 6 to 8 transmitted pulses. The first and last two pulses contain only little energy being a consequence of clipping on the chopper blades at the edge of the moving window. (b) Absolute frequency of pulse energies. Altogether $35 \cdot 8 = 280$ pulses were transmitted. Their energy distribution splits roughly into three parts: unclipped pulses (right), partially clipped (center) and “scrape through” pulses (left).

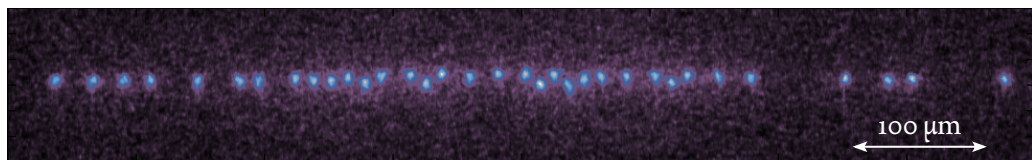
Figure 5.7.: Pulse statistics of one exposure interval lasting 1.5 s corresponding to 4500 pump-probe pulse pairs. Almost 35 complete 128 pulse long chopper cycles are contained in the interval. 4 to 5 unpaired pulses were transmitted through the chopper, the remaining pulses were blocked either partially or completely. The energy of the pump-probe pulses after passage through the TIAMO vacuum setup pair was measured with a photodiode; see fig. 2.17 on page 43.

The number of pulses that the molecular ions were exposed to was controlled by opening a mechanical shutter for the desired amount of time. It was chosen long enough for a discernible fraction ($\approx 10\%$ to 30%) of the molecular ions to dissociate by the end of the exposure interval. Depending on the available pulse energy but also on the spectrum and the chopper setting, appropriate exposure times ranged from a fraction of a second up to a minute. Immediately after the irradiation, a fluorescence image using the settings given in table A.1 on page 128 was recorded to document the number of undissociated molecular ions left in the trap. The steps of irradiation and fluorescence imaging were repeated until about 90% of the molecular ions were dissociated. Fluorescence images from one such experimental run consisting of five consecutive 1.5 s exposures are given in fig. 5.8 on the next page.

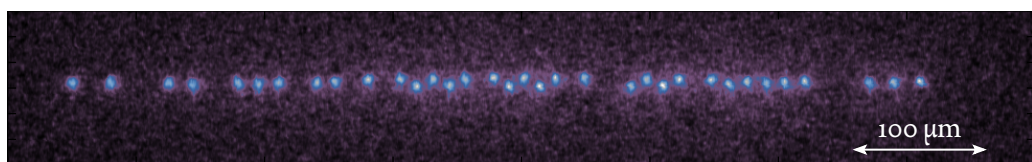
Subsequently and sometimes even simultaneously to the fluorescence imaging, new ions were loaded in chamber 1 and another experiment iteration started. If required, the pump-probe delay was set to a new value; see section 3.3 on page 60. It took about 5 min to 7 min from loading atomic $^{24}\text{Mg}^+$ ions until completion of the dissociation reaction measurements. This allowed to repeat the experiment about 150 to 180 times on days of continuous good laser performance. When there were doubts about the overlap of pulsed beams and ion crystal, the above alignment procedure



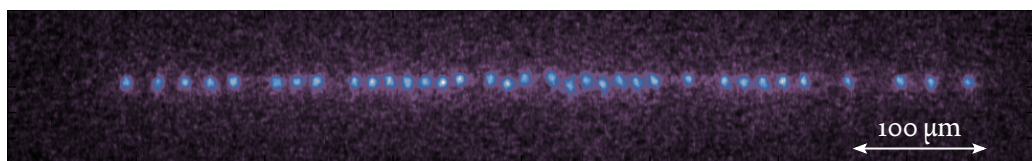
(a) Initial configuration: 34 bright, 19 dark ions. Molecular ion positions are indicated by white circles.



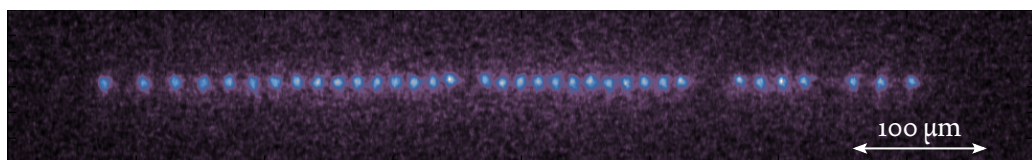
(b) exposed to 211 pump-probe pulse pairs, 34 bright, 18 dark ions



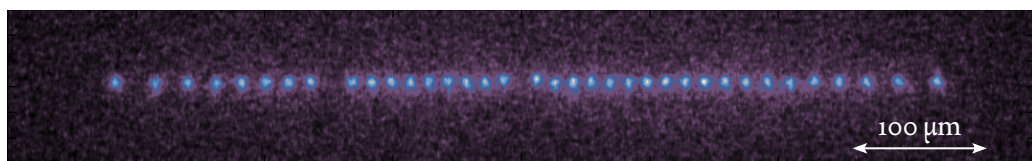
(c) exposed to 422 pump-probe pulse pairs, 34 bright, 14 dark ions



(d) exposed to 633 pump-probe pulse pairs, 35 bright, 9 dark ions



(e) exposed to 844 pump-probe pulse pairs, 35 bright, 5 dark ions



(f) exposed to 1055 pump-probe pulse pairs, 36 bright, 2 dark ions

Figure 5.8.: Sequence of false color fluorescence images documenting the dissociation process of $^{24}\text{MgH}^+$. For a description of the unambiguous counting procedure of “bright” (atomic) and “dark” (molecular) ions, refer to appendix A.2 on page 128.

needed to be repeated. Additionally, intensity and spectrum of the UV pulses were recorded regularly throughout the measurement day in order to keep track of drifts in the femtosecond laser system.

5.3. Experimental results

In this section, results of three experiments are presented. First vibrational heating of isolated and repeatedly electronically excited, identical molecular ions is discussed. In a second experiment, the quadratic dependence of the two-photon dissociation process on the laser pulse energy is verified. Finally, the central measurements of this thesis on single molecular ions using time-resolved pump-probe spectroscopy at two different wavelengths are presented.

5.3.1. vibrational heating

One of the pulsed UV experiments addressed the vibrational heating in $^{24}\text{MgH}^+$ which is discussed in the previous section. Consecutive vibronic transitions between the electronic states X and A can excite increasingly higher energetic states of the vibrational ladder due to the long progression of the Franck-Condon factors; cf. fig. 5.3 on page 99. The resulting population of vibrational states does not follow a thermal Boltzmann distribution in general since the radiative decay times of these states can be much longer than the average time between two subsequent UV pulse induced electronic excitations which prevents to redistribute the vibrational excitations accordingly.

The quantum chemical simulation of molecular ions being exposed to a stream of equal femtosecond UV pulses (see section 5.1.1 on page 96) predicts the occupation of progressively higher excited vibrational states until the correspondingly increasing radiative decay rates within the vibrational manifold of X balance the heating effect and establish a steady-state. However, vibrational highly excited molecular ions in the steady-state can be close to the dissociation threshold. Specifically, electronic excitations to the weakly bound higher lying electronic states D and E (see fig. 5.1 on page 97) followed by subsequent dissociation become more probable if the molecule is already vibrational highly excited in the beginning of the pump-probe pulse sequence. There is also the possibility to excite the molecular ion to state A or B with a single high energetic UV photon such that the dissociation threshold is surpassed and the molecular ion disintegrates. The probabilities per pulse of these processes to happen are small. However, at high pulse repetition rates a considerable loss mechanism can arise from repeated pump-probe excitations. To increase the computational efficiency, only vibrational states up to $\nu = 20$ were considered in the simulation. Depending on pulse energy, spectrum, and repetition rate, a substantial subset of those 20 states is indeed populated; see fig. 5.5 on page 103.

It is the different experimental signature of dissociation events in the electronic state A, B, D, and E that allows to distinguish the related excessive heating mediated dissociation events from the time-dependent pump-probe driven dissociation events in state C; see section 5.1.2 on page 101. The latter events are said to belong to the “neutral channel”, the former to the “charged channel”—according to the charge state of the magnesium after the dissociation; cf. fig. 5.1 on page 97. This does not only allow to attribute the dissociation events to their respective photochemical reaction channel but also to employ the molecular ion as a kind of “thermometer” for the vibrational population

distribution. Although not strictly being a thermal distribution the branching ratio of the reaction channels signals higher associated temperatures (more precisely higher vibrational excitations) by an increased dissociation probability in the “charged channel”.

The probability to electronically excite the same molecular ion from state X to A more than once within a sequence of five pulses (see section 5.1.2 on page 101) is less than 1 % for the given experimental parameters; cf. section 4.4 on page 90. During the next 123 blocked pulses ($t = 41$ ms) (see section 5.2 on page 103 for the chopper scheme), vibrational excitations can decay radiatively. Because it will take generally more time than one interval of blocked pulses to loose a considerable amount of energy stored in the vibrational states, the probability for another electronic excitation during the following few exposure intervals shall be small, too. To give an example, the probability² for $^{24}\text{MgH}^+$ not to get excited at all by a train of five pulses is $B(0|0.03, 5) = 0.86$, inducing a probability of $B(3|0.86, 3) = 0.63$ of the molecular ion to stay unexcited also during the next three chopper cycles. That is, in almost $\frac{2}{3}$ of all cases $^{24}\text{MgH}^+$ does not interact with the pump-probe laser pulses during four chopper cycles corresponding to a total of 171 ms. That time must be compared with the about twofold shorter radiative lifetime (91 ms) of the transition $\nu_X = 1 \rightarrow \nu_X = 0$ (see table 5.2 on page 102) and thus is sufficiently long to allow for a significant radiative cooling effect.

The ratio of events in the mentioned two dissociation channels was investigated as function of the effective pulse repetition rate. Five mechanical chopper settings were chosen to block an increasing number of pulses of the original 3 kHz pulse stream, establishing correspondingly longer intervals of radiative cooling. An effective pulse repetition rate can be defined by the fraction of transmitted pulses. In one experimental setting no pulses were blocked, hence the full repetition rate was used.

In agreement with the simulation, the experimental data presented in fig. 5.9 on the next page contained almost no dissociation events in the “charged channel” at low repetition rates of pulses at 280 nm and only a small fraction using 260 nm pulses. Furthermore, the fraction of “charged channel” events in all experiments using 260 nm pulses was bigger than in the experiments using 280 nm pulses, independent of the pulse repetition rate. This finding is ascribed to the higher photon energy allowing to couple to higher lying vibrational states and thus leading to a correspondingly broader vibrational distribution in X after electronic relaxation as well as the ability to surpass the dissociation threshold more readily starting from a broad vibrational distribution. At higher pulse repetition rates, the fraction of dissociation events in the “charged channel” increases which is in qualitative agreement with the simulation. The extrapolation of a linear regression of the 260 nm data to the limit of vanishing effective pulse repetition rate reveals 7 % of all dissociation events to occur in the “charged channel”. So, there is a finite “charged channel” dissociation probability even starting from the vibrational ground state. On the contrary, the “charged channel” probability drops to zero in the limit of low repetition rate at 280 nm.

The simulation takes vibrational heating into account and is able to predict the dissociation channel branching ratio dependence on the pulse repetition rate qualitatively correct. However, it was not able to describe it at the quantitative level. The simulation results of the branching ratio are off by a factor of three, favoring the “charged channel”. One possible explanation for the

² $B(k|n, p)$ denotes the probability density function of a binomial distributed random variable K giving the probability to observe $K = k$ successes in a sequence of n independent Bernoulli experiment each having the probability p .

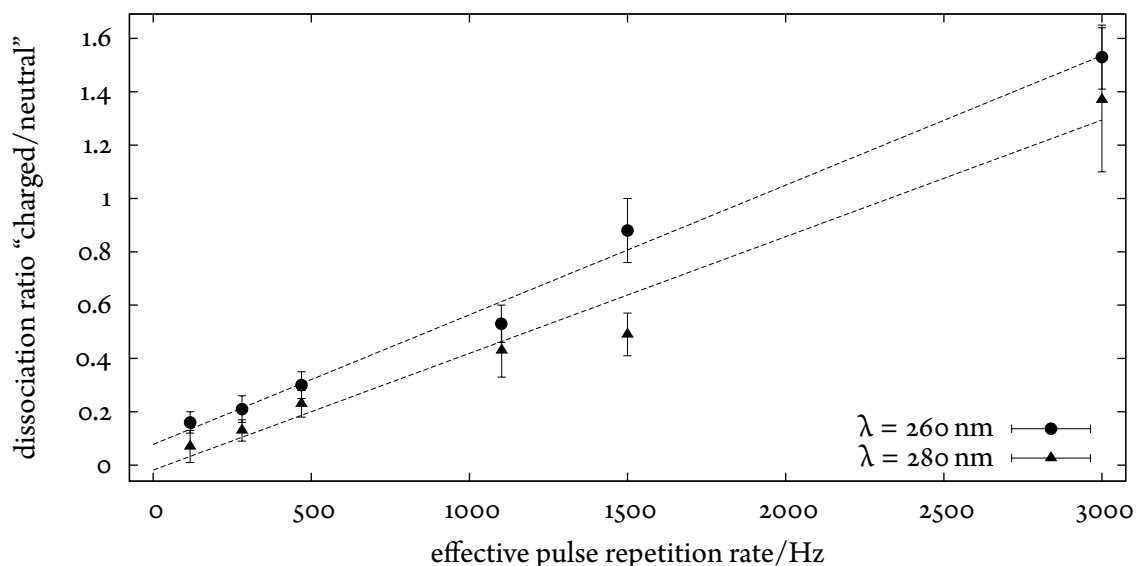


Figure 5.9.: Ratio of observed dissociation events in the “charged channel” $^{24}\text{MgH}^+ \rightarrow ^{24}\text{Mg}^+ + \text{H}$ and “neutral channel” $^{24}\text{MgH}^+ \rightarrow ^{24}\text{Mg} + \text{H}^+$ as function of the effective pulse repetition rate and the central wavelength of coincident ($\Delta t = 0$ fs) pump and probe pulses. The effective repetition rate is given by 3 kHz multiplied by the fraction of transmitted pulses $n_{\text{trans}}/128$ during one chopper cycle; see section 5.2 on page 103. The dissociation ratio is linear dependent on the pulse repetition rate (dashed lines) in the investigated regime for both pulse spectra. The increase of the ratio is attributed to a broad distribution of increasingly higher vibrational states related to vibrational heating caused by decreased duration of radiative cooling; see text. The axis intercepts of the two respective linear fits with the ordinate are slightly different. The regression line of the 260 nm data intersects at 0.07 (see text for an interpretation), that of 280 nm passes through the origin.

discrepancy might be the computational uncertainty of the absolute energy of the electronic states used in the simulation. Their error is estimated to correspond a deviation of up to 5 nm from the actual transition wavelength. This becomes particularly relevant for the electronic state C since there are no measurements available to be compared with the simulation results. The differences in the simulation results of the electronic energy states between different theoretical approaches are discussed in [3]. Further aspects are: the number of simulated vibrational states was restricted to 20, rotational energy has not been taken into account so far, and the concept to describe a train of pulses by an effective repetition rate might not reflect the experimental situation sufficiently accurate for long sequences of transmitted pulses. In future, more profound theoretical studies using an adapted simulation framework could possibly overcome the current shortcomings. In principal, the present measurements can serve as reference that new simulations should be able to reproduce.

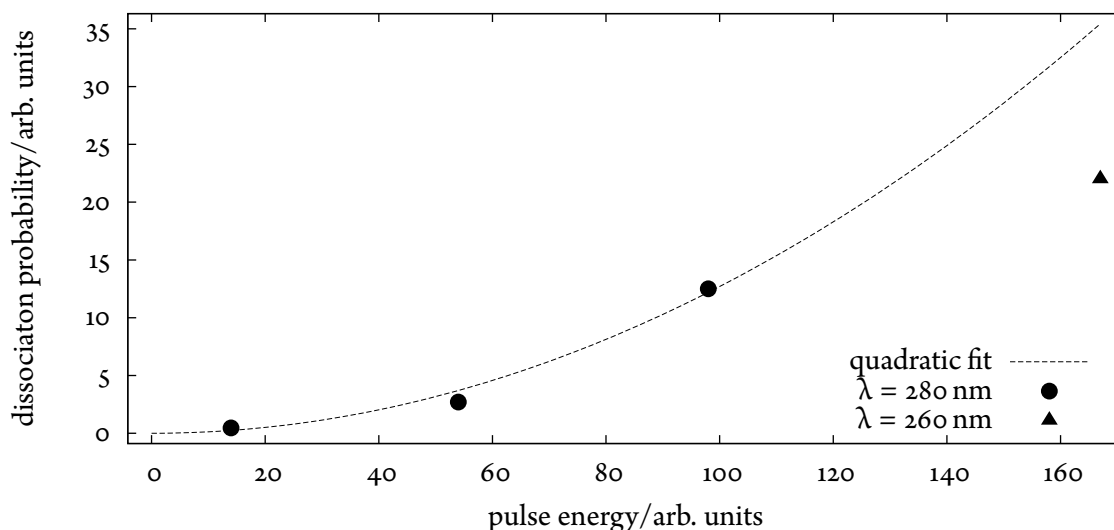


Figure 5.10.: Averaged “neutral channel” dissociation probability per pulse at no pump-probe delay ($\Delta t = 0$ fs) as function of the relative pulse energy. The two-photon assisted dissociation suggests a quadratic dependence (dashed line) which is supported by the experiment (circles, central wavelength 280 nm). For comparison, one data point for pulses at 260 nm (triangle) is shown. Its deviation is assigned to the different dissociation branching ratio (see fig. 5.9 on the preceding page), the uncertainty of the pulse energy measurements depending strongly on the pulse spectrum (see section 4.4 on page 90), and a possibly longer pulse duration (not measured, see same section) reducing the intensity for equal (measured) pulse energy.

5.3.2. intensity dependence

Dissociation in the “neutral channel” via the excited electronic state C takes two UV photons. For that reason a quadratic dependence of the dissociation yield on the total pulse energy was expected. This was confirmed by the experimental findings shown in fig. 5.10. Since the pulse energy, spectrum and focal intensity on the ions were not constant, the average dissociation probability per pulse is reported as function of a normalized pulse energy.

In order to verify the expected quadratic dependence, the dissociation probability needed to be measured for different pulse intensities. Since the third harmonic pulse energy had been carefully optimized (section 4.4 on page 90) already, it had to be reduced to obtain different settings. However, a practical lower bound is set by the required measurement times that increase quadratically with reduced intensities, easily growing to several minutes for a considerable fraction of molecular ions to dissociate. In order to record only one additional statistical relevant data point a series of repeated long-lasting experimental iterations would have to be performed under this conditions—irreconcilable with the limited amount of measurement time at the AS4B beam line. Moreover, the dissociation rate induced by the cooling laser (see section 4.3 on page 87) becomes relevant at this time scale and might render the effort useless. Therefore, the intensity dependence is based on only three but significant data points extracted from “neutral channel” pump-probe assisted dissociation events.

5.3.3. time-resolved dissociation

The proof-of-method time-resolved experiments establish the central result of this thesis. First of all, they combine all current technical abilities of the vacuum apparatus and the achievements of the preparatory steps described in section 4.1 on page 67. Secondly, they demonstrate the application of femtosecond laser pulses to isolated molecular ion targets in an ion trap. Last but not least, the time-resolved vibrational spectroscopy experiments are valuable for their actual results about $^{24}\text{MgH}^+$ and further spectroscopy applications on single molecular ions, too.

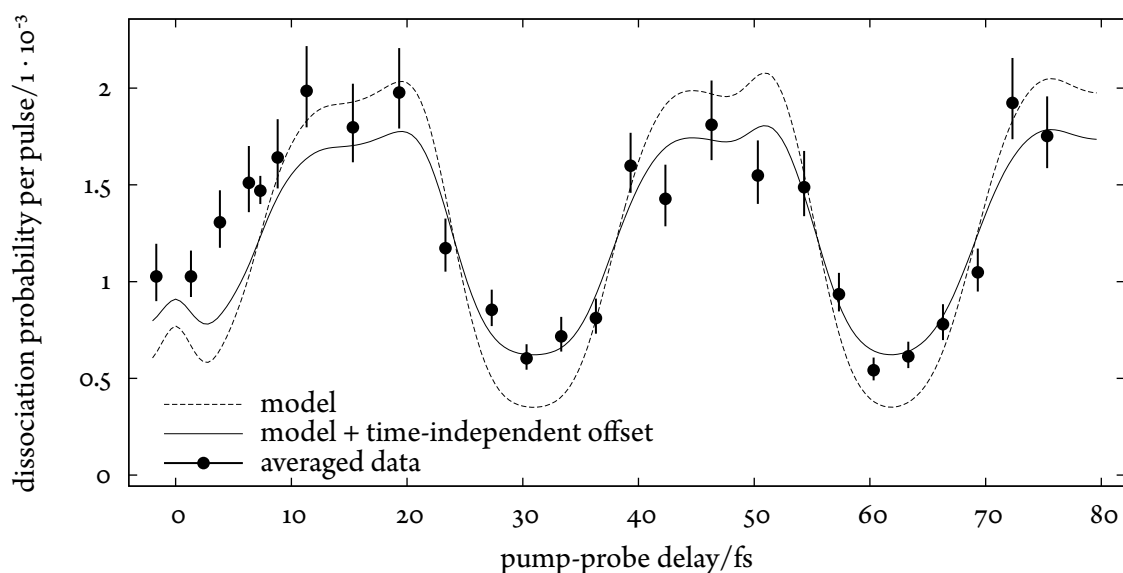
The data presented in fig. 5.11 on the facing page was gathered during one measurement day that was outstanding because of the stable femtosecond laser performance. On that day, comparable spectra and pulse energy conditions could be maintained with only few minor adjustments over a contiguous measurement period of 17 h which allowed to record a total of 122 dissociation runs at 26 different pump-probe delays ranging from $\Delta t = -2$ fs to 75 fs covering $2\frac{1}{2}$ oscillation periods. In order to further minimize systematic errors due to drifts of the femtosecond pulse properties, the data was recorded in randomized order of pump-probe delays following the description of section 5.2 on page 103.

Each data point represents an average over measurements comprising in total about 80 molecular ions under similar conditions. Error bars in the data compilations of this section indicate one standard deviation confidence intervals given by the number of observed dissociation events. A motivation of the applied maximum likelihood approach is presented in appendix C.1 on page 154. The main conclusion of this section is the standard deviation of the distribution of optimally averaged life times to be given by τ/\sqrt{N} where N denotes the total amount of molecular ions contributing to the average and τ the weighted mean.

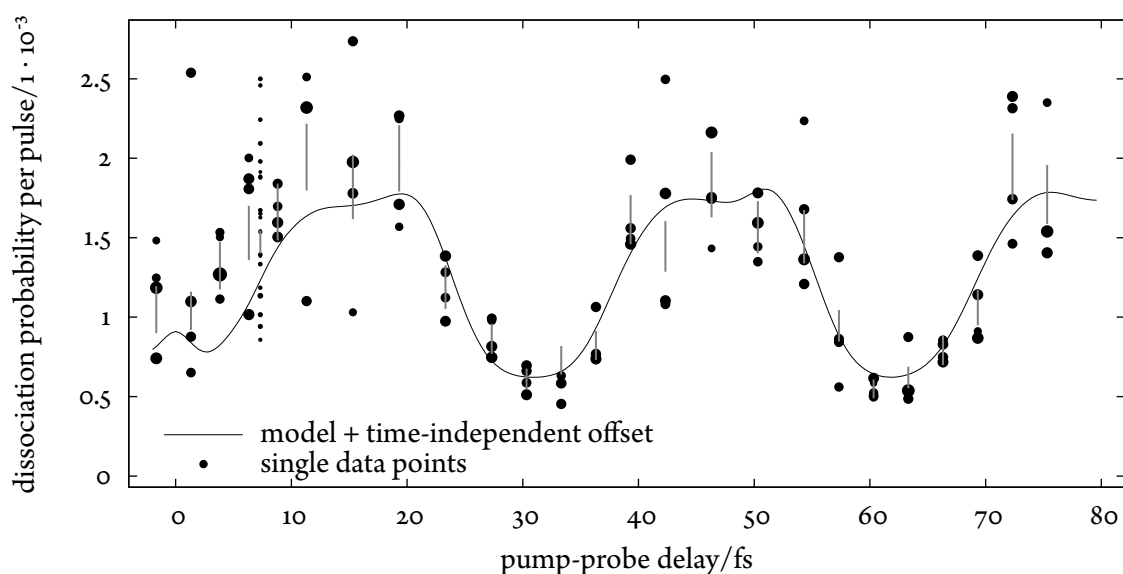
After each 4 to 6 dissociation runs, a reference measurement at $\Delta t = 0$ fs was performed. By comparing several reference measurements, a possible loss of optimum pulse overlap with the molecular ions becomes detectable. As soon as a trend seemed to be notable, dedicated and repeated measurements were applied to statistically confirm the assumption. If that was the case, the measurement campaign were only continued after the beam alignment was readjusted for sufficient overlap again.

Long term variations of the UV pulse energy could be balanced by using some of the fundamental pulse energy reserve that was clipped at an adjustable aperture in front of the third harmonic generation; see section 3.2 on page 58. Short term fluctuations had to be treated by post-processing the measurement data. To this end, the energy of all applied UV laser pulses was recorded. In the data evaluation, the mean of the squared pulse energies of all experiments contributing to one averaged data point in fig. 5.11a on the facing page was computed. Since the anticipated quadratic dependence on the pulse energy could be experimentally confirmed (see section 5.3.2 on the previous page), it is justified to normalize the dissociation probability to the mean of the squared energies of all data points. By that, the data set was corrected for slight ($\pm 5\%$) pulse energy differences and individual data points became better comparable.

As discussed in section 5.3.1 on page 108 and section 4.3 on page 87, there are not only dissociation events in the intended “neutral channel” but also in the mainly time-independent “charged channel”. For example, in the fluorescence image sequence of fig. 5.8 on page 107, two “charged” events (from



(a) Averaged measurements (circles) compared with simulation results (dashed line). The simulated dissociation probability is scaled along the ordinate in order to match the experimental data. This scaling implies a peak intensity of 180 GW cm^{-2} of pump and probe pulse each for randomly oriented molecular ions agreeing well with the estimated peak intensity of 160 GW cm^{-2} . The uncertainty of the experimentally determined time zero is taken account of by a shift of 7.3 fs along the time-axis. Introducing an additional time-independent dissociation contribution leads to almost perfect congruence (solid line) within the statistical error bars. Deviations from the model around time zero are attributed to interference effects by the coincident pump and probe pulses.



(b) Entirety of 122 data points contributing to the averaged values in (a). The relative statistical weights are encoded in the area of the circles. The solid line is identical to the one in (a).

Figure 5.11.: Dissociation probability of the reaction $^{24}\text{MgH}^+ \rightarrow \text{Mg} + \text{H}^+$ as function of the pump-probe delay. The duration of the pulses with 280 nm central wavelength is assumed to be 5 fs ; see section 4.4 on page 90. The simulation assumes $^{24}\text{MgH}^+$ being aligned with the laser polarization axis and takes the GDD of the dielectric mirrors used in the spectral filtering process into account; cf. fig. 4.18 on page 94. Error bars indicate single standard deviation limits.

figures (c) to (d) and from figures (e) to (f)) occurred. Not taking these events into account and just counting all dissociation events would lead to an overestimation of the dissociation probability in the “neutral channel”. To minimize the error by miscounting of events during the data evaluation (see appendix C.1 on page 154), the number of initial molecular ions was reduced by $\frac{1}{2}$ for each observed “charged” event during the exposure interval. A molecular ion dissociating in the “charged channel” indeed reduces the possible number of decays in the “neutral channel” but at an unknown instant. Without better knowledge, it is therefore assumed that the “charged” dissociation happened in the middle of the exposure interval and therefore statistically reduced the possible number of decays in the “neutral channel” by $\frac{1}{2}$.

A second source of misleading counting are events in which molecular $^{24}\text{MgH}^+$ ions are formed from $^{24}\text{Mg}^+$ and H_2 during the exposure. This reaction is known to be assisted by the cooling laser radiation; see section 4.1.5 on page 75. Although the cooling laser power was reduced to the minimum value at which the Coulomb crystal structure could be sustained, there was a finite rate of these events. See section 4.3 on page 87 for quantitative measurements. These events were taken account of by increasing the initial amount of molecular ions by $\frac{1}{2}$ for each molecular ion formation during the exposure. Analogous to the explanation above, the factor $\frac{1}{2}$ follows from the assumption that the formation happened after half of the exposure.

After correction of the data for pulse energy fluctuations and taking the different experimentally distinguishable reaction channels into account, they were analyzed according to the method described in appendix C.1 on page 154 and finally compared with the quantum chemical simulation. To this end, the simulated time-dependent dissociation probability was fitted to the data. The fit uses a scaling factor along the ordinate and a temporal shift along the time axis. The scaling factor accounts for the experimentally not precisely known pulse intensity. The temporal shift corrects for the uncertainty of the experimentally determined position of time zero; see section 5.2 on page 103. From the pulse intensities assumed in the simulation and the scaling factor resulting from the fit, one is able to deduce a pulse intensity of 60 GW cm^{-2} for which the measurement is best described by the model. Whereas the simulation assumes molecules that are perfectly aligned with the linearly polarized laser, the experimental situation is different. Here, the spatial average over molecules pointing in random directions compared with a perfectly aligned ensemble reduces the dissociation probability by three. Consequently, the simulation should match a measurement at an intensity of 180 GW cm^{-2} . This is in good agreement with the intensity estimation (see section 4.4 on page 90) of pulse and probe beam individually of 160 GW cm^{-2} .

The shape of the simulated dissociation curve (dashed) in fig. 5.11 on the previous page is well reproduced by the experimental data. In particular the period of oscillation ($T_{\text{osc}} \approx 31 \text{ fs}$) and the position of the slopes fit well. However, looking closely, one recognizes that the simulated dissociation probability is smaller than the measured one in the “valleys” at about 0 fs, 30 fs, and 60 fs. Additionally, between 0 fs to 7 fs, the slope of the experimental curve is not as steep as predicted by the simulation.

The deviation around time zero is assigned to the complex experimental situation that arises when pump and probe pulse arrive in coincidence at the molecular ion and interfere with each other. Since the beams are not collinear but enclose an angle of 0.6° , a spatially modulated interference pattern forms. Small but not negligible acoustic vibrations of the beam line modulate the

interference pattern also in time. It is not yet fully understood if the simulation is able to correctly reproduce these experimental conditions. Generally, spectroscopic measurements omit this region because of the superimposed side effects. In view of that, the agreement between theory and experiment around time zero is still satisfying.

In order to address the smaller measured contrast $C_{\text{exp}} = 0.51 < 0.69 = C_{\text{sim}}$, where

$$C = \frac{P_{\text{diss,max}} - P_{\text{diss,min}}}{P_{\text{diss,max}} + P_{\text{diss,min}}}$$

is the contrast given by the maximal ($P_{\text{diss,max}}$) and minimal ($P_{\text{diss,min}}$) value of the dissociation probability, the simulation is supplemented by an additional time-independent offset. Using this as third fit parameter (22 % of $P_{\text{diss,max}}$), one achieves simulation and experimental data to agree almost everywhere within the given error bars. The physical origin of the constant offset term has not been unambiguously determined. It appears most probable that several effects play a role:

- The contrast of the dissociation signal depends heavily on the exact shape and absolute energy of the electronic state C. There is however little experimental data available to compare the simulation with. In [3] two differently computed potential energy surfaces of the electronic energy state C are discussed. The potential energy surface computed within the model of this thesis adds a third approach with slightly different results. The slope of this surface defines to what extent the dissociation signal depends on the wave packet position. In the extreme case of vanishing slope there was also no time-dependence in the dissociation. The absolute energy of the potential defines to what extent a certain slope is able to modulate the dissociation signal for a given spectral width. For example, a too energetic pulse spectrum reduces the contrast in the dissociation signal since the pulse spectrum overlaps with the sloped potential curve almost along the complete wave packet trajectory.
- The simulation predicts an unbalance in the intensity of pump and probe pulse to reduce the contrast. In the extreme case of one beam having vanishing intensity (for example not hitting the molecular ion), there would be no contrast (no time-dependence) at all. Given the spatial sensitivity of the beam alignment (see section 5.2 on page 103), the effect on the dissociation contrast is estimated to be on the order of 10 %.
- Time-independent dissociation events in the “neutral” channel such as the events induced by the cooling laser radiation (see section 4.3 on page 87) are not covered in the simulation and would appear as additional constant offset. However, direct measurements in the referred section showed these rates to be comparably small for a total pump-probe experiment duration of about 5 min. Rovibronically excited molecular ions after interaction with a UV femtosecond pulse might be more easily dissociated by a cooling laser photon. But because the spontaneous decay of electronic excitations occurs on the nanosecond time scale, a significant contribution to the dissociation rate is not expected. Therefore, the reduction of the dissociation contrast by cooling laser driven photochemical reactions is estimated to be on the few percent level.
- It has been observed that the contrast but also the shape of the curve of the simulated dissociation probability depends on the pulse chirp. In this respect, the most relevant optical

element are the dielectric mirrors (see section 4.4 on page 90) whose (expected) influence is already taken account of in the simulation. Although the pulse duration has not been measured (see section 4.4 on page 90), any additional effects of other elements in the beam path (for example the pellicle; see appendix B.5 on page 148) should be able to be considered small. Accordingly, the dissociation contrast is expected to be modified on the few percent level at most.

Time-resolved dissociation using 260 nm pulses

The measurements were repeated using pulses of shorter central wavelength 260 nm. The results presented in fig. 5.12 on the next page reveal a qualitatively different dissociation curve compared with the measurements using 280 nm pulses. The dissociation probability is less modulated, i. e. the contrast is reduced. Furthermore, the temporal dependence is less harmonic. Both differences can be explained with the tendency of pulses with blue-shifted spectrum to smear out the time-dependent dissociation signal. Electronic transitions to the excited state C become possible increasingly more independent of the vibrational wave packet position in A. In this sense, the experimental observation agrees well with the model. Also, having a closer look, the agreement between simulation and measurements is astonishing: First of all, it was expected that deficiencies of the quantum chemical model would be more significant at shorter wavelengths. Higher lying electronic states D, E and F become accessible and their correct simulation accordingly more important. Also, the spectral phase of the pulses at 260 nm is expected to be more modulated; see fig. 4.18 on page 94. Slight deviations from the expected pulse form would influence the simulation significantly. Since the spectral phase could not be measured, only assumptions are included in the simulation. By that, systematic experimental deviations are likely but were not observed within the statistical uncertainty. Moreover, the existence of a temporal domain where pump and probe pulse arrive in coincidence and where the agreement with the simulation is reduced also for the 280 nm pulse experiments seems to be confirmed by the experiments at 260 nm. Finally and in contrast to the 280 nm experiment, no additional time-independent dissociation contribution had to be introduced to fit the simulation to the measurement data. This strongly supports that the quantum chemical model is based on potential energy surfaces that are correct within the experimental uncertainty, and that the assumptions on the spectral phase of the UV pulse are correct, too. In conclusion, the measurements at 260 nm and 280 nm demonstrate the success of single molecular ion time-resolved spectroscopy in an isolated environment simultaneously providing a reference for the quantum chemical model developed for $^{24}\text{MgH}^+$.

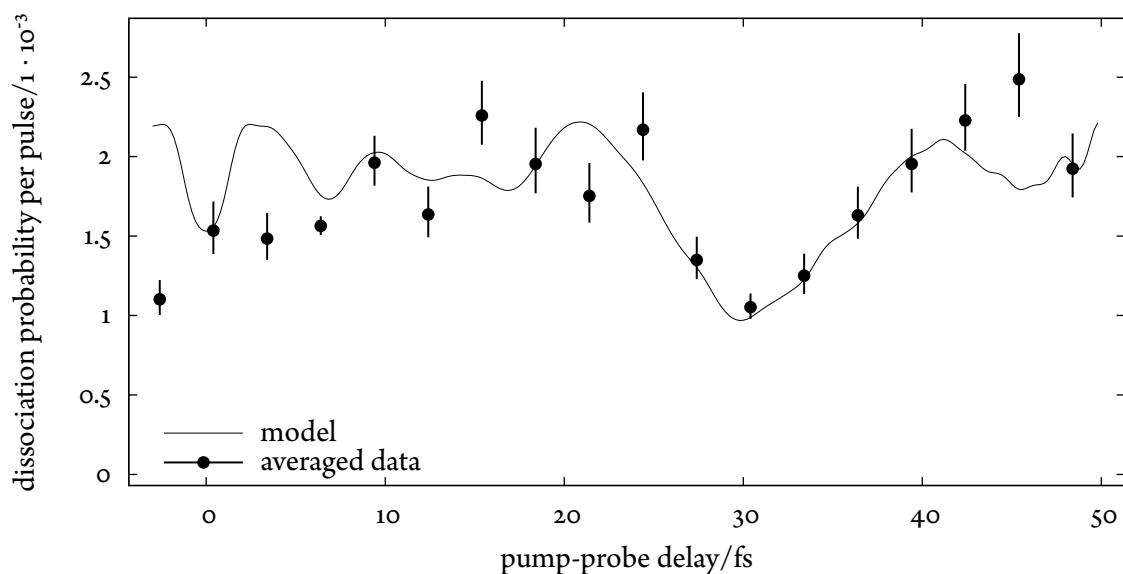


Figure 5.12.: Per pulse dissociation probability of the reaction $^{24}\text{MgH}^+ \rightarrow \text{Mg} + \text{H}^+$ as function of the pump-probe delay. The simulated dissociation probability curve is scaled along the ordinate in order to take the experimental uncertainty of the actual pulse intensity into account. This scaling implies a peak intensity of 33 GW cm^{-2} of pump and probe pulse each. The uncertainty of the experimental determined time zero is taken account of by a shift of 6.4 fs along the time-axis. The duration of the pulses with 260 nm central wavelength is assumed to be approximately 5 fs; see section 4.4 on page 90. The simulation assumes $^{24}\text{MgH}^+$ being aligned with the laser polarization axis and includes the GDD of the dielectric mirrors used in the spectral filtering process; cf. fig. 4.18 on page 94. Error bars indicate single statistical standard deviation limits.

6. Summary and Outlook

Within the framework of this thesis, an apparatus for trapping and cooling of atomic and molecular ions has been devised, designed, and set up. One prominent distinction to other radio frequency traps is the elongated nearly half meter long quadrupole ion guide equipped with ring-shaped electrodes encircling it and forming axial potentials that atomic and molecular ions can be trapped in. Encouraged by the success of similar, extended but closed trap geometries [16, 150] appropriate to store accelerated ion beams, here, an apparatus was developed in which *static* crystalline structures can be investigated but which also allows to conveniently transfer ions along the guide and by that provide the basis for further applications. For example, experiments on many molecular ions reported by the group of Prof. Schiller [121, 122, 148] show alternative applications in this direction and justify our approach towards experiments based on *single* trapped ions under precise control.

It is the goal to advance the methods and actualize a suitable apparatus that is envisioned to deliver molecular ions synchronized to some external signal at a rate of at least 100 Hz and the dispensed molecular ions being localized with a spatial resolution of below $1\ \mu\text{m}$ in ultrahigh vacuum conditions. Molecular ions under ultimate control of the external and preferentially also internal degrees of freedom are expected to be highly interesting objects of investigation for forthcoming X-ray diffraction experiments.

Since the injection of molecules from outside limits the achievable vacuum pressure to an extent that is inadmissible with the vacuum requirements (10^{-10} mbar) necessary for ion trapping with the aspired precision, a need for differential pumping sections arose. This implied an extended ion guide establishing the link between the otherwise isolated injection region and the ultrahigh vacuum environment. Although not all imaginable technical steps of development have been demonstrated yet, the important building blocks were realized and tested. A successful proof-of-method experiment exploring the applicability of the apparatus was performed in the case of isolated, spatially resolved molecular $^{24}\text{MgH}^+$ ions by the means of one-color, time-resolved pump-probe vibrational spectroscopy on the single particle level employing about 5 fs long UV pulses.

6.1. Current achievements

The challenges of this thesis required a series of experimental techniques to go hand in hand and be functional as a whole. An ultrahigh vacuum apparatus ($2 \cdot 10^{-10}$ mbar) was set up that allowed to trap and laser cool atomic $^{24}\text{Mg}^+$ ions. Crystalline structures consisting of between single and up to several hundred ions were observed by fluorescence imaging at several positions along the ion guide with a spatial resolution below $5\ \mu\text{m}$ (FWHM) limited mainly by the imaging optics. By the application of an optimized objective, this quantity can be reduced to better than $1\ \mu\text{m}$. The continuous electrode structure of the guide allowed to trap, cool and observe elongated Coulomb crystals exceeding 1 mm length. Satisfying micromotion compensation—an important prerequisite

for small motional amplitudes and relatedly good spatial localization—was achieved essentially over the entire crystal length by wire electrodes running next to the guide. Owing to the cooling laser being aligned with the long axis of the ion crystal and its beam waist sufficiently big, all atomic ions were equally irradiated providing the ability to cool the atomic ions and unambiguously detect all of them simultaneously by their emitted fluorescence light. For the generation of the cooling laser light (280 nm) as well as the laser light required for photoionization of magnesium (285 nm), two second harmonic generation enhancement resonators were built. They are optically linked via two 70 m long optical fibers to a dye laser system situated in a distant laboratory.

Molecular $^{24}\text{MgH}^+$ ions were formed within a fraction of a second from previously trapped electronically excited atomic $^{24}\text{Mg}^+$ ions and short pulses of injected hydrogen gas by the photochemical reaction $^{24}\text{Mg}^+ + \text{H}_2 \rightarrow ^{24}\text{MgH}^+ + \text{H}$. The molecular ions' amplitude of translational motion was reduced by the means of sympathetic cooling [4] until they integrated themselves into the $^{24}\text{Mg}^+$ ion crystal [20]. By that, the presence of these non-laser coolable, thus non-fluorescing, dark ions and the single particle photochemical reaction events related to them, were detectable with the help of a within this thesis dedicatedly developed image analysis software in an automated way. Also, the software developed for automatic preparation of mixed atomic and molecular ion crystals taking control of: photoionization until a certain number of trapped atomic ions was loaded, cleaning the Coulomb crystal from adverse ion species, and generation of molecular ions by hydrogen injection contributed significantly to the success of the experiments. It simplified this sequence to be repeated several hundred times a day and also assured reliably constant conditions. By all of the mentioned aspects, one first important experimental building block was realized.

Another important step was made by the ion transfer along the radio frequency guide to be functional. Whereas the efficiency with that ions are decelerated and trapped was observed to depend on the initial number of ions and the time of flight, the transfer process itself seems to be lossless. The ions traveling at a speed of approximately 1850 m s^{-1} for about $190 \mu\text{s}$ from chamber 1 to chamber 3 were decelerated in three different ways when they reached their destination. Presently, all tested mechanisms are based on abrupt voltage ramps applied to the ring electrodes. This implies strong forces on the ions and chaotic motion in the trap(s) of chamber 3. Laser cooling and sympathetic cooling allowed to reduce the motional amplitude and form a crystalline ion structure within a few seconds. It was also shown that ion crystals can be interchanged between the two traps in chamber 3 without noticeable interaction and without losing ions.

The apparatus' applicability for single particle experiments with femtosecond time-resolution was successfully demonstrated by connecting it to the AS4B beam line at MPQ where short 5 fs laser pulses were generated by our group. We rearranged the femtosecond laser system to produce third harmonic pulses [19] whose spectrum extended sufficiently far into the red-most accessible region of the given laser system. Since the molecular properties of $^{24}\text{MgH}^+$ required additional spectral filtering on the short wavelength side of the spectrum, little pulse energy turned out to be a crucial concern. This could however be cleared by careful optimization of the third harmonic process and introduction of dielectric mirrors that enhanced the overall ultraviolet transmission of the beam line by a factor of five. The pulsed UV beam was prepared for the aspired pump-probe experiment in a specially designed vacuum chamber. It has been equipped with a high accuracy motion control system that gives access to the degrees of freedom required to split the pulsed beam into two time-

delayed components and to focus and align both of them spatially and temporally with the trapped molecular ions. By using a cascade of differential pumping lines and other preventive measures, the danger of afflicting the ultrahigh vacuum conditions in the trap setup by connecting it to AS4B could be averted.

The results of the proof-of-method time-resolved dissociation experiments on isolated molecular $^{24}\text{MgH}^+$ ions demonstrate that femtosecond spectroscopy on the single particle level under the precisely controlled conditions in an ion trap is feasible and thus establish a third major building block of our approach. Detection of single reaction events was based on the disappearance of an “invisible” (dark) spot in the fluorescence images of mixed Coulomb crystals which demanded single particle resolution and a sophisticated analysis scheme. Because the conditions of molecular ions in vacuum pinpointed to better than $1\ \mu\text{m}$ in space and exposed to a sequence of intense, short laser pulses is different from usual spectroscopy setups, untypical experimental hurdles but also unique chances for new insight emerge. To mention one example, in our approach it is possible to distinguish between different reaction pathways event-wise by analyzing the reaction products that are left in the trap. This has been taken advantage of in the presented $^{24}\text{MgH}^+$ experiments. The ability to separate dissociation events resulting in a neutral magnesium atom and events leaving magnesium in the charged state $^{24}\text{Mg}^+$ allowed to use the molecular ions as a thermometer indicating the increasing amount of energy stored in the molecular vibration and how this builds up by repeated electronic excitations. This interpretation, among others, bases on the proficiency that we gained by mutually stimulating discussions in the framework of a close cooperation with the theoretical femtochemistry group of Prof. deVivie-Riedle which resulted in a computer model that is adapted to the experimental conditions, can take vibrational heating into account, and correctly reproduces the measurements.

6.2. Further development and applications

Towards structure determination using single molecular ion samples

In order to fully exploit the apparatus' potential, there is currently worked on trapping and cooling of $^{138}\text{Ba}^+$ ions. Results of this work will be included in the thesis of Günther Leschhorn. Given the ability to laser cool and trap barium ions, with almost six times bigger mass than $^{24}\text{Mg}^+$, sympathetic cooling of usually still more massive organic molecular ions is expected to be more favorable. This is because the sympathetic cooling rate is optimal if molecular ions and laser cooled ions share a similar mass-to-charge ratio [125, 5]. Presently, the apparatus is equipped with a cryogenic inlet that allows to inject gaseous neutral molecules in chamber 1 and ionize them inside the radio frequency guide by electron bombardment. However, a much bigger class of molecular ions is accessible by the means of electro-spray ionization [125]. By that, large biomolecules can be multiply charged so that their mass-to-charge ratio allows them to be trapped and efficiently sympathetically cooled by $^{138}\text{Ba}^+$, for example. This is why a suitable source has been prepared in a separate setup parallel to the one described in this thesis. Connecting it to TIAMO will open up possibilities for experiments on generic molecular ions and establish another important building block towards realization of our preparation approach of precisely controlled single molecular ions.

Further progress in that direction is expected to be made by modifications of the ion transfer protocol. Whereas the transfer itself seems to be lossless, the stopping mechanism can be improved. One possible approach is to decelerate the ions in a gentle fashion, i. e. apply time-dependent voltage ramps to the relevant ring electrodes such that the corresponding axial potential comforts the ion structure optimally at each instant during the build-up, in principal similar to the concept reported in [153].

In the current configuration of the apparatus, continuous loading, i. e. replacement of ions in chamber 3, should be possible. The required technical steps have been separately demonstrated already. Ions were shown to be photoionized and trapped in chamber 1 independently of the operations in chamber 3. Concomitant transfer of ions from chamber 1 to 3 was demonstrated, too. Finally, ions were easily interchanged between the two traps in chamber 3. In a next step the individual achievements will be combined in a concerted manner.

Yet more control over the external and internal degrees of freedom of molecular ions than already achievable with the currently integrated components is desirable for the anticipated X-ray diffraction experiments. There is however no need for a new apparatus to be developed. The molecular ions' vibrational and rotational energy can be efficiently reduced to corresponding temperatures of typically 10 K—but even sub-Kelvin temperatures are possible [62]—by the means of buffer gas cooling [50] which might be readily implemented in chamber 2. Further control over the external degrees of freedom such as orientation of the molecule in space is envisioned to be addressed by field-free laser alignment [73] techniques. Since there are unused ports on chamber 3 that provide optical access to the trapped ions, these methods can be arranged for on the spot in principal.

In order to really separate single molecular ions from a Coulomb crystal and position them reliably at a given interaction spot where, e. g. X-ray, laser pulses are supposed to hit the molecular ion target, it will probably take an additional finely segmented ion trap at the exit of the present guide. The currently used ring electrodes provide an axial potential but are too coarse for single ion operations. Segmented traps [7, 1] are more suited for this task and can be produced with high accuracy.

One might even dare to ask if single ion separation is actually needed. It might be thinkable to transfer molecular ions embedded in an atomic ion crystal for sympathetic cooling to the X-ray laser interaction spot. A fluorescence imaging system could be used to monitor the actual composition of the mixed crystal. A fast computer program should be able to detect molecular ion positions by recognizing seemingly empty lattice sites in real time, similar to what has been done in this thesis. Based on that information and provided with the excellent control over the electric trapping potential in a micro-structured trap, the ion crystal is imagined to be shifted such that one of the molecular ion coincides with the interaction spot. After a diffraction pattern has been recorded, the crystal can be rearranged for another molecular ion to be positioned. As an additional advantage of this concept, the molecular ions stay in their sympathetic cooling environment all the time.

alternative developments

Topological defects

Another research project currently worked on concentrates on the structure of, in the first instance, pure atomic laser cooled Coulomb crystals. During simulation work on crystalline structures performed within this thesis, previously unrecognized configurations were discovered. They correspond to topological defects that—in simple words—occur when two zigzag zones with opposite “phase” meet inside the same Coulomb crystal. An experimentally observed ion crystal showing this situation is presented in fig. A.9 on page 141. This topic is now further pursued since different kinds of these structures have been observed experimentally and a profound, recent theoretical framework [102] is available. In the mentioned publication, our observations are referred to as topological protected localized distortions of the crystalline structure or “kinks” or discrete solitons. There are localized modes associated with kinks, i. e. motional excitations that are separated from the normal mode spectrum of the crystalline structure in frequency space. At the moment, the kinks are generated by chance upon random crystallization and have a limited life-time of a few seconds probably due to insufficient radial cooling. Much more controlled conditions can be expected from programmed non-adiabatic axial potential ramps that force a linear chain of ions into a two-dimensional zigzag structure faster than the oscillation time of the highest frequency normal mode. Better radial laser cooling might be achieved by replacing one of the blind flanges in chamber 3 with an additional laser port that will allow to irradiate the ions transversely. By that, experiments exploring the quantum mechanical properties of the kinks, such as their stability and decoherence time, are within reach. In view of the increasing precision of methods emerging from the field of quantum information processing implemented in ion traps, it might even be possible to use solitons as quantum bits in the long run [102]. After all, detailed investigations of solitons might be a chance for an interesting complementary development in the quantum information field that otherwise tends to orient towards tiny, micro-structured traps favoring single trapped ions in tailored externally controlled potentials [1].

Single molecule fluorescence

Another experiment that should be realizable at the current status of the apparatus is the detection of fluorescence photons emitted from a single *molecular* ion, e. g. $^{24}\text{MgH}^+$. An electronic excitation with a short (in most cases presumably ultraviolet) laser pulse will be followed by spontaneous decay to the electronic ground state on the nanosecond time scale. Using a sensitive and fast detection system triggered and gated on the arrival of the laser pulse, fluorescence photons emitted a few nanoseconds after excitation should be separately detectable. However, since the total detection efficiency is estimated to be on the order of 10^{-3} only, the same molecular ions should ideally be able to be irradiated repeatedly without destroying it. That is, contrary to the dissociation experiments described in this thesis, a pulsed excitation with negligible excitation of the internal degrees of freedom will be required. The means might be provided by femtosecond UV pulses that are far red-detuned with respect to the molecular electronic transition.

Radio frequency guiding of neutral, polar molecules

Exploiting the broad experimental—already fully implemented—possibilities of the present apparatus in a different direction could lead to experiments aiming on guiding *neutral* molecules with alternating high electric fields. So far, this method—often termed “velocity filtering”, see appendix C.3 on page 159—has been based on static quadrupole fields [92, 160] and slowly (few kilohertz) switched electric fields [93, 99, 172] but the radio frequency regime has not been entered yet. Not only that guiding of neutral molecules with radio frequency fields itself might be an interesting research topic on its own, new perspectives would arise from the ability to guide ultracold molecules and let them interact with simultaneously trapped atomic or even other sympathetically cooled molecular ions. From similar experiments in different configurations [179, 12, 177] promising results have already been reported. This research might lead into the field of cold chemistry. Using the apparatus at hand chemistry could be approached with the precise methods provided by the single particle resolution of trapped ions.

Sequential photochemical analysis

The ability to keep products of a molecular ion after a photochemical reaction in the trap might allow for sequential experimental schemes. One could imagine to determine the mass of products or even spectroscopic experiments exploring the properties of isolated molecular ions after a certain chemical bond was broken, for example. In a visionary picture this could be extended to a complete sequential analysis of macromolecules such as DNA [57].

Appendix A.

Software

In the following, computer programs are described that were central to the success of the experimental work. The programs fall into three categories. There is group of programs that helped to load and prepare atomic and molecular ions in an automated way. A second category comprises the algorithms that were applied to determine the number of non-fluorescent (invisible) molecular ions in a mixed ion crystal. Thirdly, there is code that has been developed for simulating the static and dynamical properties of ion crystals in our RF-guide. These studies helped the interpretation of the ion transfer experiments; see section 4.2 on page 75.

A.1. Laboratory software

The time-resolved pump-probe experiments (see chapter 5 on page 95) required to record sometimes more than 1500 fluorescence images per day. In consequence, the complex experimental ion loading and preparation sequence needed to be repeated many hundred times. In order to efficiently use the limited beam time but also to increase reproducibility, reliability, book-keeping, and speed, the control program *director* was developed. The communication to the CCD has been devised as a separate program *iXon!* that is seamlessly integrated in the experimental control scheme; see section 2.8 on page 52.

A.1.1. *director*

director builds on the cross-platform toolkit wxWidgets [156] and offers an optimized graphical user interface (GUI) whose design is based on the sequential steps of a typical experiment; see fig. A.1 on the facing page. The actions associated with the graphical elements translate mostly into commands to the real-time measurement system ADwin; see section 2.8 on page 52. *director* also journalizes all actions and commands. By that, one can look up the time it took to load ions at which setting of the fluorescence rate threshold, how isotope cleaning, hydrogen injection and ion transfer were performed and what the mating CCD fluorescence image and pulse statistic file names are in hindsight. See section 4.1 on page 67 for a detailed discussion of the individual steps.

a. automatic loading

Automatic loading worked reliably and saved time for the actual experiment. After launching the process, the ADwin system sets several digital signals that cause the mechanical shutters of cooling and photoionization laser to open and the neutral density (ND) filter in front of chamber 1 to be

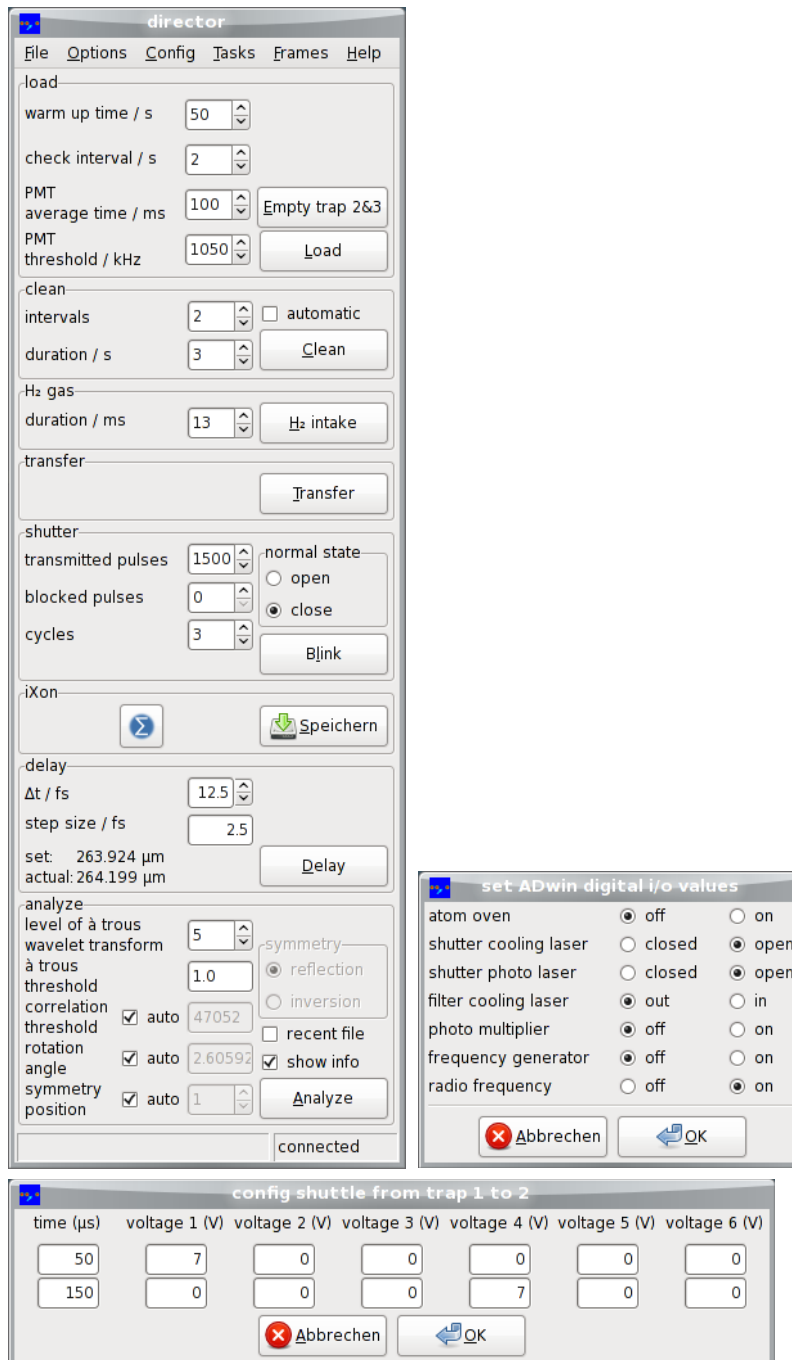


Figure A.1.: Graphical user interface of the experiment control program *director*. All relevant ADwin processes are configured and launched with the help of *director*. The user is guided through the typical experimental procedures by following the interface from the top to the bottom.

flipped out of the beam path; see fig. 2.17 on page 43. At the same time, the accelerating voltage of the PMT is blanked due to excessive stray light hazard (see appendix B.4 on page 147) and the atom oven heating current is turned on.

After the “warm up time” of the atom oven has elapsed (typically 40 s to 60 s, see section 2.5 and fig. B.4 on pages 35–146), a second phase, in which the ADwin program loops over essentially two experimental tasks, starts. In one of the tasks the photon count rate of the PMT, depending on the number of already loaded fluorescing atomic ions, is determined. To this end, the amount of UV stray light in chamber 1 is reduced by blocking the photoionization laser beam and flipping the ND filter into the path of the cooling beam. After that, the PMT is engaged and the photon count rate determined by averaging over the period “PMT average time”. In appendix B.4 on page 147 the photon count rate is shown to depend mainly linear on the number of fluorescing ions in the trap. After the first has been completed, the second task is executed, i. e. the ND filter is flipped out and the photoionization laser shutter is opened again. After the time given in “check interval” has elapsed, the loop repeats starting with the fluorescence rate detection. As soon as this rate exceeds “PMT threshold”, the loading loop is aborted, i. e. the atom oven heating is disrupted and the photoionization shutter is closed. If “automatic” isotope cleaning is not checked, the automatic loading process finishes. Total loading times ranged from 90 s to 120 s.

Otherwise, the isotope cleaning process is launched: For the number of times set in “intervals” an arbitrary wave form generator¹ is activated for the time interval “duration”. It generates a voltage resonantly driving the radial secular motion of the magnesium isotopes $^{25}\text{MgH}^+$ and $^{26}\text{MgH}^+$ simultaneously such that the motional amplitude of these ions grows big enough to overcome the trapping potential and expel the respective ion species from the trap; see section 4.1.3 on page 71. Intermissions by 1 s long phases of regular laser cooling reduces the motional amplitude of $^{24}\text{Mg}^+$ and minimize the loss of these ions during the motional excitation of the other isotopes.

b. ion transfer

Transferring ions from chamber 1 to chamber 3 (see section 4.2 on page 75) is precisely synchronized with the help of the ADwin system. The analog outputs of that system are used to control the voltages that are applied to the relevant ring electrodes. Switching these voltages can be configured in discrete time steps given by the system’s maximal temporal resolution of 2.5 μs . Up to eight synchronized analog voltages are available for timing the transfer process. All of them can be configured in a dialog accessible from *director*’s “Config” menu.

c. shutter

The shutter process can be used to block a sequence of laser pulses repeatedly. It’s adjustable parameters are: “transmitted pulses”, “blocked pulses”, “cycles”. The corresponding ADwin process sets a digital voltage which in turn controls a mechanical shutter in the beam path of the femtosecond laser. The process is synchronized to the 3 kHz pulse repetition rate by a trigger signal which derives from the Pockels cell in the femtosecond pulse amplifier. Upon the arrival of a trigger

¹ G5100A, Picotest

event the ADwin process activates the digital output and begins to count subsequent trigger events. When “transmitted” pulses have passed, the digital output is reset and remains passive until the number of blocked pulses have passed, too. The process terminates after the given iterations have been performed. Additionally, the ADwin system reads a voltage of a photodiode whose signal is proportional to the femtosecond UV pulse energy; see fig. 2.17 on page 43. After the shutter process has terminated, all registered voltage values are written to a file.

d. additional functionality

The remaining three sections of the GUI are used to

- record fluorescence images by remote controlling the acquisition computer “tiamo”,
- adjusting the time delay between pump and probe pulse; see section 3.3 on page 60,
- analyze fluorescence images according to appendix A.2 on the following page.

A.1.2. iXon!

The dedicatedly developed image acquisition software *iXon!* was used to record fluorescence images using a CCD in the detection system described in section 2.6.3 on page 40. The Windows application provides a user-friendly wxWidgets [156] based GUI and builds on top of the software development toolkit SDK v2.84 from Andor. The latter library provides convenient functions required for communication and data exchange with the camera. In order to enhance efficiency, it is independent but closely integrated into the experiment control software *director*.

Upon start, *iXon!* sets a number of parameters that configure the read-out of the CCD. A list of optimized values in regard of acquisition time, sensitivity and read-out noise for the given experimental conditions is summarized in table A.1 on the following page. *iXon!* can be operated in three different modes: “single shot”, “accumulate” and “video” mode. In “single shot” mode the CCD is read out only once. A single fluorescence image acquired with typically 100 ms integration time was in general too noisy for the image analysis algorithms to be successful; see appendix A.2.3 on page 135). In the preferred “accumulate” mode, the camera can record several (usually five) consecutive images and sum them already in its internal memory. By that, readout holdups are minimized and the noise in the averaged image reduced such that technically easy analyzable image data resulted. The corresponding total acquisition time of five accumulated images consisting of 1000 pixel × 200 pixel with 100 ms integration time each measured 607 ms including a 107 ms readout overhead. Simply using “single shot” mode with a five times longer integration time is less preferential since the maximal electron capacity of the CCD’s single pixel potential wells can saturate. The “video” mode differs from the first two by continuously retrieving data from the camera with the maximum achievable transfer rate resulting from the current parameter setting.

In order to make the image recording more efficient and fail-save, the data is written to files in a Andor specific file format (“.sif”) with automatically generated names. When *director* takes control over *iXon!* it is switched into *remote* mode which disables the GUI for user input. Image data

Table A.1.: Optimized camera configuration that is applied after starting *iXon!*.

parameter	setting
sensor temperature	-80 °C
electron multiplying gain	3300
vertical shift speed	3.722 μ s
horizontal shift speed	13 MHz
pre-amplifier gain	$\times 2$
exposure time	100 ms
number of averaged exposures	5
binning	1 \times 1
left pixel	1
right pixel	1000
bottom pixel	400
top pixel	600

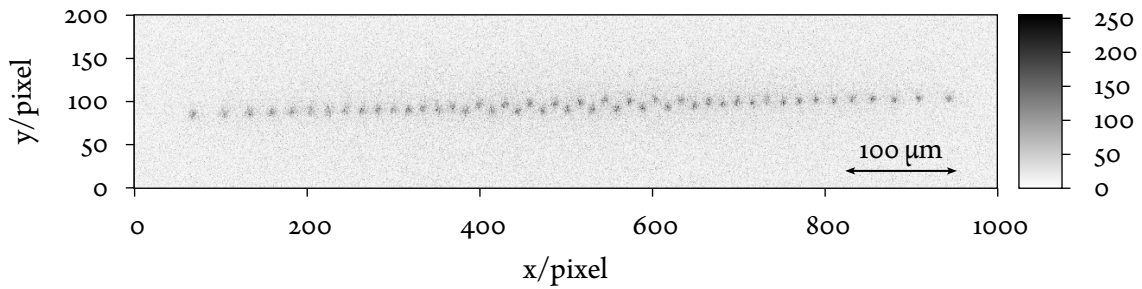
recorded in *remote* mode can be displayed, examined, analyzed, and saved via *director*. This guarantees the files to be journalized in *director*'s logbook that includes all other relevant experimental parameters associated to the fluorescence image automatically.

A.2. Image analysis software

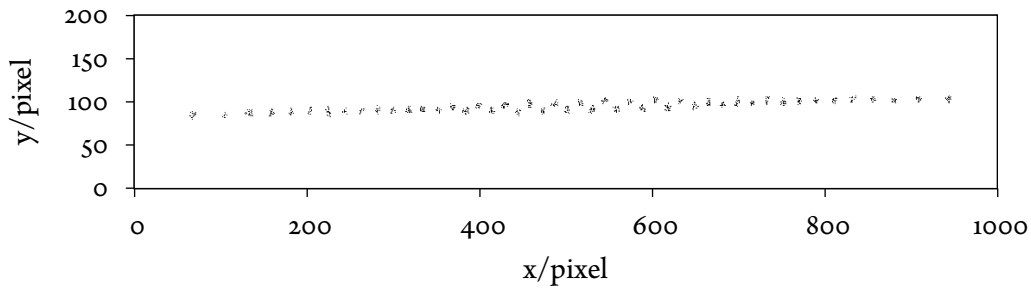
This section describes the set of adapted and independently developed algorithms used in a two-step image analysis process. The code has been implemented in the program *crystal inspector* that was applied for the evaluation of fluorescence images recorded during the pump-probe experiments described in chapter 5 on page 95. In a first step, the number of fluorescing (bright) atomic ions in these image is determined. This counting can be accomplished by humans quite reliably but not on a rational time scale in view of the huge amount of fluorescence images to be analyzed. Instead, a suitable algorithm employing the *à trous* wavelet transform was applied; see also fig. A.2 on the next page. In a second step, the number of not-fluorescing (dark) molecular ions in the mixed ion crystal was determined. This is usually a hard and time-consuming task for humans. Even computer programs are seldom correct in this point (see below for an explanation) but they are much faster. Applying verification by humans to the dark ion positions derived by the computer turned out to be an efficient and reliable strategy.

A.2.1. *À trous* wavelet transform

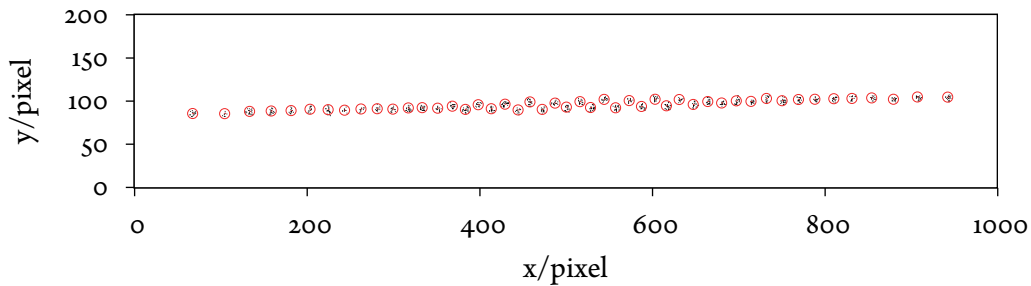
The algorithm for bright ion (called spots in the context of this section) detection bases on the so called *à trous* wavelet transform. The *à trous* transform of some given function—similar to the Fourier transform—is a completely equivalent representation. While the Fourier transform uses non-local, oscillating basis functions, wavelets are localized in the sense, that their basis functions



(a) Original (raw) fluorescence image data; see table A.1 on the preceding page for camera settings.



(b) Multiscale product correlation image after application of thresholding. The pixels carry binary information only: black (active) or white (background).



(c) Centroid positions of the identified pixel clusters depicted a circles with the image of (b) in the background.

Figure A.2.: The process of identifying the position of all 48 bright $^{24}\text{Mg}^+$ ions in the fluorescence image (a) is composed of two parts. First, the à trous algorithm and a multiscale thresholding strategy are applied to obtain a noise-filtered binary correlation image (b). Subsequently, the pixel clustering algorithm is applied to obtain the desired result (c)—centroid position coordinates for each fluorescent ion in precise consistence with the original data. See the text for a definition of the terms. The slight rotation by 1.3° visible in the images is due to the CCD camera (see section 2.6 on page 37) being mounted with a slight tilt but automatically taken account of by the analysis program.

are damped or restricted to a compact carrier [67]. Loosely speaking, wavelets are particularly suitable to frequency components of some signal as a function of time. For example, wavelet analysis is often used to investigate or store acoustic data. In these applications, the relevant quantities are time and frequency. In image analysis, they are replaced by their correspondences space and scale.

Fluorescence images are analyzed as a function of *scale*, i. e. they are decomposed into sub-images of ever decreasing detail leading to a *multi-resolution* representation. By combining all sub-images in a suitable way, the original data can be restored. However, the sub-images can also be combined differently, better serving the purpose of spot-detection.

a. *à trous* decomposition

The implementation of the applied algorithm adapts the description given in [123]. There, the original data $A_0(x, y)$ — x and y denoting pixel positions (called coefficients in the context of this section)—is convoluted with a one-dimensional kernel $h^0 = [1/16, 1/4, 3/8, 1/4, 1/16]$ which acts as a low-pass filter. The convolution smooths the original data resulting in an *approximation* $A_1(x, y)$:

$$A_1(x, y) = \sum_{l=-2}^{l=2} h^0(l)A_0(x + l, y).$$

The difference between approximation $A_1(x, y)$ and the original data $A_0(x, y)$ defines the first *wavelet* plane $W_1(x, y)$:

$$W_1(x, y) = A_0(x, y) - A_1(x, y).$$

Instead of applying the linear kernel h^0 twice in both dimensions of the fluorescence image, in *crystal inspector* a two-dimensional analogue

$$H^0(i, j) = \begin{matrix} i/j & -2 & -1 & 0 & 1 & 2 \\ -2 & \left(\begin{array}{ccccc} \frac{1}{256} & \frac{1}{64} & \frac{3}{128} & \frac{1}{64} & \frac{1}{256} \\ \frac{1}{64} & \frac{1}{16} & \frac{3}{32} & \frac{1}{16} & \frac{1}{64} \\ \frac{3}{128} & \frac{3}{32} & \frac{9}{64} & \frac{3}{32} & \frac{3}{128} \\ \frac{1}{64} & \frac{1}{16} & \frac{3}{32} & \frac{1}{16} & \frac{1}{64} \\ \frac{1}{256} & \frac{1}{64} & \frac{3}{128} & \frac{1}{64} & \frac{1}{256} \end{array} \right) \\ -1 & & & & & \\ 0 & & & & & \\ 1 & & & & & \\ 2 & & & & & \end{matrix}$$

is implemented. A_0 is convoluted coefficient-wise with the matrix H^0 . Coefficients close to the boundary are handled specially. Adjacent coefficients symmetrically reflected about the border are used to fill in missing values outside the image area.

At the next coarser level $J = 1$, A_1 serves as initial image and is convoluted with an augmented kernel H^1 resulting in a further smoothed approximation A_2 . The kernel H^1 is obtained from the original one by inserting zeros in between all pairs of neighboring entries of the matrix H^0 . The result is a 9×9 matrix whose every other entry vanishes. It is filling in zeros that the name *à trous*—with holes—stems from. Convolution with H^1 is seen to have a stronger averaging effect since the involved neighborhood of a coefficient is increased by a factor of two. The associated wavelet plane $W_2 = A_2 - A_1$ is computed accordingly.

The recursion continues until level J is reached. At this stage, there are $J + 1$ approximations, J wavelet planes and H^J contains $(2^{2+J} + 1)^2$ entries. The set $\{A_J, W_1, \dots, W_J\}$ is called the *à trous wavelet representation* since the original data

$$A_0(x, y) = A_J(x, y) + \sum_{l=1}^J W_l(x, y)$$

can be restored from it.

b. multi-scale product

Since each approximation A_l contains as many coefficients as the original image A_0 but no additional information, a lot of redundancy must be hidden in the wavelet planes. The approach described by [123] tries to exploit this redundancy. As the purpose of the analysis is to find small spots, the relevant image details can be assumed to comprise only a few coefficients. In the first levels of the wavelet analysis—when the filter support of H^l is still small—significant coefficients in the wavelet planes arise from small details only. With shrinking resolution at coarser levels $l \leq J$ of the analysis, significant coefficients in the wavelet plane are due to spatially extended image details. Small sized details tend to wash out at larger scales. The key idea is to define a coefficient-wise *multiscale product*

$$P_J(x, y) = \prod_{l=1}^J W_l(x, y).$$

Olivo-Marin [123] states that marks of small-sized details only propagate through wavelet planes of increasing scale if they originate from significant image features but reduce to negligible small values, in the case of noise for example. This correlation between coefficients throughout the W_l gets amplified by the product $P_J(x, y)$. In fact, the correlation coefficients of noisy image areas tend to vanish almost completely.

c. thresholding

In order to filter noise more efficiently, after each level l of the wavelet analysis an additional thresholding step is appended. Coefficients in the wavelet plane $W_l(x, y)$ below the threshold t_l are set to zero. According to [123] t_l is about unity if defined by

$$t_l = \frac{3}{2} k \bar{\sigma}_l.$$

Here, $\bar{\sigma}_l$ denotes the *median absolute deviation from the median* of the coefficients in the wavelet plane at level l . By a good choice of t_l , depending on the image details and noise, only the most relevant coefficients of the plane survive the thresholding.

A second thresholding step is applied after the correlation product P_J of the modified wavelets has been computed. After all coefficients $P_J(x, y)$ above a predefined value t_p are set to unity and zero otherwise a binary approximation of the original fluorescence image results. In *crystal*

inspector, t_p can be chosen freely or automatically computed such that $\frac{1}{3}$ of all coefficients exceed the threshold.

Figures A.3 and A.4 on pages 134–133 show wavelet and approximation planes up to à trous transform level $J = 5$. The (first) thresholding step is omitted in these figures in order to visually emphasize the effect of gradually increasing scale. By comparing the results, one should be aware of the different color scales. Due to the discussed pronounced averaging at larger scales, the amplitudes of the wavelet plane coefficients become vanishingly low. The final binary correlation image is shown in fig. A.2c on page 129.

A.2.2. Segmentation

At the end of the à trous algorithm, the original image is reduced to a grid of binary values. Only the active pixels contain signal. In order to extract useful information, a few coordinate pairs indicating fluorescing ions must be derived from the unordered set of active pixels.

To this end, the active pixels are clustered. The challenge is to automatically determine how many pixel clusters should be formed and which clusters the active pixels should be associated with. In this respect, the algorithm implemented in *crystal inspector* is inornate straightforward but successful. Many alternative but unapplicable approaches to the segmentation problem can be found in the literature [140]. Often, a predetermined number of clusters is assumed which is, however, essentially the most interesting but unknown information to be extracted from the fluorescence images.

a. dismissing spurious pixels

In a preparative step, the quality of the correlation image is enhanced once again by discarding *spurious* active pixels. To this end, the following loop is applied to all active pixels p_i .

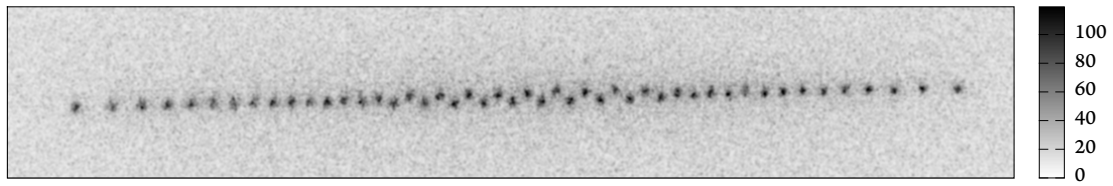
1. choose some active pixel p_i from the correlation image
2. determine the number n of all other active pixels p_j closer than R to p_i
3. if $n < N$, make the spurious active pixel p_i passive
4. repeat until all active pixels are examined

By the completion of this loop a correlation image is obtained that solely contains active pixels with at least N other active pixels in a R -neighborhood. A good choice of parameters is $N = 3$ and $R = 5$ pixel.

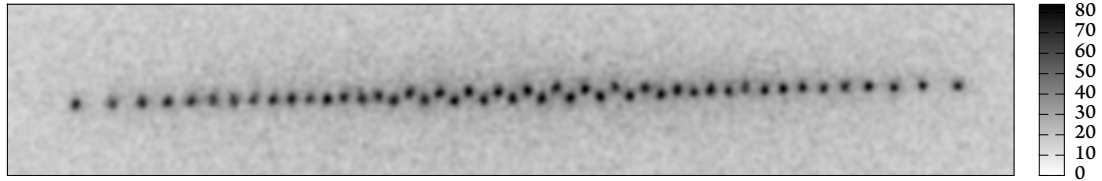
b. clustering

The actual clustering algorithm is implemented by the following loop.

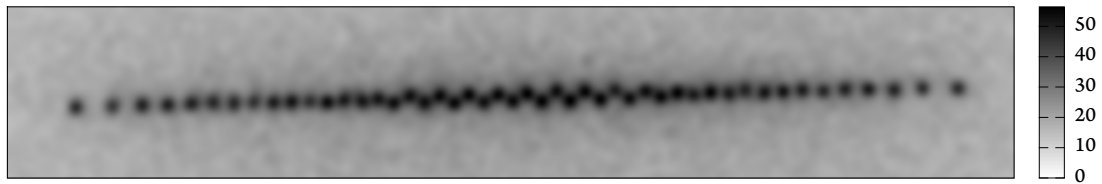
1. choose some active pixel from the correlation image that has not yet been associated with a cluster, form a new cluster c_l and associate the chosen pixel with that
2. choose some pixel p_c from cluster c_l



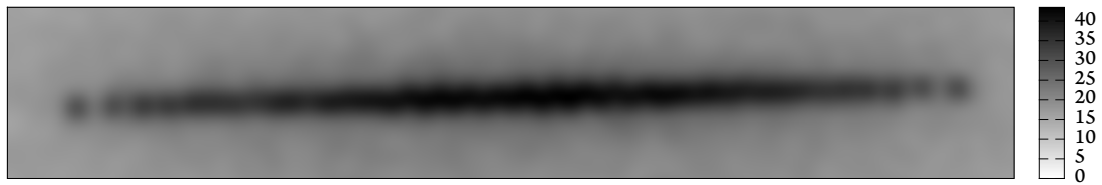
(a) $J = 1$



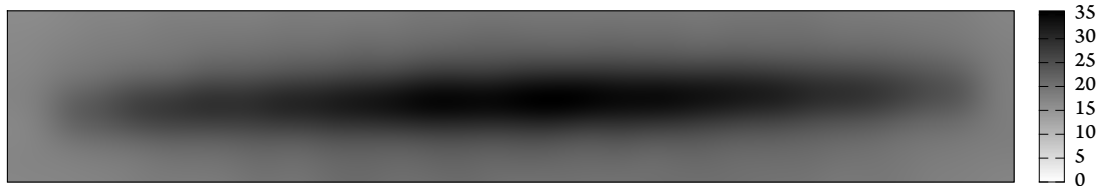
(b) $J = 2$



(c) $J = 3$



(d) $J = 4$



(e) $J = 5$

Figure A.3.: À trous approximation planes $A_J(x, y)$ of the fluorescence image shown in fig. A.2 on page 129 at scales $J = 1$ to 5.

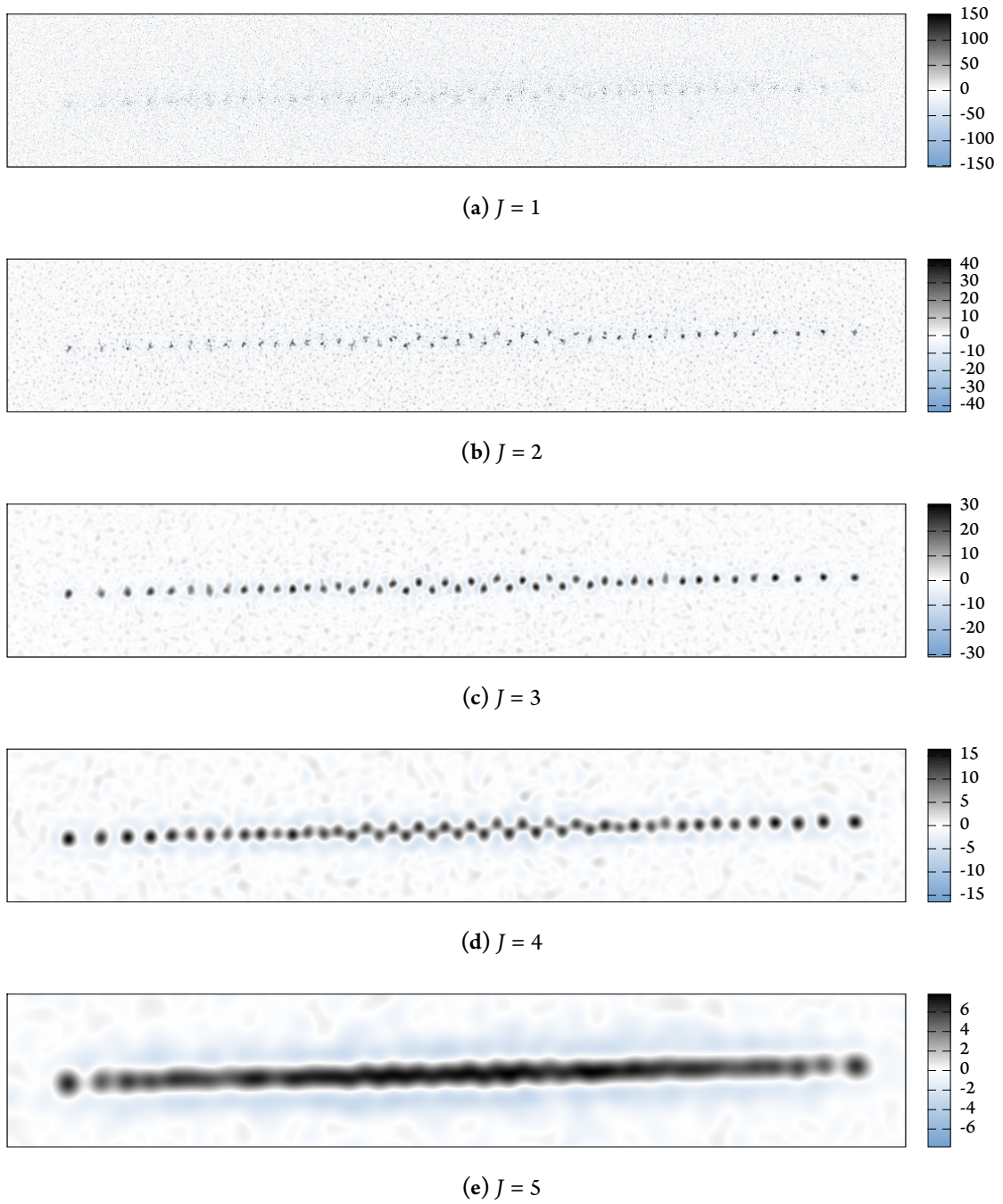


Figure A.4.: À trous wavelet planes $W_J(x, y)$ of the fluorescence image shown in fig. A.2 on page 129 at scales $J = 1$ to 5 .

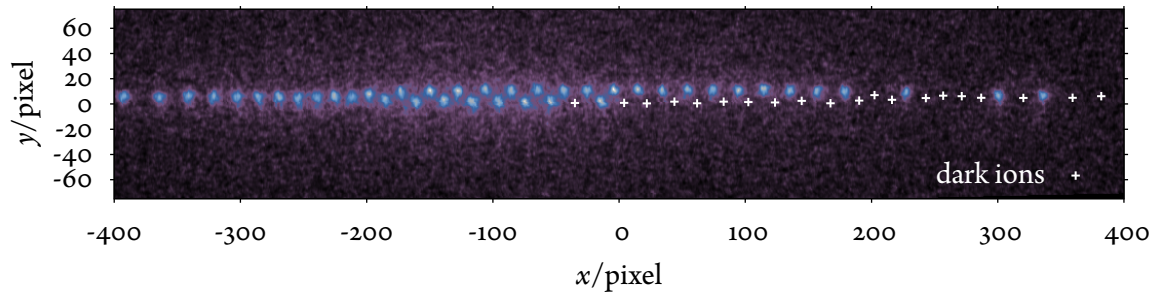


Figure A.5.: False color fluorescence image showing a mixed Coulomb crystal containing 41 laser cooled (bright) $^{24}\text{Mg}^+$ ions and 21 sympathetically cooled not visible (dark) $^{24}\text{MgH}^+$ ions indicated by white crosses.

3. find all other active pixels p_i that are closer than R to any pixel of the cluster c_l and associate them with the cluster
4. goto 2 and repeat until no other pixel can be associated with the cluster
5. goto 1 and repeat until all active pixels are associated with some cluster.

In this case, parameter R determines the cluster size and gives the largest allowed distance between any pair of pixels associated with the same cluster. From another point of view, R controls the preference of establishing new clusters over associating more pixels with less clusters. $R = 5$ pixel turned out to be a good choice for the fluorescence images recorded within this thesis.

At the end of the segmentation process, the correlation image information has been condensed once more. In summary, the image analysis consisting of the à trous decomposition and the clustering algorithm reduced the plethora of data contained in the original fluorescence image (usually $200 \text{ pixel} \times 1000 \text{ pixel}$ carrying 14 bit integer values) into only a few coordinate pairs encoding the conjectured positions of fluorescing ions. On a regular PC it takes on the order of 100 ms to run the complete process.

A.2.3. Dark ion identification

The second part of in the image analysis focuses on determining the number of sympathetically cooled (dark) molecular ions embedded in a Coulomb crystal containing only laser cooled fluorescing (bright) atomic ions otherwise. In section 1.3 on page 17 it is pointed out that molecular ions appear dark or invisible in the fluorescence images.

Task of the dark ion identification algorithm is to spot the position of dark ions whose presence manifests itself in seemingly unoccupied crystal lattice sites. Thus, dark ions become indirectly visible by surrounding bright ions only. One example of an ion crystal containing dark and bright ions is shown in fig. A.5. Different viable strategies for identification of dark ions were pursued. The solution discussed in the following was preferred because of the possibility to performed it mostly automatic. Another method is briefly mentioned at the end of this section.

The key principle of the approach exploits the symmetry property of the ion crystal that is implied by the ellipsoidal shape of the trapping potential; see section 1.1 on page 7. The individual

ion positions in the minimal energy configuration of the crystal are symmetric with respect to the minimum of the trapping potential. The two-dimensional fluorescence image projections of linear chains and zigzag structures (see section 4.1.1 on page 68) are either reflection symmetric with respect to a line along the radial direction intersecting the crystal center (origin) or inversion symmetric with respect to the origin, depending on the total number of ions contained in the crystal. For even numbers of ions, reflection symmetry applies, inversion symmetry otherwise. The dark ion identification algorithm can thus be formulated as an optimization problem for the discussed symmetry types.

To begin with, the bright ion coordinate pairs obtained in the previous step (appendix A.2.1 on page 128) are rotated such that the crystal is aligned horizontally (taking account of a slightly tilted CCD); see the related cross-hair in fig. A.6 on the facing page. This is accomplished in an automated way by fitting a line to the coordinates. The rotation angle $\alpha = \arctan(m)$ follows from the slope m of that line. In the next step, the algorithm computes the number of bright ions that have a corresponding symmetric bright ion mate assuming one of the two discussed symmetry types and some origin position. If there is no bright ion at the corresponding symmetric lattice site “on the other side” of the crystal, this position is marked to be occupied by a dark ion.

The algorithm’s output is a list of coordinate pairs of all bright and dark ion coordinates that is updated every time changes to the symmetry type or origin position are made. All three parameters (one for the symmetry type, two for the origin position) are easily adjusted using *crystal inspector’s* GUI. It is even possible to have the computer try to find the correct symmetry by looping over all possible parameter combinations and pick the one that minimizes the dark ion count. For ion crystals containing none or few ($\leq 10\%$) dark ions, the algorithm usually finds the correct solution reliably. However, depending on the fraction and the positions of the dark ions, the computer might also be wrong. Fortunately, the symmetry origin was often known beforehand from previous image analysis runs under identical trapping and cooling conditions and did not need to be determined anew all the time. In most cases only small adjustments corresponding to at most one or two pixels of the fluorescent image were sufficient to fine-tune the symmetry origin. Since the bright and dark ion positions are shown in different color as an overlay to the original fluorescence image (see fig. A.6 on the next page) and updated in real-time after a parameter was changed, the validity of the conjectured ion positions could readily be checked visually.

There are crystal configurations which the described algorithm cannot handle. This includes all cases where two dark ions occupy a pair of symmetric lattice sites. Due to a lacking symmetric bright ions mate there is no (currently implemented) way to detect pairs of dark ions in that position. Nonetheless, if bright ions surround the dark ions of that pair, this shortcoming is easily recognizable. It is however hard to detect if the overlooked two dark ions happen to sit at the very ends of the crystal. In this situation the experienced experimentalist must notice untypical ion distances of the last visible bright ions at the ends of the crystal. Comparison of the crystal to similar images or alternative methods are needed in order to investigate the situation further. The algorithm fails also if the assumption of global symmetry is not satisfied, for instance if the crystal is not in its minimal energy configuration; see fig. A.8 on page 140.

When the result of the previous method was ambiguous, an alternative dark ion detection technique was at hand. The fluorescence images were compared with templates from a catalog of

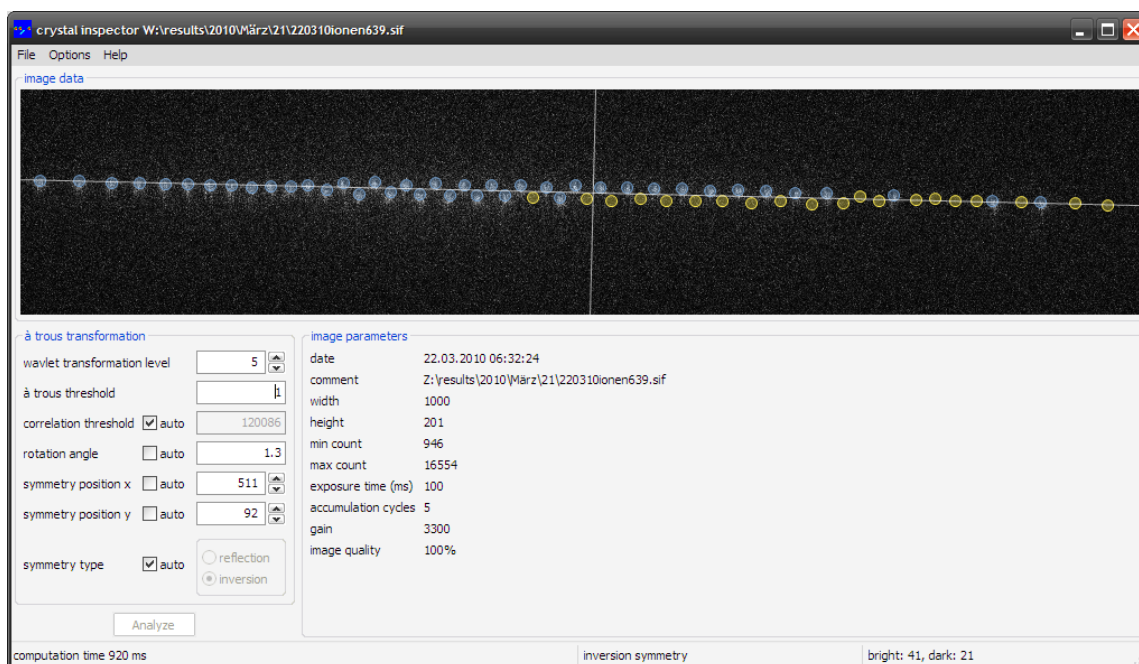


Figure A.6.: The program *crystal inspector* showing the same fluorescence image as in fig. A.5 on page 135. The original data is displayed and overlaid by circles indicating the final result of the image analysis as bright ions (blue) and suspected dark ions (yellow). The cross hairs visualize the rotation angle and the symmetry center. In the left pane, the most important parameters of the \hat{a} trous decomposition, thresholding and symmetry determination can be controlled. Information about the original data is presented in the right panel.

precomputed crystals of differing total ion number for given trapping conditions; see appendix A.3.1 on the next page. Only one template will overlap perfectly with all bright ion positions. The dark ions positions can be read off from the unoccupied lattice sites of the template. Figure A.7 on page 139 illustrates the application of this method for one mixed Coulomb crystal. One disadvantage of this approach is the high degree of human interaction. It turned out to be too time-consuming to become a standard tool. Contrastingly, the previous described algorithmic approach was efficiently applied with great success.

A.3. Simulation software

During the design process of the experimental apparatus but also in order to help the interpretation of measurement results, suitable programs for computing crystal ion structures in static and time-varying potentials became necessary. First, the program used for static simulations is described. In the second section, the dynamic case is covered.

A.3.1. Adaptive simulated annealing

There is no analytic solution for the minimum energy configuration of an ion crystal containing many ($N > 3$) ions in some (arbitrary) trapping potential. In the case of $N = 2$ identical ions of mass m trapped in a harmonic potential characterized by the frequency ω , the solution is readily found from the balance of Coulomb repulsion and the restoring external force pointing to the trap center:

$$\frac{1}{4\pi\epsilon_0} \frac{e^2}{d^2} = m\omega^2 x.$$

This allows to derive an explicit expression for the positions of the symmetrically displaced $x_1 = -x_2 = x$ ions with distance $d = 2x$:

$$x_{1/2} = \pm \left(\frac{e^2}{16\pi\epsilon_0 m\omega^2} \right)^{1/3}.$$

Conversely, the above equation shows that the trap frequency can be derived from a measurement of the distance of two identical ions. The case $N = 3$ can also be treated algebraically. For all crystals containing more than three ions, numerical methods have to be applied [86].

It is advantageous to treat this as a minimization problem for the total energy E_{tot} of the crystal:

$$E_{\text{tot}}(\mathbf{r}_1, \dots, \mathbf{r}_N) = E_{\text{trap}} + E_{\text{col}} = \sum_{i=1}^N \varphi_{\text{trap}}(\mathbf{r}_i) + \frac{e^2}{4\pi\epsilon_0} \sum_{i=1}^N \sum_{i>j}^N \frac{1}{|\mathbf{r}_i - \mathbf{r}_j|}.$$

The contributions to E_{tot} are: the potential energy of all ions in the electric potential of the trap E_{trap} and electrostatic Coulomb interaction E_{col} between the ions. The ideal algorithm should vary the ion positions \mathbf{r}_i until the total energy attains its global minimum. One should bear in mind that the posed problem is high dimensional. Every additional ion enlarges the configuration space by three dimensions (x , y and z coordinates). Hence, the search space is continuous and spans $3N$ dimensions in total. A brute force method would not be successful in finite time.

Instead, the open source algorithm called *adaptive simulated annealing* (ASA) [84, 85] was considered. Common to all simulated annealing algorithms is the notion of a state vector—here all ion positions—that is varied randomly. A new state vector will almost exclusively be accepted if it reduces the total energy below the minimal value found so far. If the energy of the new state vector is greater, it can also be accepted to a small probability exponentially decreasing with the energy difference. By that, the search is given a chance to find a way out of local minima. The variation of the state vector is usually reduced gradually, simulating a decreasing temperature (annealing). If the global minimum is far away from the current state vector, it becomes increasingly unlikely to find it at low temperatures. This is why an appropriate algorithm best samples the search space coarsely in the beginning and converges efficiently to the global minimum once an approximate position of the minimum has been determined. There are mathematical proofs [61] that identify the fastest annealing schedule that still allows to find the global optimum reliably. The annealing schedule depends mainly on the random number distribution from which the state vector variation is generated. However, one often has to sacrifice this mathematical certainty for reasons of limited

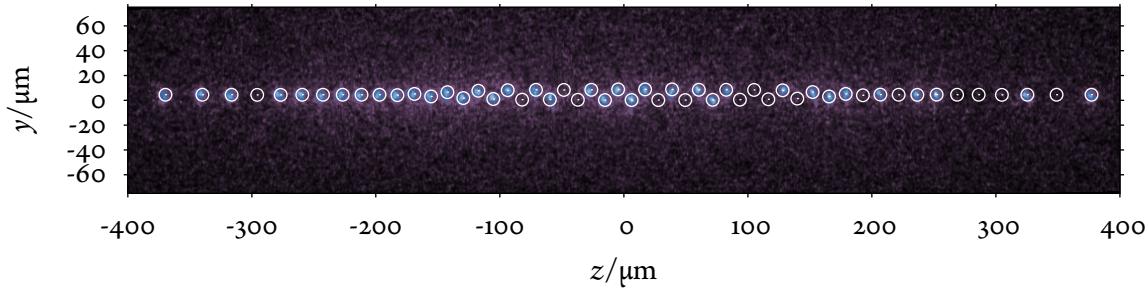


Figure A.7.: False color fluorescence image of a mixed Coulomb crystal containing 37 $^{24}\text{Mg}^+$ (bright) ions and 16 $^{24}\text{MgH}^+$ (dark) ions. Indicated as white circles are the ion positions of the the minimum energy configuration solution of a 53 ion crystal computed by the adaptive simulated annealing algorithm. It was configured to obey the following measured experimental parameters: axial trap frequency $\omega_{\text{ax}} = 2\pi \times 31$ kHz, radial trap frequency $\omega_{\text{rad}} = 2\pi \times 496$ kHz, imaging system magnification factor $M = 9.8$. The comparison of experimental and simulated data reveals the success and validity of the computed crystal structure. Thus, simulating crystal structures in advance and comparing them to fluorescence images provides a method to determine the number of dark ions contained in a Coulomb crystal; see appendix A.2.3 on page 135.

computational resources. So does the employed ASA algorithm. It implements various techniques that enhance the convergence rate. To give an example, all state vector components (ion coordinates) have individual temperatures whose annealing rates are adapted to the significance of that parameter to the energy reduction. Refer to [84] for other concepts *reannealing* and *quenching* used in ASA.

To serve the purposes of this thesis, the original implementation of ASA [85] was stripped from irrelevant parts (the original algorithm knows more than 100 options), wrapped in a C++ class, and incorporated into an application that sets up all options and the parameter space required to reflect TIAMO's real physical situation. Most important settings are the trap frequencies (see section 4.1.4 on page 72) and the number and mass of laser and not laser cooled ions in the simulated crystal. The execution time depends a lot on further settings but is usually less than 10 s for moderately sized ion crystals ($N \leq 40$) and scales roughly $\propto N^{3/2}$.

The predicted structure of Coulomb crystals containing up to ten ions was validated by comparing the solutions to the ion positions reported in [86]. However, fluorescence images recorded in the experiments provide a much more affirmative and direct comparison. To what excellent degree simulation and experiment agree is visualized in fig. A.7.

If the number of ions to be simulated is large ($N \geq 35$), the algorithm does not reliably converge to the global minimum configuration anymore but gets stuck in one of the many shallow local minima whose energy differs only on the order of the computational accuracy. Depending on the number of ions, the trapping potential, and the random number generator settings, the final solution yielded crystal structures with seemingly “misplaced ions”. First considered a deficiency of the approach, it was later recognized that a real physical relevance can be attributed to these misplaced ions. The phenomenon is currently discussed in the literature [102]. In this context, deviations from the minimal energy configuration are called *kinks*. At the time of writing this thesis

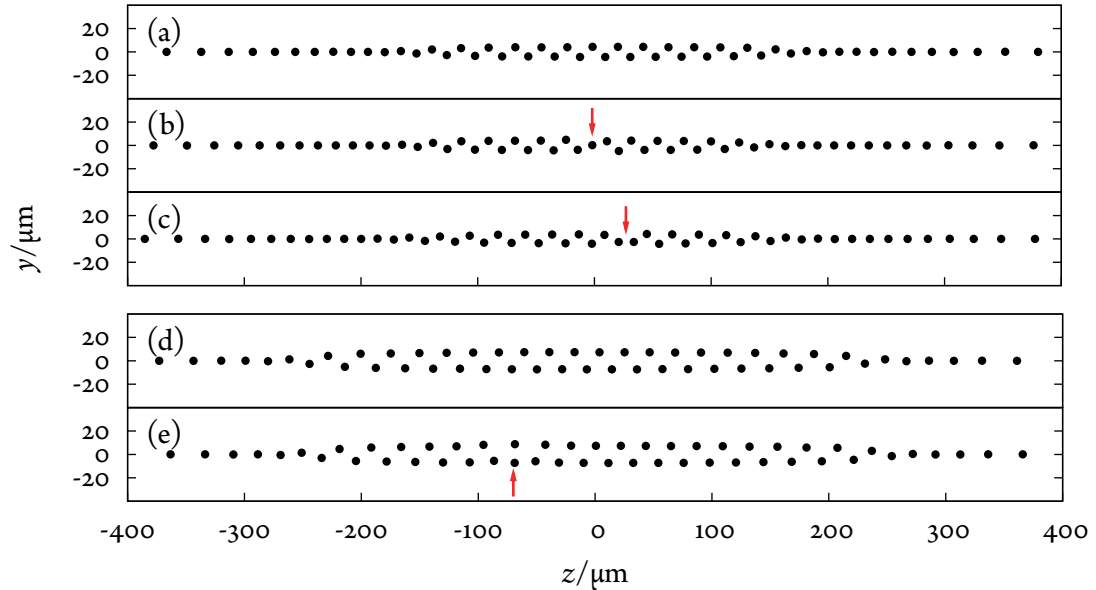


Figure A.8.: Simulation results of the search for the minimum energy configuration in a harmonic trapping potential given by the trap frequencies $\omega_z = 2\pi \times 31$ kHz and $\omega_{\text{sec}} = 2\pi \times 496$ kHz in (a) to (c). The crystal structure corresponding to the global minimum is shown in (a) as a reference for (b) and (c). The latter two show configurations with seemingly misplaced ions (or localized *kinks* [102], arrows) that represent two different local minima of the total energy function of the crystal in the given potential. An experimental observation for the kink of type (b) is shown in fig. A.9. A kink of type (c) can be seen in fig. 5.8b on page 107 at the position of ion 11 and 12 (counted from the right). A third kind of local minimum structures—so called “extended kinks” [102]—have been observed at lower radial confinement ($\omega_{\text{sec}} = 2\pi \times 345$ kHz), both in the simulation (e) and experimentally. For comparison, (d) shows the related global minimum configuration.

all three kinds of kinks presented in fig. A.8 have already also been observed experimentally. One example is shown in figure fig. A.9 on the facing page. Perspectives for further investigation of this topic are discussed in chapter 6 on page 118 and will be analyzed in detail in the thesis of Günther Leschhorn.

A.3.2. Particle dynamics

The application *shuttle simulator* has been developed to simulate the dynamical behavior of an ion crystal in potentials that are switched at arbitrary points in time like and thereby help the interpretation of the ion transfer experiments; see section 4.2 on page 75. With the help of this program the assumption on how the ions would behave during the flight through the RF-guide (see section 2.2 on page 27) could be confirmed and experimental results could be reproduced. This program is also expected to be of valuable help for further optimization of the transfer scheme in order to enhance the rate with that ions can be replaced in chamber 3; see also chapter 6 on page 118.

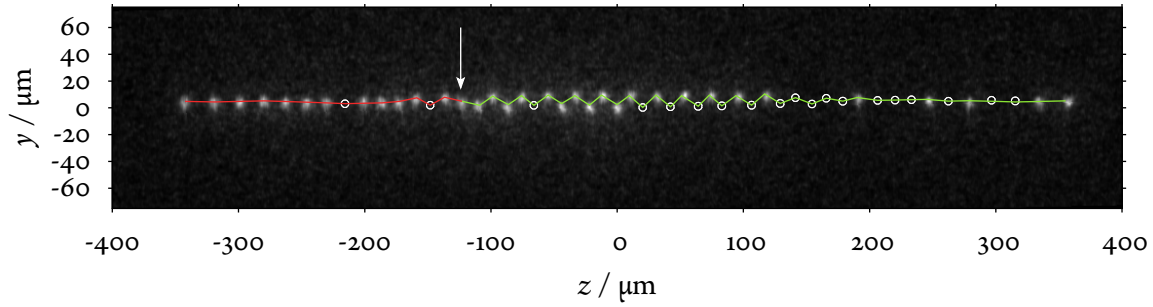


Figure A.9.: Fluorescence image of the mixed Coulomb crystal containing fluorescing atomic $^{24}\text{Mg}^+$ and dark molecular $^{24}\text{MgH}^+$ ions (indicated by circles) also used in fig. 5.8a on page 107. The kink marked by the arrow corresponds to the one shown in fig. A.8 (b). At this position, two zigzag chains (indicated by red and green lines) with opposite “phase” meet. To resolve the topological defect of the crystalline structure, all ions in one of the two zigzag chains had to be radially flipped (vertically in this projection). For sufficiently cooled ions’ with motional energies corresponding to a temperature on the order of millikelvin this is unlikely to happen spontaneously, thus stabilizes the defect.

The program solves Newton’s equation of motion for all ions taking into account their mutual Coulomb repulsion and the external electric forces in the time-dependent trapping potential. Since the description of the motion of an ion crystal containing N ions requires a system of $6N$ (three positions, three momenta) first order nonlinear coupled ordinary differential equations (ODE) to be solved for each time step Δt , an efficient computing framework was required. Additionally, a flexible configuration file format was developed. By that, almost any currently experimentally realizable situation can be described. The potentials to be simulated can be given in an analytical form, e. g. a harmonic expression, or as text files containing a list of numerical values on an arbitrarily spaced one-dimensional grid. After translating the information encoded in the configuration file into a numerical treatable form, the system of equations is built and fed to an ODE solver. Within this thesis, an implementation included in the open source GNU Scientific Library [60] was opted for. It uses the implicit fourth order Runge-Kutta method at Gaussian points. On a regular PC, it takes about 25 s to simulate the motion of 55 ions over a 100 μs interval. Simulation results are shown and compared to experimental data in section 4.2 on page 75.

Appendix B.

Devices

B.1. Electron gun

The two electron guns of TIAMO (see fig. 2.1 on page 23) are replicas of the design described by Schätz [149]. A compilation of the relevant measured properties of the electron gun in chamber 3 is presented in the following.

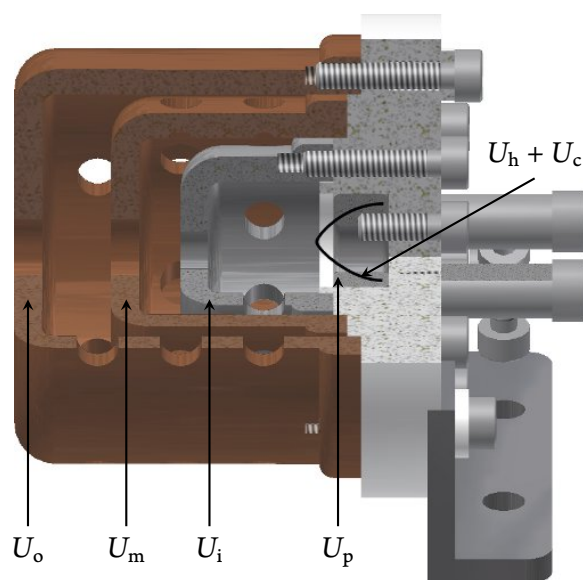


Figure B.1.: Section through a computer drawing of the electron gun. Voltages applied to four nested cylindrical electrodes allow to accelerate and focus electrons emitted from a heated (U_h) tungsten wire (radius 0.1 mm) cathode (U_c). The pierce electrode (U_p) is used for space charge compensation. The extraction voltage defined by potential difference between inner cylinder (U_i) and the cathode controls the electron acceleration. Middle (U_m) and outer cylinder (U_o) are used as electron lenses that focus the beam to a diameter of a few millimeter [149].

In order to find optimum voltage settings (cf. figs. B.1 and B.2a on pages 144–142), the electron current transmitted through the RF-guide was determined by measuring the current I_{det} from the (biased) atom oven shielding (cf. fig. 2.3 on page 26) to electrical ground. The extraction voltage $U_{\text{ex}} = U_i - U_c$ has its optimum at approximately 87 V. Up to this value, the detection current grows polynomial $I_{\text{det}} \propto U_{\text{ex}}^{2.5}$ (see fig. B.2b on page 144) but decreases at higher values. I_{det} dropped after few minutes of operation. It is assumed that surface charges building up inside the electron gun cause this effect. The same relative decrease was detected both in the emission current from the heated cathode and the detection current. The dependence of the emission current on the heating current (typical 3.8 A) through the cathode filament is exponential; see fig. B.3 on page 145.

More detailed measurements showed that 90 % of the electrons that are emitted from the cathode actually leave the gun. 52 % of the the missing electrons are absorbed on the middle cylinder, 44 % on the outer cylinder, the rest on the inner two electrodes. Only $\frac{2}{3}$ of the exiting electrons are

transmitted through the RF-guide, the remaining electrons are lost to the RF-electrodes ($U_{\text{RF}} = 60 \text{ V}$). 60 % of the emitted electrons are lost to the ring electrodes (100 V). Together with not further investigated losses this adds up to a total transmittance through the RF-guide of 2 % to 3 %.

B.2. Atom oven

The atom ovens were realized as small 15 mm long tantalum tubes (outer diameter 1 mm, inner diameter 0.8 mm) that were filled with pieces of either magnesium or barium. Heating the ovens was achieved via two spot-welded loops of tantalum wire (diameter 0.2 mm, about 45 mm total length). The loops helped also to support, mount, and position the tube. The tubes' rear opening was tightly crimped in order to force evaporated atoms to exit in the forward direction.

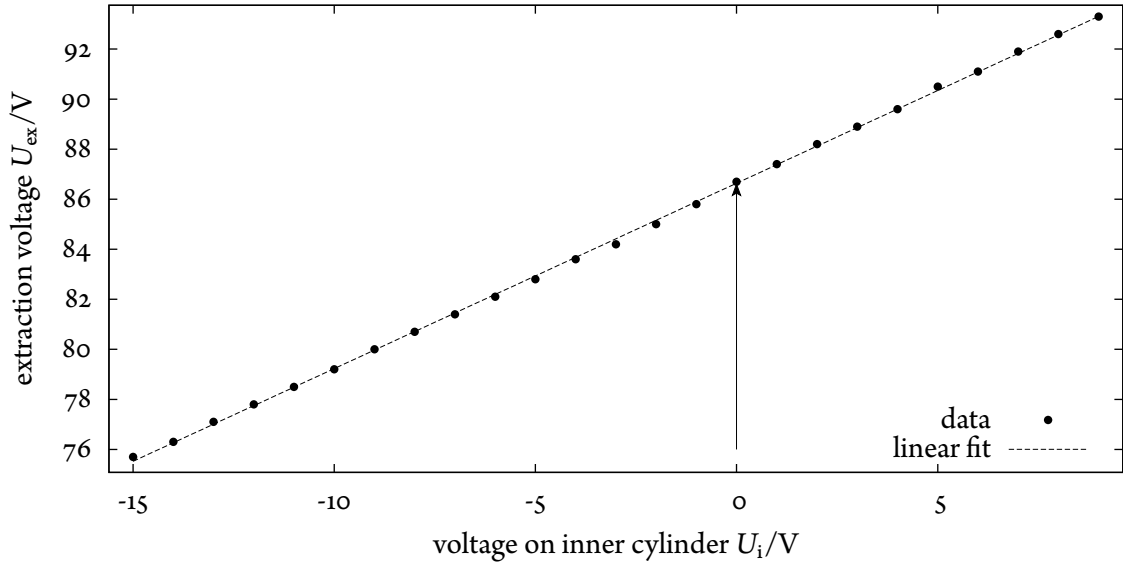
It turned out that the heating properties depend strongly on the length of the tantalum wires. Longer resistive heating wires dissipate more power and additionally provide better thermal isolation against heat losses to the supply lines and mounting pads; cf. fig. 2.14 on page 37. Due to restricted space, the actually used ovens have comparably short, slightly differing heating wires leading to relative high, differing heating currents. So, typically 3.4 A of heating current through the magnesium oven for the trap in chamber 1 were required for the loading parameters given in section 2.5 on page 35 and 4.1 A for loading from the oven in chamber 3. Imperfect thermal insulation is assumed to be the reason for the thermalization process. Starting from a cold oven, it takes typically 5 min to 10 min to reach a thermal steady-state; see figs. B.4 and B.6a on pages 146–147.

The magnesium ovens were filled with a piece of magnesium wire that had been etched (11.0 mm length, 0.75 mm diameter) in dilute citric acid. As a welcome side effect this procedure turns the passive oxide layer into a citric complex which is dissolved by the high temperatures ($< 200 \text{ }^\circ\text{C}$) during bake-out and thereby turns into a clean oxygen-free magnesium surface.

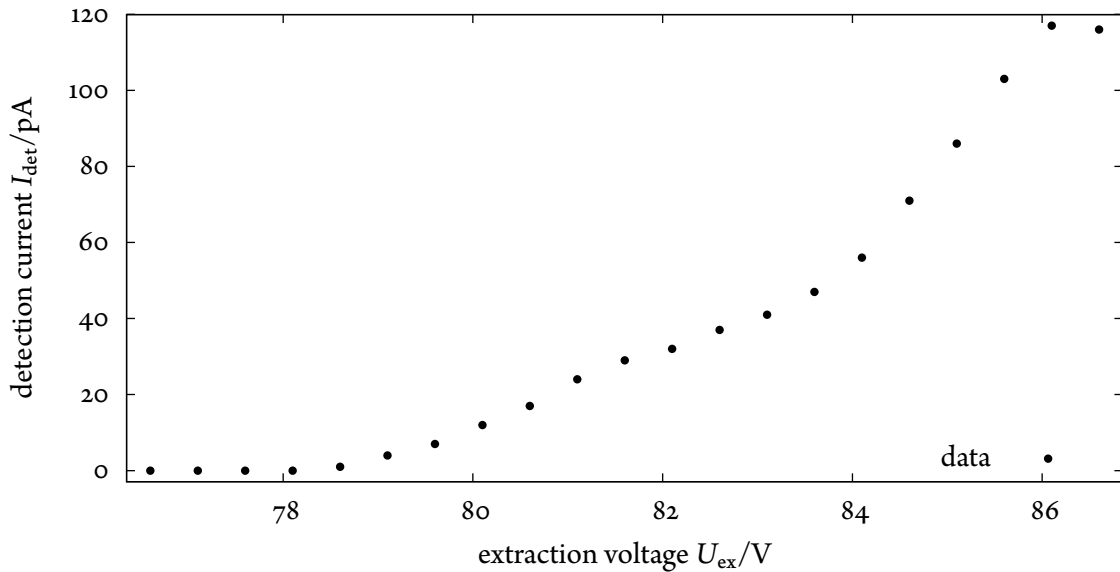
The barium ovens were filled with small barium pieces cut from a bigger chunk. In the interest of protecting the metal against hydration or oxidation (see appendix B.3 and fig. B.6b on pages 143–147), the front openings of the respective tantalum tubes were sealed with indium foil; cf. fig. B.5 on page 146. Thereby, the sealed ovens could be installed under normal laboratory conditions. Filling and sealing of the ovens required dry nitrogen atmosphere, though; see appendix B.3. Due to the low melting point of indium ($T_{\text{melt}} = 157 \text{ }^\circ\text{C}$) the seal breaks during the apparatus bake-out; cf. fig. B.7 on page 148. After the seal melted, accidental venting of the chamber would be fatal. If this happened, the barium chips would corrode within seconds rendering them useless for the experiment. New sealed tubes would have to be prepared and installed.

B.3. Barium handling

Barium had to be handled in a protective environment due its quick reaction with oxygen, nitrogen, water vapor and carbon dioxide. Even under vacuum conditions it was observed to react; see fig. B.6b on page 147. An inflatable glove bag established a proper solution for the flexible and clean working demands required for the assembly of the ovens. Inside this atmosphere, small chips of

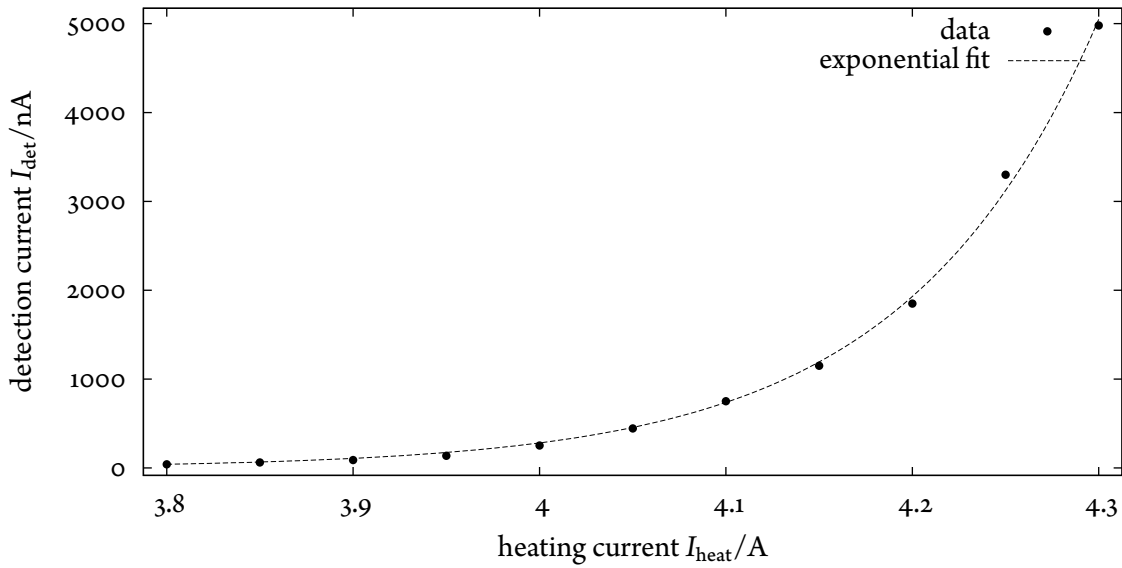


- (a) The optimum extraction voltage $U_{ex} = U_i - U_c$ as function of the voltage applied to the inner cylinder. U_{ex} was tuned to maximize the detection current I_{det} . The measurements closely follow a linear relationship: $U_{ex} = 86.6 \text{ V} + 0.74 U_i$. Along this line, the detection current is constant. $I_{heat} = 4.1 \text{ A}$, $U_o = -5.5 \text{ V}$, $U_m = -17 \text{ V}$, $U_p = -116 \text{ V}$.

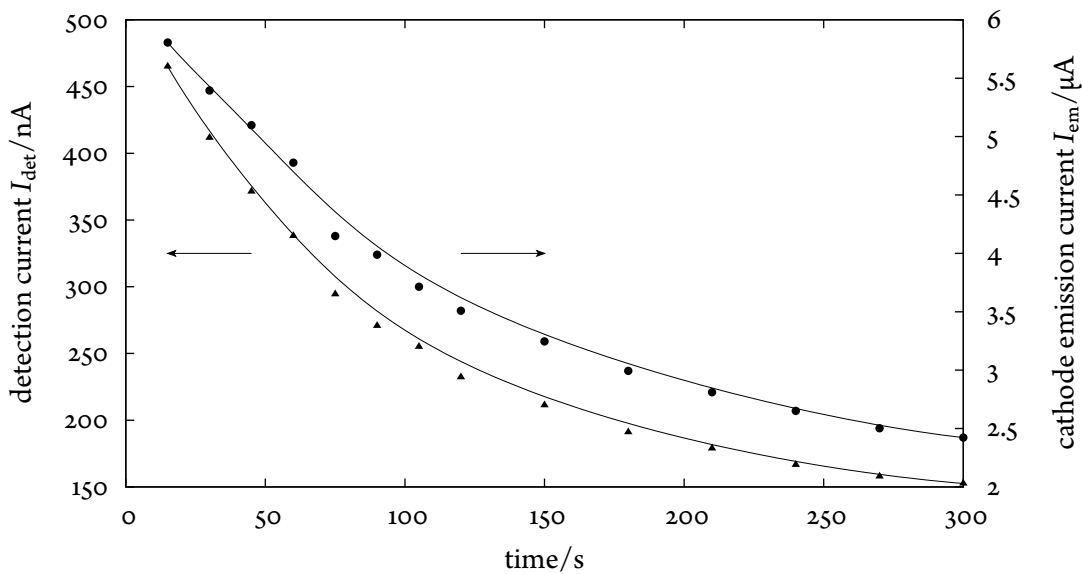


- (b) Detection current I_{em} as function of the extraction voltage U_{ex} . The extraction voltage was set by varying U_c at fixed U_i corresponding to a line indicated by the arrow in the diagram of B.2a at otherwise identical settings. Until the optimum extraction voltage of $U_{ex} = 86.6 \text{ V}$ is reached the detection current grows approximately polynomial $I_{det} \approx (U_{ex} - 76 \text{ V})^{2.5}$.

Figure B.2.: Detection current dependence on the extraction voltage.



(a) Detection current I_{det} as function of the heating current through the tungsten filament cathode. The dashed line represents an exponential fit to the data.



(b) Detection I_{det} and cathode emission current I_{em} as function of the operation time. Both decrease after a few minutes of operation by the same relative amount which keeps the ratio of the two currents approximately constant and reveals that about 10 % of the electrons leaving the cathode are actually detected on the opposite side of the RF-guide independent of the operation time. During the measurement RF and ring electrodes were grounded. The graph does not show the peak current reaching almost $I_{\text{em}} = 11 \mu\text{A}$ immediately after operation start. The lines are guides to the eye.

Figure B.3.: Detection current dependence on filament heating and operation time.

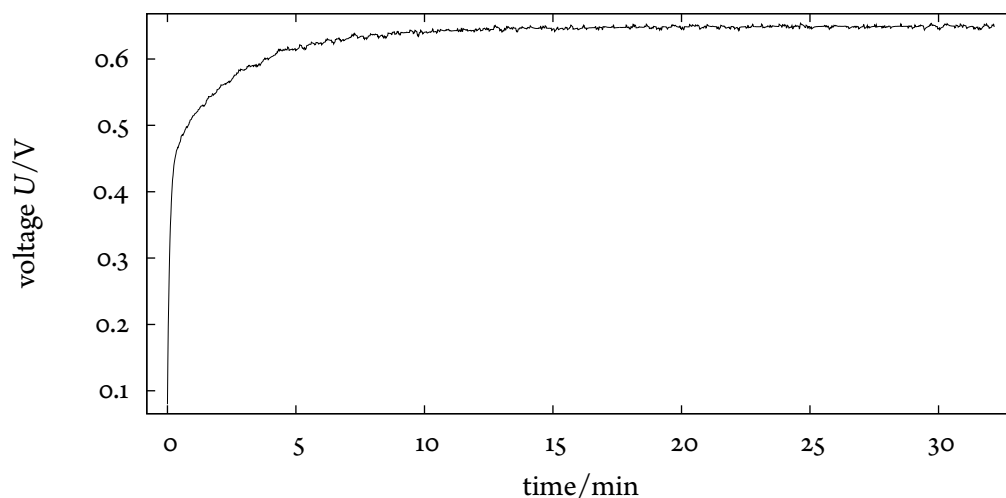


Figure B.4.: Voltage required to sustain a heating current of 3.77 A through a test atom oven as function of time. The resistance rises during the first 5 min indicating an increasing temperature of heating wires, oven, and supply lines. It settles to 0.17Ω after approximately 10 min when a balance between heat transfer to the supply lines, radiative heat loss and resistive heating is reached.

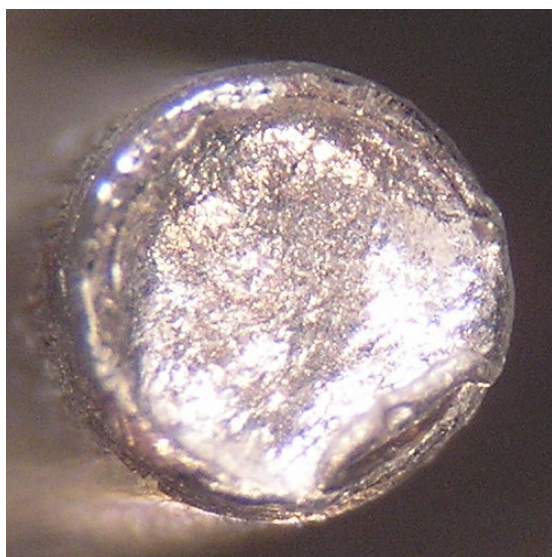
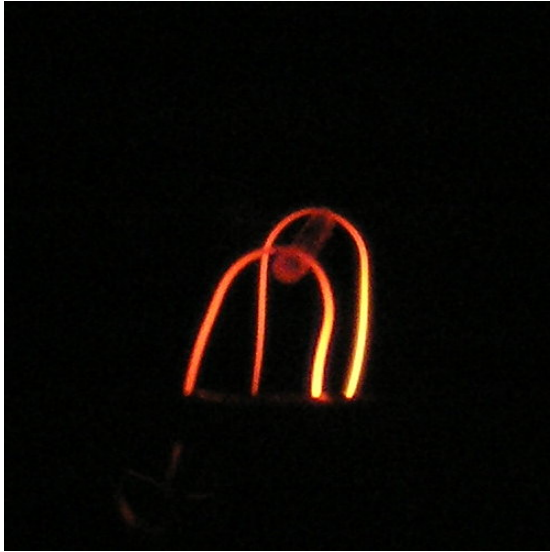
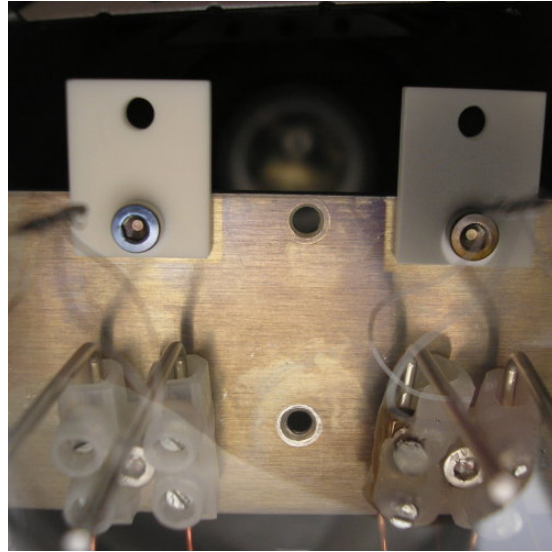


Figure B.5.: Atom oven tube sealed with indium foil to protect barium against humidity and oxygen. The test tube was put into vacuum and inspected under a microscope afterwards. One can see a bulge at the lower right rim where the foil (about 0.3 mm) flipped off. This could later be improved by firmer fastening of the foil. The tube had not been heated. The foil melts ($T_{\text{melt}} = 157 \text{ }^\circ\text{C}$) during the bake out (see fig. B.7 on page 148) of the vacuum chamber or latest at the first heating of the tube and thereby opens the tube for barium to evaporate.



(a) Heated tantalum test tube starting to glow in the visible at a heating current of 4.5 A. Heat is transferred via the two spot-welding points in which tantalum heating wires are connected to the tube. In the experiments, the ovens are heated less (3.4 A to 4.2 A). Under these conditions, the glowing is only visible with night vision gear.



(b) Coated (originally white) ceramics plates after testing barium atom ovens. The left oven was heated with 3.5 A. Uncoated shadows around the ceramics plate and the screw indicate a thin metal film deposition. The indium sealed oven to the right was heated up to 6 A. The clearly visible coating all over the test plate visualizes the large emission angle of the atomic vapor. Due to the high reactivity of barium and the large exposed surface, the deposit became transparent/white after only a few minutes even under $1 \cdot 10^{-5}$ mbar vacuum conditions.

Figure B.6.: Atom oven heating and emission properties

barium were prepared with a strong scalpel and inserted into the atom oven tubes; see appendix B.2 on page 143.

B.4. Photo multiplier

The photomultiplier tube (PMT) was used to measure the photon count rate impinging on the detector per unit time. Figure B.9 on page 150 shows this count rate as a function of cooling laser power and number of trapped $^{24}\text{Mg}^+$ ions. The number of ions was determined independently from fluorescence images. The measurements show the photon count rate to be proportional to the cooling power. For up to 30 ions the count rate is also proportional to the number of ions in the trap. It deviates for larger numbers because of the imaged crystal growing bigger than the sensitive area of the PMT. The dependency of the photon count rate on the number of ion was used in the automatic loading procedure; see appendix A.1.1.a on page 124.

Ultraviolet stray light in chamber 1 (see section 2.6.3 on page 40) could not be overcome completely. Despite careful alignment of the cooling laser beam and restrictive adjustment of a variable

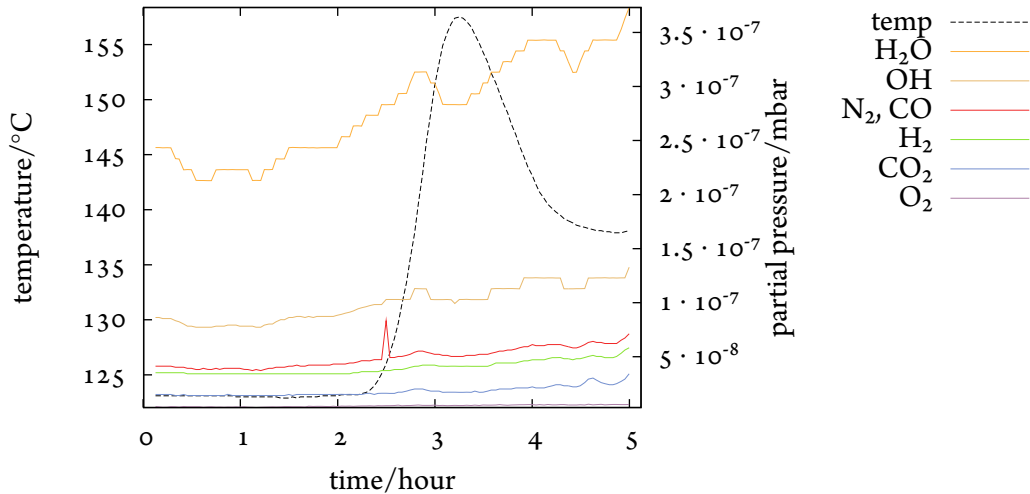


Figure B.7.: Short section of the recordings during the apparatus bake-out showing one temperature and the partial pressures of selected gases. The temperature was measured outside of chamber 1 at the reentry viewport close to the atom oven assembly. The partial pressures were measured in the backing vacuum of the main turbomolecular pumps (see section 2.1.1 on page 22) using a residual gas analyzer (QMA064, Balzers). Whereas all other partial pressure are slowly rising over a period of about 5 h, the nitrogen pressure peaks for a short moment. This is assumed to be the signature of one of the indium seals melting. Since the atom ovens were sealed under nitrogen atmosphere no other gas than nitrogen is expected to escape.

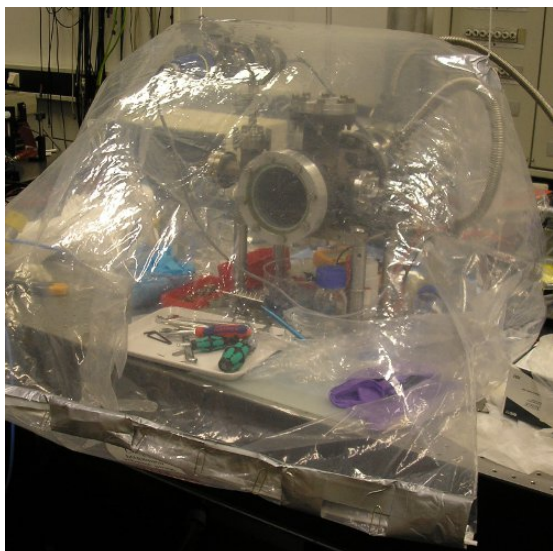
aperture in front of the PMT, the stray light count rate was comparable to the fluorescence signal count rate; see fig. B.9a on page 150. Nonetheless, these conditions still allowed the PMT to be applied for the automatic loading scheme and sufficiently reproducibly load a given number of $^{24}\text{Mg}^+$ ions. Typically, loading was aborted when the PMT counting rate reached 1100 kHz (including 310 kHz stray light induced background) corresponding to approximately 50 fluorescing $^{24}\text{Mg}^+$ ions.

B.5. Pellicle

Any kind of regular window is inappropriate for applications involving short UV pulses. To give an example, a hypothetical 50 μm thin MgF_2 window would stretch a 4 fs pulse at 280 nm by 25 % to 5 fs, 150 μm MgF_2 would stretch the pulse to 10 fs.

More elegantly, a thin transparent membrane can be employed if the pressure difference on the two sides of the membrane is sufficiently small. For the experiment of this thesis, a 1 μm thin foil¹ made of CYTOP [64], an amorphous fluoropolymer, was used. In order to produce a window-like pellicle, a ring shaped metallic holder is vacuum-compatibly glued to a tightened sheet of the material. Afterwards it is cut from the sheet. By that, a 1 μm freestanding window is formed. Its

¹ film type 602, Mirco lithography inc.



(a) An inflatable glove bag from VWR was used to provide a protective atmosphere for the assembly of the barium ovens. Several scavenging cycles with dried nitrogen purified the atmosphere to a degree that allowed to work with bare barium for several hours.

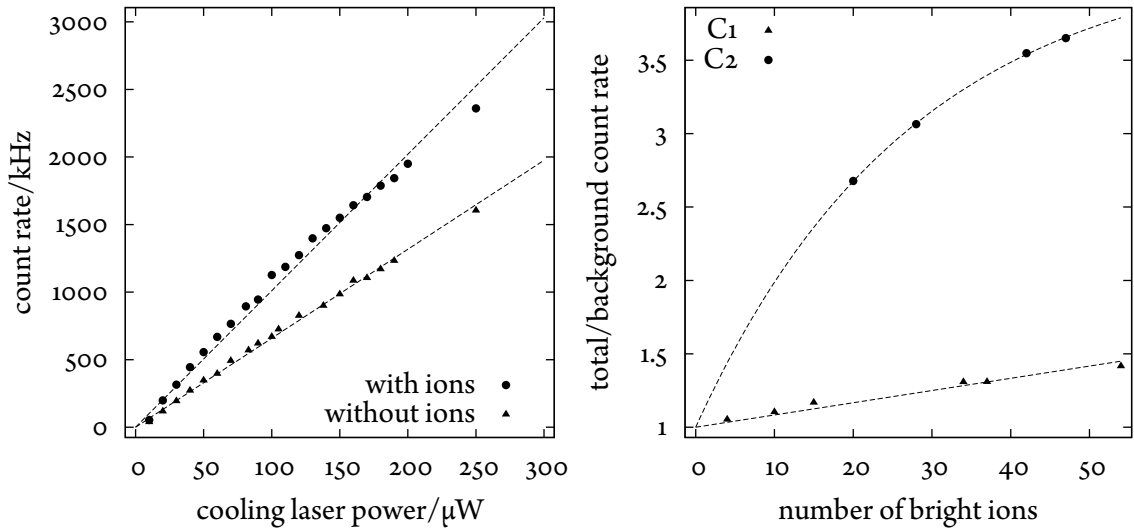


(b) Barium chunk (2 cm rods, 99 %, Sigma-Aldrich) inside a closed beaker. Since barium reacted even in the protective atmosphere inside the glove bag on a hour time scale and formed a white powdery film, an additional protection beaker was used to store barium from day to day. The metallic facing originated from a smaller piece that had been cut from the chunk some minutes earlier.

Figure B.8.: Barium handling in protective atmosphere.

transmission properties are shown in fig. B.10. The oscillations in the transmission originate from an interferometric modulated reflection caused by the thin structure that effectively forms a poor finesse ($\mathcal{F} = 0.12$) Fabry-Perot-like resonator. This is why information about the thickness d and the single surface reflectivity can be obtained from the oscillations in the transmittance. The oscillation period (free spectral range, FSR) 3370 cm^{-1} is related to the thickness of the foil by $\text{FSR} = 2nd$. The index of refraction n can be calculated from the average transmission $T = (1 - R)/(1 + R)$ and $\sqrt{R} = (1 - n)/(1 + n)$. The manufacturer's data sheet states $n = 1.353$ at 280 nm. Using that number, $d = 1.1 \mu\text{m}$ is calculated in good agreement with the specification.

Most importantly, UV pulses pick up a negligible amount of dispersion (0.05 fs^2) propagating through $1 \mu\text{m}$ of CYTOP. Secondly, the maximum reflection losses per surface are less than 5 % and on average about 2.5 %. Thirdly, the pellicle material comes in superior optical quality since the material's original application is in the field of ultraviolet lithography in the semiconductor industry where it is used for dust protection during light exposure. All three points justify the pellicle also to be permanently placed inside the beam path as a low reflecting pick-up element for the purpose of monitoring the UV beam pointing; see section 3.4 on page 64.



(a) Photon count rate composed of stray light induced background and laser cooling fluorescence photons (52 ions) under conditions C1. The count rate depends linear on the cooling laser power. Dashed lines are linear fits to the data. (b) Total count rate depending on the number of fluorescing ions. The fluorescence photon count rate exceeds the stray light induced background count rate if more than about 10 (C2) fluorescing ions are in the trap. A deviation of the count rate from a linear relationship at large number of ions is assumed to be caused by the fluorescence image lying increasingly more outside of the sensitive area of the PMT. Dashed lines are guides to the eye.

Figure B.9.: Photomultiplier count rate in the trap of chamber 1. The data was recorded under two different measurement conditions: C1 and C2. In C2 the stray light level was significantly reduced.

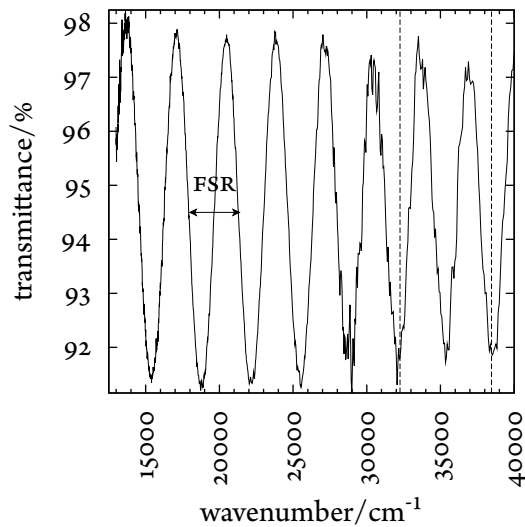


Figure B.10.: Transmission through a freestanding $1\ \mu\text{m}$ thick CYTOP pellicle window perpendicular to the beam measured with a transmission spectrometer (Bruins Instruments). Oscillations in the transmittance originate from interference at the thin structure. The transmittance does not drop below 91% anywhere in the measured spectral range justifying the pellicle's use as permanent optical element inside the beam path. The dashed lines indicate the spectral range $260\ \text{nm}$ to $310\ \text{nm}$ that supported the UV pulses used in the experiments. The arrow spans one free spectral range.

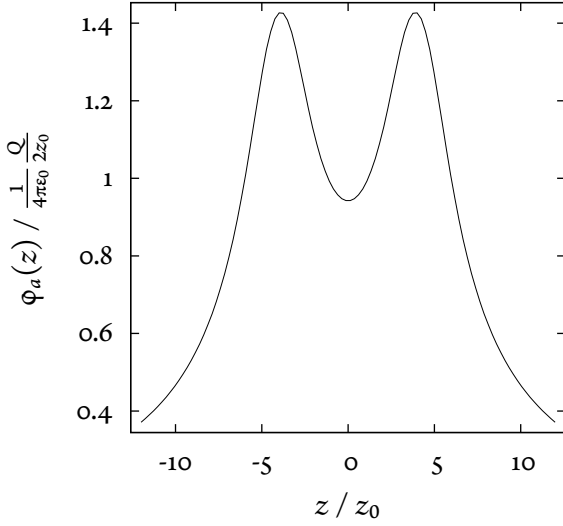


Figure B.11.: Normalized electric potential generated by a pair of equally sized and equally charged (Q) cylindrical electrodes along their common symmetry axis. The radius $r = 1.6z_0$, width $z_0 = 2.5$ mm and the spacing between the electrodes ($8z_0$) are chosen according to the experimentally realized geometry (see section 2.3 on page 30). The analytical expression does not account for the width of the rings in the radial direction. This is why numerical calculations (see section 2.3 on page 30) have to be performed in order to realistically simulate the potential.

B.6. Ring electrodes

The electric potential $\varphi_a(\rho)$ along the axis of symmetry of a thin $2z_0$ long cylindrical electrode with radius r charged by the amount Q is calculated assuming a homogeneous surface charge density $\sigma(\rho) = Q/4\pi r z_0 \delta(\rho - r)$.

$$\begin{aligned}
 \varphi_a(z) &= \varphi(\mathbf{r}, \rho = 0) \\
 &= \frac{1}{4\pi\epsilon_0} \int d\mathbf{r}' \frac{\sigma(\mathbf{r}')}{|\mathbf{r}' - \mathbf{r}|} \\
 &= \frac{1}{4\pi\epsilon_0} \int_{-z_0}^{-z_0} dz' \int_0^{2\pi} d\phi' \int_0^{2\pi} \rho' d\rho' \frac{Q}{2\pi r 2z_0} \delta(\rho' - r) \frac{1}{\sqrt{(z - z')^2 + \rho'^2}} \\
 &= \frac{1}{4\pi\epsilon_0} \frac{Q}{2z_0} \int_{-z_0}^{-z_0} dz' \frac{1}{\sqrt{(z - z')^2 + r^2}} \\
 &= -\frac{1}{4\pi\epsilon_0} \frac{Q}{2z_0} \ln \left(\frac{z - z_0 + \sqrt{(z - z_0)^2 + r^2}}{z + z_0 + \sqrt{(z + z_0)^2 + r^2}} \right)
 \end{aligned}$$

The above expression reduces to known results in the two limiting cases

$$\lim_{z \rightarrow \pm\infty} \varphi_a(z) = \frac{Q}{4\pi\epsilon_0} \frac{1}{z}, \quad \lim_{z_0 \rightarrow 0} \varphi_a(z) = \frac{Q}{4\pi\epsilon_0} \frac{1}{\sqrt{r_0^2 + z^2}},$$

i. e. in the far distance, the cylinder appears to be a point like charge. In the limit of an infinitesimal short cylinder, the formula for a circular line charge Q with radius r is recovered. The combination of two separated, short cylindrical electrodes generates a potential (cf. fig. B.11) that is suitable for ion trapping; see section 2.3 on page 30.

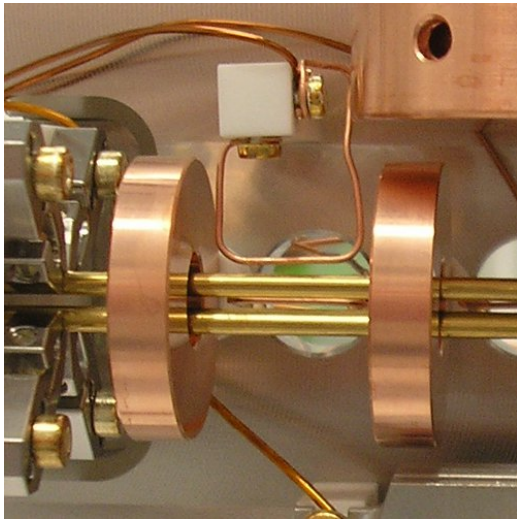
B.7. Compensation electrodes

Compensation electrodes are used to generate electric fields that minimize the micromotion of trapped ions. Micromotion occurs if the ions are not exactly in the radio frequency minimum. For the RF-guide of this thesis, the minimum is a line along the quadrupole symmetry axis; see section 1.1 on page 7. There is a manifold of forces that might push the ions out of the RF-minimum. Basically the radial component of any static electric potential, e. g. such as symmetry imperfections of the ring electrode potential used for axial confinement, induces micromotion. Other distortions disturbing symmetry can originate from mechanical deformations, depositions of metal vapor on the surface of the RF-electrodes forming *patch potentials* [27], non-perfect collinearity of the symmetry axes of the ring electrodes with the RF-minimum as well as the presence of charges close to the quadrupole guide.

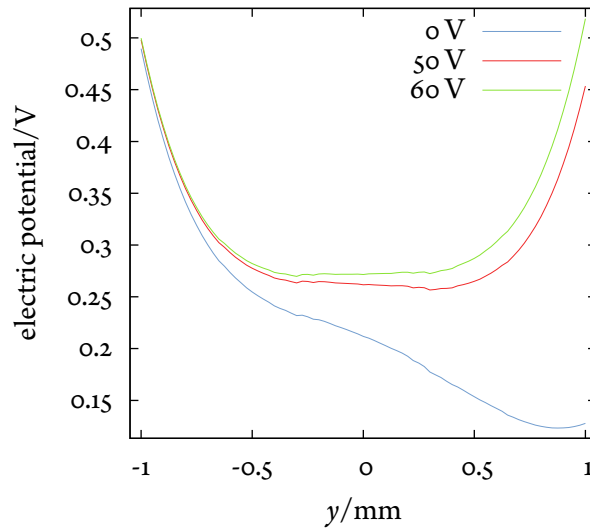
To give an example, varying the voltage of the ring electrodes should solely influence the axial potential if there was perfect symmetry. In practice, a shift of the ions in the radial direction was observed. This might give a hint for a mismatch of the symmetry axes of RF-guide and ring electrodes, see also the discussion in section 2.3 on page 30. The related radial component of the asymmetric static potential gives rise to a radial force which must be canceled by a counteracting Coulomb force by appropriate voltages applied to the compensation electrodes.

Patch potentials [27] have caused trouble in ion trapping experiments ever since [39, and references therein]. They originate from potential differences on the electrode surface due to material depositions. Magnesium vapor deposits on the gold plated surface of the RF-rods result in stray electric fields emerging from the difference of the metals' electron affinities (5.1 V - 3.66 V). The proximity of the ions to the electrode is the reason for that even tiny distortions on the electrode surface may have a severe effect on the trapping potential. Again, compensations electrode voltages are to be used to cancel these distortions—at least locally.

The obvious need for compensation electrodes implies an asymmetric radial static electric potential by itself. In TIAMO, 0.5 mm diameter wires protruding into the region between the ring electrodes (see fig. B.12a on the facing page) act as compensation electrodes in most of the places. The presence of this wire causes the electric field lines between the ring electrodes to be deflected. From the point of view of an ion in the trap, the compensation electrode shields the ring electrode in one direction. Thus, the ions are pushed less from this side which results in a radial force pointing towards the compensation electrode. In order to compensate the bare presence of the compensation electrode, it must not be on electrical ground; see fig. B.12b on the next page.



(a) Detail of chamber 3 showing a U-shaped wire in the center of the picture that is used as compensation electrode acting in the picture plane. The orthogonal compensation wire between the golden RF-rods is (partly) visible, too.



(b) Simulation showing the distortion of the static radial electric potential caused by a grounded (0 V) wire shaped compensation electrode placed next to the RF-guide in positive y direction. The related asymmetric shielding effect of the electric field generated by the ring electrodes gives rise to a force acting on the ions towards the compensation electrode. Only when a positive voltage is applied to the electrode, the original symmetry about the trap axis is approximately restored.

Figure B.12.: U-shaped wire compensation electrodes in TlAMO.

Appendix C.

Concepts

C.1. Maximum likelihood method

The following derivation verifies the *maximum likelihood method* to be suitable for the data analysis of the time-resolved dissociation experiments described in section 5.3 on page 108. This method is an important, well-known concept in statistics [26]. The likelihood function $L(\lambda | X) \propto P(X | \lambda)$ is a conditional probability function of a parameter λ , related to some statistical model, given one or more observations X . $P(X | \lambda)$ can be interpreted to express the probability for the observation X to occur in an experiment which depends parametrically on λ . But the interpretation of X and λ can be interchanged. $P(X | \lambda)$ allows also to calculate the most likely *a priori* unknown value of λ , i. e. the value that maximizes the probability of a given observation (or series of observations) X under variation of λ . In short, the latter interpretation allows to extract the most likely model parameter given a number of observations whereas the former interpretation is about calculating probabilities for observations given a *a priori* known model parameter.

The likelihood function of a set of statistically independent observations X_1, \dots, X_N can be written in product form

$$L(\lambda | X_1, \dots, X_N) = \prod_{i=1}^N P(X_i | \lambda). \quad (\text{C.1})$$

The maximum likelihood estimator λ_{\max} that maximizes L is given by the stationary point of L or, equivalently, the stationary point of the logarithm of L :

$$\left. \frac{\partial \ln L}{\partial \lambda} \right|_{\lambda_{\max}} = 0.$$

Taking the logarithm simplifies the mathematical treatment considerably if the expressions $P(X | \lambda)$ involve exponential functions.

Central to the time-resolved experiments is the dissociation probability d of one molecular $^{24}\text{MgH}^+$ ion per pump-probe pulse pair. On average, many pump-probe excitation trials were required to dissociate the molecular ion. This suggests to introduce the helpful quantity $B(0 | d, N)$, i. e. the binomial distributed probability to be not successful in dissociating the molecular ion using N pump-probe laser pulse trials. Due to the conditions $d \ll 1$ and $N > 100$, $B(0 | d, N)$ can be approximated by a Poisson distribution

$$P_{l=Nd}(0) = \frac{l^0 e^{-l}}{0!} = e^{-l} = e^{-Nd} = \lambda. \quad (\text{C.2})$$

If the same experiment is performed with n molecular ions simultaneously, one can ask for the probability to find exactly k of them undissociated after N pump-probe laser pulses. Again, the answer is given by a binomial probability distribution

$$B(k | \lambda, n) = \binom{n}{k} \lambda^k (1 - \lambda)^{n-k}. \quad (\text{C.3})$$

If M of these N -ion experiments are performed in series, the final number of molecular ions k_i of one experiment is equal to the initial number n_{i+1} of the following. Inserting the above probability into the definition eq. (C.1) on the preceding page, one obtains the explicit expressions:

$$\begin{aligned} L(\lambda | n_1, k_1, \dots, n_M, k_M) &= \prod_{i=1}^M \binom{n_i}{k_i} \lambda^{k_i} (1 - \lambda)^{n_i - k_i} \\ \ln(L(\lambda | n_1, k_1, \dots, n_M, k_M)) &= \sum_{i=1}^M \ln \binom{n_i}{k_i} + k_i \ln(\lambda) + (n_i - k_i) \ln(1 - \lambda) \\ \left. \frac{\partial \ln(L)}{\partial \lambda} \right|_{\lambda_{\max}} &= 0 \Leftrightarrow \lambda_{\max} = \frac{\sum_{i=1}^M k_i}{\sum_{i=1}^M n_i}. \end{aligned}$$

It should be noted that the expression of the maximum likelihood estimator λ_{\max} is simply given by the quotient of the sum of the residual and the sum of the initial molecular ions of successive experiments—numbers that can be read off from the fluorescence images; see appendix A.2.3 on page 135.

It is furthermore convenient to associate an exponential decay time τ and the related half-life $t_{1/2}$ with the parameter λ . This follows from the constant laser pulse repetition rate and the approximated Poisson distribution eq. (C.2) on the preceding page:

$$\lambda = e^{-Nd} = e^{-T/\tau} \Leftrightarrow \tau = -\frac{T}{\ln(\lambda)}, \quad t_{1/2} = \ln(2)\tau.$$

The exponential decay time τ is given by the exposure time T corresponding to N pump-probe laser pulses of one experiment scaled by the negative reciprocal of the logarithm of λ . Likewise, the dissociation probability per laser pulse d can be readily expressed by the logarithm of λ and N :

$$d = -\frac{\ln(\lambda)}{N}.$$

C.1.1. application to simulated data

In order to test the above derivation in a realistic scenario, a computer experiment was set up. It models the stochastic decay of molecular ions that are randomly dissociated by laser pulses impinging at a constant rate. The single pulse dissociation probability is chosen to match that of the real experiment ($d \approx 1 \cdot 10^{-3} \text{ pulse}^{-1}$). In fig. C.1 on the following page three simulated decay runs are shown. They illustrate the margin of deviation of a statistical ensemble that consists of only $M = 20$ molecular ions. It can be concluded that statistical fluctuations might lead to significant

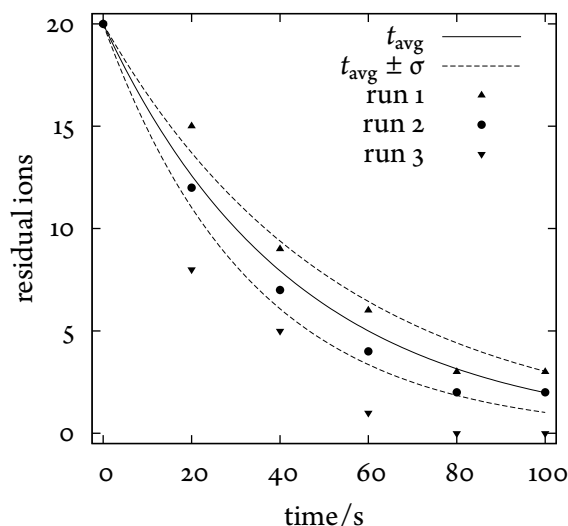


Figure C.1.: Three runs of the same stochastic decay simulation of $N = 20$ molecular ions with half-life $t_{1/2} = 30$ s. The half-life maximum likelihood estimators of run 1 to 3 are: 35.8 s, 27.1 s, 15.6 s. The lines represent the average exponential decay $\exp(-\ln(2)t/t_{1/2})$ and the $\pm 1\sigma$ standard deviation confidence intervals given by $\sigma = t_{1/2}/\sqrt{N}$; see eq. (C.5) on the next page. The relative probabilities of the three runs to occur are 2.8:10.7:1.

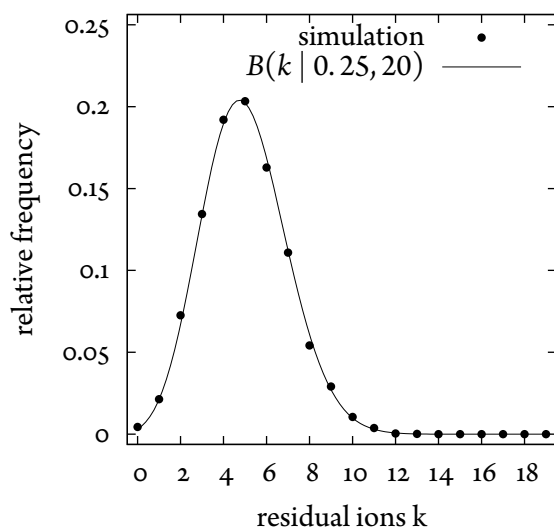


Figure C.2.: Distribution of the number of undissociated molecular ions averaged over $1 \cdot 10^5$ runs of a stochastic decay simulation of 20 molecular ions. The half-life $t_{1/2} = 12$ s corresponds to $\lambda = e^{-2 \cdot \ln(2)} = 0.25$; see eq. (C.3) on the preceding page. The exposure time $T = 2t_{1/2}$ is chosen twice as long as the half-life. As expected, decay runs that leave about a quarter of the molecular ions undissociated are most probable.

false estimations of the average exponential decay time if the experimental observations are based on only a single or few experimental runs. To illustrate the significance of this point once more, the estimated half-life of one of the decay runs in C.1 is underestimated by a factor of two, i. e. the average expectation value amounts to the double of the maximum likelihood estimator of the half-life. This is however not due to an improper analysis but caused by statistical fluctuations in the observations. Of course, decay runs of this kind are rare but still not negligible for ensembles of only few particles. The relative probability of the mentioned decay is approximately 10 %; see fig. C.1. Figure C.2 illustrates the binomial distribution of the simulated number of undissociated molecular ions after an exposure time twice as long as the average half-life time of the decay.

Introducing the exponential decay time τ in eq. (C.3) on the previous page opens up an alternative way of analyzing the data. Instead of using the maximum likelihood estimator λ_{\max} , an exponential decay can be fitted to the decreasing number of residual ions. τ is the only parameter of that function and is readily extracted from the fit. Figure C.3 on the facing page compares the distri-

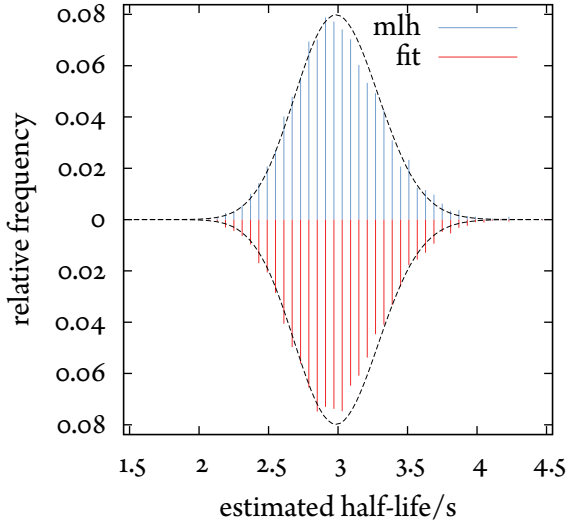


Figure C.3.: Comparison of the distribution of the half-life estimators resulting from application of the maximum likelihood method and the fit method (see text) to the same set of data. $1 \cdot 10^5$ stochastic decays runs of 100 molecular ions were simulated ($t_{1/2} = 3$ s) and the respective number of residual molecular ions at 2, 4, 6, 8 and 10 s noted. The most probable estimator of both methods (3 s) agrees with the simulation setting. The histograms of both distributions (fit results flipped about the x -axis) follow the same Poissonian distribution (dashed line); see eq. (C.4).

bution of estimated τ values following from a maximum likelihood analysis with the corresponding distribution resulting from the fit method. Clearly, the agreement between both methods is good. This allows to apply them complementary to each other if one of them fails, for example, if the fit method does not converge. These rare occasions were encountered when statistical fluctuations lead to untypical decay runs that were poorly described by exponential decays.

A detailed investigation of the half-life estimator distribution at various simulation settings led to an empiric formula which describes the distribution function satisfyingly:

$$\mathcal{P}(t | t_{1/2}, M) = \frac{M^{t/t_0}}{(t/t_0)!} e^{-M}, \quad t_0 = \frac{t_{1/2}}{M}. \quad (\text{C.4})$$

The distribution \mathcal{P} is fully characterized by the decay half-life and the number of molecular ions M . One recognizes the similarity to the Poissonian distribution function. It is however different from the usual Poisson formula $P_\lambda(k) = \lambda^k/k! \cdot \exp(-\lambda)$ in the aspect that the fixed parameter λ (M in \mathcal{P}) appears also in the argument of the function (through t_0). This results in a Poissonian-shaped function that is shifted along the argument axis. It differs also in the related standard deviation σ . Contrastingly to the well known result $\sigma[P] = \sqrt{\lambda}$, there was no closed formula found for $\sigma[\mathcal{P}]$. However, the correspondent, asymptotically correct expression applies also to $\sigma[\mathcal{P}]$:

$$\sigma[\mathcal{P}] = \sqrt{\text{var}[\mathcal{P}(t | t_{1/2}, M)]} = \frac{t_{1/2}}{\sqrt{M}}, \quad M > 4. \quad (\text{C.5})$$

The big advantage of the above formula is its simple algebraic structure that allows to analytically investigate other properties of the distribution function \mathcal{P} . One experimentally interesting property is the standard deviation of combined measurements. A sequence of K similar dissociation experiments shall be considered. The measurements are considered identical except of the involved numbers of molecular ions. Since the distribution function of the half-life estimator depends on the number of ions (see eq. (C.5)), it is not obvious how these measurements are best averaged in order to minimize the statistical uncertainty of a combined half-life estimator.

The general expression of the standard deviation of averaged measurements with unknown weighting coefficients w_i reads

$$\sigma [\mathcal{P}_1, \dots, \mathcal{P}_K] = \sqrt{\sum_{i=1}^K w_i^2 \sigma [\mathcal{P}_i]^2}. \quad (\text{C.6})$$

By inserting eq. (C.5) on the previous page into the above expression one finds that σ is minimized by the following weighting coefficients:

$$w_i = \frac{M_i}{\sum_{k=1}^K M_k}.$$

Optimum averaging is thus achieved if the contribution of each individual measurement is weighted according to the fraction of molecular ions that the measurement contributes to the sum of all molecular ions of the averaged measurement. Applying this result to eq. (C.6) leads directly to

$$\sigma [\mathcal{P}(t | t_{1/2}, M_1), \dots, \mathcal{P}(t | t_{1/2}, M_K)] = \sqrt{\sum_{i=1}^K w_i^2 \frac{t_{1/2}}{\sqrt{M_i}}} = \frac{t_{1/2}}{\sqrt{\sum_{i=1}^K M_i}} = \sigma \left[\mathcal{P}(t | t_{1/2}, \sum_{i=1}^K M_i) \right]. \quad (\text{C.7})$$

This final result confirms an important assumption of the data analysis. The standard deviation of correctly averaged individual measurements equals the standard deviation of one hypothetical measurement in which the sum of all individual measurement's molecular ions are combined. Stated differently, from a statistical point of view, it is equivalent to perform two experiments using single molecular ion or only one experiment using a pair of molecular ions.

C.2. Second harmonic generation

Second harmonic generation (SHG) or frequency doubling is a process that becomes accessible in optical materials whose response to an external electric field is non-linear. In a more mathematical formulation, the generated polarization in the material expanded in powers of the electric field [41]

$$\mathbf{P}(\mathbf{E}) = \mathbf{P}_{\text{lin}} + \mathbf{P}_{\text{nl}} = \epsilon_0 \chi(\mathbf{E}) \mathbf{E} = \epsilon_0 \sum_{i=1} \chi^{(i)} \mathbf{E}^i$$

cannot be truncated after the linear term. The optical susceptibilities $\chi^{(i)}$, $i > 1$ are tensors of rank $i - 1$ and determine the strength of the non-linear effects depending on the direction of the external field relative to the material structure. Since they are a functions of the electric field by themselves, higher order contributions of the series expansion become relevant at large field strengths in either short pulse optics or in very tight focuses of intense cw-lasers. Product terms $\mathbf{E} \cdot \mathbf{E} \propto \cos(\omega t) \cdot \cos(\omega t) \propto \cos(2\omega t)$ occurring in the $\chi^{(2)}$ term are the origin of light at twice the frequency of the fundamental light.

Appropriate materials that exhibit exceptionally high $\chi^{(2)}$ values—usually simply called non-linear materials—are required for large SHG conversion efficiencies. During the preparation of this

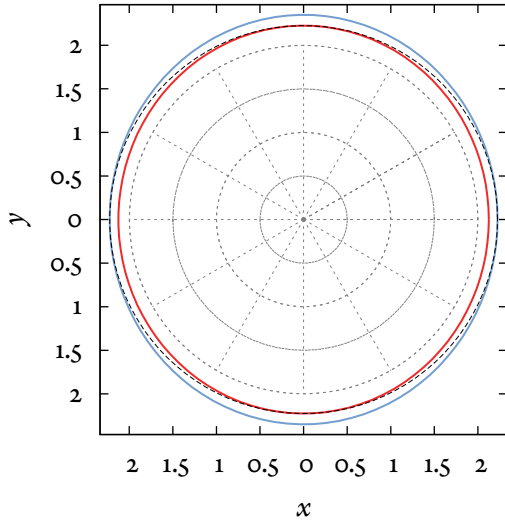


Figure C.4.: Section through the *indicatrix* of KNbO_3 in the xy -plane; see text for the coordinate frame. The red curve indicates the index of refraction of the fundamental wave as function of its polarization direction, similarly the blue curve for the second harmonic wave. Both beams propagate perpendicular to the paper plane. The dashed line draws a circle touching the red and blue curve in single points that define the phase matching condition at 41.45°C : $n(987\text{ nm}) = n(493\text{ nm}) = 2.2255$ where the IR beam is polarized along y , the visible beam along x .

thesis, the well known birefringent crystals LBO, BBO and KNbO_3 were applied for the frequency doubling schemes $1118\text{ nm} \rightarrow 559\text{ nm}$, $559\text{ nm} \rightarrow 280\text{ nm}$ and $987\text{ nm} \rightarrow 493\text{ nm}$ respectively.

For the SHG relevant polarization terms to grow big, the so called *phase matching* condition has to be fulfilled. This conditions goes back to photon momentum conservation but in practical terms is most easily expressed as the indexes of refraction to satisfy $n(\omega) = n(2\omega)$ [41]; see fig. C.4. If this is fulfilled, the second harmonic light generated along the beam path in the material interferes constructively. Phase matching can be achieved by exploiting the dependence of the index of refraction on the orientation of the crystal (critical phase matching) and/or on temperature (non-critical phase matching).

KNbO_3 is a biaxial birefringent crystal [126] with remarkably high effective nonlinearity $d_{\text{eff}} = 9.21\text{ pm V}^{-1} \propto \chi^{(2)}$ at 987 nm . Owing to the biaxial birefringence, critical phase matching is not only fulfilled along one crystal orientation but along a whole line of orientations; see fig. C.5 on the following page. The phase-matching positions making up this line are usually expressed by the azimuthal angle φ and polar angle θ in the crystal coordinate frame (x, y, z) defined by the principal axes of the index of refraction ellipsoid with $n_x < n_y < n_z$.

In general, the Poynting vector of the second harmonic light wave is not collinear with the fundamental beam, resulting in a walk-off that impairs the conversion efficiency and distorts the beam profile. However, from the rule of Biot-Savart follows that no walk-off occurs along the principal axes of the crystal. By setting the temperature of KNbO_3 to $T_{\text{opt}} = 41.45^\circ\text{C}$, the phase matching line can be made to intersect the z -axis; see fig. C.5 on the next page. This condition defines the optimum temperature and the crystal cut, often denoted as b-cut.

C.3. Velocity filtering

Velocity filtering [92]—not realized within this thesis—is a method of generating slow *neutral* molecules completely different from laser or sympathetic cooling; cf. sections 1.2 and 1.3 on pages 12–17. It has been developed in the group of Prof. Rempe at MPQ and does not aim on cooling molecules

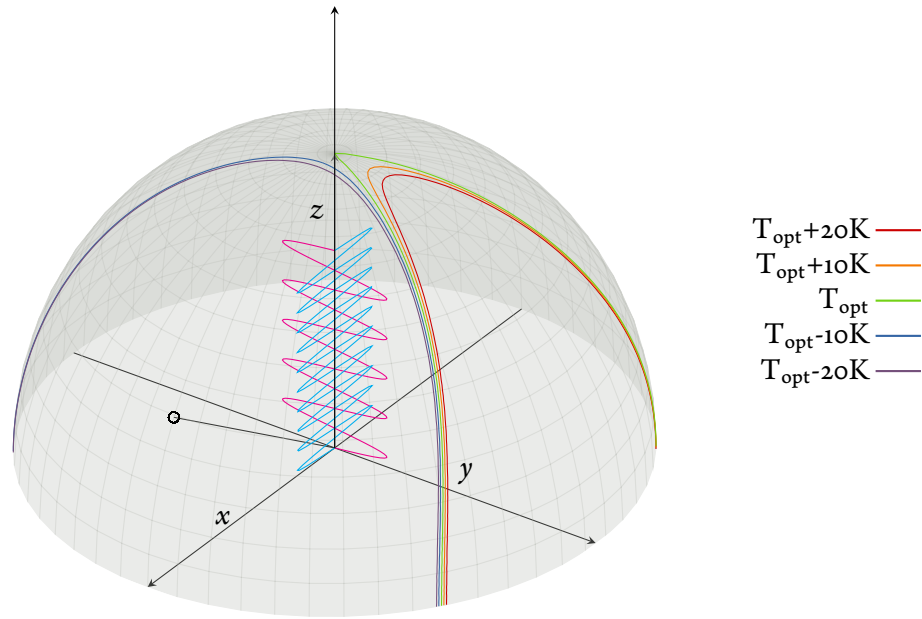


Figure C.5.: Phase matching curve for the SHG process $987 \text{ nm} \rightarrow 493 \text{ nm}$ in KNbO_3 at different temperatures shown on a half sphere around the z -axis; see text for the coordinate frame. At $T_{\text{opt}} = 41.45 \text{ }^\circ\text{C}$, the curve intersects with the z -axis avoiding walk-off for the fundamental and second harmonic wave. At this point phase matching is fulfilled if the fundamental beam polarization is parallel to the y -axis. The second harmonic is generated orthogonal polarized. The position of the optical axis is indicated as black circle. The other optical axis lies in the not shown but completely symmetric other semisphere. Data was generated using SNLO [157].

in the sense of slowing them down, but to filter the slowest of all molecules out of cryogenic or even room temperature ensembles. The method is presented only schematically in this section in order to mention its main principle and to motivate the bent structure of the RF-guide; see section 2.2 on page 27. A detailed and mathematical more elaborate description can be found in [91], for example.

The filtering process bases on the Stark-effect, i. e. the (mostly linear) dependence of the energy of the rovibrational states of polar molecules on the absolute value of an external electric field. The energy of molecular quantum states whose time averaged dipole moment orients antiparallel to the external electric field is minimized in regions of weak electric field. These molecular states are called *low-field seeking* states. A *static* quadrupole potential exhibits weak electric field strengths mainly around its center. Low-field seeking molecules can thus be confined in this potential if their transverse kinetic energy does not exceed the trap depth. The radial filtering process exploits this condition and selects only the slowest molecules.

If the quadrupole potential is formed along a guide that bends around a corner, molecules being too fast cannot follow the bend because their centrifugal force overcomes the Stark barrier. In this

way, the longitudinal velocity component can be selected, too. A larger radius of curvature leads to more modest filtering whereas only slower molecules can be guided through a bend with a small radius.

It is important to note that velocity filtering in the above way has been reported to be efficient for strong *static* electric fields generated by ± 5000 V applied to a quadrupole configuration [133] similar to the one used in this thesis. To give an example, the Stark-effect in ammonia ND_3 under these conditions is sufficiently strong to confine molecules with kinetic energies up to an equivalent temperature of 4 K moving at $v_{\text{max}} = 70 \text{ m s}^{-1}$. The fraction of molecules slower than v_{max} can be derived from the Maxwell-Boltzmann distribution which yields 2 ‰. It is the vast abundance of particles that leaves a density of $1 \cdot 10^{16} \text{ cm}^{-3}$ slow particles and a measured flux of $1 \cdot 10^{10} \text{ s}^{-1}$ although only a tiny fraction of all particles is guided.

The uncertain ability to guide neutral polar molecules in RF-fields and the comparable low maximum RF-voltages achievable in the present apparatus suggest the neutral molecule flux to be small compared with the dedicated DC velocity filtering setups mentioned above. For this reasoning, attention was given to enhance guiding efficiency at the expense of filtering strength. In particular, the radius of curvature of the quadrupole guide has been chosen comparably big compared to that used in [91], for example.

Bibliography

- [1] Jason M. Amini et al. “Toward scalable ion traps for quantum information processing”. In: *New Journal of Physics* 12.3 (2010), p. 033031. DOI: 10.1088/1367-2630/12/3/033031.
- [2] Andreas Assion et al. “Control of Chemical Reactions by Feedback-Optimized Phase-Shaped Femtosecond Laser Pulses”. In: *Science* 282.5390 (Oct. 1998), pp. 919–922. DOI: 10.1126/science.282.5390.919.
- [3] Mireille Aymar et al. “Electronic structure of the magnesium hydride molecular ion”. In: *Journal of Physics B: Atomic, Molecular and Optical Physics* 42.15 (2009), p. 154025. DOI: 10.1088/0953-4075/42/15/154025.
- [4] Takashi Baba and Izumi Waki. “Cooling and Mass-Analysis of Molecules Using Laser-Cooled Atoms”. In: *Japanese Journal of Applied Physics* 35.9A (1996), pp. L1134–L1137. DOI: 10.1143/JJAP35.L1134.
- [5] Takashi Baba and Izumi Waki. “Sympathetic cooling rate of gas-phase ions in a radio-frequency-quadrupole ion trap”. In: *Applied Physics B: Lasers and Optics* 74.4 (Apr. 2002), pp. 375–382. DOI: 10.1007/s003400200829.
- [6] Walter J. Balfour. “Rotational Analysis of the $A^1\Sigma^+ \rightarrow X^1\Sigma^+$ and $B^1\Pi \rightarrow X^1\Sigma^+$ Systems of $^{24}\text{MgH}^+$, $^{25}\text{MgH}^+$, and $^{26}\text{MgH}^+$ ”. In: *Canadian Journal of Physics* 50.11 (1972), pp. 1082–1091. DOI: 10.1139/p72-150.
- [7] Matthew D. Barrett et al. “Deterministic quantum teleportation of atomic qubits”. In: *Nature* 429.6993 (June 2004), pp. 737–739. DOI: 10.1038/nature02608.
- [8] Matthew D. Barrett et al. “Sympathetic cooling of $^9\text{Be}^+$ and $^{24}\text{Mg}^+$ for quantum logic”. In: *Physical Review A* 68.4 (Oct. 2003), p. 042302. DOI: 10.1103/PhysRevA.68.042302.
- [9] Valentin Batteiger et al. “Precision spectroscopy of the 3s-3p fine-structure doublet in Mg^+ ”. In: *Physical Review A* 80.2 (Aug. 2009), p. 022503. DOI: 10.1103/PhysRevA.80.022503.
- [10] Peter Baum, Stefan Lochbrunner, and Eberhard Riedle. “Generation of tunable 7-fs ultra-violet pulses: achromatic phase matching and chirp management”. In: *Applied Physics B: Lasers and Optics* 79.8 (Dec. 2004), pp. 1027–1032. DOI: 10.1007/s00340-004-1668-2.
- [11] Peter Baum and Ahmed H. Zewail. “4D attosecond imaging with free electrons: Diffraction methods and potential applications”. In: *Chemical Physics* 366.1-3 (Dec. 2009), pp. 2–8. DOI: 10.1016/j.chemphys.2009.07.013.
- [12] Martin T. Bell et al. “Ion-molecule chemistry at very low temperatures: cold chemical reactions between Coulomb-crystallized ions and velocity-selected neutral molecules”. In: *Faraday Discussions* 142 (2009), pp. 73–91. DOI: 10.1039/b818733a.

- [13] Anders Bertelsen et al. “Photo-dissociation of Cold $^{24}\text{MgH}^+$ ions”. In: *European Physical Journal D: Atomic, Molecular and Optical Physics* 31.2 (Nov. 2004), pp. 403–408. DOI: 10.1140/epjd/e2004-00152-9.
- [14] N. Beverini et al. “Wavelength, isotopic shift, and transition rate of the MgI resonance line”. In: *Optics Communications* 77.4 (1990), pp. 299–302. DOI: 10.1016/0030-4018(90)90095-B.
- [15] Donald H. Bilderback, Pascal Elleaume, and Edgar Weckert. “Review of third and next generation synchrotron light sources”. In: *Journal of Physics B: Atomic, Molecular and Optical Physics* 38.9 (2005), S773. DOI: 10.1088/0953-4075/38/9/022.
- [16] Gerhard Birkl, Sven Kassner, and Herbert Walther. “Multiple-shell structures of laser-cooled $^{24}\text{Mg}^+$ ions in a quadrupole storage ring”. In: *Nature* 357.6376 (May 1992), pp. 310–313. DOI: 10.1038/357310a0.
- [17] R. Blümel et al. “Chaos and order of laser-cooled ions in a Paul trap”. In: *Physical Review A* 40.2 (July 1989), p. 808. DOI: 10.1103/PhysRevA.40.808.
- [18] Elisabeth Bothschafter. “Collinear Generation and Characterization of Ultrashort UV and XUV Laser Pulses”. Diplomarbeit. Universität Stuttgart, Oct. 2009.
- [19] Elisabeth M. Bothschafter et al. “Collinear generation of ultrashort UV and XUV pulses”. In: *Optics Express* 18.9 (Apr. 2010), pp. 9173–9180. DOI: 10.1364/OE.18.009173.
- [20] Paul Bowe et al. “Sympathetic Crystallization of Trapped Ions”. In: *Physical Review Letters* 82.10 (Mar. 1999), p. 2071. DOI: 10.1103/PhysRevLett.82.2071.
- [21] G. D. Boyd and D. A. Kleinman. “Parametric Interaction of Focused Gaussian Light Beams”. In: *Journal of Applied Physics* 39.8 (July 1968), pp. 3597–3639. DOI: 10.1063/1.1656831.
- [22] Thomas Brabec and Ferenc Krausz. “Intense few-cycle laser fields: Frontiers of nonlinear optics”. In: *Reviews of Modern Physics* 72.2 (Apr. 2000), p. 545. DOI: 10.1103/RevModPhys.72.545.
- [23] Daan Brinks et al. “Visualizing and controlling vibrational wave packets of single molecules”. In: *Nature* 465.7300 (June 2010), pp. 905–908. DOI: 10.1038/nature09110.
- [24] Tobias Brixner et al. “Two-dimensional spectroscopy of electronic couplings in photosynthesis”. In: *Nature* 434.7033 (Mar. 2005), pp. 625–628. DOI: 10.1038/nature03429.
- [25] Paul Brumer and Moshe Shapiro. “Control of unimolecular reactions using coherent light”. In: *Chemical Physics Letters* 126.6 (May 1986), pp. 541–546. DOI: 10.1016/S0009-2614(86)80171-3.
- [26] Lucien Le Cam. “Maximum Likelihood: An Introduction”. In: *International Statistical Review* 58.2 (Aug., 1990), pp. 153–171. URL: <http://www.jstor.org/stable/1403464>.
- [27] J. B. Camp, T. W. Darling, and Ronald E. Brown. “Macroscopic variations of surface potentials of conductors”. In: *Journal of Applied Physics* 69.10 (May 1991), pp. 7126–7129. DOI: 10.1063/1.347601.

- [28] Adrian L. Cavalieri et al. “Attosecond spectroscopy in condensed matter”. In: *Nature* 449.7165 (Oct. 2007), pp. 1029–1032. DOI: 10.1038/nature06229.
- [29] Adrian L. Cavalieri et al. “Intense 1.5-cycle near infrared laser waveforms and their use for the generation of ultra-broadband soft-x-ray harmonic continua”. In: *New Journal of Physics* 9.7 (2007), p. 242. DOI: 10.1088/1367-2630/9/7/242.
- [30] Henry N. Chapman et al. “Femtosecond diffractive imaging with a soft-X-ray free-electron laser”. In: *Nature Physics* 2.12 (Dec. 2006), pp. 839–843. DOI: 10.1038/nphys461.
- [31] Chin-wen Chou et al. “Frequency Comparison of Two High-Accuracy Al^+ Optical Clocks”. In: *Physical Review Letters* 104.7 (Feb. 2010), p. 070802. DOI: 10.1103/PhysRevLett.104.070802.
- [32] Steven Chu. “Nobel Lecture: The manipulation of neutral particles”. In: *Reviews of Modern Physics* 70.3 (July 1998), p. 685. DOI: 10.1103/RevModPhys.70.685; Claude N. Cohen-Tannoudji. “Nobel Lecture: Manipulating atoms with photons”. In: *Reviews of Modern Physics* 70.3 (July 1998), p. 707. DOI: 10.1103/RevModPhys.70.707; William D. Phillips. “Nobel Lecture: Laser cooling and trapping of neutral atoms”. In: *Reviews of Modern Physics* 70.3 (July 1998), p. 721. DOI: 10.1103/RevModPhys.70.721.
- [33] J. Ignacio Cirac and Peter Zoller. “Quantum Computations with Cold Trapped Ions”. In: *Physical Review Letters* 74.20 (May 1995), p. 4091. DOI: 10.1103/PhysRevLett.74.4091.
- [34] E. A. Cornell and C. E. Wieman. “Nobel Lecture: Bose-Einstein condensation in a dilute gas, the first 70 years and some recent experiments”. In: *Reviews of Modern Physics* 74.3 (Aug. 2002), p. 875. DOI: 10.1103/RevModPhys.74.875; Wolfgang Ketterle. “Nobel lecture: When atoms behave as waves: Bose-Einstein condensation and the atom laser”. In: *Reviews of Modern Physics* 74.4 (Nov. 2002), p. 1131. DOI: 10.1103/RevModPhys.74.1131.
- [35] Marcos Dantus, Mark J. Rosker, and Ahmed H. Zewail. “Femtosecond real-time probing of reactions. II. The dissociation reaction of ICN”. In: *Journal of Chemical Physics* 89.10 (Nov. 1988), pp. 6128–6140. DOI: 10.1063/1.455428.
- [36] M. D. Davidson et al. “Oscillator-Strengths And Branching Ratios Of Transitions Between Low-Lying Levels In The Barium-II Spectrum”. In: *Astronomy and Astrophysics* 255.1-2 (Feb. 1992), pp. 457–458. URL: <http://adsabs.harvard.edu/abs/1992A%26A..255..457D>.
- [37] Hans Georg Dehmelt. “Radiofrequency Spectroscopy of Stored Ions I: Storage”. In: ed. by D.R. Bates and Immanuel Estermann. Vol. Volume 3. Academic Press, 1968, pp. 53–72. ISBN: 00652199. DOI: 10.1016/S0065-2199(08)60170-0.
- [38] D. R. Denison. “Operating Parameters of a Quadrupole in a Grounded Cylindrical Housing”. In: *The Journal of Vacuum Science and Technology* 8.1 (Jan. 1971), pp. 266–269. DOI: 10.1116/1.1316304.
- [39] Louis Deslauriers et al. “Scaling and Suppression of Anomalous Heating in Ion Traps”. In: *Physical Review Letters* 97.10 (Sept. 2006), p. 103007. DOI: 10.1103/PhysRevLett.97.103007.
- [40] F. Diedrich et al. “Laser Cooling to the Zero-Point Energy of Motion”. In: *Physical Review Letters* 62.4 (Jan. 1989), p. 403. DOI: 10.1103/PhysRevLett.62.403.

- [41] Jean-Claude Diels and Wolfgang Rudolph. *Ultrashort laser pulse phenomena*. 2nd ed. Amsterdam, London: Elsevier/Academic Press, 2006. 652 pp. ISBN: 9780122154935.
- [42] Hsiang-Tai Dou. “Towards Single Molecule Imaging in an Ion Trap”. Diplomarbeit. Ludwig-Maximilians-Universität München, Fakultät für Physik, Oct. 2009.
- [43] Michael Drewsen. private communication. 2010.
- [44] Michael Drewsen and Andy Brøner. “Harmonic linear Paul trap: Stability diagram and effective potentials”. In: *Physical Review A* 62.4 (Sept. 2000), p. 045401. DOI: 10.1103/PhysRevA.62.045401.
- [45] Michael Drewsen et al. “Large Ion Crystals in a Linear Paul Trap”. In: *Physical Review Letters* 81.14 (Oct. 1998), p. 2878. DOI: 10.1103/PhysRevLett.81.2878.
- [46] Charles G. Durfee et al. “Phase Matching of High-Order Harmonics in Hollow Waveguides”. In: *Physical Review Letters* 83.11 (Sept. 1999), pp. 2187–2190. DOI: 10.1103/PhysRevLett.83.2187.
- [47] Stephan Düwel. “to be submitted”. Diplomarbeit. Ludwig-Maximilians-Universität München, Fakultät für Physik, 2010.
- [48] Jason R. Dwyer et al. *Femtosecond electron diffraction: Towards making the “molecular movie”*. Ed. by Takayoshi Kobayashi et al. Vol. 2. Chemical Physics 79. Berlin, Heidelberg: Springer, 2005, pp. 144–148. 907 pp. ISBN: 9783540241102. DOI: 10.1007/b138761.
- [49] J. Gary Eden. “High-order harmonic generation and other intense optical field-matter interactions: review of recent experimental and theoretical advances”. In: *Progress in Quantum Electronics* 28.3-4 (2004), pp. 197–246. DOI: 10.1016/j.pquantelec.2004.06.002.
- [50] Dima Egorov et al. “Buffer-gas cooling of atomic and molecular beams”. In: *Physical Review A* 66.4 (Oct. 2002), p. 043401. DOI: 10.1103/PhysRevA.66.043401.
- [51] Thorsten Ergler et al. “Time-Resolved Imaging and Manipulation of H₂ Fragmentation in Intense Laser Fields”. In: *Physical Review Letters* 95.9 (Aug. 2005), p. 093001. DOI: 10.1103/PhysRevLett.95.093001.
- [52] Josef Feldhaus, John Arthur, and Jerry Hastings. “X-ray free-electron lasers”. In: *Journal of Physics B: Atomic, Molecular and Optical Physics* 38.9 (2005), S799. DOI: 10.1088/0953-4075/38/9/023.
- [53] John B. Fenn, Koichi Tanaka, and Kurt Wüthrich. *The Nobel Prize in Chemistry 2002*. Nobelprize.org. URL: http://nobelprize.org/nobel_prizes/chemistry/laureates/2002/ (visited on 07/12/2010).
- [54] John B. Fenn et al. “Electrospray Ionization for Mass Spectrometry of Large Biomolecules”. In: *Science* 246.4926 (Oct. 1989), pp. 64–71. DOI: 10.1126/science.2675315.
- [55] Fibercore. *SM-Series Singlemode Fibers. Attenuation at Visible and NIR Wavelengths*. URL: <http://www.fibercore.com/LinkClick.aspx?fileticket=BLXitwhVFOQ%3D&tabid=68&mid=506> (visited on 07/26/2010).

- [56] Axel Friedenauer et al. “High power all solid state laser system near 280 nm”. In: *Applied Physics B: Lasers and Optics* 84.3 (Jan. 2006), pp. 371–373. DOI: 10.1007/s00340-006-2274-2.
- [57] Werner Fuß. private communication. 2009.
- [58] Matthias Fuchs et al. “Laser-driven soft-X-ray undulator source”. In: *Nature Physics* 5.11 (Nov. 2009), pp. 826–829. DOI: 10.1038/nphys1404.
- [59] Takao Fuji, Takuya Horio, and Toshinori Suzuki. “Generation of 12 fs deep-ultraviolet pulses by four-wave mixing through filamentation in neon gas”. In: *Optics Letters* 32.17 (Sept. 2007), pp. 2481–2483. DOI: 10.1364/OL.32.002481.
- [60] Mark Galassi et al. *GNU Scientific Library Reference Manual*. 3rd ed. Bristol: Network Theory, 2009. 513 pp. ISBN: 0954161734. URL: <http://www.gnu.org/software/gsl/>.
- [61] Stuart Geman and Donald Geman. “Stochastic relaxation, Gibbs distributions and the Bayesian restoration of images*”. In: *Journal of Applied Statistics* 20.5 (1993), pp. 25–62. DOI: 10.1080/02664769300000058.
- [62] Dieter Gerlich and Gheorghe Borodi. “Buffer gas cooling of polyatomic ions in rf multi-electrode traps”. In: *Faraday Discussions* 142 (2009), pp. 57–72. DOI: 10.1039/b820977d.
- [63] Irina Gitlin, Jeffrey D. Carbeck, and George M. Whitesides. “Warum sind Proteine geladen? Netzwerke aus Ladungs-Ladungs-Wechselwirkungen in Proteinen, analysiert über Ladungsleitern und Kapillarelektrophorese”. In: *Angewandte Chemie* 118.19 (2006), pp. 3090–3131. DOI: 10.1002/ange.200502530.
- [64] ASAHI GLASS. *What’s CYTOP?* URL: <http://www.agc.co.jp/english/chemicals/shinsei/cytop/about.html> (visited on 06/11/2010).
- [65] Roy J. Glauber, John L. Hall, and Theodor W. Hänsch. *The Nobel Prize in Physics 2005*. Nobelprize.org. URL: http://nobelprize.org/nobel_prizes/physics/laureates/2005/ (visited on 07/12/2010).
- [66] Caroline Gollub. “Femtosecond quantum control studies on vibrational quantum information processing”. PhD thesis. Fakultät für Chemie und Pharmazie, Ludwig-Maximilians-Universität München, 2009. URL: http://edoc.ub.uni-muenchen.de/9620/1/Gollub_Caroline.pdf.
- [67] Rafael C. Gonzalez and Richard Eugene Woods. *Digital Image Processing*. 2nd ed. Upper Saddle River, New Jersey: Prentice Hall, 2002. 716 pp. ISBN: 0130946508.
- [68] Eleftherios Goulielmakis. “Complete Characterization of Light Waves using Attosecond Pulses”. PhD thesis. Ludwig-Maximilians-Universität München: Fakultät für Physik, 2005. URL: http://edoc.ub.uni-muenchen.de/4111/1/Goulielmakis_Eleftherios.pdf.
- [69] Ulrich Graf. “Generation and Characterization of Intense sub-4-fs Pulses in the deep UV”. Diplomarbeit. Ludwig-Maximilians-Universität München, Fakultät für Physik, 2008.
- [70] Ulrich Graf et al. “Intense few-cycle light pulses in the deep ultraviolet”. In: *Optics Express* 16.23 (Nov. 2008), pp. 18956–18963. DOI: 10.1364/OE.16.018956.

- [71] John Griffiths. "II. Photochemistry of azobenzene and its derivatives". In: *Chemical Society Reviews* 1.4 (1972), pp. 481–493. DOI: 10.1039/CS9720100481.
- [72] A. K. Gupta and J. H. Leck. "An evaluation of the titanium sublimation pump". In: *Vacuum* 25.8 (Aug. 1975), pp. 362–372. DOI: 10.1016/0042-207X(75)91654-1.
- [73] Edward Hamilton et al. "Alignment of symmetric top molecules by short laser pulses". In: *Physical Review A* 72.4 (2005), p. 043402. DOI: 10.1103/PhysRevA.72.043402.
- [74] Rainer W. Hasse and John P. Schiffer. "The structure of the cylindrically confined Coulomb lattice". In: *Annals of Physics* 203.2 (Nov. 1990), pp. 419–448. DOI: 10.1016/0003-4916(90)90177-P.
- [75] Jennifer L. Herek et al. "Quantum control of energy flow in light harvesting". In: *Nature* 417.6888 (May 2002), pp. 533–535. DOI: 10.1038/417533a.
- [76] Maximilian Herrmann et al. "Frequency Metrology on Single Trapped Ions in the Weak Binding Limit: The $3S_{1/2}$ - $3P_{3/2}$ Transition in $^{24}\text{Mg}^+$ ". In: *Physical Review Letters* 102.1 (Jan. 2009), p. 013006. DOI: 10.1103/PhysRevLett.102.013006.
- [77] Manfred Hesse, Herbert Meier, and Bernd Zeeh. *Spektroskopische Methoden in der organischen Chemie*. 7th ed. Stuttgart, New York: Thieme, 2005. 456 pp. ISBN: 9783135761077.
- [78] Roy J. Glauber. "Nobel Lecture: One hundred years of light quanta". In: *Reviews of Modern Physics* 78.4 (Nov. 2006), p. 1267. DOI: 10.1103/RevModPhys.78.1267; John L. Hall. "Nobel Lecture: Defining and measuring optical frequencies". In: *Reviews of Modern Physics* 78.4 (Nov. 2006), p. 1279. DOI: 10.1103/RevModPhys.78.1279; Theodor W. Hänsch. "Nobel Lecture: Passion for precision". In: *Reviews of Modern Physics* 78.4 (Nov. 2006), p. 1297. DOI: 10.1103/RevModPhys.78.1297.
- [79] Theodor W. Hänsch and Bernard Couillaud. "Laser frequency stabilization by polarization spectroscopy of a reflecting reference cavity". In: *Optics Communications* 35.3 (Dec. 1980), pp. 441–444. DOI: 10.1016/0030-4018(80)90069-3.
- [80] Matthias Hoener et al. "Ultraintense X-Ray Induced Ionization, Dissociation, and Frustrated Absorption in Molecular Nitrogen". In: *Physical Review Letters* 104.25 (June 2010), p. 253002. DOI: 10.1103/PhysRevLett.104.253002.
- [81] Lotte Holmegaard et al. "Laser-Induced Alignment and Orientation of Quantum-State-Selected Large Molecules". In: *Physical Review Letters* 102.2 (Jan. 2009), p. 023001. DOI: 10.1103/PhysRevLett.102.023001.
- [82] Liv Hornekær. "Single- and Multi-Species Coulomb Ion Crystals: Structures, Dynamics and Sympathetic Cooling". PhD thesis. Danish National Research Foundation Center for Quantum Optics - Quantop Department of Physics and Astronomy, The University of Aarhus, 2000. URL: http://phys.au.dk/fileadmin/site_files/forskning/iontrap/pdfs/PhD_Hornekaer_2000.pdf.

- [83] Klaus P. Huber and Gerhard Herzberg. “Constants of Diatomic Molecules (data prepared by J.W. Gallagher and R.D. Johnson, III)”. In: *NIST Standard Reference Database Number 69*. Ed. by P.J. Linstrom and Mallard W.G. Gaithersburg MD, 20899: National Institute of Standards and Technology, <http://webbook.nist.gov>, (retrieved June 28, 2010).
- [84] Lester Ingber. “Adaptive simulated annealing (ASA): Lessons learned”. In: *Control and Cybernetics* 25.1 (1996), pp. 33–54. URL: http://www.ingber.com/asa96_lessons.ps.gz.
- [85] Lester Ingber. ASA. Comp. software. Version 26.39. URL: <http://www.ingber.com/>.
- [86] Daniel F. V. James. “Quantum dynamics of cold trapped ions with application to quantum computation”. In: *Applied Physics B: Lasers and Optics* 66.2 (Feb. 1998), pp. 181–190. DOI: 10.1007/s003400050373.
- [87] Richard H. Jarman and Barry C. Johnson. “Characteristics of domain formation and poling in potassium niobate”. In: *Inorganic Crystals for Optics, Electro-Optics, and Frequency Conversion*. Ed. by Peter F. Bordui. Vol. 1561. 1. San Diego, CA, USA: SPIE, 1991, pp. 33–42. DOI: 10.1117/12.50751.
- [88] David J. Jones et al. “Carrier-Envelope Phase Control of Femtosecond Mode-Locked Lasers and Direct Optical Frequency Synthesis”. In: *Science* 288.5466 (Apr. 2000), pp. 635–639. DOI: 10.1126/science.288.5466.635.
- [89] Karl Jousten, ed. *Wutz Handbuch Vakuumtechnik*. Theorie und Praxis. 8th ed. Wiesbaden: Vieweg, 2004. 912 pp. ISBN: 9783528648848.
- [90] Solvejg Jørgensen, Michael Drewsen, and Ronnie Kosloff. “Intensity and wavelength control of a single molecule reaction: Simulation of photodissociation of cold-trapped MgH^+ ”. In: *Journal of Chemical Physics* 123.9 (Sept. 2005), p. 094302. DOI: 10.1063/1.2011398.
- [91] Tobias Junglen. “Guiding and Trapping of Cold Dipolar Molecules”. PhD thesis. Fakultät für Physik, Technische Universität München, Nov. 2005. URL: <http://mediatum2.ub.tum.de/download/603106/603106.pdf>.
- [92] Tobias Junglen et al. “Slow ammonia molecules in an electrostatic quadrupole guide”. In: *The European Physical Journal D - Atomic, Molecular, Optical and Plasma Physics* 31.2 (Nov. 2004), pp. 365–373. DOI: 10.1140/epjd/e2004-00130-3.
- [93] Tobias Junglen et al. “Two-Dimensional Trapping of Dipolar Molecules in Time-Varying Electric Fields”. In: *Physical Review Letters* 92.22 (June 2004), p. 223001. DOI: 10.1103/PhysRevLett.92.223001.
- [94] Steffen Kahra. “Phasenmodulation von Femtosekundenimpulsen im UV und deren Anwendung zur kohärenten Kontrolle von Molekülen”. Diplomarbeit. Ludwig-Maximilians-Universität München, Fakultät für Physik, 2005.
- [95] Erich Kamke. “Gewöhnliche Differentialgleichungen”. In: *Mathematik und ihre Anwendungen in Physik und Technik*. Vol. 18.1: *Differentialgleichungen Lösungsmethoden und Lösungen*. Found. by E. Hilb. Ed. by R. Kochendörfer and A. Kratzer. 7th ed. Reihe A. Leipzig: Akademische Gesellschaft Geest & Portig K.-G., 1961.

- [96] David Kielpinski, Chris Monroe, and David J. Wineland. “Architecture for a large-scale ion-trap quantum computer”. In: *Nature* 417.6890 (June 2002), pp. 709–711. DOI: 10.1038/nature00784.
- [97] Niels Kjærgaard et al. “Isotope selective loading of an ion trap using resonance-enhanced two-photon ionization”. In: *Applied Physics B: Lasers and Optics* 71.2 (Aug. 2000), pp. 207–210. DOI: 10.1007/s003400000296.
- [98] Markus Kowalewski et al. “Cavity cooling of translational and ro-vibrational motion of molecules: ab initio-based simulations for OH and NO”. In: *Applied Physics B: Lasers and Optics* 89.4 (Dec. 2007), pp. 459–467. DOI: 10.1007/s00340-007-2860-y.
- [99] Jochen Küpper, Frank Filsinger, and Gerard Meijer. “Manipulating the motion of large neutral molecules”. In: *Faraday Discussions* 142 (2009), pp. 155–173. DOI: 10.1039/b820045a.
- [100] Ferenc Krausz and Misha Ivanov. “Attosecond physics”. In: *Rev. Mod. Phys.* 81.1 (Feb. 2009), pp. 163–234. DOI: 10.1103/RevModPhys.81.163.
- [101] Manuel Kremer et al. “Electron Localization in Molecular Fragmentation of H₂ by Carrier-Envelope Phase Stabilized Laser Pulses”. In: *Physical Review Letters* 103.21 (Nov. 2009), p. 213003. DOI: 10.1103/PhysRevLett.103.213003.
- [102] Haggai Landa et al. “Quantum Coherence of Discrete Kink Solitons in Ion Traps”. In: *Physical Review Letters* 104.4 (Jan. 2010), p. 043004. DOI: 10.1103/PhysRevLett.104.043004.
- [103] Kevin F. Lee et al. “Field-Free Three-Dimensional Alignment of Polyatomic Molecules”. In: *Physical Review Letters* 97.17 (Oct. 2006), p. 173001. DOI: 10.1103/PhysRevLett.97.173001.
- [104] Günther Leschhorn. “Speichern und Kühlen molekularer Ionen in einer linearen Paulfalle”. Diplomarbeit. Ludwig-Maximilians-Universität München, Fakultät für Physik, June 2007.
- [105] CPO Ltd. *CPO Charged Particle Optics*. Comp. software. Version November 2005 edition. Manchester, UK, Nov. 2005. URL: <http://www.electronoptics.com/>.
- [106] Andrew D. Ludlow, H. Mark Nelson, and Scott D. Bergeson. “Two-photon absorption in potassium niobate”. In: *Journal of the Optical Society of America B* 18.12 (Dec. 2001), pp. 1813–1820. DOI: 10.1364/JOSAB.18.001813.
- [107] Volker Ludsteck. “Experimente mit einer linearen Ionenkette zur Realisierung eines Quantencomputers”. PhD thesis. Fakultät für Physik, Ludwig-Maximilians-Universität München, May 2004. URL: http://edoc.ub.uni-muenchen.de/2417/1/Ludsteck_Volker.pdf.
- [108] John M. J. Madey. “Stimulated Emission of Bremsstrahlung in a Periodic Magnetic Field”. In: *Journal of Applied Physics* 42.5 (1971), pp. 1906–1913. DOI: 10.1063/1.1660466.
- [109] D. N. Madsen et al. “Measurements on photo-ionization of 3s3p ¹P₁ magnesium atoms”. In: *Journal of Physics B: Atomic, Molecular and Optical Physics* 33.22 (2000), p. 4981. DOI: 10.1088/0953-4075/33/22/302.
- [110] Theodore H. Maimann. “Stimulated Optical Radiation in Ruby”. In: *Nature* 187.4736 (Aug. 1960), pp. 493–494. DOI: 10.1038/187493a0.

- [111] Erik G. Marklund et al. “Structural stability of electrosprayed proteins: temperature and hydration effects”. In: *Physical Chemistry Chemical Physics* 11.36 (2009), pp. 8069–8078. DOI: 10.1039/b903846a.
- [112] Brian McNeil. “Free electron lasers: First light from hard X-ray laser”. In: *Nature Photonics* 3.7 (July 2009), pp. 375–377. DOI: 10.1038/nphoton.2009.110.
- [113] Harold J. Metcalf and Peter Van der Straten. *Laser cooling and trapping*. New York, London: Springer, 1999. 323 pp. ISBN: 0387987479.
- [114] Harold J. Metcalf and Peter van der Straten. “Laser cooling and trapping of atoms”. In: *Journal of the Optical Society of America B: Optical Physics* 20.5 (May 2003), pp. 887–908. DOI: 10.1364/JOSAB.20.000887.
- [115] Jens Möhring et al. “Generation of phase-controlled ultraviolet pulses and characterization by a simple autocorrelator setup”. In: *Journal of the Optical Society of America B* 26.8 (Aug. 2009), pp. 1538–1544. DOI: 10.1364/JOSAB.26.001538.
- [116] Kristian Mølhave and Michael Drewsen. “Formation of translationally cold MgH^+ and MgD^+ molecules in an ion trap”. In: *Physical Review A* 62.1 (June 2000), p. 011401. DOI: 10.1103/PhysRevA.62.011401.
- [117] Richard Neutze et al. “Potential for biomolecular imaging with femtosecond X-ray pulses”. In: *Nature* 406.6797 (Aug. 2000), pp. 752–757. DOI: 10.1038/35021099.
- [118] Mauro Nisoli et al. “A novel-high energy pulse compression system: generation of multigigawatt sub-5-fs pulses”. In: *Applied Physics B: Lasers and Optics* 65.2 (Aug. 1997), pp. 189–196. DOI: 10.1007/s003400050263.
- [119] Mauro Nisoli et al. “Compression of high-energy laser pulses below 5 fs”. In: *Optics Letters* 22.8 (Apr. 1997), pp. 522–524. DOI: 10.1364/OL.22.000522.
- [120] Dirk Nolting, Christel Marian, and Rainer Weinkauff. “Protonation effect on the electronic spectrum of tryptophan in the gas phase”. In: *Physical Chemistry Chemical Physics* 6.10 (2004), pp. 2633–2640. DOI: 10.1039/b316669d.
- [121] David Offenberger et al. “Measurement of small photodestruction rates of cold, charged biomolecules in an ion trap”. In: *Journal of Physics B: Atomic, Molecular and Optical Physics* 42.3 (2009), p. 035101. DOI: 10.1088/0953-4075/42/3/035101.
- [122] David Offenberger et al. “Measurement of small photodestruction rates of cold, charged biomolecules in an ion trap”. In: *Journal of Physics B: Atomic, Molecular and Optical Physics* 42.3 (2009), p. 035101. DOI: 10.1088/0953-4075/42/3/035101.
- [123] Jean-Christophe Olivo-Marin. “Extraction of spots in biological images using multiscale products”. In: *Pattern Recognition* 35.9 (Sept. 2002), pp. 1989–1996. DOI: 10.1016/S0031-3203(01)00127-3.

- [124] Alexander Ostendorf. “Sympathetische Kühlung von Molekülonen durch lasergekühlte Bariumionen in einer linearen Paulfalle”. PhD thesis. Heinrich-Heine-Universität Düsseldorf, Mathematisch- Naturwissenschaftliche Fakultät, Feb. 2006. URL: <http://docserv.uni-duesseldorf.de/servlets/DocumentServlet?id=3404>.
- [125] Alexander Ostendorf et al. “Sympathetic Cooling of Complex Molecular Ions to Millikelvin Temperatures”. In: *Physical Review Letters* 97.24 (Dec. 2006), p. 243005. DOI: 10.1103/PhysRevLett.97.243005.
- [126] Michael V. Pack, Darrell J. Armstrong, and Arlee V. Smith. “Measurement of the $\chi(2)$ tensor of the potassium niobate crystal”. In: *Journal of the Optical Society of America B* 20.10 (Oct. 2003), pp. 2109–2116. DOI: 10.1364/JOSAB.20.002109.
- [127] Wolfgang Paul. “Electromagnetic traps for charged and neutral particles”. In: *Reviews of Modern Physics* 62.3 (July 1990), pp. 531–540. DOI: 10.1103/RevModPhys.62.531.
- [128] Wolfgang Paul and Helmut Steinwedel. “Ein neues Massenspektrometer ohne Magnetfeld”. In: *Zeitschrift Naturforschung Teil A* 8 (1953), pp. 448–. URL: <http://adsabs.harvard.edu/abs/1953ZNatA...8..448P>.
- [129] Lutz Petersen. “Quantum Simulations in Ion Traps: Towards Simulating the Early Expanding Universe”. Diplomarbeit. Ludwig-Maximilians-Universität München, Fakultät für Physik, Dec. 2006.
- [130] Martin E. Poitzsch et al. “Cryogenic linear ion trap for accurate spectroscopy”. In: *Review of Scientific Instruments* 67.1 (Jan. 1996), pp. 129–134. DOI: 10.1063/1.1146560.
- [131] Alexancer Pukhov and Jürgen Meyer-ter Vehn. “Laser wake field acceleration: the highly non-linear broken-wave regime”. In: *Applied Physics B: Lasers and Optics* 74.4 (Apr. 2002), pp. 355–361. DOI: 10.1007/s003400200795.
- [132] Norman F. Ramsey, Hans G. Dehmelt, and Wolfgang Paul. *The Nobel Prize in Physics 1989*. Nobelprize.org. URL: http://nobelprize.org/nobel_prizes/physics/laureates/1989/ (visited on 07/12/2010).
- [133] Sadiq A. Rangwala et al. “Continuous source of translationally cold dipolar molecules”. In: *Physical Review A* 67.4 (Apr. 2003), p. 043406. DOI: 10.1103/PhysRevA.67.043406.
- [134] Peter Reckenthäler et al. “Time-Resolved Electron Diffraction from Selectively Aligned Molecules”. In: *Physical Review Letters* 102.21 (May 2009), p. 213001. DOI: 10.1103/PhysRevLett.102.213001.
- [135] Dirk Reiß, Albrecht Lindner, and Rainer Blatt. “Cooling of trapped multilevel ions: A numerical analysis”. In: *Physical Review A* 54.6 (Dec. 1996), p. 5133. DOI: 10.1103/PhysRevA.54.5133.
- [136] Florentin Reiter et al. “Generation of sub-3 fs pulses in the deep ultraviolet”. In: *Optics Letters* 35.13 (July 2010), pp. 2248–2250. DOI: 10.1364/OL.35.002248.

- [137] Harald Rohde et al. “Sympathetic ground-state cooling and coherent manipulation with two-ion crystals”. In: *Journal of Optics B: Quantum and Semiclassical Optics* 3.1 (2001), S34. DOI: 10.1088/1464-4266/3/1/357.
- [138] Bernhard Roth and Stephan Schiller. *Sympathetically cooled molecular ions: from principles to first applications*. 2008. arXiv:0812.1154v1.
- [139] Claude Rullière. *Femtosecond Laser Pulses, Principles and Experiments*. 2nd ed. Springer, 2005. 426 pp. ISBN: 9780387017693. DOI: 10.1007/b137908.
- [140] J. P. Marques de Sá. *Pattern recognition: Concepts, Methods and Applications*. Berlin, New York: Springer, 2001. 318 pp. ISBN: 3540422978.
- [141] Giuseppe Sansone et al. “Electron localization following attosecond molecular photoionization”. In: *Nature* 465.7299 (June 2010), pp. 763–766. DOI: 10.1038/nature09084.
- [142] Arthur L. Schawlow and Charles H. Townes. “Infrared and Optical Masers”. In: *Physical Review* 112.6 (Dec. 1958), pp. 1940–1949. DOI: 10.1103/PhysRev.112.1940.
- [143] John P. Schiffer et al. “Temperature, ordering, and equilibrium with time-dependent confining forces”. In: *Proceedings of the National Academy of Sciences of the United States of America* 97.20 (Sept. 2000), pp. 10697–10700. DOI: 10.1073/pnas.190320397.
- [144] Hector Schmitz. “Über Quantensimulationen in einer Paulfalle”. PhD thesis. Fakultät für Physik, Ludwig-Maximilians-Universität München, in preparation.
- [145] Hector Schmitz et al. “Quantum Walk of a Trapped Ion in Phase Space”. In: *Physical Review Letters* 103.9 (Aug. 2009), p. 090504. DOI: 10.1103/PhysRevLett.103.090504.
- [146] Christian Schneider et al. *Optical Trapping of an Ion*. 2010. arXiv:1001.2953v1.
- [147] Jochen Schneider. “Scientific Highlights from Operation of FLASH and New Opportunities with LCLS”. In: *OSA Technical Digest (CD)*. Optical Society of America, May 2010. URL: <http://www.opticsinfobase.org/abstract.cfm?URI=CLEO-2010-JFA1>.
- [148] Tobias Schneider et al. “All-optical preparation of molecular ions in the rovibrational ground state”. In: *Nature Physics* 6.4 (Apr. 2010), pp. 275–278. DOI: 10.1038/nphys1605.
- [149] Tobias Schätz. “Kristalline Ionenstrahlen”. PhD thesis. Fakultät für Physik, Ludwig-Maximilians-Universität München, Nov. 2001. URL: http://edoc.ub.uni-muenchen.de/444/1/Schaetz_Tobias.pdf.
- [150] Tobias Schätz, Ulrich Schramm, and Dietrich Habs. “Crystalline ion beams”. In: *Nature* 412.6848 (Aug. 2001), pp. 717–720. DOI: 10.1038/35089045.
- [151] Tobias Schätz et al. “Towards (scalable) quantum simulations in ion traps”. In: *Journal of Modern Optics* 54.16 (2007), pp. 2317–2325. DOI: 10.1080/09500340701639631.
- [152] Martin Schultze et al. “Delay in Photoemission”. In: *Science* 328.5986 (June 2010), pp. 1658–1662. DOI: 10.1126/science.1189401.

- [153] Stephan Schulz et al. "Optimization of segmented linear Paul traps and transport of stored particles". In: *Fortschritte der Physik* 54.8-10 (2006), pp. 648–665. DOI: 10.1002/prop.200610324.
- [154] L. Shiv et al. "Inhibited light - induced absorption in KNbO₃". In: *Optics Letter* 20.22 (Nov. 1995), pp. 2270–2272. DOI: 10.1364/OL.20.002270.
- [155] Jack Simons and Jeff Nichols. *Quantum Mechanics in Chemistry*. Ed. by Donald G. Truhlar. 1st ed. Vol. 3. Topics in Physical Chemistry. New York, Oxford: Oxford University Press, Jan. 1997. ISBN: 0195082001.
- [156] Julian Smart, Roebing Roebing, and Vadim Zeitlin. *wxWidgets: A portable C++ and Python GUI toolkit*. Comp. software. Version 2.8. URL: <http://www.wxwidgets.org/>.
- [157] Arlee V. Smith. *SNLO*. Comp. software. Version 51. Nov. 2009. URL: <http://www.as-photonics.com/snlo.html>.
- [158] P. W. Smith and Theodor W. Hänsch. "Cross-Relaxation Effects in the Saturation of the 6328Å Neon-Laser Line". In: *Physical Review Letters* 26.13 (Mar. 1971), p. 740. DOI: 10.1103/PhysRevLett.26.740.
- [159] Richard G. Smith. "Optical Power Handling Capacity of Low Loss Optical Fibers as Determined by Stimulated Raman and Brillouin Scattering". In: *Applied Optics* 11.11 (Nov. 1972), pp. 2489–2494. DOI: 10.1364/AO.11.002489.
- [160] Christian Sommer et al. "Continuous guided beams of slow and internally cold polar molecules." In: *Faraday Discussions* 142 (2009), pp. 203–220. DOI: 10.1039/b819726a.
- [161] John C. H. Spence and R. Bruce Doak. "Single Molecule Diffraction". In: *Physical Review Letters* 92.19 (May 2004), p. 198102. DOI: 10.1103/PhysRevLett.92.198102.
- [162] R. Srinivasan et al. "Ultrafast electron diffraction (UED); A new development for the 4D determination of transient molecular structures". In: *Helvetica Chimica Acta* 86.6 (2003), pp. 1763–1838. DOI: 10.1002/hlca.200390147.
- [163] Peter F. Staunum et al. "Rotational laser cooling of vibrationally and translationally cold molecular ions". In: *Nature Physics* 6.4 (Apr. 2010), pp. 271–274. DOI: 10.1038/nphys1604.
- [164] Kai Stock et al. "Reaction path dependent coherent wavepacket dynamics in excited state intramolecular double proton transfer". In: *Chemical Physics* 349.1-3 (June 2008), pp. 197–203. DOI: 10.1016/j.chemphys.2008.03.007.
- [165] Donna Strickland and Gerard Mourou. "Compression of amplified chirped optical pulses". In: *Optics Communications* 56.3 (Dec. 1985), pp. 219–221. DOI: 10.1016/0030-4018(85)90120-8.
- [166] David J. Tannor, Ronnie Kosloff, and Stuart A. Rice. "Coherent pulse sequence induced control of selectivity of reactions: Exact quantum mechanical calculations". In: *The Journal of Chemical Physics* 85.10 (1986), pp. 5805–5820. DOI: 10.1063/1.451542.

- [167] Murilo L. Tiago, Sohrab Ismail-Beigi, and Steven G. Louie. “Photoisomerization of azobenzene from first-principles constrained density-functional calculations”. In: *Journal of Chemical Physics* 122.9 (2005), p. 094311. DOI: 10.1063/1.1861873.
- [168] Rick Trebino. *Frequency-resolved optical gating : the measurement of ultrashort laser pulses*. Boston, London: Kluwer Academic Publishers, 2000. 425 pp. ISBN: 1402070667.
- [169] John G. Underwood, Benjamin J. Sussman, and Albert Stolow. “Field-free three dimensional molecular axis alignment”. In: *Physical Review Letters* 94.14 (2005), p. 143002. DOI: 10.1103/PhysRevLett.94.143002.
- [170] Friso van der Veen and Franz Pfeiffer. “Coherent x-ray scattering”. In: *Journal of Physics: Condensed Matter* 16.28 (2004), p. 5003. DOI: 10.1088/0953-8984/16/28/020.
- [171] Simon S. Viftrup et al. “Holding and Spinning Molecules in Space”. In: *Physical Review Letters* 99.14 (Oct. 2007), p. 143602. DOI: 10.1103/PhysRevLett.99.143602.
- [172] Thomas E. Wall et al. “Transport of polar molecules by an alternating-gradient guide”. In: *Physical Review A* 80.4 (Oct. 2009), p. 043407. DOI: 10.1103/PhysRevA.80.043407.
- [173] Gordon Webster and Rolf Hilgenfeld. “Perspectives on Single Molecule Diffraction Using the X-Ray Free Electron Laser”. In: *Single Molecules* 3.1 (2002), pp. 63–68. DOI: 10.1002/1438-5171(200204)3:1<63::AID-SIMO63>3.0.CO;2-O.
- [174] Andrew M. Weiner. *Ultrafast Optics*. Ed. by Glenn Boremann. Wiley series in pure and applied optics. Hoboken, New Jersey: John Wiley & Sons, Inc., 2009. 580 pp. ISBN: 9780471415398. DOI: 10.1002/9780470473467.
- [175] Rainer Weinkauff et al. “Molecular physics of building blocks of life under isolated or defined conditions”. In: *The European Physical Journal D - Atomic, Molecular, Optical and Plasma Physics* 20.3 (Sept. 2002), pp. 309–316. DOI: 10.1140/epjd/e2002-00185-0.
- [176] Mitchel Weissbluth. *Atoms and Molecules*. New York, San Francisco, London: Academic Press, 1978. 713 pp. ISBN: 0127444505.
- [177] Roland Wester. “Radiofrequency multipole traps: tools for spectroscopy and dynamics of cold molecular ions”. In: *Journal of Physics B: Atomic, Molecular and Optical Physics* 42.15 (2009), p. 154001. DOI: 10.1088/0953-4075/42/15/154001.
- [178] Carl Wieman and Theodor Wolfgang Hänsch. “Doppler-Free Laser Polarization Spectroscopy”. In: *Physical Review Letters* 36.20 (May 1976), p. 1170. DOI: 10.1103/PhysRevLett.36.1170.
- [179] Stefan Willitsch et al. “Cold Reactive Collisions between Laser-Cooled Ions and Velocity-Selected Neutral Molecules”. In: *Physical Review Letters* 100.4 (2008), p. 043203. DOI: 10.1103/PhysRevLett.100.043203.
- [180] David J. Wineland. “Quantum information processing and quantum control with trapped atomic ions”. In: *Physica Scripta* 2009.T137 (2009), p. 014007. DOI: 10.1088/0031-8949/2009/T137/014007.

- [181] David J. Wineland et al. “Atomic-Ion Coulomb Clusters in an Ion Trap”. In: *Physical Review Letters* 59.26 (Dec. 1987), p. 2935. DOI: 10.1103/PhysRevLett.59.2935.
- [182] wwPDB. *RCSB Protein Data Bank*. URL: <http://www.pdb.org/> (visited on 07/19/2010).
- [183] Kaoru Yamanouchi. “Laser Chemistry and Physics: The Next Frontier”. In: *Science* 295.5560 (Mar. 2002), pp. 1659–1660. DOI: 10.1126/science.1068449.
- [184] Jun Ye and Steven T. Cundiff, eds. *Femtosecond optical frequency comb. principle, operation, and applications*. New York, NY: Springer, 2005. 361 pp. ISBN: 9780387237909. DOI: 10.1007/b102450.
- [185] Linda Young et al. “Femtosecond electronic response of atoms to ultra-intense X-rays”. In: *Nature* 466.7302 (July 2010), pp. 56–61. DOI: 10.1038/nature09177.
- [186] Nan Yu, Warren Nagourney, and Hans Dehmelt. “Radiative Lifetime Measurement of the Ba⁺ Metastable D_{3/2} State”. In: *Physical Review Letters* 78.26 (June 1997), p. 4898. DOI: 10.1103/PhysRevLett.78.4898.
- [187] Ahmed H. Zewail. “4D ultrafast electron diffraction, crystallography, and microscopy”. In: *Annual Review of Physical Chemistry* 57 (2006), pp. 65–103. DOI: 10.1146/annurev.physchem.57.032905.104748.
- [188] Ahmed H. Zewail. *The Nobel Prize in Chemistry 1999*. Nobelprize.org. URL: http://nobelprize.org/nobel_prizes/chemistry/laureates/1999/ (visited on 07/12/2010).
- [189] Chaobo B. Zhang et al. “Molecular-dynamics simulations of cold single-species and multi-species ion ensembles in a linear Paul trap”. In: *Physical Review A* 76.1 (July 2007), p. 012719. DOI: 10.1103/PhysRevA.76.012719.
- [190] Xing Zhang et al. “3.3 Å Cryo-EM Structure of a Nonenveloped Virus Reveals a Priming Mechanism for Cell Entry”. In: *Cell* 141.3 (Apr. 2010), pp. 472–482. DOI: 10.1016/j.cell.2010.03.041.

Danksagung

Zum Schluß möchte ich mich bei allen bedanken, die zum Gelingen dieser Arbeit beigetragen haben.

- An erster Stelle und in ganz besonderem Maße möchte ich meinem Doktorvater Dr. Tobias Schätz Dank aussprechen. Ein "Molekülprojekt" in seiner Gruppe begründen zu dürfen, hat mich von Anfang an mit Ehrgeiz erfüllt. Unterstützt durch seine unversiegbare Motivationskraft, seine Begeisterung auch für kleinere Zwischenerfolge und seinen Einsatz für TIAMO in stürmischen Zeiten, konnte aus einer kühnen Idee ein vielseitiger experimenteller Aufbau wachsen. Ich freue mich besonders, bei ihm stets ein offenes Ohr bei Diskussionsbedarf gefunden zu haben.
- Günther Leschhorn ist mit der Apparatur in ähnlicher Weise tief verwurzelt wie ich. Seit er als Diplomand von der experimentellen Idee infiziert wurde, haben wir gemeinsam ungezählte Höhen und Tiefen, Umzüge und durchwachte Messnächte gemeistert. Ich bin froh mit Günther einen so uneingeschränkt verlässlichen und motivierten Mitstreiter gehabt zu haben. Den 1. Juli 2008 werden wir wohl nie vergessen.
- Bei Tai Dou bedanke ich mich für den Planungseinsatz im Rahmen seiner Diplomarbeit in der Vorbereitungsphase der Verbindung von TIAMO mit der AS4b beam line. Ich denke auch gern an den Abend zurück, an dem wir erstmals Ionen kontrolliert und unter Zuhilfenahme der von ihm gelöteten "Tai-box", transferieren konnten.
- Ich bedanke mich bei Clemens Kerzl für seine Unterstützung meiner Arbeit während seines Fachhochschulpraktikums. Es hat Spaß gemacht, die Begeisterung für die Sache mit ihm zu teilen und gemeinsam all die hunderte von Schrauben und Einzelteilen der Apparatur im für Wochen zum Waschsalon umfunktionierten Chemielabor UHV-tauglich zu reinigen.
- Meine Zeit in der Schätz-Gruppe wäre ohne die anderen unübertrefflichen Doktoranden und Diplomanden des Quantensimulationsprojektes nicht annähernd so angenehm gewesen. Immer herrschte eine freundliche, hilfsbereite, fast familiäre Atmosphäre. Unvergessen werden der Spekulationseifer während der Mittagsdiskussionen, die kulinarischen Höhenflüge und Taldurchschreitungen des gemeinsamen Kochens als auch das befreiende Gipfelstürmen bei den Gruppenausflügen bleiben.
- Bei meinen Kollegen an der AS4b, insbesondere bei Elisabeth Bothschafter und Agustin Schiffrin, bedanke ich mich dafür, dass sie uns vertrauensvoll Hand an ihre Aufbauten haben legen lassen und uns geduldig in die Geheimnisse des Femtosekundenlasers einwiesen.
- Mit Markus Kowalewski habe ich einen theoretischen Chemiker kennengelernt, der stets interessiert und offen für die Berücksichtigung von experimentellen Belangen war. Es war

eine große Freude und fachliche Bereicherung mit ihm zusammen das Modell für Magnesiumhydrid immer noch eine Stufe weiterzuentwickeln.

- Ich schätze die internationale, niveauvolle und lockere Stimmung der International Max Planck Research School am MPQ. Allen Beteiligten sei herzlichst für die interessanten und unterhaltsamen workshops gedankt und viel Erfolg für die Fortführung gewünscht.
- Mit Dr. Werner Fuss habe ich interessante und äußerst lehrreiche Gespräche über Molekülphysik, Chemie und spannende Fragen darüber hinaus führen dürfen. Dafür bedanke ich mich bei ihm wie auch bei Dr. Wolfram Schmid, der unserem Projekt durch die Nachentwicklung der ESI-Ansteuerung eine wohl erst in Zukunft in vollem Umfang deutlich werdende Unterstützung beschert hat.
- Schon während meiner Diplomarbeit durfte ich mit Arnold Steyer ein allseits versiertes Unikum kennenlernen. Auf seine schnelle Hilfe bei mechanischen und organisatorischen Aufgaben war immer Verlass.
- Gute technische Unterstützung bei einem neu aufzubauenden Experiment ist von großer Bedeutung. Deshalb möchte ich mich für die ausgezeichnete Arbeit und für Hilfestellungen auch auf den letzten Drücker bei der Werkstatt und allen Technikern, besonders aber bei Josef Bayerl, Thomas Wiesmeier und Helmut Brückner bedanken.

Meinen Eltern danke ich für ihr ermutigendes Vertrauen und Unterstützung in allen Lebenslagen.

Mein größter Dank gilt Tanja!



Lebenslauf

Steffen Kahra geboren am 7. Mai 1980 in Rochlitz

Schule

1992 – 1998 Johann-Mathesius-Gymnasium in Rochlitz

Wehrdienst

Nov 1998 – Aug 1999 Luftlande-Versorgungskompanie 260 in 66663 Merzig

Studium

Okt 1999 – Sep 2001 Grundstudium Physik an der Technischen Universität Dresden

Okt 2001 – Sep 2005 Hauptstudium Physik an der Ludwig-Maximilians-Universität München

Apr 2004 – Apr 2005 Diplomarbeit „Phasenmodulation von Femtosekundenimpulsen im UV und deren Anwendung zur kohärenten Kontrolle von Molekülen“ bei Prof. Motzkus am Max-Planck-Institut für Quantenoptik

Aug 2002 – Jun 2003 Physik an Lund universitet, Schweden
Erasmus-Austausch

Okt 2001 – Jan 2002 Betreuung Physikalisches Praktikum für Mediziner

Mär 2002 – Apr 2002 Werkstudent am Werner-Heisenberg-Institut Experimentelle Abteilung, H₁-Detektor bei Prof. Kiesling

Okt 2003 – Jan 2004 Werkstudent am Max-Planck-Institut für Quantenoptik
Abteilung Laserchemie bei Prof. Motzkus

Apr 2005 – Jul 2005 Werkstudent am Max-Planck-Institut für Quantenoptik
Abteilung Laserchemie bei Prof. Motzkus

Promotion

Sep 2005 – Sep 2010 Doktorarbeit am Max-Planck-Institut für Quantenoptik bei Dr. T. Schätz
„Trapping and cooling of single molecular ions for time resolved experiments“

Apr 2006 – Jun 2009 Stipendium der International Max Planck Research School of Advanced Photon science